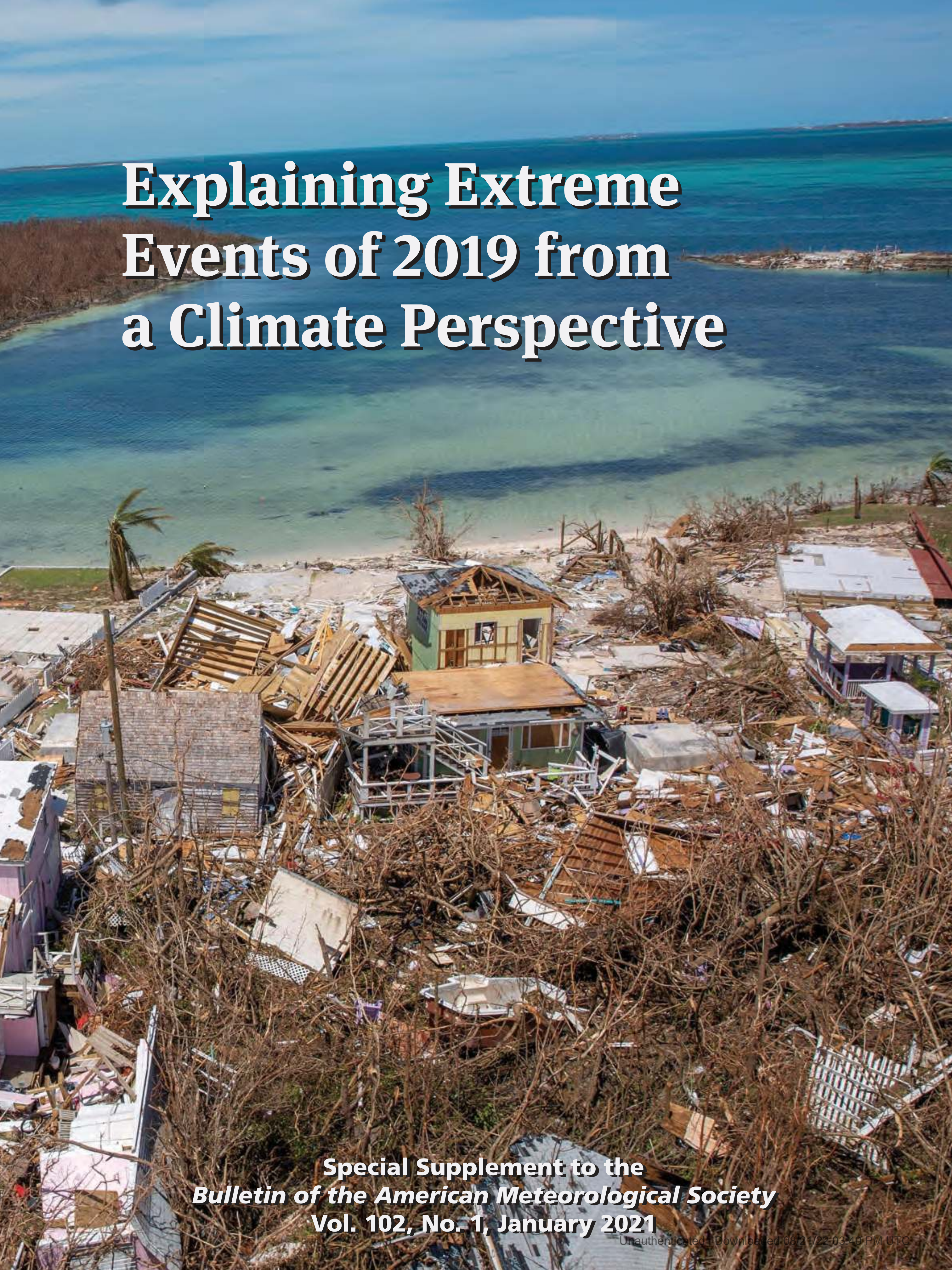

Explaining Extreme Events of 2019 from a Climate Perspective

Special Supplement to the
Bulletin of the American Meteorological Society
Vol. 102, No. 1, January 2021

EXPLAINING EXTREME EVENTS OF 2019 FROM A CLIMATE PERSPECTIVE

Editors

Stephanie C. Herring, Nikolaos Christidis, Andrew Hoell,
Martin P. Hoerling, and Peter A. Stott

***BAMS* Special Editors for Climate**

Andrew King, Thomas Knutson,
John Nielsen-Gammon, and Friederike Otto

Special Supplement to the

Bulletin of the American Meteorological Society

Vol. 102, No. 1, January 2021

American Meteorological Society

Corresponding Editor:

Stephanie C. Herring, Ph.D.
NOAA National Centers for Environmental Information
325 Broadway, E/CC23, Rm 1B-131
Boulder, CO 80305-3328
E-mail: stephanie.herring@noaa.gov

Cover: Ruins and rubble are all that are left of homes destroyed by Hurricane Dorian viewed from a U.S. Customs and Border Protection rescue helicopter 5 September 2019 in Marsh Harbour, Abaco, Bahamas. Dorian struck the small island nation as a Category 5 storm with winds of 185 mph. (credit: Planetpix/Alamy Stock Photo)

HOW TO CITE THIS DOCUMENT

Citing the complete report:

Herring, S. C., N. Christidis, A. Hoell, M. P. Hoerling, and P. A. Stott, Eds., 2021: Explaining Extreme Events of 2019 from a Climate Perspective. *Bull. Amer. Meteor. Soc.*, **102** (1), S1–S112, https:/doi.org/10.1175/BAMS-ExplainingExtremeEvents2019.1.

Citing a section (example):

Amaya, D. J., M. A. Alexander, A. Capotondi, C. Deser, K. B. Karnauskas, A. J. Miller, and N. J. Mantua, 2021: Are Long-Term Changes in Mixed Layer Depth Influencing North Pacific Marine Heatwaves? [in "Explaining Extremes of 2019 from a Climate Perspective"]. *Bull. Amer. Meteor. Soc.*, **102** (1), S59–S66, doi:https://doi.org/10.1175/BAMS-D-20-0144.1.

TABLE OF CONTENTS

Increased Risk of the 2019 Alaskan July Fires due to Anthropogenic Activity

Yan Yu, John P. Dunne, Elena Shevliakova, Paul Ginoux, Sergey Malyshev, Jasmin G. John, and John P. Krasting

July 2019 saw record-breaking wildfires burning 3,600 km^2 in Alaska. The GFDL Earth system model indicates a threefold increased risk of Alaska's extreme fires during recent decades due to primarily anthropogenic ignition and secondarily climate-induced biofuel abundance.

AFFILIATIONS: Yu—Atmospheric and Oceanic Sciences Program, Princeton University, Princeton, New Jersey; **Dunne, Shevliakova, Ginoux, Malyshev, John, and Krasting**—NOAA Geophysical Fluid Dynamics Laboratory, Princeton, New Jersey

CORRESPONDING AUTHOR: Yan Yu, yanyu@princeton.edu

DOI:10.1175/BAMS-D-20-0154.1

A supplement to this article is available online (10.1175/BAMS-D-20-0154.2)

With more than 700 wildfires and over two million acres burned in Alaska, 2019 was ranked 8th and 11th in Alaska's history in fire counts and burned area, respectively (Alaska Interagency Coordination Center 2020). Smoke plumes from July 2019 fires degraded air quality over most of Alaska, inducing the first ever dense smoke advisory (visibility less than a mile) for Anchorage, and some of the world's worst air quality in Anchorage and Fairbanks (Di Liberto 2019). Ignited by a lightning strike, the Swan Lake Fire, the most expensive fire in Alaska history, originated in the Kenai National Wildlife Refuge in southern Alaska early June and lasted for several months (Hollander 2019).

Extremely hot and dry conditions supported the unusually early and strong peak of the Alaska fire season in July 2019 (Fig. 1). Anomalous heat in spring and early sum-

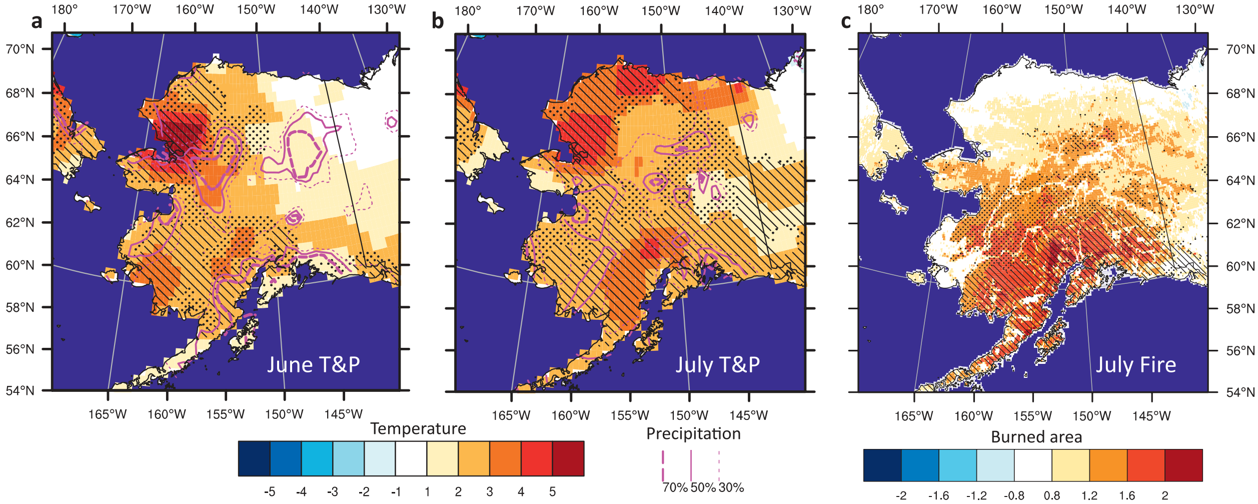

Fig. 1. Observed meteorological conditions in Alaska during the June to July fire season in 2019. (a),(b) Anomalies in 2-m air temperature (°C; color) and precipitation (contours represent 30%, 50%, and 70% lower than climatology) in (a) June and (b) July 2019, compared to the long-term average from 1979–2018. (c) Burned fraction anomalies (%) in July 2019, compared to the long-term average from 2000–18. Slashes indicate areas where the temperature in (a) and (b) or the burned fraction anomaly in (c) exceeded the highest value from the past. Stitches indicate areas where anomalies exceeded the 95th percentile in (a) and (b) and 90th percentile in (c) from the past. Analyzed datasets include National Oceanic and Atmospheric Administration (NOAA) Climate Prediction Center (CPC) Global Unified Gauge-Based Analysis of Daily temperature and precipitation (Chen et al. 2008) and MODIS burned area fraction.

mer of 2019 (Fig. 1a) and continued hot and dry conditions into July (Fig. 1b) enhanced biofuel flammability, especially over the southern and central forests in Alaska, leading to the record-breaking July burned area fraction in these regions (Fig. 1c). Indeed, 2019 saw Alaska's hottest July on record, during which its largest city, Anchorage, had a daily maximum temperature exceeding 90°F (32°C) for the first time (Di Liberto 2019). To assess the risk of extreme fires in Alaska, a previous study analyzed a Buildup Index (BUI) for potential biofuel availability and flammability, derived from cumulative scoring of daily temperature, relative humidity, and precipitation (Partain et al. 2016). Based on the BUI, Partain et al. (2016) attributed the increased risk of an extreme Alaskan fire season to anthropogenic climate change, especially warming. However, this weather-based BUI did not account for direct anthropogenic influence on fire ignition or more complex response of the land biosphere to human-induced climate change and CO_2 fertilization.

Indeed, the human-induced increase in the risk of extreme fires in Alaska is also likely attributed to elevated abundance of biofuel (Liu et al. 2015) and increased number of human-ignited fires (Kasischke et al. 2010), in addition to the higher chance of biofuel drying (Pithan and Mauritsen 2014). High-latitude ecosystems such as Alaska are believed to be most vulnerable to warming under anthropogenic climate change (Pithan and Mauritsen 2014). The CO_2 fertilization and excessive heat have resulted in an expansion and early-season growth of vegetation in the boreal forests (Mao et al. 2016; Liu et al. 2015), potentially causing early fuel abundance, more frequent and long-lasting fire events, and dense smoke releases, such as those seen in July 2019. Furthermore, an analysis of Alaska's fire ignition database indicated that human presence increased the number of ignitions near settlements, roads, and rivers during the past decades (Kasischke et al. 2010). These complex interactions between fire, climate, land ecosystem, and human activity, cannot be neglected in attribution studies of wildfires.

The present study takes advantage of the modeling capability of the Geophysical Fluid Dynamics Laboratory (GFDL) Earth System Model 4.1 (ESM4.1) to simulate all these interactions in order to assess the influence of anthropogenic activities on extreme fires in Alaska. By combining ESM4.1 simulations with satellite data, we are able to evaluate the contribution of natural and anthropogenic ignition activities, anthropogenic climate variability and change, and human influence on the land ecosystem on the occurrence of extreme fire season in Alaska.

Data and method.

To assess the influence of anthropogenic activity on the risk of extreme Alaska fire, we analyze simulations from the GFDL ESM4.1 (Dunne et al. 2020) for phase 6 of the Coupled Model Intercomparison Project (CMIP6) (Eyring et al. 2016). ESM4.1 provides coupled carbon–chemistry–climate simulations and contributes to multiple endorsed intercomparisons in CMIP6 (Eyring et al. 2016). ESM4.1 features vastly improved representation of climate mean and variability patterns from GFDL's previous chemistry and carbon coupled models (Dunne et al. 2020). The terrestrial component of ESM4.1, LM4.1 (Shevliakova et al. 2020, manuscript submitted to *J. Adv. Model. Earth Syst.*), includes a new fire model with separate data-based parameterizations for croplands and pastures (Rabin et al. 2018) and process-based parameterizations for primary and secondary lands (i.e., Fire Including Natural and Agricultural Lands model version 2, FINAL v2) (Ward et al. 2018; Rabin et al. 2018, 2015). This dynamical fire model enables representation of multi-day and crown wildfires and accounts for effects of both changes in land surface meteorological conditions and state of vegetation (Shevliakova et al. 2020, manuscript submitted to *J. Adv. Model. Earth Syst.*), thereby facilitating comprehensive projection of joint states of climate, vegetation, and fire.

The fraction of attributable risk (FAR) methodology (Stott et al. 2016) is used to examine how anthropogenic warming and ignition have changed the occurrence of an extreme fire season in Alaska, in terms of burned area and fire carbon emission. Here we analyze the risk ratio (RR) metric to quantify the factor by which the risk of an extreme event has been changed by external forcing (Fischer and Knutti 2015). To obtain such risks in the actual and natural world, lognormal cumulative distribution functions (CDFs) of Alaska's burned area and fire carbon emission in July are estimated from the time series of preindustrial and historical simulations by ESM4.1, as well as observational datasets. The Kolmogorov–Smirnov test is applied for determining the statistical significance of the difference between these CDFs (Marsaglia et al. 2003). RR is subsequently defined as $P_{\text{historical}}/P_{\text{preindustrial,}}$ where $P_{\text{historical}}$ is the probability of exceeding the extremeness of the observed July 2019 event in the observational CDF, and $P_{\text{preindustrial}}$ is the probability of exceeding such extremeness in the preindustrial CDF. To account for potential model biases, the threshold value to be attributed is obtained by projecting the observed percentile of the July 2019 value in the observational distribution onto the historical distribution during 2003–19. Here the extended historical ESM4.1 time series for 1850–2019 is obtained by combining years 1850–2014 from the historical simulation (Krasting et al. 2018a) and years 2015–19 from the future projection simulation under the Shared Socioeconomic Pathway (SSP) 5–8.5 (O'Neill et al. 2016; John et al. 2018). Analyzed observational datasets for 2003–19 include burned area from the Moderate Resolution Imaging Spectroradiometer (MODIS) onboard both the *Terra* and *Aqua* satellites (Melchiorre and Boschetti 2018) and fire carbon emission from the European Center for Medium-Range Weather Forecasts (ECMWF) Copernicus Atmosphere Monitoring Service (CAMS) Global Fire Assimilation System (GFAS) (Kaiser et al. 2012). Corresponding to the observational data length, various 17-yr time windows from the 500-yr preindustrial control run time series (Krasting et al. 2018b) are utilized for the estimation of CDF and RR, thereby facilitating uncertainty quantification. In addition to the historical and preindustrial simulations, the simulation forced by 1% yr^{-1} CO_2 concentration increase (1pctCO_2) (Eyring et al. 2016; Krasting et al. 2018c) is analyzed for disentangling the specific anthropogenic influences on the occurrence of extreme fire season in Alaska.

Results.

The comparison of simulated burned area and carbon emission from fires across Alaska with satellite data indicates satisfactory results with ESM4.1 (see Fig. ES1 in the supplemental material). Indeed, the historical simulation and observations of burned area and fire carbon emission consistently identify fire hotspots in the boreal forest region dominated by evergreen conifer trees in interior Alaska. Although the simulated historical burned fraction and fire carbon emission are generally smaller than observed, the model performance warrants credible attribution of the historical occurrence of an extreme fire season in Alaska.

According to ESM4.1, Alaska's July burned area and fire carbon emission increased since 1950s in ESM4.1, resulting in higher occurrence of a 2019-like event during recent decades, attributable to anthropogenic activity (Fig. 2). The probability of exceeding the burned area equivalent to the 2019 extreme fire season in Alaska increased from 2% before the 1950s to 7% after the 1950s (Fig. 2a). Furthermore, 63 out of the 100 consecutive 17-yr windows during 1850–1949 showed significant difference with 2003–19 in terms of probability distribution, whereas none of the 17-yr windows after 1950 showed significant difference with 2003–19 (Fig. 2a). The historical increase in the occurrence of an extremely fire-active July in Alaska is attributable to anthropogenic

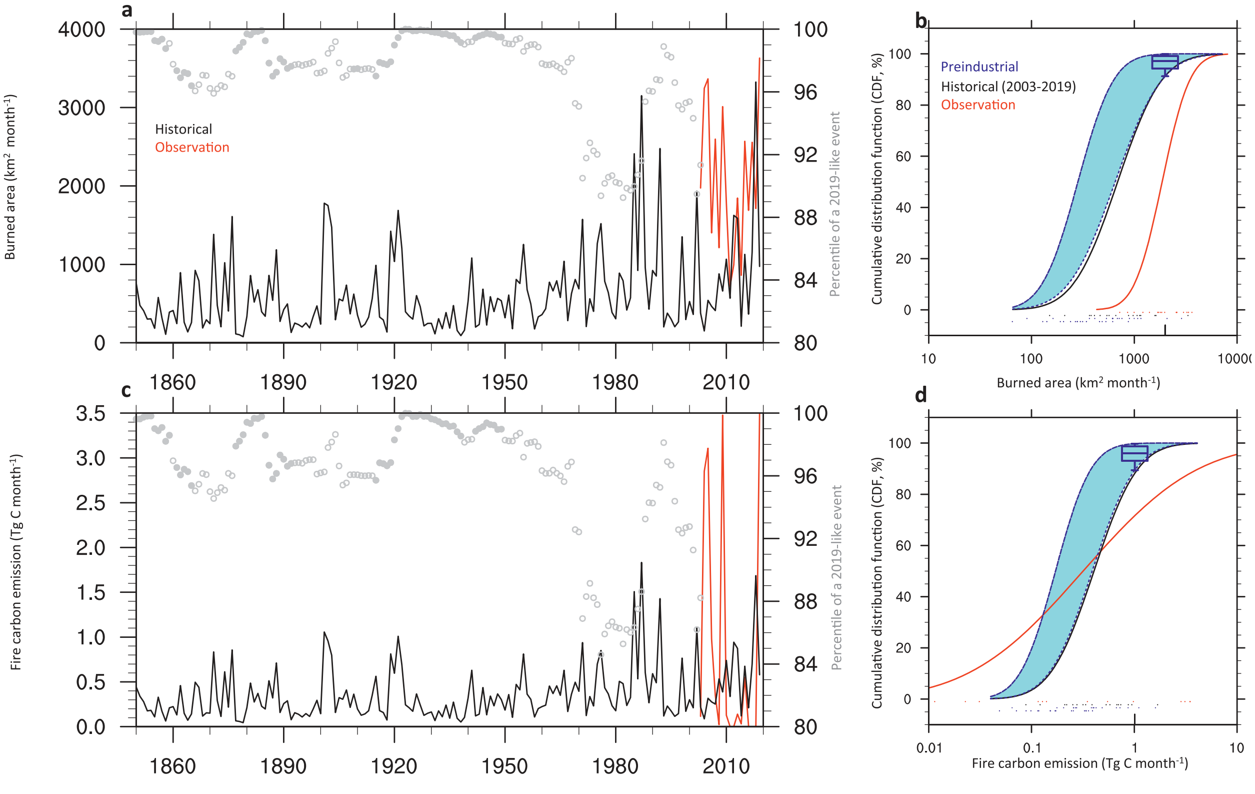

Fig. 2. Observational, historical, and preindustrial distribution of Alaska's July fire activity. (a),(c) Time series of Alaska' July burned area (km² month⁻¹) and fire carbon emission (Tg C month⁻¹), respectively, from ESM4.1 (black) and observation (red), referring to the left *y* axis. The gray circles represent the percentile of a 2019-like event in the consecutive 17-yr window, referring to the right *y* axis. The filled circles indicate 17-yr periods with significantly ($p < 0.05$) different distribution than 2003–19 in the ESM4.1 simulation. (b),(d) Cumulative distribution function (CDF; %) of burned area and fire carbon emission, respectively, in Alaska in July from observations (red) and ESM4.1 historical simulation (black) during 2003–19, as well as 500 years of ESM4.1 preindustrial simulation (blue). Dots indicate burned area and fire carbon emission in each sampled year from observation and each simulation. The boxplots show the 5th, 25th, 50th, 75th, and 95th percentiles of the percentile of a 2019-like event in all consecutive 17-yr windows from the preindustrial time series (sample size = 484). The uncertainty range of the preindustrial CDF is (the dashed blue curves) bounded by the CDFs derived from the 17-yr windows that produce the 5th and 95th percentiles of the percentile of a 2019-like event.

activity. In terms of burned area, 96% of the 484 preindustrial 17-yr windows show significantly different ($p < 0.05$) distribution than the historical 2003–19 according to the Kolmogorov–Smirnov test. The burned area associated with a 2019-like event, namely the 91st percentile in the historical times series, is equivalent to the 97th percentile in the preindustrial time series, with a 90% confidence interval of the 92nd to 100th percentile (Fig. 2b). These CDFs result in a RR, $P_{\text{historical}}/P_{\text{preindustrial}}$, of 3, with a 90% confidence interval of 1.12 to infinite. The large uncertainty in the estimated RR is mainly due to the small sample size associated with the short observational record. The historical evolution and attribution of fire carbon emission were largely consistent with those of burned area across Alaska in July (Figs. 2c,d).

The historical expansion in Alaska's burned area in July was primarily caused by an increase in anthropogenic ignition, and secondarily through climate-induced biomass abundance (Fig. 3). The historical trend in burned area, approximately proportional to the product of number of fires per area (N_{fire}) and burned area per fire ($\text{BA}_{\text{perfire}}$), was mainly due to the former, N_{fire}, which exhibits a significant, positive trend ($p < 0.001$) according to the Mann–Kendall trend test (Fig. 3a), whereas $\text{BA}_{\text{perfire}}$ shows a moderate, marginally insignificant ($p = 0.06$) trend (Fig. 3b). In FINAL v2 [Rabin et al. 2018, Eq. (4) therein], the evolution of N_{fire} can be further decomposed as the product of an ignition term, a direct climate factor, a climate-induced aboveground biomass factor, and an anthropogenic suppression on ignition efficiency factor ($1 - \text{Suppression}_{\text{PD}}$). The ignition term includes both natural and anthropogenic components. Anthropogenic ignition includes intentional or unintentional activities, such as land and ecosystem management, smoking, railroad sparks, and power lines (Fusco et al. 2016), and is represented as a function of population density in FINAL v2 (Rabin et al. 2018). Between 48% and 86% of the observed fires in Alaska were caused by anthropogenic ignition in the recent decade

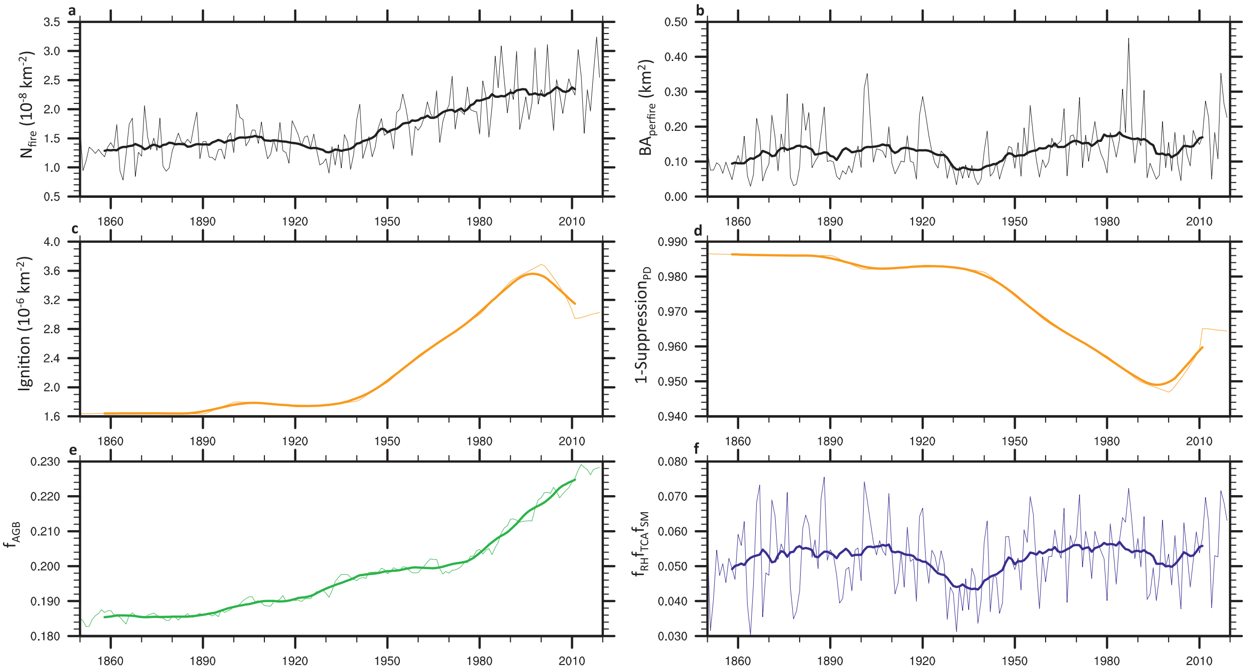

Fig. 3. Time series of Alaska's fire number, size, and contributing factors in July during 1850–2019, from the ESM4.1 historical simulation. The analyzed variables include (a) the number of fires per area (10^{-8} km^{-2}), (b) the burned area per fire (km^2), (c) total ignitions (10^{-6} km^{-2}), (d) the function of population density, expressed as unity subtracted by human-induced suppression on fire number, (e) the function of aboveground biomass (unitless), and (f) the product of the function of relative humidity, canopy air temperature, and soil moisture. In ESM4.1, number of fires per area is calculated by multiplying the factors shown in (c)–(f). The thick lines represent the 17-yr running average.

(Alaska Interagency Coordination Center 2020). Given the input of an invariant seasonal cycle of lightning to FINAL, the temporal variation in ignition is controlled by anthropogenic ignition. The historical N_{fire} increased from 1.2×10^{-8} km^{-2} during 1850–66 to 2.4×10^{-8} km^{-2} during 2003–19. Based on the decomposition, this twofold increase in N_{fire} was primarily driven by the trend in anthropogenic ignition, as the total ignition intensity increased from 1.6×10^{-6} km^{-2} during 1850–66 to 2.9×10^{-6} km^{-2}, out of which 62% were caused by anthropogenic ignition, during 2003–19. Although increased population density also resulted in elevated human suppression on ignition efficiency (Fig. 3d), this 1 – $\mathrm{Suppression}_{\mathrm{PD}}$ term decreased only slightly from 0.986 during 1850–66 to 0.948 during 2003–19, because of the moderate population density in Alaska. A secondary contribution came from the climate-induced abundance in aboveground biomass, whose contributing factor increased from 0.19 during 1850–66 to 0.22 during 2003–19. Direct influence of anthropogenic climate change on weather patterns appeared to play a minor role in the historical increase of N_{fire} in Alaska in July. As a further evidence of the key influence of climate-induced biofuel abundance on the historically increased number of fires in Alaska, the 1pctCO$_2$ experiment, which does not involve changes in anthropogenic ignition or anthropogenic suppression on ignition efficiency, shows comparable relative increase in fire carbon emission and the contribution from climate-induced biofuel abundance during the simulated 150 years (Fig. ES2).

Conclusions and discussion.

July 2019 saw record-breaking wildfires that burned over 3,600 km^2 and emitted an estimate of 3.5 Tg of carbon in Alaska, accompanied by extremely hot and dry conditions in June and July. According to GFDL ESM4.1, in July burned area and fire carbon emission increased since 1950s in Alaska, resulting in higher occurrence of a 2019-like event during recent decades. The historical increase in the occurrence of an extremely fire-active July was attributed to anthropogenic activity, which caused a threefold increase in the risk of a 2019-like fire season. The anthropogenic influence on the increased occurrence of an extreme fire season in Alaska was primarily through an increase in anthropogenic ignition, and secondarily through climate-induced biomass abundance.

A limitation of our analysis is the use of a single Earth system model, thereby introducing uncertainty in the detection and attribution of an extreme fire season in Alaska. For example, the historical ESM4.1 simulation features a general underestimation of both burned area and fire carbon emission across Alaska (Fig. ES1), unrealistic representation of observed year-to-year variations in regional burned area (Fig. 2a), and a narrower distribution of the historical, regional fire carbon emission (Figs. 2c,d). This model bias is potentially caused by underrepresentation of the trends and interannual variability in fire ignition due to lightning (Rabin et al. 2018). Although this apparent model bias is partially accounted for in the analysis, its quantitative influence on the RR remains unclear. Another possible bias is the inconsistent modeling of radiative impact of aerosols from fires. The model is based on CMIP6 emission inventory rather than using the injected aerosols from the simulated fires to calculate the radiative forcing. Other factors that are not included in the model may further complicate the human–ecosystem–fire interactions. For example, ESM4.1 does not include changing tree mortality from beetles that might also drive changes in fire spread (Hicke et al. 2012). To quantify the uncertainties introduced by analyzing a single model ESM4.1, future studies are encouraged to expand the current analysis to multiple Earth system models that represent fire dynamics.

Acknowledgments. This research is supported by NOAA and Princeton University's Cooperative Institute for Climate Science. The authors thank Isabel Martínez Cano and Khaled Ghannam for their helpful comments on the early version of this paper. The comments from two reviewers were greatly appreciated.

References

Alaska Interagency Coordination Center, 2020: Alaska fire numbers 2019. Accessed 6 April 2020, https://fire.ak.blm.gov/content/aicc/Statistics Directory/Previous Years Data and FFR Handouts/2019 Fire Data/Alaska Fire Season 2019 Presentation.pdf.

Chen, M., W. Shi, P. Xie, V. B. S. Silva, V. E. Kousky, R. W. Higgins, and J. E. Janowiak, 2008: Assessing objective techniques for gauge-based analyses of global daily precipitation. *J. Geophys. Res.*, **113**, D04110, https://doi.org/10.1029/2007JD009132.

Di Liberto, T., 2019: High temperatures smash all-time records in Alaska in early July 2019. NOAA, Accessed 6 April 2020, https://www.climate.gov/news-features/event-tracker/high-temperatures-smash-all-time-records-alaska-early-july-2019.

Dunne, J. P., and Coauthors, 2020: The GFDL Earth System Model version 4.1 (GFDL-ESM 4.1): Overall coupled model description and simulation characteristics. *J. Adv. Model. Earth Syst.*, https://doi.org/10.1029/2019MS002015, in press.

Eyring, V., S. Bony, G. A. Meehl, C. A. Senior, B. Stevens, R. J. Stouffer, and K. E. Taylor, 2016: Overview of the Coupled Model Intercomparison Project Phase 6 (CMIP6) experimental design and organization. *Geosci. Model Dev.*, **9**, 1937–1958, https://doi.org/10.5194/gmd-9-1937-2016.

Fischer, E. M., and R. Knutti, 2015: Anthropogenic contribution to global occurrence of heavy-precipitation and high-temperature extremes. *Nat. Climate Change*, **5**, 560–564, https://doi.org/10.1038/nclimate2617.

Fusco, E. J., J. T. Abatzoglou, J. K. Balch, J. T. Finn, and B. A. Bradley, 2016: Quantifying the human influence on fire ignition across the western USA. *Ecol. Appl.*, **26**, 2390–2401, https://doi.org/10.1002/eap.1395.

Hicke, J. A., M. C. Johnson, J. L. Hayes, and H. K. Preisler, 2012: Effects of bark beetle–caused tree mortality on wildfire. *For. Ecol. Manage.*, **271**, 81–90, https://doi.org/10.1016/j.foreco.2012.02.005.

Hollander, Z., 2019: An Alaska wildfire is the nation's most expensive so far this season. https://www.adn.com/alaska-news/2019/09/19/an-alaskan-wildfire-is-the-nations-most-expensive-so-far-this-season/.

John, J. G., and Coauthors, 2018: NOAA-GFDL GFDL-ESM4 model output prepared for CMIP6 ScenarioMIP ssp585. Earth System Grid Federation, accessed 27 January 2020, https://doi.org/10.22033/ESGF/CMIP6.8706.

Kaiser, J. W., and Coauthors, 2012: Biomass burning emissions estimated with a global fire assimilation system based on observed fire radiative power. *Biogeosciences*, **9**, 527–554, https://doi.org/10.5194/bg-9-527-2012.

Kasischke, E. S., and Coauthors, 2010: Alaska's changing fire regime–Implications for the vulnerability of its boreal forests. *Can. J. For. Res.*, **40**, 1313–1324, https://doi.org/10.1139/X10-098.

Krasting, J. P., and Coauthors, 2018a: NOAA-GFDL GFDL-ESM4 model output prepared for CMIP6 CMIP historical. Earth System Grid Federation, accessed 27 January 2020, https://doi.org/10.22033/ESGF/CMIP6.8597.

Krasting, J. P., and Coauthors, 2018b: NOAA-GFDL GFDL-ESM4 model output prepared for CMIP6 CMIP piControl. Earth System Grid Federation, accessed 27 January 2020, https://doi.org/10.22033/ESGF/CMIP6.8669.

Krasting, J. P., and Coauthors, 2018c: NOAA-GFDL GFDL-ESM4 model output prepared for CMIP6 CMIP 1pctCO2. Earth System Grid Federation, accessed 27 January 2020, https://doi.org/10.22033/ESGF/CMIP6.8473.

Liu, Y. Y., A. I. J. M. van Dijk, R. A. M. de Jeu, J. G. Canadell, M. F. McCabe, J. P. Evans, and G. Wang, 2015: Recent reversal in loss of global terrestrial biomass. *Nat. Climate Change*, **5**, 470–474, https://doi.org/10.1038/nclimate2581.

Mao, J., and Coauthors, 2016: Human-induced greening of the northern extratropical land surface. *Nat. Climate Change*, **6**, 959–963, https://doi.org/10.1038/nclimate3056.

Marsaglia, G., W. W. Tsang, and J. Wang, 2003: Evaluating Kolmogorov's distribution. *J. Stat. Software*, **8** (18), 1–4, https://doi.org/10.18637/jss.v008.i18.

Melchiorre, A., and L. Boschetti, 2018: Global analysis of burned area persistence time with MODIS data. *Remote Sens.*, **10**, 750, https://doi.org/10.3390/rs10050750.

O'Neill, B. C., and Coauthors, 2016: The Scenario Model Intercomparison Project (ScenarioMIP) for CMIP6. *Geosci. Model Dev.*, **9**, 3461–3482, https://doi.org/10.5194/gmd-9-3461-2016.

Partain, J. L., Jr., and Coauthors, 2016: An assessment of the role of anthropogenic climate change in the Alaska fire season of 2015. *Bull. Amer. Meteor. Soc.*, **97**, S14–S18, https://doi.org/10.1175/BAMS-D-16-0149.1.

Pithan, F., and T. Mauritsen, 2014: Arctic amplification dominated by temperature feedbacks in contemporary climate models. *Nat. Geosci.*, **7**, 181–184, https://doi.org/10.1038/ngeo2071.

Rabin, S. S., B. I. Magi, E. Shevliakova, and S. W. Pacala, 2015: Quantifying regional, time-varying effects of cropland and pasture on vegetation fire. *Biogeosciences*, **12**, 6591–6604, https://doi.org/10.5194/bg-12-6591-2015.

Rabin, S. S., D. S. Ward, S. L. Malyshev, B. I. Magi, E. Shevliakova, and S. W. Pacala, 2018: A fire model with distinct crop, pasture, and non-agricultural burning: Use of new data and a model-fitting algorithm for FINAL.1. *Geosci. Model Dev.*, **11**, 815–842, https://doi.org/10.5194/gmd-11-815-2018.

Stott, P. A., and Coauthors, 2016: Attribution of extreme weather and climate-related events. *Wiley Interdiscip. Rev.: Climate Change*, **7**, 23–41, https://doi.org/10.1002/wcc.380.

Ward, D. S., E. Shevliakova, S. Malyshev, and S. Rabin, 2018: Trends and variability of global fire emissions due to historical anthropogenic activities. *Global Biogeochem. Cycles*, **32**, 122–142, https://doi.org/10.1002/2017GB005787.

Anthropogenic Influence on Hurricane Dorian's Extreme Rainfall

Kevin A. Reed, Michael F. Wehner, Alyssa M. Stansfield, and Colin M. Zarzycki

Hindcast attribution simulations suggest that anthropogenic climate change increased the likelihood of Hurricane Dorian's extreme 3-hourly rainfall amounts and total accumulated rainfall by 8%–18% and 5%–10%, respectively.

AFFILIATIONS: Reed and Stansfield—School of Marine and Atmospheric Sciences, Stony Brook University, Stony Brook, New York; **Wehner**—Lawrence Berkeley National Laboratory, Berkeley, California; **Zarzycki**—Pennsylvania State University, State College, Pennsylvania

CORRESPONDING AUTHOR: Kevin Reed, kevin.reed@stonybrook.edu

DOI:10.1175/BAMS-D-20-0160.1

A supplement to this article is available online (10.1175/BAMS-D-20-0160.2)

Hurricane Dorian formed on 24 August 2019 from a tropical wave and developed into a Category 5 hurricane on 1 September 2019 before making landfall in the Bahamas (Avila et al. 2020). The impacts on the Bahamas were extreme, including rainfall totals over 0.5 m in the region (Avila et al. 2020). This was on the heels of the recent damaging North Atlantic hurricanes of 2017 and 2018, which impacted various regions with different combinations of hazards (Klotzbach et al. 2018a; Avila 2019).

Tropical cyclones are very costly natural disasters (Klotzbach et al. 2018b) due to a diverse set of impacts, including high winds, extreme rainfall, storm surge, and fresh and/or saltwater flooding. Previous work has explored the potential impact of climate change, both in the past and projected into the future, on these hazards (e.g., Knutson et al. 2010, 2019, 2020; Christensen et al. 2013; Walsh et al. 2016). A recent review by Knutson et al.

(2020) estimates that the global mean near-storm rainfall increases at about 7% per 1°C. Significant advances have been made in attribution frameworks to help quantify the effect of climate change on individual hurricanes. Investigations of individual storms using various attribution methodologies suggest that changes in rainfall can exceed the Knutson et al. (2020) estimate, although there are uncertainties associated with the use of different rainfall metrics (e.g., Risser and Wehner 2017; van Oldenborgh et al. 2017; Emanuel 2017; Wang et al. 2018; Keellings and Hernández Ayala 2019). Here we apply a hindcast attribution methodology to Hurricane Dorian previously developed and tested for Hurricane Florence (Reed et al. 2020), Typhoon Haiyan (Wehner et al. 2019), and numerous other tropical cyclones (Patricola and Wehner 2018) that focuses on storm rainfall due to confidence in the model's ability to simulate precipitation processes.

Methods.

This work makes use of the variable-resolution configuration of the Community Atmosphere Model version 5 (CAM5; Neale et al. 2012) with a 28-km nest over the North Atlantic [as in Reed et al. (2020)]. CAM5, at grid spacings of 28 km, has been used previously to explore tropical cyclones and rainfall at both climate (e.g., Wehner et al. 2014; Zarzycki and Jablonowski 2014; Wehner et al. 2015; Bacmeister et al. 2018; Stansfield et al. 2020a) and weather time scales (e.g., Zarzycki and Jablonowski 2015; Wehner et al. 2019; Reed et al. 2020). Following the methodology of Zarzycki and Jablonowski (2015), short 7-day ensemble hindcasts are initialized both in advance of and after Hurricane Dorian's landfall in the Bahamas at 12-h increments starting at 1200 UTC 30 August and ending at 0000 UTC 4 September for a total of 10 initialization times. The CAM5 hindcasts are initialized with atmospheric and ocean surface analyses from NOAA's GDAS and OISST, respectively, to construct an ensemble under the "actual" climate and weather conditions. Twenty ensemble members are created at each initialization time by perturbing a set of three parameters (convective time scale, precipitation coefficient, and parcel fractional mass entrainment rate) in the Zhang and McFarlane (1995) deep convection parameterization [following Reed et al. (2020), who used the parameter ranges from He and Posselt (2015)], resulting in a 200-member ensemble. Note that since modifying parameters in the convective parameterization can modulate precipitation (e.g., Zhao et al. 2012) the ensembles are perturbed with the same values on a member-to-member basis across all experiments.

A "counterfactual" ensemble (20 members at each initialization time) is constructed by removing the anthropogenic signal from the 3D air temperature, 3D specific humidity, and 2D sea surface temperature (SST) initial conditions used for the actual ensemble. Following Reed et al. (2020), the anthropogenic signal is approximated by computing the difference between the All-Hist (with prescribed SST, sea ice, greenhouse gases, and aerosols derived from observations) and Nat-Hist (with prescribed SST, surface ice, greenhouse gases, and aerosols boundary conditions modified to remove anthropogenic forcings) CAM5 simulations completed under Climate of the Twentieth Century (C20C+) Detection and Attribution Project protocols (available at portal.nersc.gov/c20c), designed for event attribution (Stone et al. 2019), for the average of August and September for the last 20 years (1996–2016). This results in a difference of SST of about 0.75°C in the Bahamas region. Dynamical fields, such as zonal and meridional wind, are not adjusted in the initial conditions counterfactual ensemble, consistent with Reed et al. (2020).

For both the actual and counterfactual ensembles, the TempestExtremes software package (Ullrich and Zarzycki 2017) is used to detect and track the simulated storms and extract storm-related rainfall using the approach of Stansfield et al. (2020b), which specifies storm rainfall to be within an outer radius defined by a 8 m s^{-1} threshold of the azimuthally averaged azimuthal wind speed. Hurricane Dorian's observed rainfall estimates from NASA's Integrated Multi-satellitE Retrievals for GPM (IMERG; https://pmm.nasa.gov/data-access/downloads/gpm) are used to calculate the maximum 3-hourly rainfall amount, while recognizing that there are substantial uncertainties associated with heavy tropical cyclone rainfall in satellite estimates (e.g., underestimating storm rainfall over land; Chen et al. 2013).

Given resolution limitations, this work focuses on characterizing changes in the precipitation associated with Hurricane Dorian in the CAM5 hindcasts simulations. It is well known that intensity can influence storm rainfall and that numerical simulations at these grid spacings are limited in their ability to represent intensity (i.e., maximum surface wind; Davis et al. 2018). Furthermore, the work of Patricola and Wehner (2018) demonstrated, using a comparable hindcast attribution framework with the Weather Research and Forecasting (WRF) Model, that while the simulated intensity (i.e., maximum wind speed) of hurricanes is underestimated at 27-km grid spacing compared to 3-km grid spacing, changes in storm rainfall due to warming are relatively insensitive to this resolution difference. The CAM5 actual ensemble simulates an average intensity bias at a lead time of 72 h (120 h) of approximately 47 hPa (39 hPa), which is comparable to the intensity errors for the 27-km grid spacing simulation of other category 5 hurricanes in Patricola and Wehner (2018) and consistent with other operational numerical weather prediction for an intensifying major hurricane. While imperfect, CAM5 hindcasts of tropical cyclones have demonstrated skill in representing storm rainfall (Reed et al. 2020) and tracks comparable to forecasts from operational numerical weather prediction (Zarzycki and Jablonowski 2015).

Results.

Comparing 3-hourly rainfall amounts and total accumulated rainfall across the actual and counterfactual ensembles allows for an analysis of the potential impact of observed climate change on Hurricane Dorian. The ensemble mean accumulated precipitation throughout the lifetime of the simulated storms at all initialization times is shown in Fig. 1. The spatial ensemble mean rainfall patterns suggest that there are similarities in the simulated tracks for the actual and counterfactual ensembles for a given initialization time, allowing for direct comparison. However, there are variations in the simulated tracks across different initialization times (Fig. ES1), consistent with real-time operational forecasts. Furthermore, additional analysis shows that the average CAM5 hindcast track error at a lead time of 72 h (120 h) is 144 km (230 km), which is within range of track errors associated with the official operational models used by the National Hurricane Center. When comparing the magnitude of the ensemble mean accumulated rainfall at individual initialization times between the actual and counterfactual ensembles, Fig. 1 indicates that many areas experience increased precipitation in the actual ensemble compared to the counterfactual. This is also true in the region near the Bahamas (defined to be 25.5°–29.5°N, 76°–80°W; outlined in Fig. 1) where the most extreme rainfall accumulations were observed to occur (Fig. ES2), providing some evidence that the model represents extreme rainfall sufficiently well in the region. The Bahamas region is simulated to experience the highest rainfall accumulations in the ensembles during the initializations between 0000 UTC 31 August and 1200 UTC 2 September.

Figure 2a shows the probability distribution of the 3-hourly rainfall amounts associated with the simulated storm over its lifetime for all ensembles. The results suggest that there is a shift toward higher 3-hourly rainfall amounts in the actual ensemble with climate change. The likelihood of 3-hourly precipitation above the IMERG estimated maximum of 0.136 m increases from approximately 0.145% in the counterfactual ensemble to about 0.168% in the actual ensemble, representing an increase of 16% (95% confidence interval: 14%–18%) in the likelihood of such events. It is worth noting that a Dorian-like storm with rainfall at or above the IMERG estimated 3-hourly maximum is a 99.8th percentile event across the 200-member CAM5 ensemble, which is indeed a rare event at the tail of the simulated distribution, suggesting that the model framework has some skill in reproducing the extreme rainfall rates observed for Hurri-

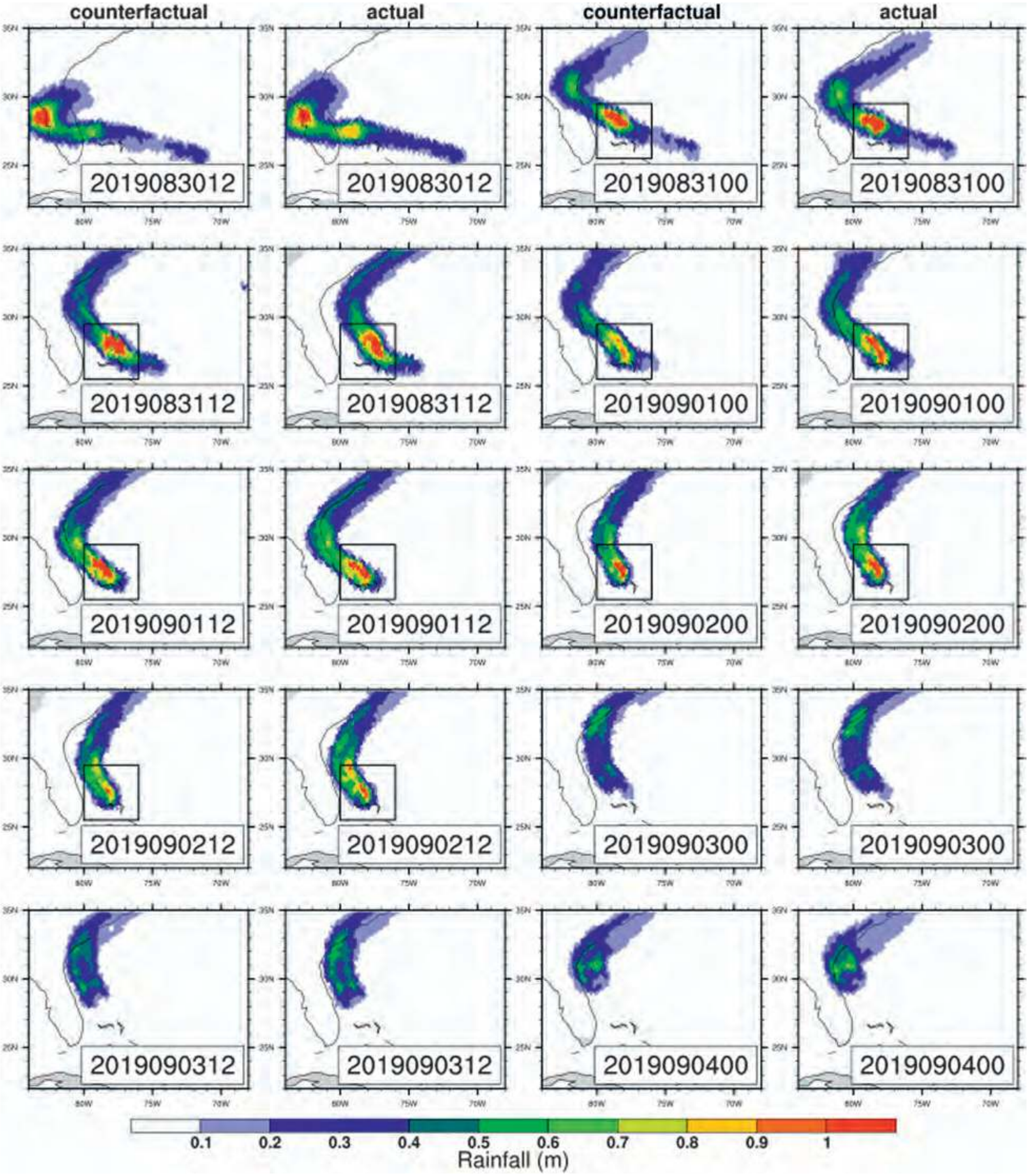

Fig. 1. Total accumulated ensemble mean storm-related rainfall (m) over the entire forecast period (excluding the first 12 h) for each initialization time (as labeled) of the counterfactual and actual realizations of Hurricane Dorian. Each initialization time contains 20 ensemble members. The Bahamas region is denoted (black outline) for the initialization times used for the region-specific analysis.

cane Dorian. Given that the IMERG maximum is an estimate, we performed a sensitivity analysis by repeating the calculation for a maximum 3-hourly rainfall amount of 0.1 and 0.17 m (representing a ±25% change from the estimated maximum), and the percentage increase ranges from 8% to 13% in the likelihood of such events. Analysis of the maximum 3-hourly rainfall amounts (Fig. 2c) in each ensemble reveals an increase in the maximum precipitation of 2% (95% confidence interval: −1% to 4%). Figure 2b shows the same probability distribution but for the Bahamas region (outlined in Fig. 1) associated with the initialization times that produce large rainfall amounts in the region. The results again suggest that there is a shift toward higher 3-hourly rainfall amounts in the actual ensemble with climate change, particularly at the highest rain rates. The maximum 3-hourly rainfall in the Bahamas region (Fig. 2d) is simulated to have increased by 2% (95% confidence interval: 1%–3%) due to climate change, while the likelihood of 0.136 m amounts increases marginally (<1%).

A more integrated measure of rainfall associated with Hurricane Dorian is the sum of all accumulated precipitation during the simulated storms, in which CAM5 demonstrates some skill in reproducing the accumulated amounts and spatial distribution (Fig. 1) when compared to IMERG estimates (Fig. ES2). For the full ensemble there is a clear increase in the total accumulated precipitation of 7% (95% confidence interval: 5% to 10%) and in the subset ensemble in the Bahamas region of 3% (95% confidence interval: −1% to 7%). Note that for all analysis in this section the 95% confidence interval is derived from a bootstrap analysis of 1000 samples.

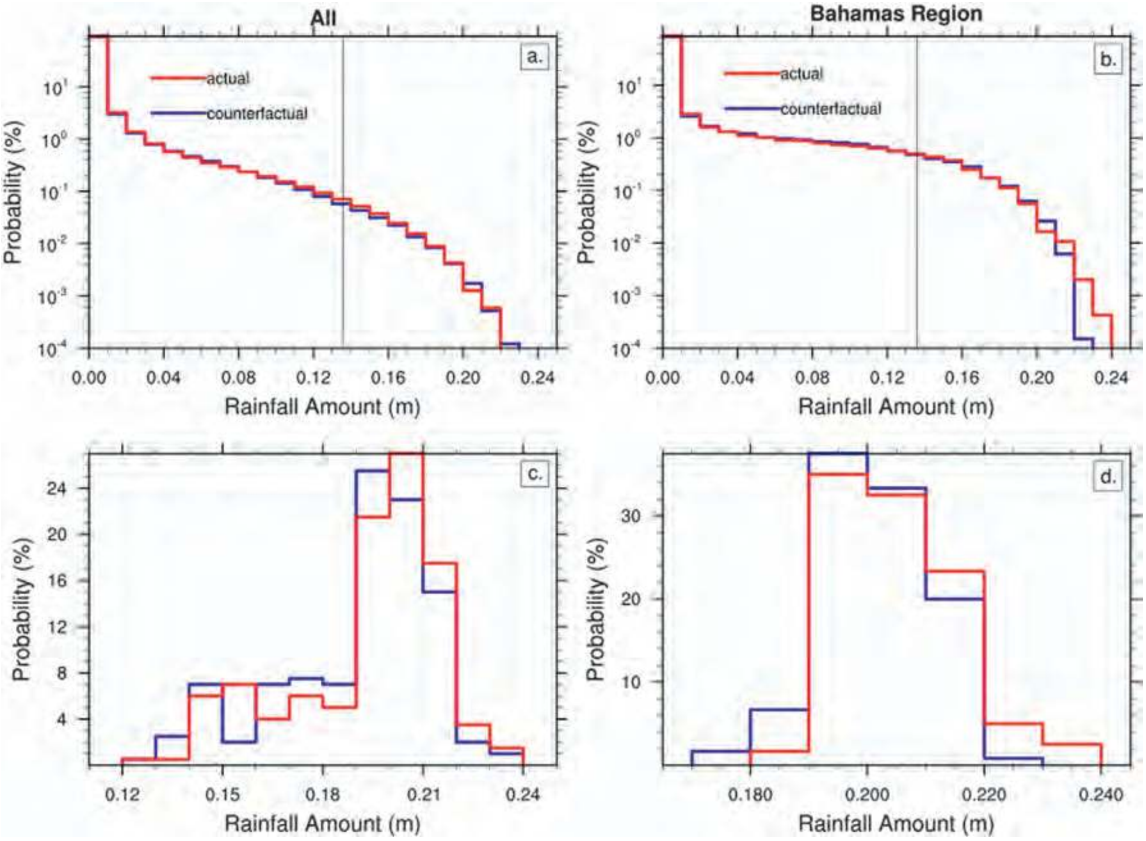

Fig. 2. Probability distributions of the (a),(b) 3-hourly rainfall amounts and (c),(d) maximum 3-hourly rainfall amounts associated with Hurricane Dorian in the actual and counterfactual ensembles. Results are shown for (left) rainfall at all initialization times throughout the domain and (right) the six subset initialization times and Bahamas region only (see Fig. 1). The vertical line in (a),(b) represents observed maximum 3-hourly rainfall amount as estimated by IMERG.

Conclusions.

The work explores the potential impact of climate change on the rainfall associated with Hurricane Dorian using the CAM5 hindcast attribution framework. The analysis indicates the likelihood of 3-hourly rainfall accumulations above 0.136 m (observed) increases by 16%, while the maximum 3-hourly rainfall amount increases by 2% due to climate change. When focusing on the extreme accumulations of rainfall that occurred over multiple days, the analysis reveals the total accumulated rainfall over the area of the simulated storm increased by 7%. This work provides additional evidence that climate change has increased the magnitude and probability of extreme rainfall associated with recent devastating hurricanes (Risser and Wehner 2017; van Oldenborgh et al. 2017; Emanuel 2017; Wang et al. 2018; Trenberth et al. 2018; Keellings and Hernández Ayala 2019; Reed et al. 2020) and is consistent with projected changes in tropical cyclone–related precipitation under future climate change scenarios (e.g., Villarini et al. 2014; Knutson et al. 2020; Stansfield et al. 2020a). Depending on the rainfall metric used the simulated change presented here for Hurricane Dorian is closer to, or below, the theoretical Clausius–Clapeyron scaling of ~4% to 6% (given the 0.75°C SST change). However, differences in metrics and methodologies, including sensitivities to model resolution which will be the focus of future work, among the various hurricane precipitation attribution studies are critical to the interpretation of these numbers. As global SSTs continue to warm, rainfall accumulations associated with storms like Hurricane Dorian will undoubtedly continue to increase.

Acknowledgments. This work was partially supported by the Stony Brook Foundation's Minghua Zhang Early Career Faculty Innovation Fund, NASA under Grant 80NSSC19K0717, the NSF Research Traineeship (NRT) program (1633299), and the Regional and Global Model Analysis (RGMA) program area of the DOE's Office of Science under Contract DE-AC02-05CH11231.

References

Avila, L. A., 2019: The 2018 Atlantic hurricane season: Another catastrophic year for the United States. *Weatherwise*, **72**, 14–21, https://doi.org/10.1080/00431672.2019.1612201.

——, S. R. Stewart, R. Berg, and A. B. Hagen, 2020: National Hurricane Center Tropical Cyclone Report, Tropical Cyclone Report Hurricane Dorian AL052019, National Hurricane Center, 74 pp., https://www.nhc.noaa.gov/data/tcr/AL052019_Dorian.pdf.

Bacmeister, J. T., K. A. Reed, C. Hannay, P. J. Lawrence, S. C. Bates, J. E. Truesdale, N. A. Rosenbloom, and M. N. Levy, 2018: Projected changes in tropical cyclone activity under future warming scenarios using a high-resolution climate model. *Climatic Change*, **146**, 547–560, https://doi.org/10.1007/s10584-016-1750-x.

Chen, Y., E. E. Ebert, K. J. E. Walsh, and N. E. Davidson, 2013: Evaluation of TRMM 3B42 precipitation estimates of tropical cyclone rainfall using PACRAIN data. *J. Geophys. Res. Atmos.*, **118**, 2184–2196, https://doi.org/10.1002/jgrd.50250.

Christensen, J. H., and Coauthors, 2013: Climate phenomena and their relevance for future regional climate change. Climate Change 2013: The Physical Science Basis, T. F. Stocker et al., Eds., Cambridge University Press, 1217–1308.

Davis, C. A., 2018: Resolving tropical cyclone intensity in models. *Geophys. Res. Lett.*, **45**, 2082–2087. https://doi.org/10.1002/2017GL076966.

Emanuel, K., 2017: Assessing the present and future probability of Hurricane Harvey's rainfall. *Proc. Natl. Acad. Sci. USA*, **114**, 12 681–12 684, https://doi.org/10.1073/pnas.1716222114.

He, F., and D. J. Posselt, 2015: Impact of parameterized physical processes on simulated tropical cyclone characteristics in the Community Atmosphere Model. *J. Climate*, **28**, 9857–9872, https://doi.org/10.1175/JCLI-D-15-0255.1.

Keellings, D., and J. J. Hernández Ayala, 2019: Extreme rainfall associated with Hurricane Maria over Puerto Rico and its connections to climate variability and change. *Geophys. Res. Lett.*, **46**, 2964–2973, https://doi.org/10.1029/2019GL082077.

Klotzbach, P. J., C. J. Schreck III, J. M. Collins, M. M. Bell, E. S. Blake, and D. Roache, 2018a: The extremely active 2017 North Atlantic hurricane season. *Mon. Wea. Rev.*, **146**, 3425–3443, https://doi.org/10.1175/MWR-D-18-0078.1.

——, S. G. Bowen, R. Pielke, and M. Bell, 2018b: Continental U.S. hurricane landfall frequency and associated damage: Observations and future risks. *Bull. Amer. Meteor. Soc.*, **99**, 1359–1376, https://doi.org/10.1175/BAMS-D-17-0184.1.

Knutson, T. R., and Coauthors, 2010: Tropical cyclones and climate change. *Nat. Geosci.*, **3**, 157–163, https://doi.org/10.1038/ngeo779.

——, and Coauthors, 2019: Tropical cyclones and climate change assessment: Part I. Detection and attribution. *Bull. Amer. Meteor. Soc.*, **100**, 1987–2007, https://doi.org/10.1175/BAMS-D-18-0189.1.

——, and Coauthors, 2020: Tropical cyclones and climate change assessment: Part II. Projected response to anthropogenic warming. *Bull. Amer. Meteor. Soc.*, **101**, E303–E322, https://doi.org/10.1175/BAMS-D-18-0194.1.

Neale, R. B., C. C. Chen, A. Gettelman, P. H. Lauritzen, S. Park, D. L. Williamson, and M. A. Taylor, 2012: Description of the NCAR Community Atmosphere Model (CAM 5.0). NCAR Tech. Note NCAR/TN-486+STR, 274 pp., www.cesm.ucar.edu/models/cesm1.0/cam/docs/description/cam5_desc.pdf.

Patricola, C. M., and M. F. Wehner, 2018: Anthropogenic influences on major tropical cyclone events. *Nature*, **563**, 339–346, https://doi.org/10.1038/s41586-018-0673-2.

Reed, K. A., A. M. Stansfield, M. F. Wehner, and C. M. Zarzycki, 2020: Forecasted attribution of the human influence on Hurricane Florence. *Sci. Adv.*, **6**, eaaw9253, https://doi.org/10.1126/sciadv.aaw9253.

Risser, M. D., and M. F. Wehner, 2017: Attributable human-induced changes in the likelihood and magnitude of the observed extreme precipitation during Hurricane Harvey. *Geophys. Res. Lett.*, **44**, 12 457–12 464, https://doi.org/10.1002/2017GL075888.

Stansfield, A. M., K. A. Reed, and C. M. Zarzycki, 2020a: Changes in precipitation from North Atlantic tropical cyclones under RCP scenarios in the variable-resolution Community Atmosphere Model. *Geophys. Res. Lett.*, **47**, e2019GL086930, https://doi.org/10.1029/2019GL086930.

——, ——, ——, P. A. Ullrich, and D. R. Chavas, 2020b: Assessing tropical cyclones' contribution to precipitation over the eastern United States and sensitivity to the variable-resolution domain extent. *J. Hydrometeor.*, **21**, 1425–1445, https://doi.org/10.1175/JHM-D-19-0240.1.

Stone, D. A., and Coauthors, 2019: Experiment design of the International CLIVAR C20C+ detection and attribution project. *Wea. Climate Extrem.*, **24**, 100206, https://doi.org/10.1016/j.wace.2019.100206.

Trenberth, K. E., L. Cheng, P. Jacobs, Y. Zhang, and J. Fasullo, 2018: Hurricane Harvey links to ocean heat content and climate change adaptation. *Earth's Future*, **6**, 730–744, https://doi.org/10.1029/2018EF000825.

Ullrich, P. A., and C. M. Zarzycki, 2017: TempestExtremes: A framework for scale-insensitive pointwise feature tracking on unstructured grids. *Geosci. Model Dev.*, **10**, 1069–1090, https://doi.org/10.5194/gmd-10-1069-2017.

van Oldenborgh, G. J., and Coauthors, 2017: Attribution of extreme rainfall from Hurricane Harvey, August 2017. *Environ. Res. Lett.*, **12**, 124009, https://doi.org/10.1088/1748-9326/aa9ef2.

Villarini, G., D. A. Lavers, E. Scoccimarro, M. Zhao, M. F. Wehner, G. A. Vecchi, T. R. Knutson, and K. A. Reed, 2014: Sensitivity of tropical cyclone rainfall to idealized global scale forcings. *J. Climate*, **27**, 4622–4641, https://doi.org/10.1175/JCLI-D-13-00780.1.

Walsh, K. J., and Coauthors, 2016: Tropical cyclones and climate change. *Wiley Interdiscip. Rev.: Climate Change*, **7**, 65–89, https://doi.org/10.1002/WCC.371.

Wang, S.-Y. S., L. Zhao, J.-H. Yoon, P. Klotzbach, and R. R. Gillies, 2018: Quantitative attribution of climate effects on Hurricane Harvey's extreme rainfall in Texas. *Environ. Res. Lett.*, **13**, 054014, https://doi.org/10.1088/1748-9326/aabb85.

Wehner, M., and Coauthors, 2014: The effect of horizontal resolution on simulation quality in the Community Atmospheric Model, CAM5.1. *J. Adv. Model. Earth Syst.*, **6**, 980–997, https://doi.org/10.1002/2013MS000276.

——, K. A. Reed, D. Stone, W. D. Collins, and J. Bacmeister, 2015: Resolution dependence of future tropical cyclone projections of CAM5.1 in the U.S. CLIVAR hurricane working group idealized configurations. *J. Climate*, **28**, 3905–3925, https://doi.org/10.1175/JCLI-D-14-00311.1.

——, C. Zarzycki, and C. Patricola, 2019: Estimating the human influence on tropical cyclone intensity as the climate changes. Hurricane Risk, Vol. I, J. Collins and K. Walsh, Eds., Springer, 235–260.

Zarzycki, C. M., and C. Jablonowski, 2014: A multidecadal simulation of Atlantic tropical cyclones using a variable-resolution global atmospheric general circulation model. *J. Adv. Model. Earth Syst.*, **6**, 805–828, https://doi.org/10.1002/2014MS000352.

——, and ——, 2015: Experimental tropical cyclone forecasts using a variable-resolution global model. *Mon. Wea. Rev.*, **143**, 4012–4037, https://doi.org/10.1175/MWR-D-15-0159.1.

Zhang, G. J., and N. A. McFarlane, 1995: Sensitivity of climate simulations to the parameterization of cumulus convection in the Canadian Climate Centre general circulation model. *Atmos.–Ocean*, **33**, 407–446, https://doi.org/10.1080/07055900.1995.9649539.

Zhao, M., I. M. Held, and S. Lin, 2012: Some counterintuitive dependencies of tropical cyclone frequency on parameters in a GCM. *J. Atmos. Sci.*, **69**, 2272–2283, https://doi.org/10.1175/JAS-D-11-0238.1.

Quantifying Human-Induced Dynamic and Thermodynamic Contributions to Severe Cold Outbreaks Like November 2019 in the Eastern United States

Chunlüe Zhou, Aiguo Dai, Junhong Wang, and Deliang Chen

The eastern U.S. 2019 November cold outbreak was mainly caused by extreme northerly winds. CMIP6 results find nonsignificant dynamical effects of anthropogenic climate change on such regional winds; thermodynamic effects alone decreased the probability of this cold event by 70%.

AFFILIATIONS: Zhou and Dai—Department of Atmospheric and Environmental Sciences, University at Albany, State University of New York, Albany, New York; **Wang**—Department of Atmospheric and Environmental Sciences, and New York State Mesonet, University at Albany, State University of New York, Albany, New York; **Chen**—Regional Climate Group, Department of Earth Sciences, University of Gothenburg, Gothenburg, Sweden

CORRESPONDING AUTHOR: Dr. Chunlüe Zhou, chunluezhou@gmail.com

DOI:10.1175/BAMS-D-20-0171.1

A supplement to this article is available online (10.1175/BAMS-D-20-0171.2)

In November 2019, although most of the world was anomalously warm (as the second warmest globally in November since 1900), 42 stations in the northeastern United States broke the historical record-low temperature since 1900 (stars in Fig. 1a). November average daily minimum temperatures (Tmin) at 536 stations in the eastern United States were below their 10th percentiles, in contrast to above-normal Tmin in the western United States (filled circles in Fig. 1a). This severe cold outbreak had a significant impact on society; for example, it increased residential energy consumption in the eastern United States by 84% in November 2019 relative to the 2000–18 November mean (https://www.ncdc.noaa.gov/societal-impacts/redti/).

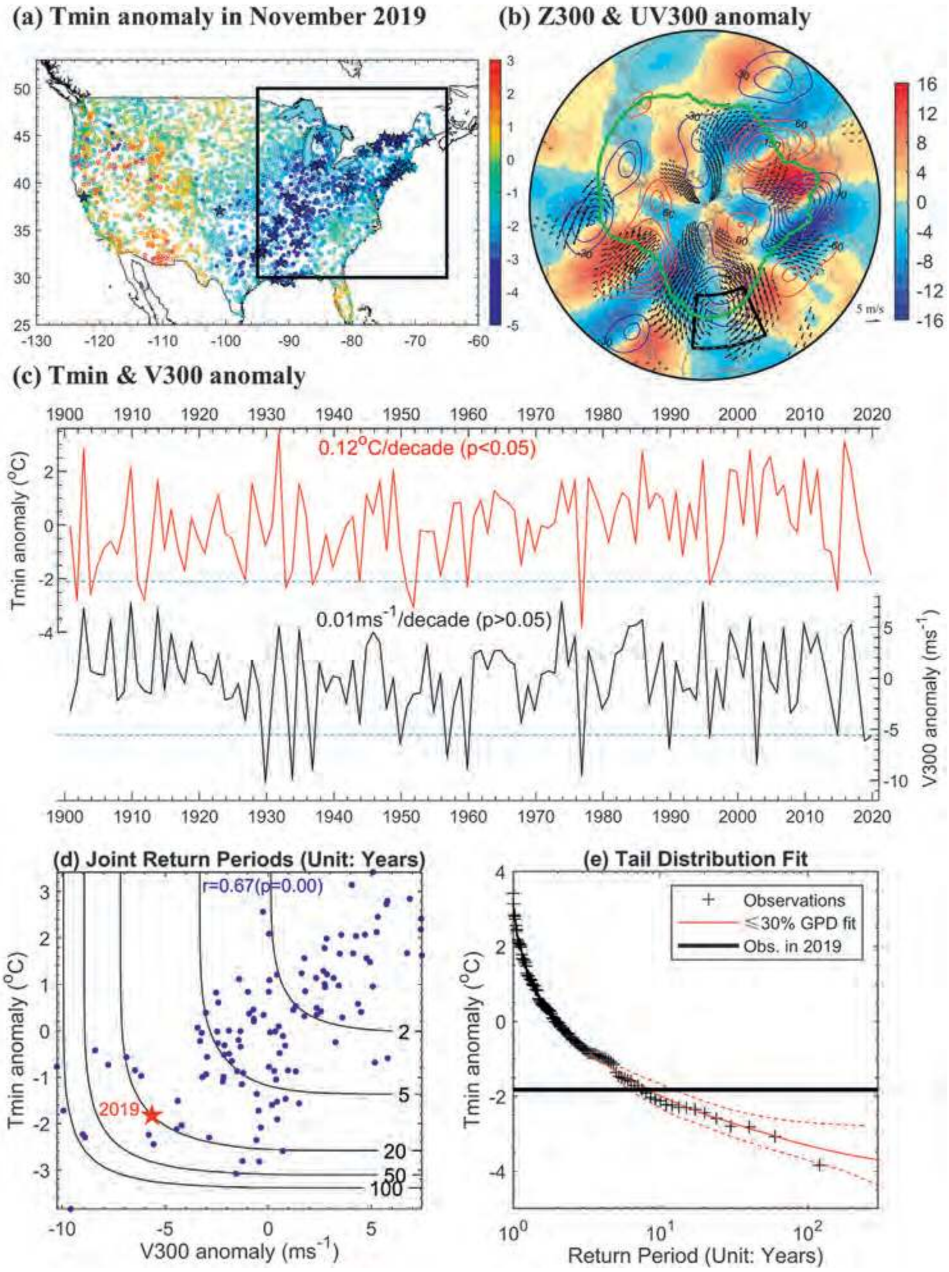

Fig. 1. (a) Spatial pattern of the average daily minimum air temperature (Tmin) anomalies (relative to 1900–2019 mean) in November 2019 over the contiguous United States. Stations marked respectively as stars and filled circles underwent the record-breaking and extremely low Tmin anomalies in November 2019 since 1900. Study region is shown as the black rectangle (for land areas only). (b) The 300-hPa geopotential height anomalies (Z300; red/blue contours with a 30-m interval) and meridional wind anomalies (V300; color shading; m s^{-1}) in November 2019. The 300-hPa wind anomalies regressed onto the November 2019 Tmin anomalies are shown as arrows for areas where regressions of the V300 anomalies are significant at the 5% level. The average jet stream position with maximum wind speed is shown as a green contour. The region for the average V300 anomalies is shown as the black frame. (c) Time series of regional average Tmin and V300 anomalies. Trends are shown at the middle. The 10th percentile line is shown as light blue horizontal line. (d) Joint return periods (contours) of the observed Tmin and V300 anomalies (blue dots). The 2019 values are shown as a red star. Note that the weak winds during the five cold events are related to the uncertainty of reanalysis V300 during the early period, i.e., 1900–30. (e) Generalized Pareto distribution (GPD) fit (red; dashed line for 5%–95% confidence intervals) of the observed November Tmin anomalies (black pluses).

For the past regional cold air outbreaks, a persistent and meandering anomalous polar jet stream was found to propagate the Arctic cold air into many parts of the eastern United States through anomalous northerlies (Francis et al. 2017; Cohen et al. 2018; Xie et al. 2019). Global warming raises the background mean temperature, which increases the frequency of the warm events but decreases the chance of cold events, especially in regions north of 50°N where surface warming has been the largest (Alexander et al. 2006; Hartmann et al. 2013; Christiansen et al. 2018). However, the frequency of winter extreme cold events in the eastern United States and some Eurasian regions has increased in recent decades, especially in mid- to late winter (Scherer and Diffenbaugh 2014; Cohen et al. 2018). These increases in cold extremes have been mainly attributed to changes in the frequency of certain weather patterns that displace cold airmasses southward to different sectors of the northern midlatitudes (Zhou ang Wang 2016; Singh et al. 2016; Deng et al. 2020; Luo et al. 2020). However, whether recent global warming has contributed to the weather pattern change remains unknown.

While the thermodynamic effect of global warming alone is expected to increase warm event frequencies, it cannot directly explain the increased cold events. Based on our prior work of regional heat wave attribution (Zhou et al. 2020), in addition to estimating the role of anomalous northerlies, we also attempted to quantify the roles of human influences in the probability of the eastern U.S. 2019 cold outbreak from both dynamic and thermodynamic perspectives. Our results should provide a physical way to reconcile the interpretations of human influences on warm and cold events.

In summary, this study tries to answer three questions: 1) What does the eastern U.S. 2019 November cold air outbreak look like in the historical context? 2) How much do the anomalous northerlies contribute to the probability of severe cold outbreaks like this one? 3) What are relative roles of human-induced dynamic and thermodynamic changes in shaping severe cold events like November 2019 over the eastern United States?

Data and methods.

To show the 2019 cold event in historical context and its spatial pattern, we used the November Tmin monthly data at ~1,600 stations with more than 30 years of data from 1900 to 2019 in the study region (land areas within 65°–95°W, 30°–50°N; Fig. 1a) from the latest Berkeley homogenized observation dataset (available at http://berkeleyearth.org/) (Muller et al. 2013). This temperature dataset was homogenized by comparing with nearest neighbor stations (Muller et al. 2013) and employed in studying regional extremes (Zhou and Wang 2016).

To depict the atmospheric circulation pattern behind the event, we used the 1° × 1° 300 hPa geopotential height (Z300), zonal wind (U300), and meridional wind (V300) data from NOAA-20CRv3 (the Twentieth Century Reanalysis version 3 produced by the National Oceanic and Atmospheric Administration) from 1900 to 2015 (available at https://www.esrl.noaa.gov/psd/data) (Slivinski et al. 2019). These data were extended to 2019 using JRA-55 (the 55-Year Japanese Re-Analysis) reanalysis data (available at http://jra.kishou.go.jp/) (Kobayashi et al. 2015) by correcting their 1958–2015 mean differences. Jet stream position is shown here as the November average latitude (northward of 30°N) where the 6-hourly wind speed at 300 hPa reaches its maximum (Fig. 1b).

Monthly outputs from the models participated in CMIP6 (phase 6 of the Coupled Model Intercomparison Project Phase 6; https://esgf-node.llnl.gov/search/cmip6/) (Eyring et al. 2016) were used to quantify human influences on the probability of the eastern U.S. 2019 cold air outbreak. Twenty out of 29 CMIP6 historical all-forcings (ALL; see Table ES1 in the supplemental material) runs were selected in this study because of (i) comparable histograms ($p > 0.05$ via a Kolmogorov–Smirnov test) of the November Tmin (V300) anomalies between CMIP6 ALL runs and observations (reanalyses), and (ii) significant ($p < 0.05$) positive temporal correlations between the detrended Tmin and V300 anomalies from CMIP6 ALL runs and observations. The Tmin and V300 anomaly series and their trends during 1900–2019 are shown in Fig. ES1. To better represent the current climate for the 2019 event and consider sample size, we used a centered 40-yr window (2000–39) to represent climate conditions circa 2019 consisting of the selected ALL runs and the extended Shared Socioeconomic Pathway 2_45 (SSP2_45) runs. The resampled data from natural-forcings-only (NAT) runs (Table ES1) were adopted for comparison.

To be consistent, all the data were converted into anomalies relative to the 1900–2019 mean. Observations were first averaged onto 1° × 1° grids and model data were interpolated into the 1° × 1° observation grids using bilinear interpolation; they were then averaged (with area as weight) over the study region. To estimate the occurrence probability of the event, we constructed the probability density function (PDF) of the November Tmin and V300 anomalies using a Gaussian kernel estimate for the interior and a generalized Pareto distribution (GPD) estimate for the upper and lower tails. The boundaries of the lower and upper tails are the 30th and 70th percentiles. A Student's *t* copula (Demarta and McNeil 2005) was used to derive a correlation between their fitted probability distributions.

To estimate the regional circulation changes induced by human influences, following Zhou et al. (2019), we calculated the probability ratio (PR) of the V300 anomalies at or below the 2019 regional mean value (≤ -5.64 m s^{-1} from reanalysis) between the ALL and NAT runs. The November Tmin anomalies were decomposed into dynamic and thermodynamic parts. The dynamic part was calculated by regressing the regional mean November Tmin anomalies onto the V300 anomalies and the local thermodynamic part is the residual. We used the V300-related Tmin variations to represent the circulation-induced or dynamic contribution, even though a circulation change would advect airmasses with different thermodynamic properties such as air temperature and humidity. To further quantify the human-induced dynamic and thermodynamic contributions to the probability of the eastern U.S. 2019 cold outbreak, we respectively calculated the PRs of the dynamic and thermodynamic parts at or below the 2019 values when anomalous northerlies (≤ -5.64 m s^{-1}) occur in ALL and NAT runs. The 95% confidence intervals (CI) were estimated with a 10,000-member bootstrap (with replacement).

Results.

The 2019 November cold air outbreak in historical context. In November 2019, 300-hPa meridional wind anomalies exhibited a meandering planetary-scale wave pattern over the northern mid- to high latitudes (color shading in Fig. 1b), with anomalous northerlies over North America (arrows at a significance level of 0.05 in Fig. 1b). The persistent wavier polar jet stream pushed cold air masses from Canada down across the Great Lakes, and then into the central and northeastern United States (green contour in Fig. 1b), leading to a cold air outbreak over the eastern United States (Fig. 1a).

The Tmin anomaly averaged over the eastern United States is –1.82°C in November 2019, close to the 10th percentile during 1900–2019 (Fig. 1c). The PDF fit of the observed November Tmin anomalies suggests that the eastern U.S. 2019 cold outbreak is a 1-in-8-yr event (95% CI: 1 in 6–12 yr) (Fig. 1e). The detrended November Tmin anomalies show a significant correlation ($r = 0.70$, $p < 0.001$) with the detrended V300 anomalies over the region 90°–120°W, 40°–60°N. A Student's *t* copula fit suggests the November Tmin and V300 anomalies have a 1-in-20-yr concurrent return period (Fig. 1d).

Role of anomalous northerlies. To identify the roles of anomalous northerlies in the eastern U.S. 2019 cold outbreak, we estimated the probabilities of the November Tmin anomalies at or below the 2019 value (≤ -1.82°C) for two cases in CMIP6 ALL runs: one with strong northerly winds (i.e., V300 ≤ -5.64 m s^{-1}; red in Fig. 2c) and one with neutral or weak winds (i.e., $-1 \leq$ V300 ≤ 1 m s^{-1}; gray in Fig. 2c). They are 0.273 (95% CI: 0.12–0.36) and 0.014 (95% CI: 0.01–0.03) (Fig. 2c), respectively. Thus, the chance for such a cold outbreak event to occur over the eastern United States under strong northerlies is approximately 18 times (PR; 95% CI: 7–55 times) that under weak winds (Fig. 2e). This suggests a crucial role of northerly wind in causing winter cold outbreak over the eastern United States, as the northerly wind advects cold air from Canada into the central and eastern United States (Fig. 1b). The large uncertainty in this PR is mainly ascribed to low event probability and its large uncertainty during weak winds (Fig. 2e).

Human-induced dynamic and thermodynamic contributions. Figures 2a and 2b show a significant lower probability in CMIP6 ALL runs than in NAT runs for the November Tmin anomalies to be ≤–1.82°C, but a nonsignificantly higher probability for the November V300 anomalies to be ≤–5.64 m s^{-1}. Their PRs are 0.23 (95% CI: 0.16–0.31) and 1.25 (95% CI: 0.91–1.95), respectively. This suggests that human influences might tend to increase the occurrence frequency of the anomalous northerlies and thus the likelihood of the cold outbreak events, which could partly offset United States.

We further focused on estimating human influences for the cases with V300 ≤ –5.64 m s^{-1}, which represent conditions with strong northerlies like that in November

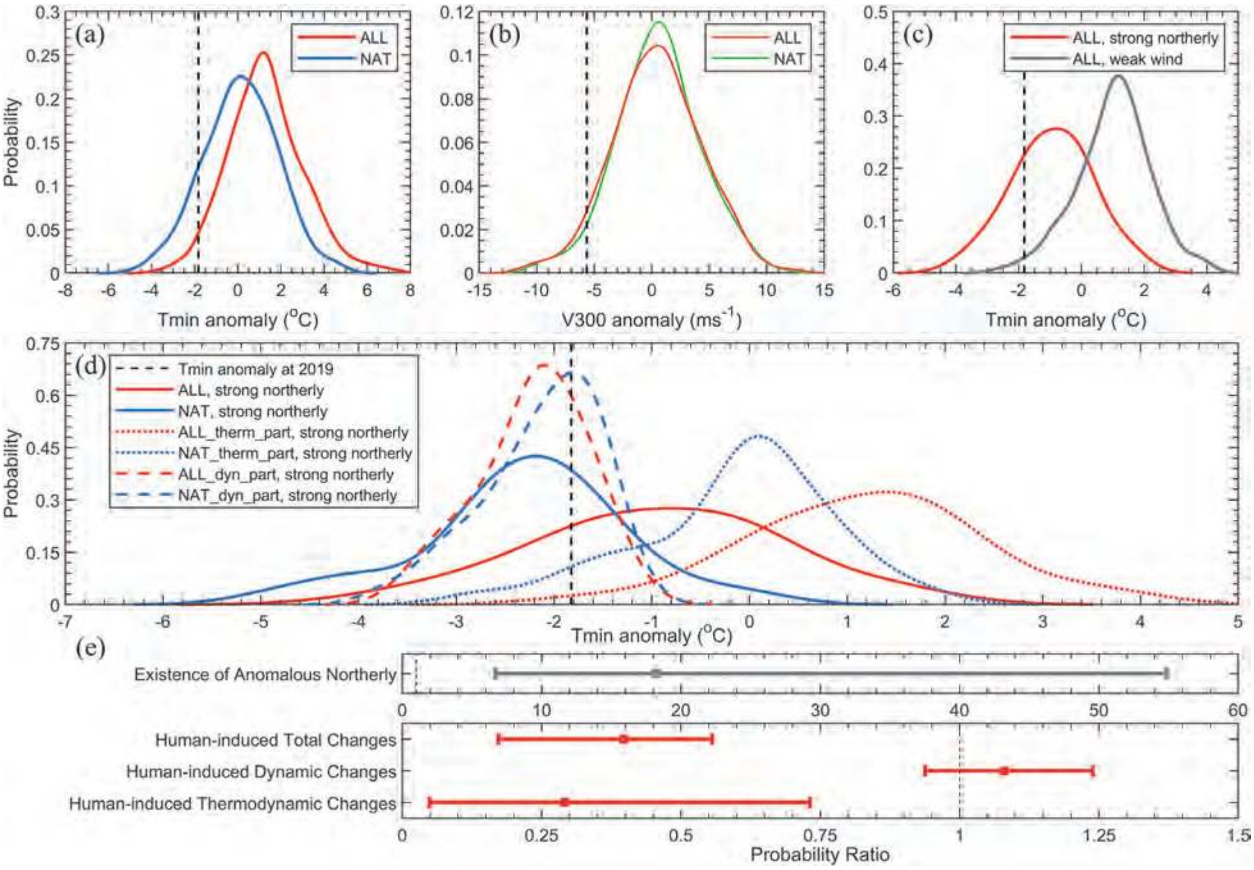

Fig. 2. (a) Estimated probability density functions (PDFs) of the November average daily minimum air temperature (Tmin) anomalies averaged over the eastern United States during a 40-yr window (2000–39) simulated by 20 CMIP6 models under the all-forcing (ALL; red) and natural-forcing-only (NAT; blue) scenarios. The observed value for November 2019 is shown as the black vertical line. The PDF plots were smoothed by kernel density function with 200 equallys spaced points. (b) As in (a), but for V300 anomalies (dashed line from reanalysis). (c) As in (a), but for two cases in the ALL runs: with strong northerly winds (V300 ≤ –5.64 m s^{-1}, the value in November 2019; red) and one with wind winds (–1 ≤ V300 ≤ 1 m s^{-1}; gray). (d) As in (a), but for cases with strong northerly winds in the ALL and NAT runs (solid curves; unit: %). These two PDFs are further decomposed into a dynamic (dashed curves) and a thermodynamic part (dot lines) (see text for details). (e) Probability ratios (PR) between the CMIP6 ALL and NAT runs of the cold outbreaks like November 2019 due to the occurrence of northerlies (gray) and human influences (red). The human influences are also estimated for the dynamic and thermodynamic parts.

2019. For these cases with strong northerlies, we compared the probabilities for the November Tmin anomalies to be ≤ –1.82°C in the ALL and NAT runs (solid red and blue curves, respectively, in Fig. 2d), and found that their PR is 0.40 (95% CI: 0.17–0.56; Fig. 2e). This indicates that human influences might have decreased the probability of the eastern U.S. 2019 cold air outbreak by ~60%.

To better understand human influences on the 2019 event in a physical way, we further quantified the contributions from the dynamic and thermodynamic perspectives. We first decomposed the November Tmin anomalies into the dynamic and thermodynamic parts (as described above). We then calculated the PRs between the ALL and NAT runs for the dynamic and thermodynamic parts of the Tmin anomalies at or below the 2019 values for cases with anomalous northerlies (i.e., V300 ≤ $-5.64\ \mathrm{m \cdot s^{-1}}$) (dashed and dotted lines in Fig. 2d) and found the PRs to be 1.08 (95% CI: 0.95–1.24) and 0.30 (95% CI: 0.05–0.73) for the dynamic and thermodynamic parts, respectively (Fig. 2e). In other words, the human-induced dynamic (i.e., northerly wind) changes increase the chance (by ~8%, nonsignificant at a level of 0.05) of severe cold outbreaks like November 2019 over the eastern United States, while the human-induced thermodynamic changes alone decrease their chance by ~70%. Note that the larger PR uncertainty for the thermodynamic part than for the dynamic part may be related to the use of the V300-regressed Tmin variations as the dynamic part and the residual as the thermodynamic part, since the V300-regressed Tmin variations only represent the effect from large-scale circulation (see section "Data and methods").

Summary.

The eastern United States experienced a cold air outbreak in November 2019 with regional-mean Tmin anomaly (–1.82°C) close to the 10th percentile of 1900–2019. Our analyses of observations and reanalysis show that extreme northerly winds ($\leq -5.64\ \mathrm{m\ s^{-1}}$) were a principal factor responsible for this cold outbreak. An analysis of CMIP6 model data further suggests that the existence of such anomalous northerlies can increase the probability of such cold outbreaks to about 18 times compared with cases with weak winds ($-1 \leq \mathrm{V300} \leq 1\ \mathrm{m\ s^{-1}}$).

Comparing the probabilities of such cold outbreaks under conditions with strong anomalous northerlies (V300 ≤ $-5.64\ \mathrm{m \cdot s^{-1}}$) in CMIP6 ALL and NAT runs, we found that human influences might have decreased the likelihood of such cold outbreaks by ~60% (95% CI: 44%–83%). The analyses of the V300-based regressions and event probability ratios further indicate that the human-induced dynamic (i.e., northerly wind) changes might have increased the likelihood of such events by 8% (nonsignificant at a level of 0.05), whereas the human-induced thermodynamic changes might have decreased the chances of the events by 70%. This event attribution helps us to better understand the roles of human influences on the formation and evolution of the cold air outbreaks over the eastern United States.

Acknowledgments. This study was supported the U.S. National Oceanic and Atmospheric Administration (NA18OAR4310425). A. Dai was also supported by the National Science Foundation (OISE-1743738). Dr. Martin P. Hoerling and three anonymous reviewers are thanked for providing constructive reviews to improve the paper.

References

Alexander, L., and Coauthors, 2006: Global observed changes in daily climate extremes of temperature and precipitation. *J. Geophys. Res.*, **111**, D05109, https://doi.org/10.1029/2005JD006290.

Christiansen, B., and Coauthors, 2018: Was the cold European winter of 2009/10 modified by anthropogenic climate change? An attribution study. *J. Climate*, **31**, 3387–3410, https://doi.org/10.1175/JCLI-D-17-0589.1.

Cohen, J., K. Pfeiffer, and J. A. Francis, 2018: Warm Arctic episodes linked with increased frequency of extreme winter weather in the United States. *Nat. Commun.*, **9**, 869, https://doi.org/10.1038/s41467-018-02992-9.

Demarta, S., and A. J. McNeil, 2005: The t copula and related copulas. *Int. Stat. Rev.*, **73**, 111–129, https://doi.org/10.1111/j.1751-5823.2005.tb00254.x.

Deng, J., A. Dai, and D. Chyi, 2020: Northern Hemisphere winter air temperature patterns and their associated atmospheric and ocean conditions. *J. Climate*, **33**, 6165–6186, https://doi.org/10.1175/JCLI-D-19-0533.1.

Eyring, V., S. Bony, G. A. Meehl, C. A. Senior, B. Stevens, R. J. Stouffer, and K. E. Taylor, 2016: Overview of the Coupled Model Intercomparison Project phase 6 (CMIP6) experimental design and organization. *Geosci. Model Dev.*, **9**, 1937–1958, https://doi.org/10.5194/gmd-9-1937-2016.

Francis, J. A., S. J. Vavrus, and J. Cohen, 2017: Amplified Arctic warming and mid-latitude weather: New perspectives on emerging connections. *Wiley Interdiscip. Rev.: Climate Change*, **8**, e474, https://doi.org/10.1002/wcc.474.

Hartmann, D. L., and Coauthors, 2013: Observations: Atmosphere and surface. Climate Change 2013: The Physical Science Basis, Cambridge University Press, 159–254.

Kobayashi, S., and Coauthors, 2015: The JRA-55 reanalysis: General specifications and basic characteristics. *J. Meteor. Soc. Japan*, **93**, 5–48, https://doi.org/10.2151/jmsj.2015-001.

Luo, B., D. Luo, A. Dai, I. Simmonds, and L. Wu, 2020: Combined influences on North American winter air temperature variability from North Pacific blocking and the North Atlantic Oscillation. *J. Climate*, **33**, 7101–7123, https://doi.org/10.1175/JCLI-D-19-0327.1.

Muller, R. A., and Coauthors, 2013: Earth atmospheric land surface temperature and station quality in the contiguous United States. *Geoinfor. Geostat.*, **1**, 3, https://doi.org/10.4172/2327-4581.1000107.

Scherer, M., and N. S. Diffenbaugh, 2014: Transient twenty-first century changes in daily-scale temperature extremes in the United States. *Climate Dyn.*, **42**, 1383–1404, https://doi.org/10.1007/s00382-013-1829-2.

Singh, D., D. L. Swain, J. S. Mankin, D. E. Horton, L. N. Thomas, B. Rajaratnam, and N. S. Diffenbaugh, 2016: Recent amplification of the North American winter temperature dipole. *J. Geophys. Res. Atmos.*, **121**, 9911–9928, https://doi.org/10.1002/2016JD025116.

Slivinski, L. C., and Coauthors, 2019: Towards a more reliable historical reanalysis: Improvements for version 3 of the Twentieth Century Reanalysis system. *Quart. J. Roy. Meteor. Soc.*, **145**, 2876–2908, https://doi.org/10.1002/qj.3598.

Xie, Z., R. X. Black, and Y. Deng, 2019: Planetary and synoptic-scale dynamic control of extreme cold wave patterns over the United States. *Climate Dyn.*, **53**, 1477–1495, https://doi.org/10.1007/s00382-019-04683-7.

Zhou, C., and K. Wang, 2016: Coldest temperature extreme monotonically increased and hottest extreme oscillated over Northern Hemisphere land during last 114 years. *Sci. Rep.*, **6**, 25721, https://doi.org/10.1038/srep25721.

——, ——, D. Qi, and J. Tan, 2019: Attribution of a record-breaking heatwave event in summer 2017 over Yangtze River Delta. *Bull. Amer. Meteor. Soc.*, **100** (1), S97–S103, https://doi.org/10.1175/BAMS-D-18-0134.1.

——, D. Chen, K. Wang, A. Dai, and D. Qi, 2020: Conditional attribution of the 2018 summer extreme heat over Northeast China: Roles of urbanization, global warming, and warming-induced circulation changes. *Bull. Amer. Meteor. Soc.*, **101** (1), S71–S76, https://doi.org/10.1175/BAMS-D-19-0197.1.

Anthropogenic Influences on Extreme Annual Streamflow into Chesapeake Bay from the Susquehanna River

Andrew C. Ross, Charles A. Stock, Dennis Adams-Smith, Keith Dixon, Kirsten L. Findell, Vincent Saba, and Bruce Vogt

AFFILIATIONS: Ross—Princeton University Cooperative Institute for Modeling the Earth System and NOAA Geophysical Fluid Dynamics Laboratory, Princeton, New Jersey; **Stock, Dixon, and Findell**—NOAA Geophysical Fluid Dynamics Laboratory, Princeton, New Jersey; **Adams-Smith**—Princeton University Cooperative Institute for Modeling the Earth System, Princeton, New Jersey, and University Corporation for Atmospheric Research (UCAR)/Cooperative Programs for the Advancement of Earth System Science (CPAESS), Boulder, Colorado; **Saba**—NOAA Northeast Fisheries Science Center, Geophysical Fluid Dynamics Laboratory, Princeton, New Jersey; **Vogt**—NOAA Chesapeake Bay Office, Annapolis, Maryland

CORRESPONDING AUTHOR: Andrew C. Ross, andrew.c.ross@noaa.gov

DOI:10.1175/BAMS-D-20-0129.1

A supplement to this article is available online (10.1175/BAMS-D-20-0129.2)

2019 water-year mean streamflow into Chesapeake Bay from the Susquehanna River was the third highest since 1891. Anthropogenic climate change has increased the probability of extreme Susquehanna River mean streamflows.

Averaged over the 2019 water year (1 October 2018 to 30 September 2019), freshwater discharge into the Chesapeake Bay was the largest since measurements began in 1937 (USGS 2019), and streamflow in the Susquehanna River, the largest tributary of the Chesapeake Bay (Fig. 1a), measured at Harrisburg, Pennsylvania (USGS station 01570500) was the third highest since records began in 1891 (Fig. 1b). These extreme anomalies in Susquehanna River streamflow can impact upper Chesapeake Bay salinity, temperature, turbidity, and biogeochemistry. Consequently, valuable living marine resources such as blue crabs (Jensen and Miller 2005), striped bass (Millette et al. 2020), and oysters (Kimmel et al. 2014) can be impacted, either positively or negatively, by these streamflow extremes.

While 2019 was the third highest mean streamflow in the Susquehanna, the all-time record was set in 2011, and the second highest was observed in 2004. This sudden

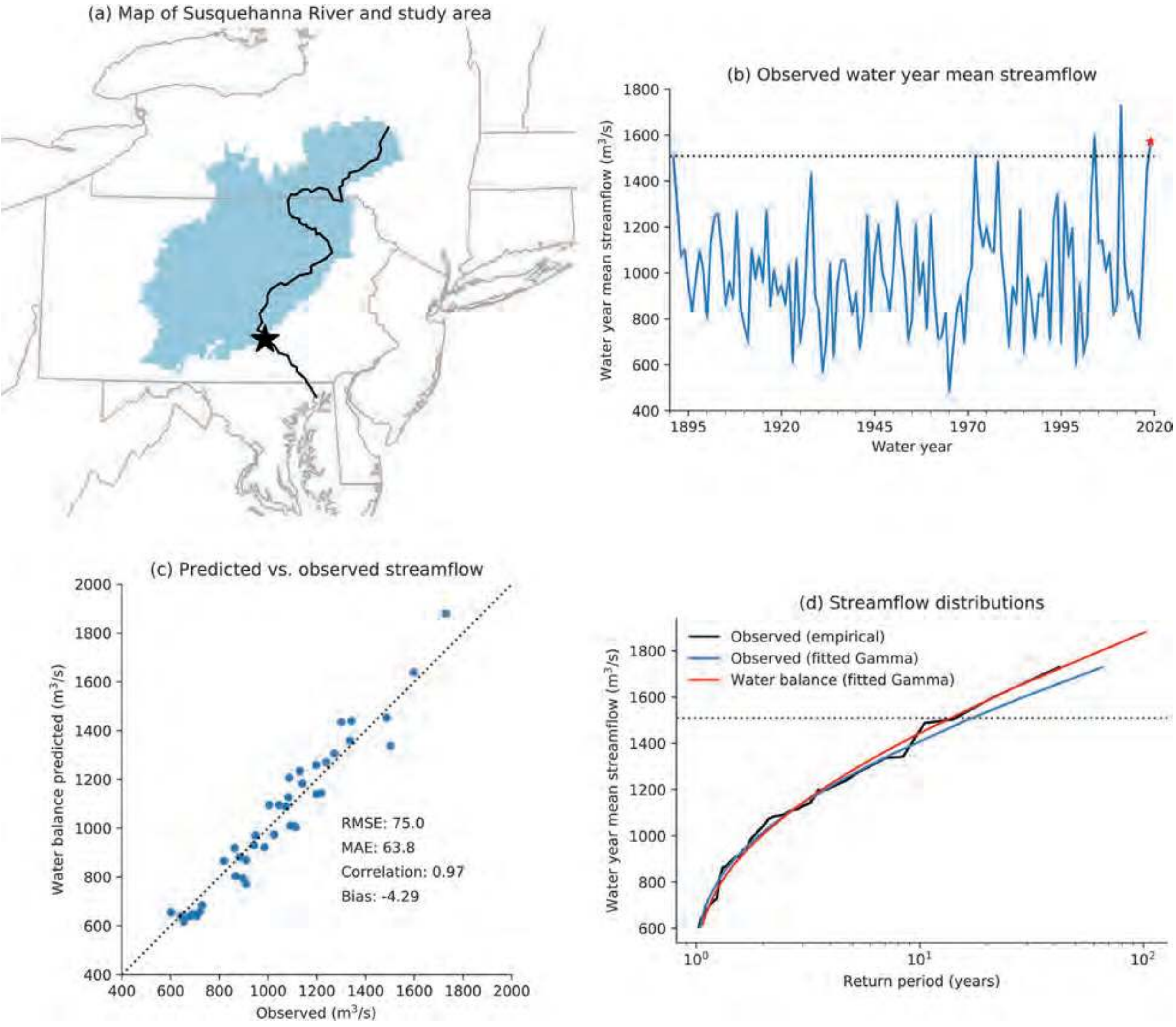

Fig. 1. (a) Map of the Susquehanna River, the stream gauge at Harrisburg (star), and the upstream watershed (shaded). (b) Time series of observed water year mean streamflow at Harrisburg. Red star denotes 2019, and the dotted line shows the threshold for an extreme event used in this study. (c) Comparison of water-year (WY) mean streamflow predicted by the water balance model driven by Livneh data vs the observed mean streamflow during the calibration period (1971–2011). (d) Comparison of probability distributions from the observations and Livneh-driven water balance simulation during the calibration period.

run of record events is consistent with recent increases in precipitation totals and extremes in the mid-Atlantic and Northeast regions of the United States (Guilbert et al. 2015; Hoerling et al. 2016; Howarth et al. 2019; Huang et al. 2017, 2018; Knutson and Zeng 2018). In the U.S. Northeast, climate models commonly project increased annual and extreme precipitation as a result of anthropogenic climate change (ACC) (Lynch et al. 2016; Ning et al. 2015). ACC has already increased the risk of extreme precipitation events and totals in the U.S. Northeast (Winter et al. 2020) and has likely increased annual and seasonal-mean precipitation over 1901–2010 (Knutson and Zeng 2018). A natural question, then, is whether any change in the frequency of extreme streamflow can be attributed to ACC. This attribution is complicated by a concurrent greenhouse gas–driven warming that, in isolation, would increase evapotranspiration and reduce runoff and streamflow (Knutson et al. 2013; Vose et al. 2017).

In this study, we use a water balance model to attribute the combined effects of changing mean temperature and precipitation on water year mean streamflow in the

Susquehanna River. We use simulations from phase 6 of the Coupled Model Intercomparison Project (CMIP6) to compare the probability of an extreme streamflow year like 2019 with the probability in a counterfactual climate without anthropogenic changes in radiative forcing. Using the water balance model also allows a separation of the effects of changing precipitation and temperature on extreme streamflow risk.

Data and methods.

Streamflow in the Susquehanna River at Harrisburg, Pennsylvania, was simulated from CMIP6 climate model data using a water balance model that predicts monthly mean runoff from monthly total precipitation and potential evapotranspiration (Wolock and McCabe 1999; McCabe and Markstrom 2007). Our use of the model was similar to Muhling et al. (2018), except we used the Hargreaves–Samani method (Hargreaves and Samani 1982, 1985) to calculate potential evapotranspiration (E_P) from climate model temperature data rather than the Hamon (1961) method. The Hargreaves–Samani method has a sensitivity to warming that is more consistent with non-water-stressed evapotranspiration calculated during climate model simulations (Milly and Dunne 2016, 2017). The water balance model was calibrated for the Susquehanna River basin by adjusting the model parameters for evapotranspiration, rain/snow mixing, runoff, soil storage, and snowmelt and underestimation using an optimization algorithm to minimize the root-mean-square error (RMSE) of monthly mean streamflow when using the last 41 years (1971–2011) of the Livneh et al. (2013) gridded temperature and precipitation observations as input. All water balance simulations predicted total runoff at a monthly time step, which is sufficient for capturing extremes in water year mean streamflow for a large river basin like the Susquehanna. Total runoff was converted to mean streamflow by integrating the time rate of runoff over the watershed area.

We ran an ensemble of water balance model simulations using climate model data from CMIP6. We used 52 ensemble members from eight different climate models that participated in the Detection and Attribution Model Intercomparison Project (DAMIP) (Gillett et al. 2016) and provided the output needed to calculate E_P (see Table ES1 in the supplemental information). The model temperature and precipitation data were averaged over the Susquehanna River basin upstream of Harrisburg and corrected for biases using the quantile delta mapping (QDM) method (Cannon et al. 2015) with the Livneh et al. (2013) gridded data used to calibrate the water balance model as the reference for the bias correction. As a result, the water balance model did not need to be recalibrated to run with the bias-corrected climate model data.

To calculate the present-day probability of an extreme water-year mean streamflow (P_1), we 1) set a threshold value of 1,509 $m^3 s^{-1}$, the value observed in 1891 and that water years 2004, 2011, and 2019 have exceeded; 2) fit a gamma distribution to the pooled water-year mean streamflows simulated by models following the combined CMIP6 historical and SSP245 scenario for a 41-yr period centered around 2019 (1999 to 2039); and 3) calculated the probability of an extreme streamflow year above the 1,509 $m^3 s^{-1}$ threshold using the fitted distribution. To determine the probability of an extreme streamflow in a counterfactual climate (P_0), we repeated the same process using streamflow simulations from models following the last 41 years (1974 to 2014) of historical forcing from the hist-nat scenario, which includes the historical time series of natural solar and volcanic forcings but excludes anthropogenic emissions. Extensions of the hist-nat scenario into the future, which would be necessary to center the hist-nat simulations around 2019, are not available for most models, but centering is less important than for the historical scenario because the natural forcing does not contain large anthropogenic trends. We then calculated the risk ratio as P_1/P_0 and the fraction of attributable risk as $1 - (P_0/P_1)$ (Stott et al. 2016). A confidence interval for the risk ratio was determined using bootstrapping and a significance level of 0.1. The significance level and 41-yr time period were chosen to provide sufficient power to test our hypothesis. A posteriori tests using shorter or longer time periods showed that confidence intervals in the results would change but the conclusions generally would not. The conclusions are also not sensitive to the definition of the threshold for an extreme event.

As an additional assessment, we also report results derived using a nonparametric approach described in Paciorek et al. (2018) with confidence intervals using the method of Koopman (1984). This approach has the advantage of not requiring an assumption about the probability distribution. However, whereas the gamma distribution method uses all available data to estimate the shape of the distribution and the probability of extremes, the nonparametric method relies only on the fraction of data points exceeding the extreme threshold and will have high uncertainty (Paciorek et al. 2018). As a result, the nonparametric method has significantly less power than the gamma fitting method (in other words, the nonparametric method is less likely to identify a real change in risk as statistically significant). We thus primarily rely on the gamma method, but present the nonparametric results for completeness and as a consistency check.

Finally, to separate the effects of changing temperature and precipitation on streamflow risk, we re-ran the water balance simulations driven by data from the hist-nat scenario with climate change factors applied to only the temperature or precipitation data. These change factors were derived by calculating the mean difference or ratio between the 1999–2039 historical/SSP245 and 1974–2014 hist-nat scenarios for each climate model. For temperature, the difference was added to the hist-nat time series, and for precipitation, the hist-nat time series was multiplied by the ratio. For temperature, we also considered separately the effects of evapotranspiration and the rain/snow ratio by applying the change factor to the data used to calculate E_P but not to the data used to apportion rain and snow, and conversely.

Results.

The water balance model accurately predicts historical water year mean streamflow when driven by observed temperature and precipitation (Fig. 1c). The streamflow simulation is essentially unbiased, highly correlated with the observations, and has a mean error [RMSE or mean absolute error (MAE); Fig. 1c] that is an order of magnitude less than the mean streamflow. We also used leave-one-out cross-validation, iteratively leaving one water-year of data out at a time and recalibrating and reevaluating the model, to test the robustness of the model calibration and predictive capability. This approach results in only a minor degradation of model predictive skill for the left-out year (RMSE of 77.5 $m^3 s^{-1}$, MAE of 65.8 $m^3 s^{-1}$, same correlation and bias), which confirms the robustness of our model. The observed and modeled streamflow can be well represented by a gamma distribution (Fig. 1d), supporting our use of the more powerful gamma method as our primary attribution test. Because the internal climate variability in the CMIP6-driven water balance model simulations is not in phase with the observed internal variability, we cannot directly compare these simulations with the observed time series. Instead, we use the Kolmogorov–Smirnov two-sample test to verify that the pooled streamflow simulations driven by the CMIP6 GCMs under the combined historical and SSP245 scenario have a similar probability distribution to the observed water-year mean streamflow. This test confirms that the distribution of simulated streamflow is similar to the observed distribution during the full observational period of 1891–2019 ($D = 0.0893$, $p = 0.265$).

From the water balance model simulations driven by CMIP6 models, the gamma distribution method estimates that there was a 2.52% chance of exceeding the threshold of 1,509 $m^3 s^{-1}$ in a year with climate forcing similar to 2019 (Table 1). In the counterfactual scenario without anthropogenic emissions, this probability was lower at 1.63%, resulting in a risk ratio of 1.55 (90% confidence interval 1.23–1.92). The 90% confidence interval on the risk ratio excludes 1, so we conclude that anthropogenic climate change significantly increased the risk of experiencing an extreme water-year

Table 1. Probabilities of an extreme streamflow event in the counterfactual (hist-nat) and historical/SSP245 scenarios and the resulting risk ratio and fraction of attributable risk.

Method	P_0 (counterfactual)	P_1 (historical)	RR (90% CI)	FAR
Gamma	0.0163	0.0252	1.55 (1.23, 1.92)	0.355
Nonparametric	0.0164	0.0197	1.20 (0.828, 1.74)	0.167

mean streamflow in 2019. The best estimate of the fraction of attributable risk is 0.355, indicating that about 1/3 of the present risk of streamflow extremes is attributable to anthropogenic climate change.

The nonparametric method, which has weaker power than the gamma distribution method, produces qualitatively similar but less confident results (Table 1). The nonparametric method gives a slightly lower historical probability of an extreme streamflow compared to the gamma method (1.97%) and a similar counterfactual probability (1.64%). The resulting risk ratio (1.20) and FAR (0.167) are lower, but the confidence intervals on the risk ratio are much wider and include 1. The consistency of streamflow data with the gamma distribution (Fig. 1d) supports our reliance on the more powerful gamma method as the primary quantitative test, with the qualitative consistency between the gamma and less powerful nonparametric approach providing no reason to reject this result.

In Fig. 2, we compare the separate effects of modeled temperature, evapotranspiration, and precipitation changes on simulated streamflow. In the CMIP6 models, the most robust signal of anthropogenic climate change in this region is a rapid warming beginning in the 1980s and projected to continue into the future (Fig. 2a). In the absence of any precipitation changes, this warming would have reduced the risk of an extreme streamflow event (orange bar in Fig. 2b) by increasing evapotranspiration (blue). In the water balance model, temperature is also used to determine the rain/snow mixing ratio, and warming shifts the winter ratio toward rain, but this is modeled to have had a negligible effect on water year mean streamflow extremes (purple). Modeled precipitation begins to increase around the same time as temperature and emerges above the range of natural variability around the end of the historical experiment (2014). When considering the 41-yr window centered on 2019, the overall projection is for mean precipitation above the 1974–2014 natural baseline, which alone would cause a significant increase in the risk for extreme streamflow (green bar in Fig. 2b). Finally, the gamma and nonparametric methods yield similar results for each experiment, although the nonparametric results have much wider confidence intervals.

Conclusions.

Three extreme annual mean streamflow events have occurred in the last two decades in the Susquehanna River, and we found that ACC has increased the probability of these extreme events. In the model simulations, the increased risk from higher precipitation has exceeded the reduced risk from increased evapotranspiration. This attribution may be useful for guiding management decisions; for example, the Susquehanna River typically accounts for around half of the freshwater discharge into Chesapeake Bay, so an increased risk of extreme streamflow in the river may increase the risk of poor water quality and shifts in fish habitat in the bay. Similarly, the Chesapeake Bay Program supports efforts to improve stream health and function throughout the Susquehanna River watershed. Given the likelihood for increases in extreme mean streamflow events, it is important to consider their impact on the siting and design of stream restoration projects to ensure long-term success and improved effectiveness under changing climate conditions.

There are several limitations of our analysis. Tropical cyclones have contributed to some recent extreme precipitation and streamflow events in the study region (Huang

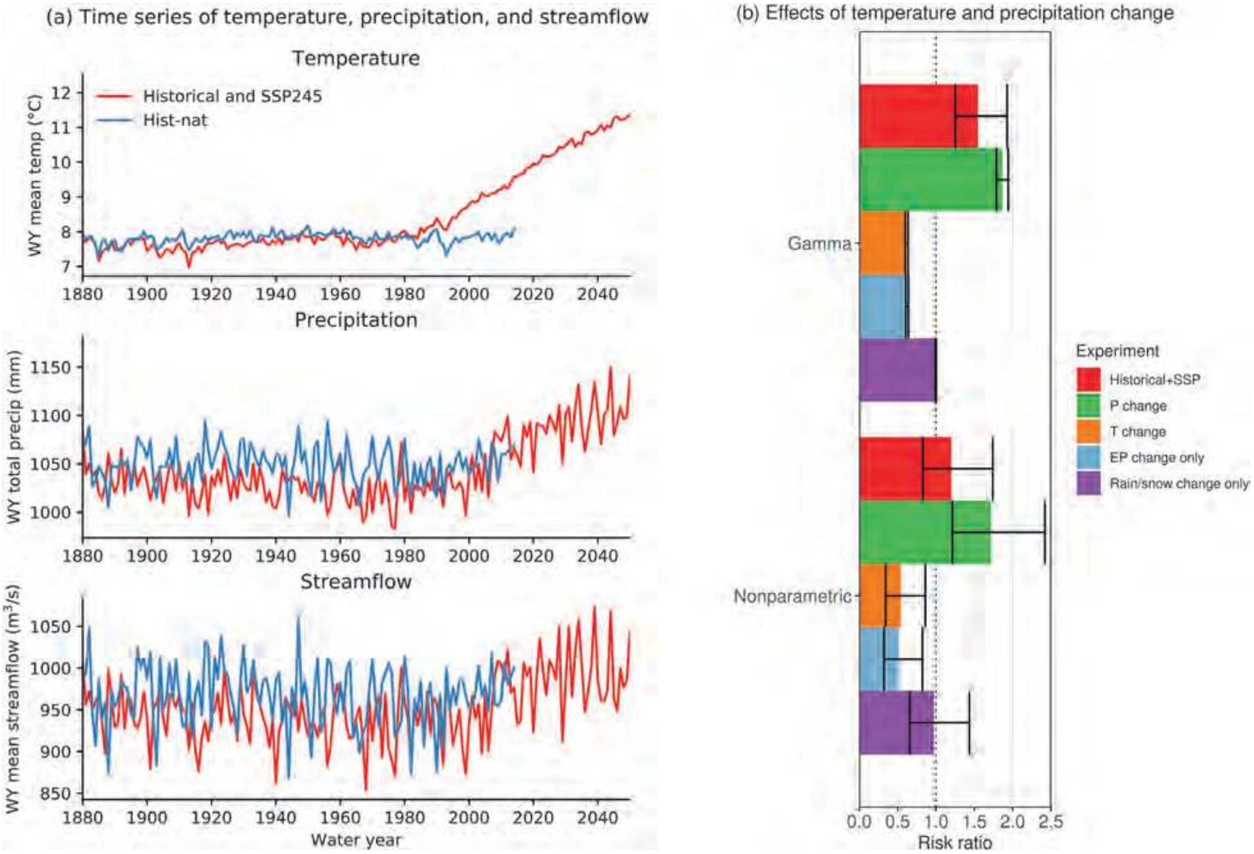

Fig. 2. (a) Time series of model mean temperature, precipitation, and water balance simulated streamflow under the two climate forcing scenarios. (b) Separate effects of changing temperature and precipitation on streamflow risk. Experiment "T change" accounts for the effects of warming on both evapotranspiration and rain/snow mixing ratios, while experiments "EP change only" and "Rain/snow change only" capture the effect of warming only on the respective factors.

et al. 2018), but any changes in these storms are unlikely to be captured in the coarse resolution global climate models examined here (van der Wiel et al. 2016). Potential and actual evapotranspiration are complex functions of many factors including temperature, radiation, and wind. The value of E_p is typically approximated using a few reliable climate model variables, such as the monthly mean minimum and maximum temperatures used by the Hargreaves and Samani (1982, 1985) method in this study. Other methods, like the Hamon (1961) method, assume that E_p can be approximated solely by monthly mean temperature, and experiments showed that this method would flip the streamflow risk ratios (see Table ES2). However, methods that use only mean temperature exaggerate the drying effect of warming (Milly and Dunne 2017; Seong et al. 2018), in part because they do not account for reductions in stomatal conductance as atmospheric CO_2 increases (Milly and Dunne 2016). While the Hargreaves–Samani (H-S) method also fails to account for stomatal changes, it does use the diurnal temperature range to modulate solar radiation, making its sensitivity more reliable than methods that only use mean temperature, and in our study region, the H-S method predicts a similar response of potential evapotranspiration to climate change as methods that do account for radiation, winds, and humidity (Milly and Dunne 2017). We did not apply weighting to account for the varying ensemble sizes of the CMIP6 models used in this study, so our results are heavily influenced by CanESM5 and other models that contributed more runs. However, considering several model subsets with equal distributions of ensemble size would not change our conclusions (Table ES2). We did not consider the effects of changes in land use, reservoir storage, or consumptive use, all of which likely had a small effect on annual mean flows to the Chesapeake Bay (e.g., Najjar 1999). The effects of changes in precipitation intensity and frequency at submonthly time scales are also not included. However, the observation-driven water balance model was able to accurately simulate the 1971–2011 calibration period without considering these changes.

Several of the potential limitations to this study also suggest fruitful areas for future research. Our confidence about changes in hydrological extremes can be improved by research into the uncertainty contributed by the choices of potential evapotranspiration formula, climate models and scenarios, and bias correction and downscaling algorithms. Although the monthly water balance model performed well, more sophisticated hydrological models could account for changes in variables other than temperature and precipitation, such as wind speed, and could be used to attribute changes in extremes in smaller watersheds and rivers. Finally, we found that the gamma and nonparametric attribution methods for determining probability yielded similar results but disagreed about whether the identified increase in the risk of extreme streamflow is statistically significant; future work would benefit from additional research into hydrological extreme event attribution methods.

Acknowledgments. Funding from NOAA (NA18OAR4320123) and the Integrated Ecosystem Assessment program. The statements, findings, conclusions, and recommendations are those of the authors and do not necessarily reflect the views of NOAA or the U.S. Department of Commerce. We acknowledge the World Climate Research Programme, Earth System Grid Federation, and climate modeling groups who supported and provided the data used in this study. Jasmin John, Thomas Knutson, John Lanzante, three anonymous reviewers, and the editor provided helpful comments on drafts of this manuscript. We thank Larry Horowitz, Jasmin John, and John Krasting for coordinating GFDL's ESM4 contribution and providing information about CMIP6.

References

Cannon, A. J., S. R. Sobie, and T. Q. Murdock, 2015: Bias correction of GCM precipitation by quantile mapping: How well do methods preserve changes in quantiles and extremes? *J. Climate*, **28**, 6938–6959, https://doi.org/10.1175/JCLI-D-14-00754.1.

Gillett, N. P., and Coauthors, 2016: The Detection and Attribution Model Intercomparison Project (DAMIP v1.0) contribution to CMIP6. *Geosci. Model Dev.*, **9**, 3685–3697, https://doi.org/10.5194/gmd-9-3685-2016.

Guilbert, J., A. K. Betts, D. M. Rizzo, B. Beckage, and A. Bomblies, 2015: Characterization of increased persistence and intensity of precipitation in the northeastern United States. *Geophys. Res. Lett.*, **42**, 1888–1893, https://doi.org/10.1002/2015GL063124.

Hamon, W. R., 1961: Estimating potential evapotranspiration. *Proc. Amer. Soc. Civ. Eng.*, **87**, 107–120.

Hargreaves, G. H., and Z. A. Samani, 1982: Estimating potential evapotranspiration. *J. Irrig. Drain. Div.*, **108**, 225–230.

——, and ——, 1985: Reference crop evapotranspiration from temperature. *Appl. Eng. Agric.*, **1**, 96–99, https://doi.org/10.13031/2013.26773.

Hoerling, M., J. Eischeid, J. Perlwitz, X.-W. Quan, K. Wolter, and L. Cheng, 2016: Characterizing recent trends in U.S. heavy precipitation. *J. Climate*, **29**, 2313–2332, https://doi.org/10.1175/JCLI-D-15-0441.1.

Howarth, M. E., C. D. Thorncroft, and L. F. Bosart, 2019: Changes in extreme precipitation in the northeast United States: 1979–2014. *J. Hydrometeor.*, **20**, 673–689, https://doi.org/10.1175/JHM-D-18-0155.1.

Huang, H., J. M. Winter, E. C. Osterberg, R. M. Horton, and B. Beckage, 2017: Total and extreme precipitation changes over the northeastern United States. *J. Hydrometeor.*, **18**, 1783–1798, https://doi.org/10.1175/JHM-D-16-0195.1.

——, ——, and ——, 2018: Mechanisms of abrupt extreme precipitation change over the northeastern United States. *J. Geophys. Res. Atmos.*, **123**, 7179–7192, https://doi.org/10.1029/2017JD028136.

Jensen, O. P., and T. J. Miller, 2005: Geostatistical analysis of the abundance and winter distribution patterns of the blue crab Callinectes sapidus in Chesapeake Bay. *Trans. Amer. Fish. Soc.*, **134**, 1582–1598, https://doi.org/10.1577/T04-218.1.

Kimmel, D. G., M. Tarnowski, and R. I. E. Newell, 2014: The relationship between interannual climate variability and juvenile eastern oyster abundance at a regional scale in Chesapeake Bay. *North Amer. J. Fish. Manage.*, **34**, 1–15, https://doi.org/10.1080/02755947.2013.830999.

Knutson, T. R., and F. Zeng, 2018: Model assessment of observed precipitation trends over land regions: Detectable human influences and possible low bias in model trends. *J. Climate*, **31**, 4617–4637, https://doi.org/10.1175/JCLI-D-17-0672.1.

——, ——, and A. T. Wittenberg, 2013: Multimodel assessment of regional surface temperature trends: CMIP3 and CMIP5 twentieth-century simulations. *J. Climate*, **26**, 8709–8743, https://doi.org/10.1175/JCLI-D-12-00567.1.

Koopman, P. A. R., 1984: Confidence intervals for the ratio of two binomial proportions. *Biometrics*, **40**, 513, https://doi.org/10.2307/2531405.

Livneh, B., E. A. Rosenberg, C. Lin, B. Nijssen, V. Mishra, K. M. Andreadis, E. P. Maurer, and D. P. Lettenmaier, 2013: A long-term hydrologically based dataset of land surface fluxes and states for the conterminous United States: Update and extensions. *J. Climate*, **26**, 9384–9392, https://doi.org/10.1175/JCLI-D-12-00508.1.

Lynch, C., A. Seth, and J. Thibeault, 2016: Recent and projected annual cycles of temperature and precipitation in the northeast United States from CMIP5. *J. Climate*, **29**, 347–365, https://doi.org/10.1175/JCLI-D-14-00781.1.

McCabe, G. J., and S. L. Markstrom, 2007: A monthly water-balance model driven by a graphical user interface. U.S. Geological Survey Open-File Rep. 2007-1088, 6 pp., https://pubs.usgs.gov/of/2007/1088/pdf/of07-1088_508.pdf.

Millette, N. C., J. J. Pierson, and E. W. North, 2020: Water temperature during winter may control striped bass recruitment during spring by affecting the development time of copepod nauplii. *ICES J. Mar. Sci.*, **77**, 300–314, https://doi.org/10.1093/icesjms/fsz203.

Milly, P. C. D., and K. A. Dunne, 2016: Potential evapotranspiration and continental drying. *Nat. Climate Change*, **6**, 946–949, https://doi.org/10.1038/nclimate3046.

——, and ——, 2017: A hydrologic drying bias in water-resource impact analyses of anthropogenic climate change. *J. Amer. Water Resour. Assoc.*, **53**, 822–838, https://doi.org/10.1111/1752-1688.12538.

Muhling, B. A., C. F. Gaitán, C. A. Stock, V. S. Saba, D. Tommasi, and K. W. Dixon, 2018: Potential salinity and temperature futures for the Chesapeake Bay using a statistical downscaling spatial disaggregation framework. *Estuaries Coasts*, **41**, 349–372, https://doi.org/10.1007/s12237-017-0280-8.

Najjar, R. G. R. G., 1999: The water balance of the Susquehanna River Basin and its response to climate change. *J. Hydrol.*, **219**, 7–19, https://doi.org/10.1016/S0022-1694(99)00041-4.

Ning, L., E. E. Riddle, and R. S. Bradley, 2015: Projected changes in climate extremes over the northeastern United States. *J. Climate*, **28**, 3289–3310, https://doi.org/10.1175/JCLI-D-14-00150.1.

Paciorek, C. J., D. A. Stone, and M. F. Wehner, 2018: Quantifying statistical uncertainty in the attribution of human influence on severe weather. *Wea. Climate Extremes*, **20**, 69–80, https://doi.org/10.1016/j.wace.2018.01.002.

Seong, C., V. Sridhar, and M. M. Billah, 2018: Implications of potential evapotranspiration methods for streamflow estimations under changing climatic conditions. *Int. J. Climatol.*, **38**, 896–914, https://doi.org/10.1002/joc.5218.

Stott, P. A., and Coauthors, 2016: Attribution of extreme weather and climate-related events. *Wiley Interdiscip. Rev.: Climate Change*, **7**, 23–41, https://doi.org/10.1002/wcc.380.

USGS, 2019: Record freshwater flow in water year 2019 affects conditions in the Chesapeake Bay. U.S. Geological Survey, accessed 13 April 2020, https://www.usgs.gov/centers/cba/science/record-freshwater-flow-water-year-2019-affects-conditions-chesapeake-bay.

van der Wiel, K., and Coauthors, 2016: The resolution dependence of contiguous U.S. precipitation extremes in response to CO2 forcing. *J. Climate*, **29**, 7991–8012, https://doi.org/10.1175/JCLI-D-16-0307.1.

Vose, R. S., D. R. Easterling, K. E. Kunkel, A. N. LeGrande, and M. F. Wehner, 2017: Temperature changes in the United States. Climate Science Special Report: Fourth National Climate Assessment, D. J. Wuebbles et al., Eds., Vol. I, U. S. Global Change Research Program, 185–206, https://doi.org/10.7930/J0N29V45.

Winter, J. M., H. Huang, E. C. Osterberg, and J. S. Mankin, 2020: Anthropogenic impacts on the exceptional precipitation of 2018 in the mid-Atlantic United States. *Bull. Amer. Meteor. Soc.*, **101**, S5–S10, https://doi.org/10.1175/BAMS-D-19-0172.1.

Wolock, D., and G. McCabe, 1999: Explaining spatial variability in mean annual runoff in the conterminous United States. *Climate Res.*, **11**, 149–159, https://doi.org/10.3354/cr011149.

Anthropogenic Contribution to the Rainfall Associated with the 2019 Ottawa River Flood

Megan C. Kirchmeier-Young, Hui Wan, and Xuebin Zhang

Anthropogenic forcing increased the likelihood of the 30-day high rainfall over Ontario and Quebec that contributed to the 2019 Ottawa River floods by a factor of 2 to 3.

Spring 2019 saw a record-setting flood on the Ottawa River, impacting parts of the provinces of Ontario and Quebec in Canada. The river crested on 1 May, but the state of emergency in Ottawa lasted into the second week of June. The floods resulted in thousands of people evacuated, extended states of emergency, and about $200 million in insured losses (IBC 2019). This flood came just two years after the previous record flood for the region.

The 2019 flood was fed by a month of well above average rainfall over the basin, demonstrated in Fig. 1a using the maximum 30-day accumulation from spring (March–May) expressed as an anomaly relative to the 1981–2010 mean of spring 30-day accumulations. This included contributions from several days with heavy rainfall, shown in Fig. 1b as counts of days exceeding the local 1981–2010 90th percentile. In addition, the ground was still frozen throughout this period, limiting infiltration of the rainwater and increasing flow over the land surface. The melting of above-average snowpack upstream also contributed to the flood.

AFFILIATIONS: Kirchmeier-Young, Wan, and Zhang—Climate Research Division, Environment and Climate Change Canada

CORRESPONDING AUTHOR: Megan C. Kirchmeier-Young, megan.kirchmeier-young@canada.ca

DOI:10.1175/BAMS-D-20-0191.1

A supplement to this article is available online (10.1175/BAMS-D-20-0191.2)

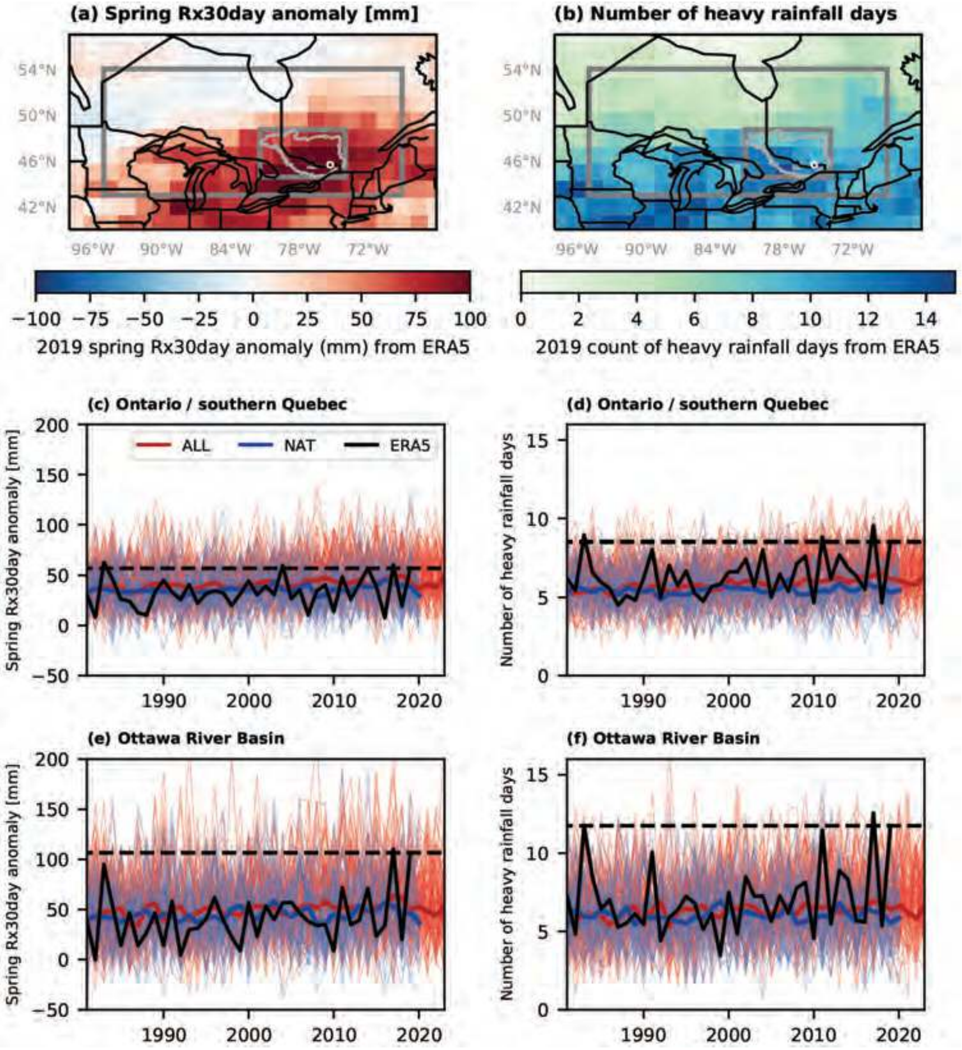

Fig. 1. (a) Spring Rx30day anomaly in mm and (b) the count of heavy rainfall days during spring (March–May) from ERA5. The light gray outline is the Ottawa River Basin (ORB) and the white circle the city of Ottawa. The dark gray boxes indicate the two regions used in this analysis, the smaller encompassing the ORB (~271,000 km^2) and the larger including much of Ontario and southern Quebec (ON/QC) (~2,576,000 km^2). (c),(e) Time series for the Rx30day anomaly and (d),(f) count of heavy rainfall events averaged over (c),(d) the larger ON/QC region and (e),(f) the smaller ORB region. Individual realizations from ALL simulations are in red and NAT simulations in blue. Multimodel ensemble means are in bold, with equal weight for each model. ERA5 is in black, with the 2019 value emphasized with the horizontal dashed line.

In this region, most spring floods are related to snowmelt, often in combination with heavy rainfall (Buttle et al. 2016; Teufel et al. 2019; Lin et al. 2019). Here, we investigate the anthropogenic influence on the 2019 Ottawa River flood, with a focus on the rainfall component.

Data and methods.

We use a multimodel ensemble of CMIP6 simulations (Eyring et al. 2016; see Table ES1) with all available realizations that provide daily rainfall data. This includes 90 realizations with both anthropogenic and natural forcing (ALL) that combine historical forcing with SSP3–7.0 beginning in 2015 (O’Neill et al. 2016). The different scenarios do not noticeably diverge through the dates we use (2023); thus scenario choice should have little impact. A set of 48 natural-only (NAT) forcing simulations from the Detection and

Attribution Model Intercomparison Project (DAMIP; Gillett et al. 2016) will represent the reference, or counterfactual world, for the attribution. The ERA5 reanalysis (C3S 2017) serves as a representation of the observations. ERA5 improves the biases of its predecessor, ERA-Interim, and in terms of driving a hydrologic model is as skillful as using observations in most regions of North America (Tarek et al. 2020). The ranges of the trend and variability of monthly precipitation over 1981–2019 from the CMIP6 models both include the values from ERA5. There is not sufficient station density in this region to estimate a regional average that is comparable to the models, but the timing of the 2019 spring maximum 30-day rainfall from ERA5 is similar to that from two stations in Ottawa, Ontario (see Fig. ES1 in the online supplemental material).

The Ottawa River system contains several reservoirs, particularly in the northern tributaries. The reservoirs are typically emptied prior to the spring freshet for flood prevention and receive contributions from snowmelt from almost half of the basin. Because of this regulation capacity, major flood events are usually caused by a long period of heavy rainfall over a few weeks, in combination with the snowmelt. As such, the spring maximum 30-day rainfall accumulation (Rx30day) was calculated for each year to represent rainfall contributing to a spring flood. Similarly, monthly precipitation was used in an event attribution study for a previous flood in this basin (Teufel et al. 2019). Rainfall accumulations were determined by summing precipitation from days with a mean temperature greater than 0°C, which should capture the distinction between rain and snow in most cases. Model anomalies were remapped to a common 1.5° grid. After calculating regional averages, the maximum 30-day period was chosen. Additional data processing details are described in the supplemental material. Regional averages were determined for a rectangle enclosing the Ottawa River Basin (ORB), which is where the flood occurred. Changes in extreme precipitation are often small compared to natural variability, especially at small scales. Since variability is smaller over a larger region, we also use an area covering the majority of Ontario and southern Quebec (Fig. 1). For attribution, the event threshold was the standardized (by subtracting the mean and dividing by the standard deviation; see supplemental material) 2019 spring Rx30day from ERA5. NAT anomalies and standardization were computed relative to ALL simulations of the same model.

To account for the role of heavy rainfall, we also calculated the number of heavy rainfall days during spring each year. Heavy rainfall days were defined for each grid box as those exceeding the 90th percentile from spring days over 1981–2010 and using the method of Zhang et al. (2005). Exceedance counts were determined on each model's native grid and then remapped to the common grid before the calculation of regional averages. NAT exceedances used the 90th percentile from an ALL simulation by the same model. For attribution, we used event thresholds from 7 to 12 days.

For event attribution, we use the standard risk (probability) ratio (PR) framework (e.g., NASEM 2016) to compare the ratio of the probability of occurrence between ALL and NAT forcing simulations. To calculate probabilities by counting exceedances, ALL data were pooled from ensemble members for 2014–23, a 10-yr period centered on the 2019 event, and NAT from 1996–2020. The NAT simulations end in 2020 and, given the general stationarity, a longer period can provide more robust estimates of smaller probabilities. The 5th to 95th percentile range was determined by randomly resampling both ALL and NAT independently.

Results.

Maps of the 2019 spring Rx30day anomaly and the number of heavy rainfall days from the ERA5 reanalysis are shown in Figs. 1a and 1b, respectively. There is a large area of positive rainfall anomalies over the ORB, southeastern Ontario, and the Great Lakes region. This area coincides with some high counts of heavy rainfall days.

For the spring Rx30day anomalies using ERA5, the 2019 anomaly is one of the largest in the record (Figs. 1c,e). The 2017 value is only slightly larger and was associated with another high-impact spring flood. A slight positive trend is apparent in the reanalysis data between 1981 and 2019. In the CMIP6 ensemble, ALL anomalies are generally more positive than NAT anomalies, indicating higher rainfall with ALL forcing. The ensemble mean is calculated giving equal weight to each model, but only minor differences were noted if equal weight is instead given to each realization. The ensemble spread covers a wide range of anomalies.

Histograms for the standardized Rx30day anomalies show the ALL data shifted slightly toward larger values, compared to the NAT realizations. The difference between the ALL and NAT distributions is more distinct for the larger Ontario/Quebec region than for the smaller ORB region. The PR for the standardized 2019 spring Rx30day is greater than 1.0 for both the regions (Fig. 2c), implying an increase in likelihood due to anthropogenic forcing. We estimate that the 2019 Rx30day is about 3 times as likely with the inclusion of anthropogenic forcing for the larger region and about 2 times as likely for the smaller region. The error bars are wide, implying large uncertainty on the estimated PR. However, there is confidence of an increase in likelihood, particularly for the larger region.

Similarly, for the number of heavy rainfall days, 2019 and also 2017 show the largest values in the record for ERA5 (Figs. 1d,f). Slightly larger values, including the most extreme counts, are found in the ALL simulations compared to those from NAT. A shift

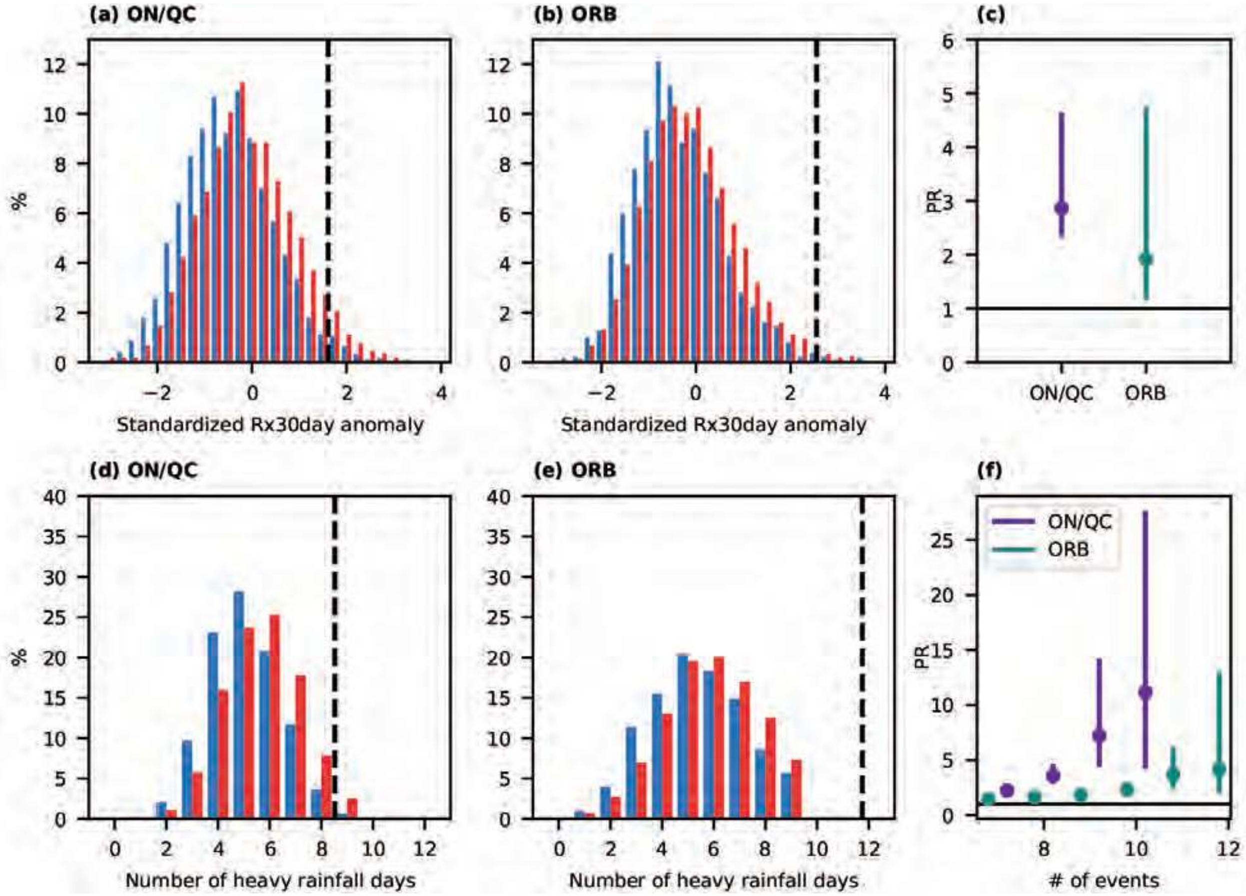

Fig. 2. Histograms for (a),(b) the standardized spring Rx30day anomaly and (d),(e) the number of heavy rainfall days expressed in percent of values. ALL is shown in red and NAT in blue. Probability ratios for the (c) standardized Rx30day anomaly and (f) number of events are shown for the larger region in purple and the smaller region in teal. The higher counts in the larger region do not occur in either the ALL or NAT simulations. A horizontal line at 1.0 indicates equal likelihood between ALL and NAT, with values larger than 1.0 indicating an increase in likelihood in the ALL simulations.

toward higher counts of heavy rainfall days under ALL is also demonstrated through the histograms in Figs. 2d and 2e. PRs for the number of days are only slightly larger than 1.0 for the smaller count thresholds (Fig. 2f). Larger PRs but also larger uncertainties are found with most of the higher count thresholds. Overall, we find that anthropogenic forcing resulted in an increase in the likelihood of a higher number of heavy rainfall days.

Conclusions.

An increased likelihood of flood-producing rainfall has been identified for other events in Canada and the neighboring regions of the United States (Teufel et al. 2019, 2017; Szeto et al. 2015; Winter et al. 2020). Our results are in agreement with those of Teufel et al. (2019), who performed an assessment of the 2017 Ottawa River floods. Using a different set of model simulations at a much higher resolution, they found a small increase in likelihood for the flood-producing monthly rainfall. However, they did not identify an attributable change in surface runoff and it was suggested that a warming-induced decrease in spring snowpack could offset the increased precipitation.

Event attribution PRs depend on the event definition, including the specific location and spatial and temporal scales used. For our analysis of flood-inducing precipitation, different regions, in size and/or location, different event thresholds, a different spring time period, or a different set of models in the ensemble may change the attribution results. Exact PR values will likely depend on the specific choices, but we expect the finding of a small increase in likelihood to be consistent across slight changes in framing. This is confirmed in Fig. ES2, where the PRs change only slightly if an Rx-20day metric or a 15-year ALL period is used instead. Even with making different methodological choices, we reach the same general conclusion as Teufel et al. (2019) for the 2017 flood. Additionally, Kirchmeier-Young et al. (2019) demonstrated consistent changes in likelihood between Rx1day and Rx30day in this region. Finally, increases in extreme precipitation are consistent with a warming atmosphere.

Flood events are complex and often the result of the interaction of many variables, including rainfall, snowpack, and characteristics of the land surface. While increases in the likelihood of large positive precipitation anomalies are increasingly identified and attributed to anthropogenic climate change, the interaction of rainfall with other variables to produce a high-impact flood in a warming climate remains uncertain.

Acknowledgments. We thank the editors, three anonymous reviewers, and Nathan Gillett for their helpful comments on this manuscript and Megan Hartwell for providing the station data. We also thank the numerous modelling centers for their contributions to CMIP6 and Copernicus Climate Change Service for providing the ERA5 data.

References

Buttle, J. M., and Coauthors, 2016: Flood processes in Canada: Regional and special aspects. *Can. Water Resour. J.*, **41**, 7–30, https://doi.org/10.1080/07011784.2015.1131629.

C3S, 2017: ERA5: Fifth generation of ECMWF atmospheric reanalyses of the global climate. Copernicus Climate Change Service (C3S) Climate Data Store (CDS), accessed 19 February 2020, https://cds.climate.copernicus.eu/#!/search?text=ERA5&type=dataset.

Eyring, V., and Coauthors, 2016: Overview of the Coupled Model Intercomparison Project Phase 6 (CMIP6) experimental design and organization. *Geosci. Model Dev.*, **9**, 1937–1958, https://doi.org/10.5194/gmd-9-1937-2016.

Gillett, N. P., and Coauthors, 2016: The Detection and Attribution Model Intercomparison Project (DAMIP v1.0) contribution to CMIP6. *Geosci. Model Dev.*, **9**, 3685–3697, https://doi.org/10.5194/gmd-9-3685-2016.

IBC, 2019: Eastern Canada spring flooding caused close to $208 million in Insured Damage. Insurance Bureau of Canada, accessed 2020, http://www.ibc.ca/on/resources/media-centre/media-releases/eastern-canada-spring-flooding-caused-close-to-208-million-in-insured-damage.

Kirchmeier-Young, M. C., H. Wan, X. Zhang, and S. I. Seneviratne, 2019: Importance of framing for extreme event attribution: The role of spatial and temporal scales. *Earth's Future*, **7**, 1192–1204, https://doi.org/10.1029/2019EF001253.

Lin, H., R. Mo, F. Vitart, and C. Stan, 2019: Eastern Canada flooding 2017 and its subseasonal predictions. *Atmos.–Ocean*, **57**, 195–207, https://doi.org/10.1080/07055900.2018.1547679.

NASEM, 2016: Attribution of Extreme Weather Events in the Context of Climate Change. The National Academies Press, 186 pp., https://doi.org/10.17226/21852.

O'Neill, B. C., and Coauthors, 2016: The Scenario Model Intercomparison Project (ScenarioMIP) for CMIP6. *Geosci. Model Dev.*, **9**, 3461–3482, https://doi.org/10.5194/gmd-9-3461-2016.

Szeto, K., J. Brimelow, P. Gysbers, and R. Stewart, 2015: The 2014 Extreme flood on the southeastern Canadian Prairies." [in "Explaining Extreme Events of 2014 from a Climate Perspective"]. *Bull. Amer. Meteor. Soc.*, **96**, S20–S24, https://doi.org/10.1175/BAMS-D-15-00110.1.

Tarek, M., F. P. Brissette, and R. Arsenault, 2020: Evaluation of the ERA5 reanalysis as a potential reference dataset for hydrological modeling over North America. *Hydrol. Earth Syst. Sci.*, **24**, 2527–2544, https://doi.org/10.5194/hess-24-2527-2020.

Teufel, B., and Coauthors, 2017: Investigation of the 2013 Alberta flood from weather and climate perspectives. *Climate Dyn.*, **48**, 2881–2899, https://doi.org/10.1007/s00382-016-3239-8.

——, and Coauthors, 2019: Investigation of the mechanisms leading to the 2017 Montreal flood. *Climate Dyn.*, **52**, 4193–4206, https://doi.org/10.1007/s00382-018-4375-0.

Winter, J. M., H. Huang, E. C. Osterberg, and J. S. Mankin, 2020: Anthropogenic impacts on the exceptional precipitation of 2018 in the mid-Atlantic United States [in "Explaining Extreme Events of 2018 from a Climate Perspective"]. *Bull. Amer. Meteor. Soc.*, **101**, S5–S10, https://doi.org/10.1175/BAMS-D-19-0172.1.

Zhang, X., G. Hegerl, F. W. Zwiers, and J. Kenyon, 2005: Avoiding inhomogeneity in percentile-based indices of temperature extremes. *J. Climate*, **18**, 1641–1651, https://doi.org/10.1175/JCLI3366.1.

Extremely Warm Days in the United Kingdom in Winter 2018/19

Nikolaos Christidis and Peter A. Stott

Extremely warm winter days in central England, as in 2018/19, are still very rare, but human influence is estimated to have made them about 300 times more likely.

In stark contrast to the frigid close of the 2017/18 winter in the United Kingdom (Christidis and Stott 2020), daytime winter temperatures above 20°C were recorded for the first time in the country only a year later, with a maximum of 21.2°C at Kew Gardens on 26 February 2019.[1] Strong anticyclonic conditions at the end of the winter season steered exceptionally mild tropical maritime air over western Europe and were identified by Kendon et al. (2020) as a key driver of the extreme U.K. temperatures. Their study suggests that the atmospheric state alone would be sufficient to raise U.K. temperatures above 20°C, even without the effect of human influence on the climate. Here, we carry out a complementary attribution study to investigate extremes in the warmest day in winter, described by the maximum daytime temperature (Tmax) in

AFFILIATIONS: Christidis and Stott—Met Office Hadley Centre, Exeter, United Kingdom

CORRESPONDING AUTHOR: Nikolaos Christidis, nikos.christidis@metoffice.gov.uk

DOI:10.1175/BAMS-D-20-0123.1

A supplement to this article is available online (10.1175/BAMS-D-20-0123.2)

---

[1] See https://www.metoffice.gov.uk/about-us/press-office/news/weather-and-climate/2019/february-and-winter-statistics.

central England, and we quantify the anthropogenic effect on their present and future probabilities. Central England Tmax observations are available since 1878 (CET dataset; Parker et al. 1992) and manifest a record of 18.1°C on 26 February 2019 (i.e., the same date as the U.K. national record).

Observations and atmospheric circulation.

Time series of the daily Tmax plotted for every winter (December to February) in the CET dataset (Fig. 1a) show a steep increase at the end of winter 2018/19 with temperatures rising well above previous records. The year also stands out as a striking extreme in the observational time series of the warmest winter day in central England (Fig. 1b), reaching an anomaly that is approximately 5 times the standard deviation of the detrended observations. The observed anomaly of +5.2°C relative to the base period 1901–30 sets the threshold for the definition of extreme events in this study: the warmest day anomalies above this threshold are counted as extremes. The anomaly is 1.5 times higher than the previous record (+3.5°C) and 6 times higher than the 1900–2018 warming (+0.87°C) estimated by fitting a linear trend to the CET data. 500-hPa geopotential height (Z500) data from the NCEP–NCAR reanalysis (Kalnay et al. 1996) illustrate the deep anticyclonic anomaly over northwestern Europe present on the day

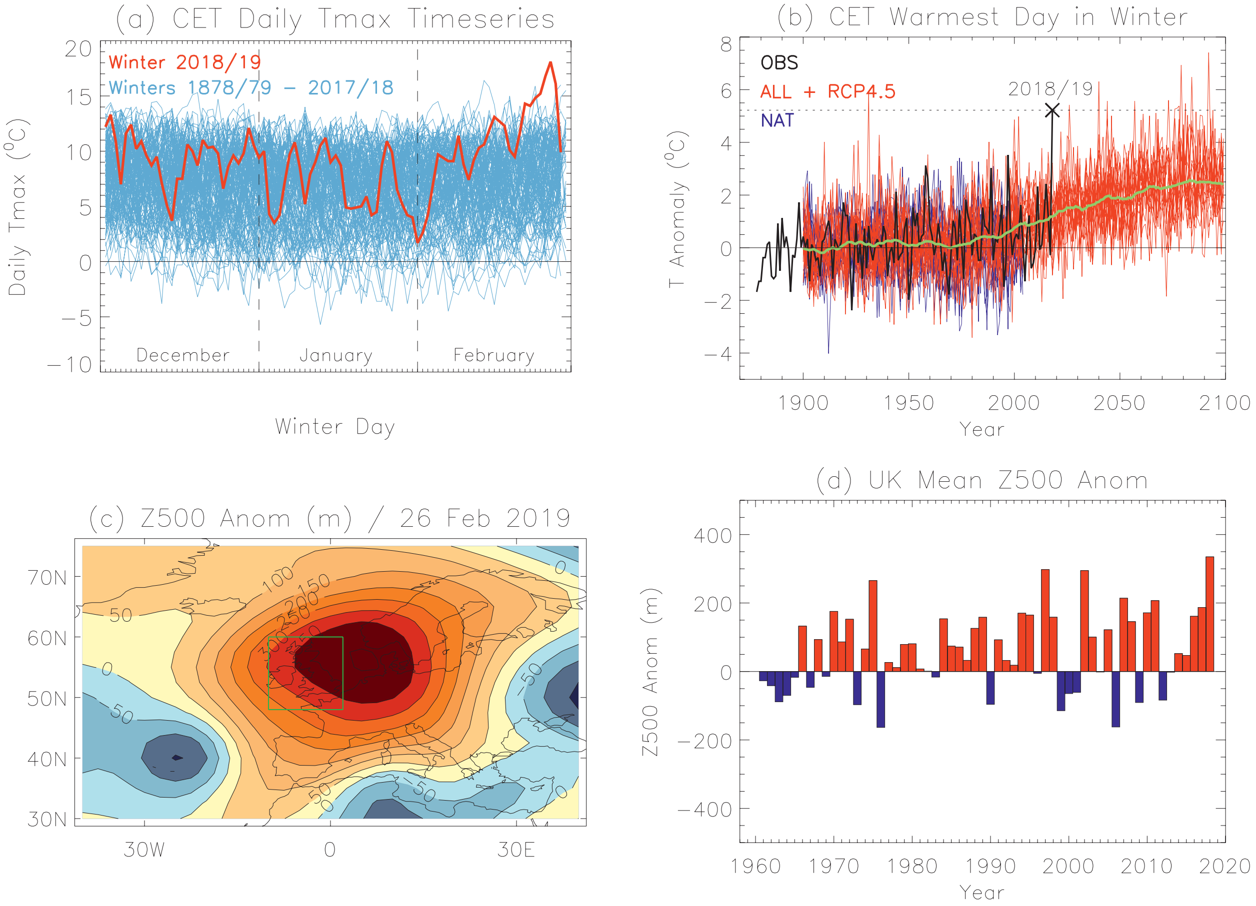

Fig. 1. (a) Time series of the observed daily Tmax in central England during winter months. 2018/19 is shown in red and all other winters in blue. (b) Time series of the warmest day in winter in central England. Anomalies are relative to 1901/02–1930/31. Observations are plotted in black and bias-corrected CMIP5 data from ALL and NAT simulations in red and blue respectively. 2018/19 is marked by the cross and the horizontal dotted line. The yellow line represents the forced response (mean of the ALL simulations). (c) NCEP–NCAR Z500 anomalies on 26 Feb 2019. Anomalies are relative to the winter mean Z500 during 1961/62–90/91. (d) Time series of Z500 anomalies over the United Kingdom [green box in (c)] for the warmest day in winter.

of the Tmax record (Fig. 1c). Positive Z500 anomalies are usually associated with the warmest day in winter in most years, as illustrated in Fig. 1d, which shows the mean Z500 anomaly over the United Kingdom on the days of the CET winter maxima since the 1960s.

CMIP5 data.

The change in the likelihood of extreme events is assessed with a risk-based attribution methodology (Stott et al. 2016), by comparing their probability in the real world with all external forcings acting on the climate (ALL), and a hypothetical "natural" world without the anthropogenic effect (NAT). We use data from 16 models that contributed to the phase 5 of the Coupled Model Intercomparison Project (CMIP5; see the online supplemental material). Although the models typically generate several simulations of the ALL and NAT climate, here we employ one simulation per model per experiment and estimate for each simulation the warmest winter's day Tmax anomaly over central England in all years since 1900 (Fig. 1b). The ALL simulations were extended to the end of the twenty-first century with the RCP4.5 scenario. The forced response is estimated by the mean of the ALL simulations (yellow line in Fig. 1b).

Evaluating the models against CET observations (see the supplemental material) shows that although they yield trends consistent with the observations, their variability is smaller. A simple bias correction is thus applied that inflates their standard deviation to match it to the observations. Once the models are corrected, their variability and distribution of the warmest day in winter agree well with the CET dataset. The variability correction is pointed out as a major caveat of the analysis that could adversely affect the probability estimates, especially if there are future changes in variability that are not correctly captured by the models. However, neither the observations nor the models indicate a notable temporal change in the variability of the warmest day in winter during the observational period, so the effect is likely to be minor.

Our analysis compares the likelihood of extreme events under different climatic conditions. The NAT climate is assumed stationary and we therefore utilize a sample of all simulated years (16 NAT simulations × 105 years in the period 1900/01–2004/05). Since the ALL climate has a warming trend, we first remove an estimate of the response to external forcings from each model's time series and subsequently adjust them to the mean forced response in (a) years 1900–20 (early twentieth century), (b) 2008–28 (present climate), and (c) 2080–2100 (late twenty-first century). This produces samples of 3200 simulated events (16 simulations × 200 years in the period 1900/01–2099/2100).

CMIP5 attribution.

Probabilities of extreme events (i.e., instances of threshold exceedance) are computed from the CMIP5 data with the generalized extreme value (GEV) distribution and their uncertainty is estimated with a simple Monte Carlo bootstrap procedure (Christidis et al. 2013). Return time (inverse probability) and risk ratio estimates are reported in Table 1. Extreme years like 2018/19 are currently highly rare with return times of the order of a thousand years, but they become increasingly common, expected to occur once or twice a century by 2100. Their likelihood in the natural climate is too small to be estimated with the limited sample size from the NAT simulations, but is approximated with the larger ALL sample for the early twentieth century and found to be near-zero (Table 1). The temporal shift in the distribution of the warmest day is depicted in Fig. 2a. The intensity of extremes is also on the rise: events as rare as 2018/19 presently correspond to a + 5.2°C anomaly, which would only be +4.4°C in the early twentieth century, increasing to +7°C by 2100.

As an independent check of the model results, empirical return time estimates are also derived from the observations. As in Christidis and Stott (2020), nonstationarity is accounted for by removing the modeled forced response from the observa-

Table 1. Return time and risk ratio estimates from the CMIP5 analysis. Extremes in the warmest day in winter in central England have temperature anomalies above the +5.2°C threshold observed in winter 2018/19. Reported best estimates correspond to the 50th percentile and the 5%–95% uncertainty range is given in parentheses.

	Return time (yr)
Present day (2008–28)	1161 (740 to 5020)
Early twentieth century (1900–1920)	3.4×10^5 (5.7×10^4 to infinity)
Risk Ratio: Prob (present)/Prob (past)	282 (26 to infinity)
	Return time (yr)
Late twenty-first century (2080–2100)	64 (54 to 90)
Risk ratio: Prob (future)/Prob (past)	5136 (806 to infinity)

tional time series and then adjusting them to the mean forced response in different periods. Using the GEV distribution, it is estimated that the return time increases from ~10^5 years in the early twentieth century to 1400 years at present and 78.5 years by 2100. The observationally based estimates are hence in good agreement with the CMIP5 results.

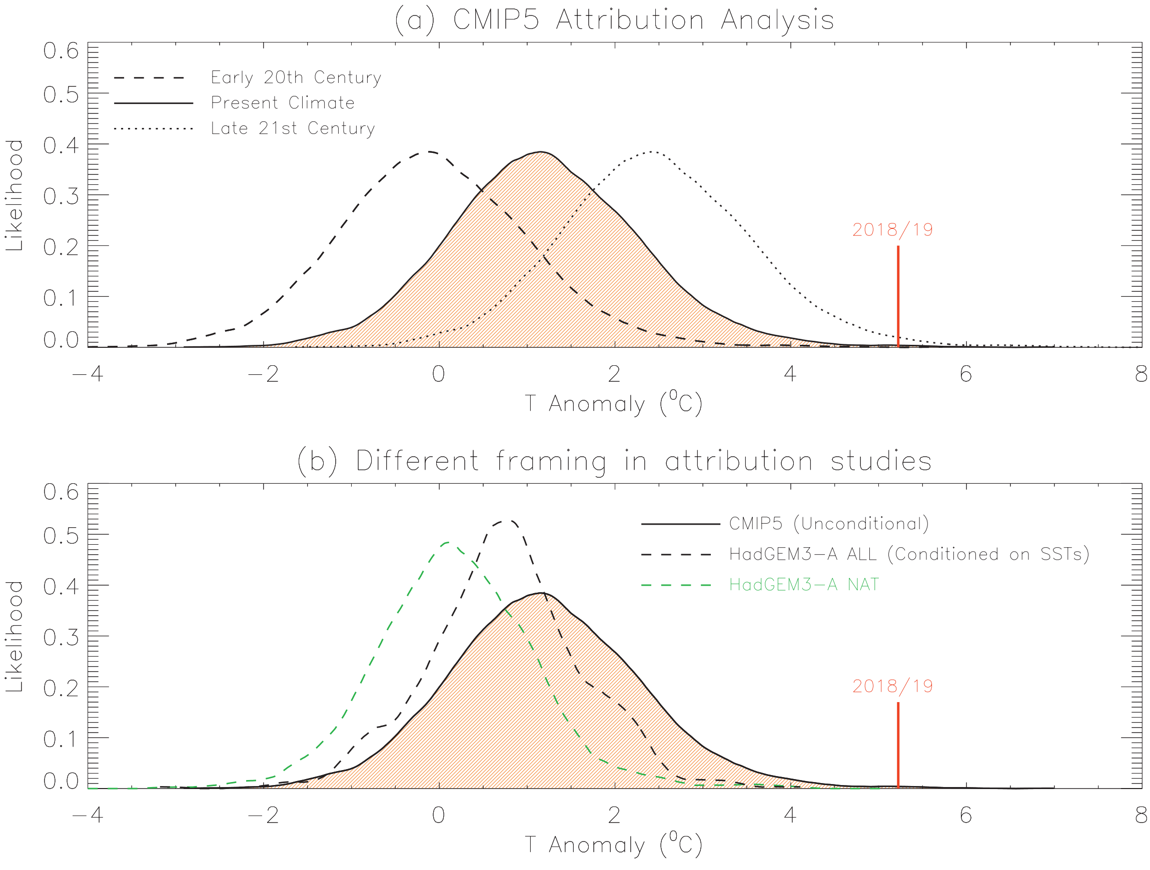

Fig. 2. (a) Normalized distributions of the warmest day in winter in central England constructed with CMIP5 data from the ALL simulations for the present climate (years 2008–28; solid line, filled curve), the climate of the early twentieth century (years 1900–1920; dashed line), and the climate of the late twenty-first century (years 2080–2100; dotted line). (b) The same CMIP5 distribution as in (a) is shown for the present climate (solid line, filled curve), together with the distribution constructed with HadGEM3-A data from the ALL (black dashed line) and NAT (green dashed line) simulations for the same period. The 2018/19 anomaly is marked by the red vertical line.

HadGEM3-A attribution.

A complementary analysis with ALL and NAT simulations of the winter 2018/19 produced by the HadGEM3-A attribution system of the Hadley Centre (Ciavarella et al. 2018) is also carried out. HadGEM3-A provides 525 simulations for each experiment and as it is an atmosphere-only model, it prescribes the oceanic state using HadISST observations (Rayner et al. 2003; also, see the online supplemental material). Like the CMIP5 ensemble, the model variance is also small and is corrected as described earlier. The sample size of simulated events is too small to compute the near-zero likelihood in the NAT climate. Unlike the CMIP5 analysis, it is also not feasible to estimate the probability in the ALL climate of 2018/19, since the HadGEM3-A distribution is narrower and thus the event lies farther into the warm tail (Fig. 2b). The use of a single model (HadGEM3-A) rather than a multimodel ensemble with a mixture of climate change sensitivities as well as the conditioning on the observed oceanic state may both contribute to the smaller spread of the distribution. As atmosphere–ocean coupled models sample the range of all possible states of the ocean, they may indeed yield a broader distribution than atmospheric models, providing a general probability estimate irrespective of the oceanic conditions.

Discussion.

Our study employs two methodologies that frame the attribution question in two different ways. The question in the multimodel CMIP5 analysis is “What is the likelihood of extremes with and without human influence in the general case (i.e. under any possible conditions)?”. On the other hand, the single-model HadGEM3-A analysis asks: “What is the likelihood, given the oceanic conditions at the time of the 2018/19 event?”. Both questions are valid and useful, but the two approaches can lead to different answers, as demonstrated in Fig. 2b. While a recent report by the United States National Academies of Sciences, Engineering, and Medicine (NASEM 2016) encouraged multimethod approaches in studies of extreme events, one should also be careful not to interpret apparent inconsistencies as limitations, when different methods may simply attempt to answer different questions. A more detailed assessment of the framing effect in event attribution is given in Christidis et al. (2018) and Fischer et al. (2018).

The CMIP5 analysis reveals that winter CET extremes like in 2018/19 are rare even in today’s warmer climate, but still about 300 times more likely because of human influence. Moreover, they are shown to become decidedly more common in the future, expected to occur at least once a century by 2100, and probably more frequently under higher emissions scenarios than RCP4.5. While the effect of the atmospheric circulation was key for the reference event, here we only consider an unconditional framing without explicitly assessing the effect of dynamics. Previous work has suggested that Arctic warming may impact U.K. extremes via dynamical changes (Hanna et al. 2017), although this link has not been robustly established (Blackport and Screen 2020). A possible strengthening of the Atlantic jet (Lee et al. 2019) may constitute another dynamical driver of winter changes. Taking the overall effect of anthropogenic climate change into account, milder winters are expected in the United Kingdom (Murphy et al. 2018), with less frequent cold extremes and new high temperature records.

Acknowledgments. This work was supported by the Met Office Hadley Centre Climate Programme funded by BEIS and Defra and the EUPHEME project, which is part of ERA4CS, an ERA-NET initiated by JPI Climate and co-funded by the European Union (Grant 690462).

References

Blackport, R., and J. A. Screen, 2020: Insignificant effect of Arctic amplification on the amplitude of midlatitude atmospheric waves. *Sci. Adv.*, **6**, eaay2880, https://doi.org/10.1126/sciadv.aay2880.

Christidis, N., and P. A. Stott, 2020: The extremely cold start of the spring of 2018 in the United Kingdom, [in "Explaining Extremes of 2018 from a Climate Perspective"]. *Bull. Amer. Meteor. Soc.*, **101**, S23–S28, https://doi.org/10.1175/BAMS-D-19-0084.1.

Christidis, N., P. A. Stott, A. Scaife, A. Arribas, G. S. Jones, D. Copsey, J. R. Knight, and W. J. Tennant, 2013: A new HadGEM3-A based system for attribution of weather and climate-related extreme events. *J. Climate*, **26**, 2756–2783, https://doi.org/10.1175/JCLI-D-12-00169.1.

Christidis, N., A. Ciavarella, and P. A. Stott, 2018: Different ways of framing event attribution questions: The example of warm and wet winters in the UK similar to 2015/16. *J. Climate*, **31**, 4827–4845, https://doi.org/10.1175/JCLI-D-17-0464.1.

Ciavarella, A., and Coauthors, 2018: Upgrade of the HadGEM3-A based attribution system to high resolution and a new validation framework for probabilistic event attribution. *Wea. Climate Extremes*, **20**, 9–32, https://doi.org/10.1016/j.wace.2018.03.003.

Fischer, E. M., U. Beyerle, C. F. Schleussner, A. D. King, and R. Knutti, 2018: Biased estimates of changes in climate extremes from prescribed SST simulations. *Geophys. Res. Lett.*, **45**, 8500–8509, https://doi.org/10.1029/2018GL079176.

Hanna, E., R. J. Hall, and J. E. Overland, 2017: Can Arctic warming influence UK extreme weather? *Weather*, **72**, 346–352, https://doi.org/10.1002/wea.2981.

Kalnay, E., and Coauthors, 1996: The NCEP/NCAR 40-Year Reanalysis Project. *Bull. Amer. Meteor. Soc.*, **77**, 437–471, https://doi.org/10.1175/1520-0477(1996)077<0437:TNYRP>2.0.CO;2.

Kendon, M., D. Sexton, and M. McCarthy, 2020: 20°C in the UK winter: A sign of the future? *Weather*, **75**, 318–306, https://doi.org/10.1002/wea.3811.

Lee, S. H., P. D. Williams, and T. H. A. Frame, 2019: Increased shear in the North Atlantic upper-level jet stream over the past four decades. *Nature*, **572**, 639–642, https://doi.org/10.1038/s41586-019-1465-z.

Murphy, J. M., and Coauthors, 2018: UKCP18 land projections: Science report. Met Office, https://www.metoffice.gov.uk/research/collaboration/ukcp/guidance-science-reports.

National Academies of Sciences, Engineering and Medicine (NASEM), 2016: Attribution of Extreme Weather Events in the Context of Climate Change. The National Academies Press, 186 pp., https://doi.org/10.17226/21852.

Parker, D. E., T. P. Legg, and C. K. Folland, 1992: A new daily central England temperature series, 1772–1991. *Int. J. Climatol.*, **12**, 317–342, https://doi.org/10.1002/joc.3370120402.

Rayner, N. A., D. E. Parker, E. B. Horton, C. K. Folland, L. V. Alexander, D. P. Rowell, E. C. Kent, and A. Kaplan, 2003: Global analyses of sea surface temperature, sea ice, and night marine air temperature since the late nineteenth century. *J. Geophys. Res.*, **108**, 4407, https://doi.org/10.1029/2002JD002670.

Stott, P. A., and Coauthors, 2016: Attribution of extreme weather and climate-related events. *Wiley Interdiscip. Rev.: Climate Change*, **7**, 23–41, https://doi.org/10.1002/wcc.380.

CMIP6 Model-Based Assessment of Anthropogenic Influence on the Long Sustained Western Cape Drought over 2015–19

Jonghun Kam, Seung-Ki Min, Piotr Wolski, and Jong-Seong Kug

AFFILIATIONS: Kam, Min, and Kug—Division of Environmental Science and Engineering, Pohang University of Science and Technology, Pohang, South Korea; **Wolski**—Climate System Analysis Group, University of Cape Town, Cape Town, South Africa

CORRESPONDING AUTHOR: Jonghun Kam, jhkam@postech.ac.kr

DOI:10.1175/BAMS-D-20-0159.1

A supplement to this article is available online (10.1175/BAMS-D-20-0159.2)

CMIP6 simulations suggest that anthropogenic greenhouse gas forcing has at least doubled the likelihood of 2015–19 like prolonged droughts over the South African Western Cape, with large cancellation due to other anthropogenic effects.

South Africa's Western Cape (WC) with its agriculture-based economy and reservoir-based water supply system, is vulnerable to drought, and during 2015–19 it experienced a multiyear drought condition. A recent study (Otto et al. 2018) reported that anthropogenic influence increased the likelihood of exceeding rainfall reduction over the Cape Town region during the first three years of that drought (2015–17) by a factor of 3. During that period, Cape Town experienced a water crisis threatening a shutdown of water supply to the four million residents (Masante et al. 2018) with water supply dropping to 20% of capacity in January 2018 (Muller 2018). In 2019, the WC experienced further dry conditions, extending the earlier drought and resulting in 2019 crop yield reduction by 25% (AGRI SA 2020).

The recent anthropogenic warming (IPCC 2018) likely caused drying trends over Southern Hemisphere subtropics associated with Hadley cell expansion (Purich et al. 2013; Burls et al. 2019) and is expected to increase drought durations over South Africa in the future (e.g., Ukkola et al. 2020). However, understanding of anthropogenic influence on the observed prolonged drought duration (e.g., multiple years) remains limited. Here, we investigate anthropogenic impact on meteorological drought *duration* in the broader WC region, posing the following questions: How unusual is the duration of the 2015–19 WC drought? Is there an anthropogenic contribution, particularly the contribution of greenhouse gas increases, to such prolonged droughts? By answering these questions, this study provides actionable information to policy makers and local stakeholders for drought mitigation and management.

Data and methods.

First, we computed regional averages of monthly precipitation over the WC from CRU (version TS v4.04; Harris et al. 2014), GPCC (version 2018; Schneider et al. 2011), and GPCP (version 2.3; Adler et al. 2018) datasets, rather than from station observations that cover only the western (wetter) part of the WC (1933–2017; Wolski et al. 2020). We found some stations excluded in the CRU and GPCC data since 2000 and 2010, respectively. The impact of changing numbers of stations is lower in GPCC than in CRU over the WC (Wolski et al. 2020); also, GPCC includes fewer observational stations before 1950 and after 1998 than CRU (Otto et al. 2018). Nevertheless, an overall consistency is found between gridded data and station observations (Figs. 1a–c).

Next, we computed the 12-month Standard Precipitation Index (SPI-12) over the study region (Fig. 1f; McKee et al. 1993) as the WC drought index. SPI-12 threshold values of −0.8 and 0.2 were used to identify drought onset and recovery, respectively, following Mo (2011). We also computed the Standardized Precipitation Evapotranspiration Index (SPEI) using the CRU data and found no significant difference from SPI (not shown), confirming the dominant role of precipitation in determining the WC drought (Otto et al. 2018).

To identify anthropogenic influence on the long-lasting drought, five CMIP6 model simulations were analyzed over 1901–2019: historical (ALL; 32 ensemble runs), natural-only (NAT; 30), and greenhouse gas-only (GHG; 25), which give 289, 324, and 233 drought events, respectively. First, seven CMIP6 models were selected based on the availability of multiple ensemble members (≥3 members for ALL, NAT, and GHG; see Table ES1 in the online supplemental information) and then the five models were finally selected based on the performance of the seasonality of precipitation over WC (Fig. ES1). The ALL simulations (ended in 2014) were extended up to 2019 using the corresponding Shared Socioeconomic Pathway 2.45 or 3.70 scenario runs, which were chosen based on the data availability considering their similar radiative forcing over 2015–19 (O'Neill et al. 2016). The ALL simulations include anthropogenic (increases in greenhouse gases and aerosols) and natural forcings (changes in solar and volcanic activities) while the NAT simulations contain only natural forcings. The GHG simulations are driven by only greenhouse gas increases, designed to isolate responses to GHG forcing from other forcings including aerosols, solar, and volcanic forcings (Meinshausen et al. 2017).

We used an areal conservative remapping method to interpolate all model data onto the observed grids (50 km × 50 km) before taking WC area means, which accounts for fractional contributions of the input grid boxes to each output grid box. Next, we fitted gamma distribution to regional mean precipitation from ALL simulations and then used it to compute SPI-12 for the ALL, GHG, and NAT simulations of the corresponding

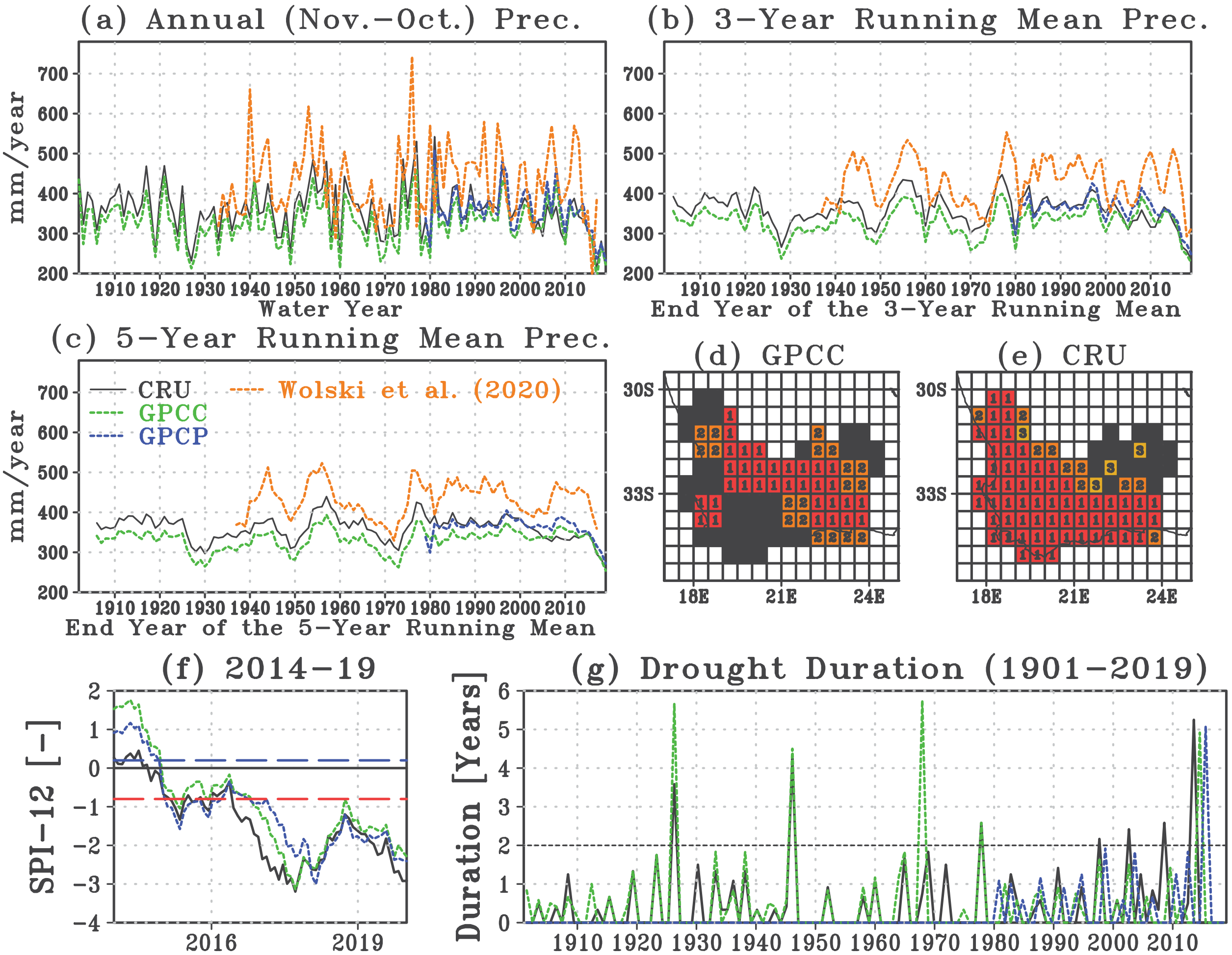

Fig. 1. Time series of the water year (WY; November through October of the following year) (a) total precipitation and the (b) 3-yr and (c) 5-yr running means of the WY annual total precipitation. In (a)–(c), orange dotted lines depict the stations data (1933–2017) used in Wolski et al. (2020). Also shown are ranks of the 5-yr mean precipitation over November 2014 through October 2019 from the (d) GPCC and (e) CRU data. Colored grid cells in (d) and (e) depict our study region, the Western Cape (red, orange, and yellow depict the lowest, second lowest, and third lowest, respectively, since 1901). Time series of monthly drought (SPI-12) index over 2014–19 (f). Red and blue dashed lines depict the threshold values for drought onset and recovery, respectively. (g) Duration of the observed drought events identified from the SPI-12 values: CRU (black), GPCC (green), and GPCP (blue).

model. Finally, we computed the duration of each drought event as done in the observations and compared the simulated frequency of long-term (≥2 yr) droughts [the ratio of the number of long-term drought events to the number of all drought events] within a 20-yr moving window (McCabe et al. 2004) with the observed.

To construct a multimodel probability distribution of drought duration, we used the last 30-yr segment (1990–2019) from the ALL, GHG, and NAT simulations and fitted the gamma distribution function to durations of identified drought events. We used the maximum likelihood estimation method for parameter estimation. Fitted gamma distributions are well matched with histograms of drought durations (positively skewed with a large range from months to years; see Fig. ES2).

We estimated the probability ratio of long-term drought duration [PR = (P_{ALL} or P_{GHG})/(P_{NAT}), where P_{ALL}, P_{GHG}, and P_{NAT} are the probabilities of exceeding the drought duration thresholds (2, 3, 4, or 5 years) from the ALL, GHG, and NAT ensemble runs, respectively]. We computed 90% confidence interval (CI) of PR using a bootstrap method.

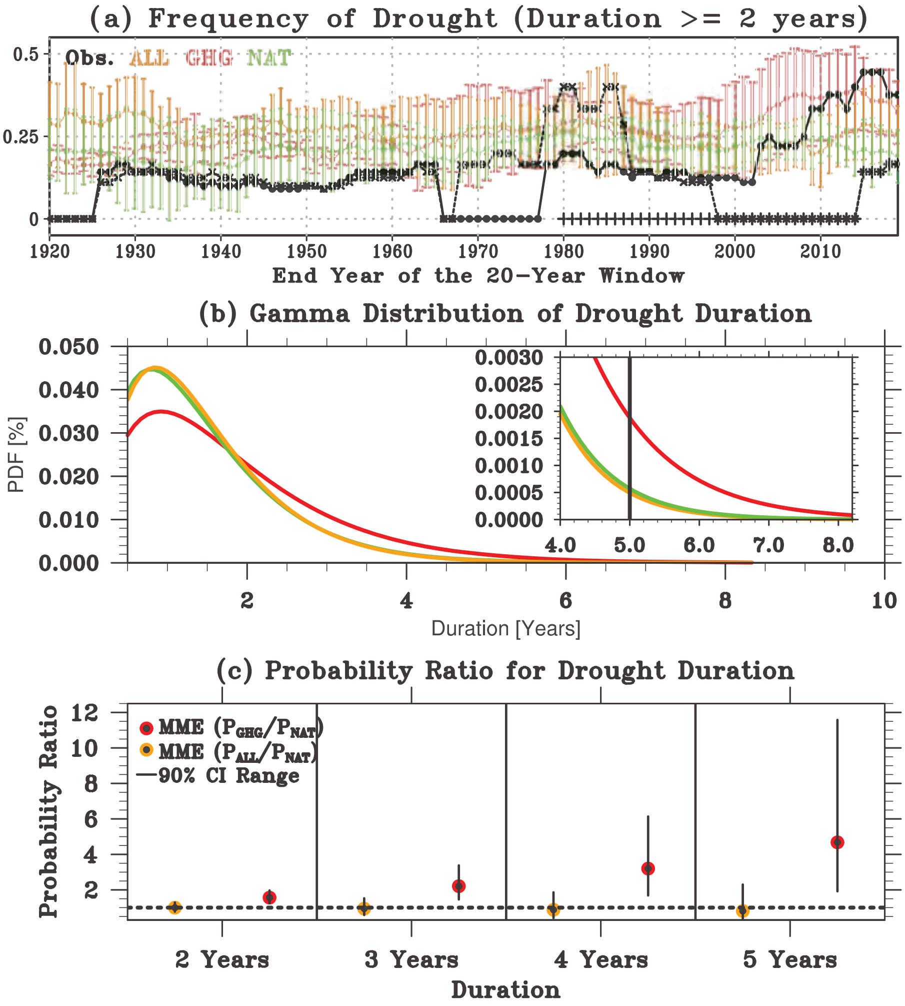

Fig. 2. (a) 20-yr moving averages of the frequency of long-term drought events from the observations (black circles, plus signs, and cross signs depicts CRU, GPCC, and GPCP, respectively) and the frequency of long-term drought events (divided by total number of drought events within the 20-yr moving window) from model simulations. Orange, red and green dots depict the MME drought frequency from the ALL, GHG, and NAT forcing runs, respectively. The error bars depict the range within plus or minus one standard deviation of the MME from each experiment runs. (b) Gamma distributions fitted to drought duration from the ALL (orange), GHG (red), and NAT (green) forcing runs over the 1990–2019 period (see Fig. ES2 for histograms). (c) Probability ratios (PRs) between ALL and NAT (orange) and between GHG and NAT (red) for drought duration ≥ 2, 3, 4, and 5 years, respectively. Lines indicate 90% confidence interval (CI) range of PRs. See text for details.

We first randomly select a sample (with repetition) of 289, 324, and 233 drought events from the fitted distribution of ALL, NAT, and GHG simulations, respectively. Then, we fit the gamma distribution to the drought durations of random samples and calculate P_{ALL}, P_{GHG}, and P_{NAT} and PRs. Finally, we repeated the entire procedure 10,000 times and estimated the 90% CI of PR.

Results.

The WC had anomalously low precipitation during the water year 2019 (WY 2019; defined based on precipitation's seasonality as November 2018–October 2019; Fig. 1a). WY 2019 is the second and fourth driest since 1901 in CRU and GPCC, respectively. Three- and five-year averages ending in 2019 are the driest in all three datasets

(Figs. 1b,c). The extremely long-lasting drought started in early 2015 and continued by WY 2017 (Otto et al. 2018). Rainfall in WY 2018 was still low but slightly higher than rainfall in WY 2016. The dry conditions during 2019 ranked the 2015–19 precipitation the lowest (since 1901) over 37% (GPCC) or 68% (CRU) area of WC (Figs. 1d,e), extending the 2015–17 drought to December 2019 (Fig. 1f).

We detected 41, 43, and 15 events over 119, 119, and 41 years from the CRU, GPCC, and GPCP precipitation-based drought index, respectively (Fig. 1g). The expected return period of identified droughts ranges from 2.7 (119 years/43 events or 41/15) to 2.9 years (119/41). CRU and GPCC share longest droughts over 1925–28, 1944–48, and 2015–19 but with different ranks. The 2015–19 drought duration is the longest (CRU) or third longest (GPCC) longest since 1901, with small differences (<4 months) among the observational data (63, 59, and 61 months from CRU, GPCC, and GPCP, respectively). GPCC and GPCP show no significant trend in the short-term (herein, <2 yr) and long-term (≥2 yr) drought frequencies. CRU shows that four out of seven long-term droughts occurred after 1995, but this might be partly due to station base changes identified by Wolski et al. (2020). The disparity between datasets warrants further investigation of uncertainty sources in gridded data.

The frequencies of long-term droughts in the GHG simulations show an upward trend since 2000 (consistent with the CRU data) while the ALL and NAT simulations show no trend over time (Fig. 2a). Over 1970s–1990s, high frequencies of long-term droughts in GPCC are consistent with those in the ALL and GHG simulations. The multimodel estimated gamma distribution (a red line in Fig. 2b) for GHG has a longer tail than that for the ALL or NAT simulations, with little difference found between ALL and NAT. This implies that the likelihood to have long sustained drought is significantly increased by GHG increases while other external forcing such as anthropogenic aerosols may offset the GHG-induced increase in long-term drought frequency.

The PR value from ALL and NAT simulations for 5-yr duration or longer is 0.8 (90% CI of 0.3–2.3; Fig. 2c). The PR estimates for the duration of two, three, and four years or longer are similar: 0.99 (0.8–1.3), 0.94 (0.6–1.6), and 0.9 (0.4–1.9), respectively. Little difference in PR between ALL and NAT suggests a lack of significant anthropogenic influence on multiyear drought frequencies over the WC region. In contrast, the PR estimates from GHG and NAT simulations show that greenhouse gas–induced warming increases the likelihood of droughts >5 years in duration (like the 2015–19 drought) by a factor of 4.7 (the 90% CI of 1.9 to 11.6). The PR estimates for the drought with duration of 2, 3, and 4 years or longer are also larger than unity: 1.6 (1.2–2.0), 2.2 (1.4–3.4), and 3.2 (1.7–6.1), respectively, supporting the important role of GHG forcing in driving long-lasting droughts.

In summary, the 2015–19 WC drought is the longest (either the longest or third longest) drought on record since 1901, and still continues as of the end of 2019. Based on the five CMIP6 simulations, which can reproduce the observed precipitation seasonality, GHG forcing has likely contributed to the increased probability of such long-lasting drought, at least by a factor of 2, compared to conditions without human influences (NAT). Results remain unaffected when including the two models that have lower performance in precipitation seasonality, suggesting weak sensitivity of our attribution results to model skills. Although some previous studies suggested Hadley cell expansion as a possible mechanism for increased duration of short-term droughts (Ukkola et al. 2020), historical simulations (ALL), including non-GHG anthropogenic forcings, do not show clear increases in the frequency of long-term droughts. It suggests possible offsetting effects by anthropogenic aerosols (cf. Rowell et al. 2015). Quantifying the relative contribution of GHG and other anthropogenic effects and exploring the associated physical mechanisms including Hadley expansion influence (Garfinkel et al. 2015; Nguyen et al. 2015; Zhao et al. 2020) as well as El Niño (Yuan et al. 2013; Otto et al. 2018) is an important task for the future risk assessment of the WC droughts.

Acknowledgments. We thank the CMIP6 project, for making available the CMIP6 data; and the Climate Research Unit and NOAA ESRL Physical Sciences Laboratory for providing observational precipitation datasets. J.K. and P.W. are partially supported by the NRF Basic Research Program (NRF-2020R1A4A1018818) and AXA Chair in African Climate Risk, respectively.

References

Adler, R. F., and Coauthors, 2018: The Global Precipitation Climatology Project (GPCP) monthly analysis (new version 2.3) and a review of 2017 global precipitation. *Atmosphere*, **9**, 138, https://doi.org/10.3390/atmos9040138.

AGRI SA, 2020: Agriculture Drought Report 2019/2020: "We are in a financial drought!" AGRI SA, 42 pp., https://rpo.co.za/wp-content/uploads/2019/12/Agriculture-Drought-Report-2019.pdf.

Burls, N. J., R. C. Blamey, B. A. Cash, E. T. Swenson, A. al Fahad, M. J. M. Bopape, D. M. Straus, and C. J. Reason, 2019: The Cape Town "Day Zero" drought and Hadley cell expansion. *npj Climate Atmos. Sci.*, **2**, 27, https://doi.org/10.1038/s41612-019-0084-6.

Eyring, V., S. Bony, Meehl, Senior, B. Stevens, Stouffer, and Taylor, 2016: Overview of the Coupled Model Intercomparison Project phase 6 (CMIP6) experimental design and organization. *Geosci. Model Dev.*, **9**, 1937–1958, https://doi.org/10.5194/gmd-9-1937-2016.

Garfinkel, C. I., D. W. Waugh, and L. M. Polvani, 2015: Recent Hadley cell expansion: The role of internal atmospheric variability in reconciling modeled and observed trends. *Geophys. Res. Lett.*, **42**, 10 824–10 831, https://doi.org/10.1002/2015GL066942.

Harris, I. P. D. J., P. D. Jones, T. J. Osborn, and D. H. Lister, 2014: Updated high-resolution grids of monthly climatic observations—The CRU TS3.10 dataset. *Int. J. Climatol.*, **34**, 623–642, https://doi.org/10.1002/joc.3711.

IPCC, 2018: Summary for policymakers. Global Warming of 1.5°C, V. Masson-Delmotte et al., Eds., World Meteorological Organization, 1–32.

Masante, D., N. McCormick, J. Vogt, C. Carmona-Moreno, E. Cordano, and I. Ameztoy, 2018: Drought and Water Crisis in Southern Africa. European Commission, Ispra, 28 pp., https://doi.org/10.2760/81873.

McCabe, G. J., M. A. Palecki, and J. L. Betancourt, 2004: Pacific and Atlantic Ocean influences on multidecadal drought frequency in the United States. *Proc. Natl. Acad. Sci. USA*, **101**, 4136–4141, https://doi.org/10.1073/pnas.0306738101.

McKee, T. B., N. J. Doesken, and J. Kleist, 1993: The relationship of drought frequency and duration to time scales. Proc. Eighth Conf. on Applied Climatology, Anaheim, CA, Amer. Meteor. Soc., 179–184.

Meinshausen, M., and Coauthors, 2017: Historical greenhouse gas concentrations for climate modelling (CMIP6). *Geosci. Model Dev.*, **10**, 2057–2116, https://doi.org/10.5194/gmd-10-2057-2017.

Mo, K. C., 2011: Drought onset and recovery over the United States. *J. Geophys. Res.*, **116**, D20106, https://doi.org/10.1029/2011JD016168.

Muller, M., 2020: Cape Town's drought: Don't blame climate change. *Nature*, **559**, 174–176, https://doi.org/10.1038/d41586-018-05649-1.

Nguyen, H., C. Lucas, A. Evans, B. Timbal, and L. Hanson, 2015: Expansion of the Southern Hemisphere Hadley cell in response to greenhouse gas forcing. *J. Climate*, **28**, 8067–8077, https://doi.org/10.1175/JCLI-D-15-0139.1.

O'Neill, B. C., and Coauthors, 2016: The Scenario Model Intercomparison Project (ScenarioMIP) for CMIP6. *Geosci. Model Dev.*, **9**, 3461–3482, https://doi.org/10.5194/gmd-9-3461-2016.

Otto, F. E., and Coauthors, 2018: Anthropogenic influence on the drivers of the Western Cape drought 2015–2017. *Environ. Res. Lett.*, **13**, 124010, https://doi.org/10.1088/1748-9326/aae9f9.

Purich, A., T. Cowan, S. Min, and W. Cai, 2013: Autumn precipitation trends over Southern Hemisphere midlatitudes as simulated by CMIP5 models. *J. Climate*, **26**, 8341–8356, https://doi.org/10.1175/JCLI-D-13-00007.1.

Rowell, D. P., B. B. B. Booth, S. E. Nicholson, and P. Good, 2015: Reconciling past and future rainfall trends over East Africa. *J. Climate*, **28**, 9768–9788, https://doi.org/10.1175/JCLI-D-15-0140.1.

Schneider, U., A. Becker, P. Finger, A. Meyer-Christoffer, B. Rudolf, and M. Ziese, 2011: GPCC full data reanalysis version 6.0 at 0.5: Monthly land-surface precipitation from rain-gauges built on GTS-based and historic data. GPCC, accessed 6 October 2020, https://doi.org/10.5676/DWD_GPCC/FD_M_V6_050.

Stott, P. A., D. A. Stone, and M. R. Allen, 2004: Human contribution to the European heatwave of 2003. *Nature*, **432**, 610–614, https://doi.org/10.1038/nature03089.

Ukkola, A. M., M. G. De Kauwe, M. L. Roderick, G. Abramowitz, and A. J. Pitman, 2020: Robust future changes in meteorological drought in CMIP6 projections despite uncertainty in precipitation. *Geophys. Res. Lett.*, **47**, e2020GL087820, https://doi.org/10.1029/2020GL087820.

Wolski, P., S. Conradie, C. Jack, and M. Tadross, 2020: Spatio-temporal patterns of rainfall trends and the 2015–2017 drought over the winter rainfall region of South Africa. *Int. J. Climatol.*, https://doi.org/10.1002/joc.6768, in press.

Yuan, X., E. F. Wood, N. W. Chaney, J. Sheffield, J. Kam, M. Liang, and K. Guan, 2013: Probabilistic seasonal forecasting of African drought by dynamical models. *J. Hydrometeor.*, **14**, 1706–1720, https://doi.org/10.1175/JHM-D-13-054.1.

Zhao, X., Allen, T. Wood, and Maycock, 2020: Tropical belt width proportionately more sensitive to aerosols than greenhouse gases. *Geophys. Res. Lett.*, **47**, e2019GL086425, https://doi.org/10.1029/2019GL086425.

Has Global Warming Contributed to the Largest Number of Typhoons Affecting South Korea in September 2019?

Seung-Ki Min, Min-Gyu Seong, Dong-Hyun Cha, Minkyu Lee, Fraser C. Lott, Andrew Ciavarella, Peter A. Stott, Maeng-Ki Kim, Kyung-On Boo, and Young-Hwa Byun

AFFILIATIONS: Min—Division of Environmental Science and Engineering, Pohang University of Science and Technology, Pohang, and Institute for Convergence Research and Education in Advanced Technology, Yonsei University, Incheon, South Korea; **Seong**—Division of Environmental Science and Engineering, Pohang University of Science and Technology, Pohang, South Korea; **Cha and Lee**—School of Urban and Environmental Engineering, Ulsan National Institute of Science and Technology, Ulsan, South Korea; **Lott, Ciavarella, and Stott**—Met Office, Exeter, United Kingdom; **Kim**—Department of Atmospheric Sciences, Kongju National University, Gongju, South Korea; **Boo and Byun**—National Institute of Meteorological Sciences, Korea Meteorological Administration, Seogwipo, South Korea

CORRESPONDING AUTHOR: Seung-Ki Min, skmin@postech.ac.kr

DOI:10.1175/BAMS-D-20-0156.1

A supplement to this article is available online (10.1175/BAMS-D-20-0156.2)

A multimodel analysis indicates that the 2019 September record high number of typhoons affecting South Korea was contributed to mostly by the very strong convection over northwestern India with no discernible anthropogenic contribution.

During 2019, seven typhoons [i.e., tropical cyclones (TCs)] hit South Korea, resulting in tremendous damages on the country's infrastructure and economy through heavy rain and high winds (reported in *The Korea Herald*[1,2]). This is the largest number of annual TCs affecting South Korea since 1959; in particular, it was the first time since records began in 1904 that three typhoons struck South Korea during September (Figs. 1a,c). While warm sea surface over the western North Pacific is important for overall typhoon activities (e.g., Zhang et al. 2016), the western North Pacific subtropical high (WNPSH) is known to strongly modulate typhoon landfall over East Asia since typhoons usually move northward along its western boundary (Ho et al. 2004; M. Lee et al. 2019; Zhou and Lu 2019). In September 2019, the WNPSH was unusually strong with an extreme northwest

---

[1] http://www.koreaherald.com/view.php?ud=20190908000142.
[2] http://www.koreaherald.com/view.php?ud=20190922000168.

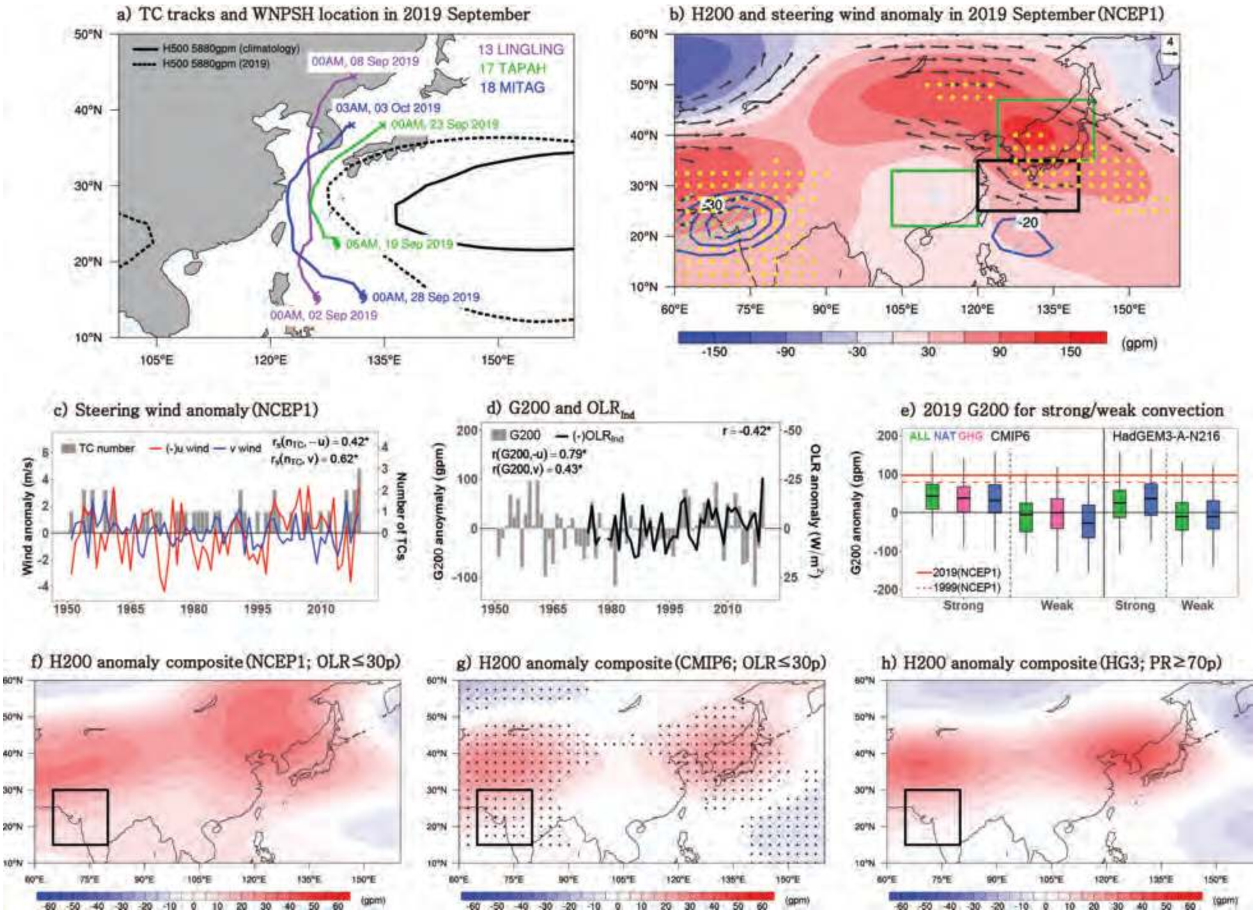

Fig. 1. (a) September 2019 typhoon tracks and WNPSH (western North Pacific subtropical high) boundary location. (b) Spatial patterns of anomalous geopotential height at 200 hPa (H200; shading), steering winds (vectors; only for wind speed ≥ 4 $m\ s^{-1}$), and OLR (outgoing longwave radiation; blue contours; only for ≤ –20 $W\ m^{-2}$). Green boxes indicate two regions used to define G200 (H200 gradient index; see text for its definition). Yellow dots and cyan hatches represent record high H200 and OLR, respectively. Time series of (c) numbers of TCs affecting South Korea (n_{TC}) and anomalous zonal and meridional steering winds (u, v) averaged over the East China Sea area [120°–140°E, 25°–35°N; black box in (b)], and (d) G200 and area-mean OLR anomalies over northwestern India (OLR_{Ind}). Pearson correlation (r) and Spearman's rank correlation coefficients (r_s) are provided. (e) Boxplots of G200 anomalies from CMIP6 and HadGEM3-A-N216 runs for strong and weak northwestern Indian convection in comparison with the 2019 (red solid) and 1999 (red dotted) observed values. Composites of H200 anomalies (gpm) from (f) NCEP1, (g) CMIP6, and (h) HadGEM3-A-N216 (HG3) from years with stronger convection over northwestern India (black box) during 1981–2010; 30p and 70p represent 30th and 70th percentile, respectively. Black cross marks in (g) indicate more than 70% intermodel agreement in sign.

shift, as indicated by 5,880-gpm contours in Fig. 1a, which are typically used to depict its boundary (Liu and Chan 2013). The extreme development of the WNPSH was associated with anomalous anticyclonic circulation developed in the upper troposphere from northeast China to Japan (Fig. 1b), which intensified southeasterly steering winds (mass-weighted horizontal winds from 850 to 300 hPa) over the East China Sea area (black box in Fig. 1b), guiding the typhoons toward the Korean Peninsula (cf. Zhou and Lu 2019). Both the zonal and meridional components of the area-mean steering flows are significantly correlated with the TC numbers affecting South Korea at 5% level (Fig. 1c, based on Spearman's rank correlation using years with non-zero TCs). Given the observed and projected intensification of TCs landfalling over the northwest Pacific under warming (e.g., Mei and Xie 2016; H. Lee et al. 2019), the present study attempts to answer the question of whether global warming has contributed to the anomalous extreme steering winds.

During September 2019, there was strong convection in northwestern India [Figs. 1b,d, based on outgoing longwave radiation (OLR) anomalies] related to the strong Indian monsoon and its delayed withdrawal (reported in *The Indian Express*[3]). The strong convection over northwestern India is known to induce anomalous upper-troposphere highs over South Korea during summer through the Rossby wave propagation mechanism (Kim et al. 2019, 2020; Yeo et al. 2019; Min et al. 2020). A similar teleconnection pattern was observed in September (Figs. 1d,f), which can be reproduced by the models (Figs. 1g,h; Fig. ES1). This suggests that the unusually strong Indian monsoon may have contributed to the extreme number of TCs affecting South Korea.

The present study assesses anthropogenic and natural contributions to the September 2019 atmospheric circulation pattern conducive to the record high number of typhoons affecting South Korea using CMIP6 multimodel simulations as well as HadGEM3-A large-ensemble simulations performed with and without anthropogenic forcing (see below for details). Using a standard risk ratio (RR) approach to event attribution (Stott et al. 2016; Otto 2017), we compared the probabilities of occurrence of the TC-related circulation pattern between real and counterfactual conditions (to assess anthropogenic contribution) as well as between strong and weak tropical convection conditions (to assess natural contribution).

Data and methods.

Observational data include monthly mean geopotential height and horizontal winds throughout the troposphere for 1951–2019 from NCEP1 reanalysis (Kalnay et al. 1996), TC information for 1951–2019 from the Korea Meteorological Administration (KMA; https://data.kma.go.kr/), monthly mean OLR for 1974–2019 (https://psl.noaa.gov/data/gridded/data.interp_OLR.html).

Multimodel datasets from phase 6 of the Coupled Model Intercomparison Project (CMIP6; Eyring et al. 2016) are used, which include historical (natural plus anthropogenic, called ALL), natural-only (NAT), and greenhouse-only forcing (GHG) simulations (see Table ES1 in the online supplemental material). The data for 2010–19 from each experiment were used, assuming similar climate to 2019 conditions. Historical simulations (2010–14) were combined with corresponding Shared Socioeconomic Pathway (SSP) 2–4.5 scenarios (2015–19). High-resolution large-ensemble HadGEM3-A simulations performed for 2019 (referred to as HadGEM3-A-N216; Ciavarella et al. 2018; Vautard et al. 2019) were also used (Table ES2), which provide 525 members for real world (ALL) and counterfactual world (NAT) conditions. The observed 2019 SST and sea ice concentrations from HadISST1 (Rayner et al. 2003) was prescribed for ALL simulations. For NAT simulations, adjusted SST and sea ice concentrations were prescribed after removing anthropogenic SST changes (delta-SST) from HadISST1. The delta-SST was estimated from four CMIP5 models (as ALL–NAT) and an observed trend, each of which have 105 ensemble members (Table ES2). Observations and all model simulations were interpolated on the same 2.5° × 2.5° grids of NCEP1 reanalysis. All variables were normalized prior to analysis using mean and standard deviation of each data obtained from 1981–2010 for robust comparison between observations and models (see below for sensitivity tests to model samples). NAT and GHG runs were normalized based on ALL climatology of each model.

As a proxy of anomalous southeasterly steering wind over the East China Sea area, we defined a gradient index of 200-hPa geopotential height anomalies (hereafter, G200) between the East Sea (Sea of Japan) area and the southern China area (green boxes, Fig. 1b). The resulting observed G200 has significant correlations with steering winds, northwestern Indian convection (Fig. 1d), and also with the number of TCs affecting South Korea ($r_s = 0.50$). G200 indices were calculated for CMIP6 and Had-

---

[3] https://indianexpress.com/article/explained/india-monsoon-rainfall-bihar-patna-floods-6054167/.

GEM3-A-N216 simulations (Fig. 1e) and the RR was obtained for the 2019 G200 value in two ways. One ($RR_{ALL/NAT}$) is to calculate the ratio of the probability of occurrence of 2019-like positive G200 events between ALL and NAT, which quantifies human impacts on TC-related atmospheric circulation patterns. The other ($RR_{SC/WC}$) is to calculate the probability ratio between model samples with strong and weak Indian convection for ALL, NAT, or GHG separately (Fig. 1e) in order to examine Indian monsoon influences on the extreme G200 events. For this analysis, using normalized OLR (for CMIP6, based on each model) or precipitation (for HadGEM3-A-N216, due to data availability) averaged over northwestern India (black box in Fig. 1f), we selected samples with OLR ≤ 30th percentile for strong convection (SC), with OLR ≥ 70th percentile for weak convection (WC), and vice versa for precipitation. To test RR sensitivity to a less extreme G200 threshold, we used the value observed in 1999 (dashed line in Fig. 1e), when two TCs affected South Korea. The 5%–95% confidence intervals of RRs were estimated using the likelihood ratio method following Paciorek et al. (2018).

Results.

Figure 2 illustrates the Gaussian kernel density function of the normalized G200 for ALL, NAT, and GHG simulations from CMIP6 and for ALL and NAT runs from HadGEM3-A-N216. CMIP6 results show that the probability of extreme G200 events exceeding the observed 2019 value is 2.97%, 3.24%, and 2.97% in ALL (P_{ALL}), NAT (P_{NAT}), and GHG (P_{GHG}), respectively (Table 1), indicating that the 2019-like extreme southeasterly flows occur rarely with similar probability across different forcings. The corresponding $RR_{ALL/NAT}$ is about 0.92 (5%–95% confidence interval is 0.46–1.81; Fig. 2f), suggesting no detectable human influences. HadGEM3-A-N216 results present P_{ALL} and P_{NAT} as 1.33% and 2.86%, respectively (Table 1), resulting in $RR_{ALL/NAT}$ = 0.47 (0.21–0.96). A simple analysis (Fig. ES3a) indicates that relatively low probability of ALL runs from HadGEM3-A-N216 is partly due to the identical SST forcing prescribed, as opposed to the NAT runs, which include five different SSTs (see Table ES2). When applying the 1999 observed threshold, $RR_{ALL/NAT}$ remains close to unity for both model ensembles (Table 1). This result indicates that the September 2019 TC-related extreme circulation pattern is not attributable to human-induced global warming.

To assess the possible contribution of strong northwestern Indian convection on the extreme TC-related circulation pattern, we compared the probabilities of occurrence of the extreme G200 events between model samples with SC and those with WC. Results reveal that when the northwestern Indian convection is stronger, G200 density distri-

Table 1. Probability (%) of occurrence exceeding the observed G200 values from total samples (P_{TOT}) and subsample with strong and weak convection over northwestern India (P_{SC} and P_{WC}, respectively). RR is calculated between ALL and NAT ($RR_{ALL/NAT}$) as well as between strong and weak convection ($RR_{SC/WC}$). The 5%–95% uncertainty ranges of RR are provided in brackets.

Model	Observed year	Experiment	P_{TOT} (%)	P_{SC} (%)	P_{WC} (%)	$RR_{SC/WC}$	$RR_{ALL/NAT}$
CMIP6	2019	ALL	2.97	7.27	0.00	∞ [5.49–∞]	0.92 [0.46–1.81]
		NAT	3.24	8.11	0.00	∞ [6.24–∞]	
		GHG	2.97	5.41	1.80	3.00 [0.89–14.02]	
	1999	ALL	6.76	14.41	2.70	5.33 [2.15–17.17]	0.83 [0.54–1.28]
		NAT	8.11	17.12	0.90	19.00 [4.97–182.47]	
		GHG	7.30	14.41	2.70	5.33 [2.15–17.17]	
HadGEM3-A-N216	2019	ALL	1.33	1.90	1.27	1.50 [0.34–7.76]	0.47 [0.21–0.96]
		NAT	2.86	6.96	0.63	11.00 [2.71–107.64]	
	1999	ALL	4.95	7.59	3.80	2.00 [0.92–4.70]	0.74 [0.49–1.12]
		NAT	6.67	11.39	3.80	3.00 [1.47–6.80]	

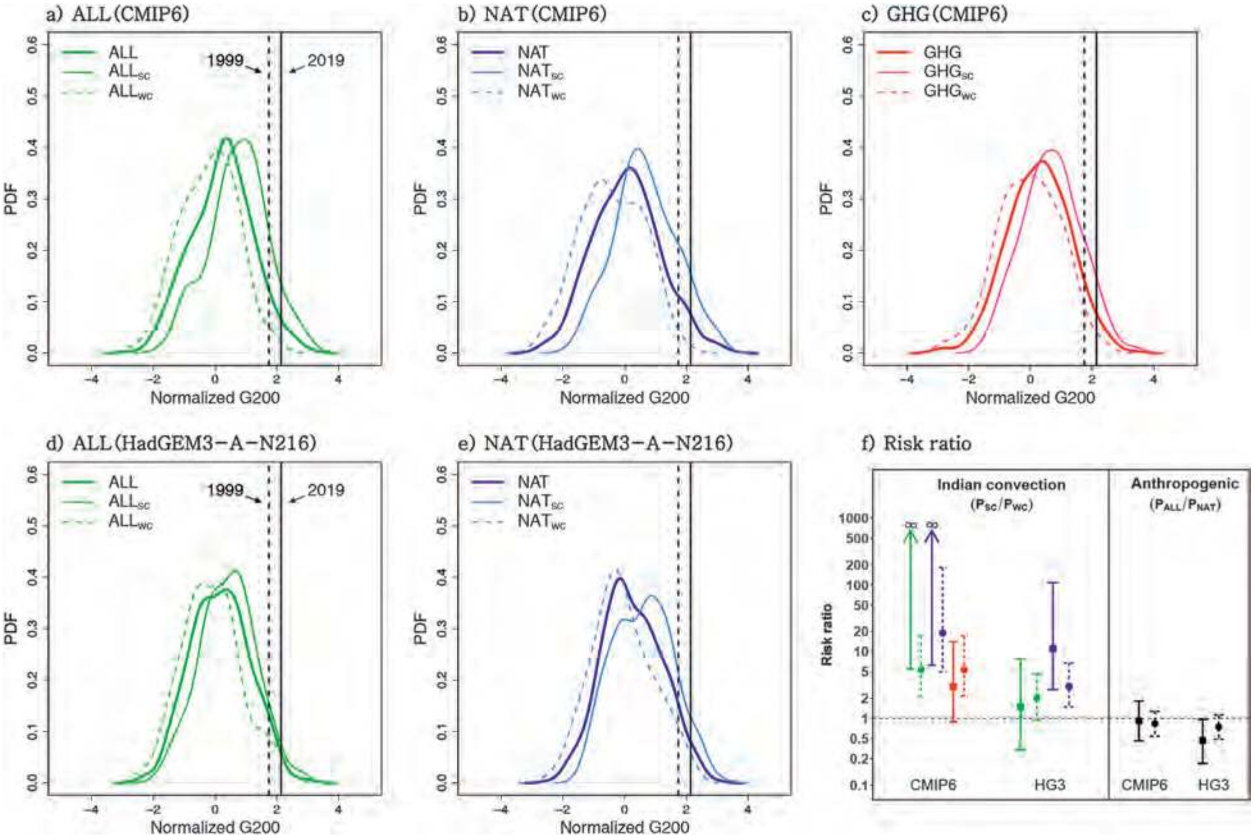

Fig. 2. Kernel density functions of normalized G200 for (a)–(c) CMIP6 ALL, NAT, and GHG simulations and (d),(e) HadGEM3-A-N216 (HG3) ALL and NAT simulations, respectively. The thick solid lines indicate results from all simulations and thin and dashed lines represent subsampled results with stronger convection (SC) and weaker convection (WC) conditions, respectively. Black solid and dashed vertical lines represent the 2019 and 1999 observed values from NCEP1. (f) RR (mark) and its 5%–95% confidence intervals (error bars) obtained (left) between P_{SC} and P_{WC} ($RR_{SC/WC}$) and (right) between P_{ALL} and P_{NAT} ($RR_{ALL/NAT}$) for CMIP6 and HG3 models. Solid and dashed error bars indicate RR results for the 2019 and 1999 observed thresholds, respectively. Refer to Table 1 for corresponding RR values and Fig. ES2 for corresponding return periods.

butions shift to right both for CMIP6 and HadGEM3-A-N216 (Fig. 2). The resulting P_{ALL}, P_{NAT}, and P_{GHG} clearly increase upon the stronger convection (Table 1), which can also be seen when applying the 1999 G200 threshold. WC samples exhibit the opposite results with decreased probability of extreme G200 events. $RR_{SC/WC}$ for CMIP6 is found to be at least 3 (based on best estimates), implying that the unusually strong northwestern Indian convection has contributed to the increased risk of September TCs affecting South Korea by intensifying anomalous southeasterly steering winds. HadGEM3-A-N216 results also show that P_{ALL} and P_{NAT} are increased upon stronger convection and vice versa. Compared to CMIP6, however, $RR_{SC/WC}$ from this model is generally lower and its confidence interval includes unity in ALL simulations. This can be associated with the narrower ensemble spread related to the single SST prescribed as discussed above. When applying the 1999 observed threshold, $RR_{SC/WC}$ and its confidence intervals are increased, supporting the contribution of the extreme northwestern Indian convection to the record high number of TCs affecting South Korea by increasing the probability of occurrence of extreme steering flow patterns. Overall results can be interpreted based on the corresponding return periods (Fig. ES2). Sensitivity tests support the robustness of our results to different sampling of models based on model skills for the Indian convection and teleconnection response (see Table ES1 and Figs. ES3b–e for details) although more comprehensive model evaluations are needed.

Concluding remarks.

Our multimodel event attribution analysis indicates no discernible anthropogenic influences on the September 2019 extreme steering winds over the East China Sea region, which were closely associated with the record high number of typhoons affecting South Korea. It is rather found that the unusually strong September monsoon over northwest India could well have contributed to the extreme circulation patterns, increasing the probability of a 2019-like event by at least 3 times in CMIP6 models and about 1.5 times in the HadGEM3-A-N216 ensemble. Further investigation is warranted to better understand details of how anomalous northwestern Indian convection induces extreme circulation patterns over Northeast Asia (e.g., Kim et al. 2019, 2020) and also to quantify human and natural contribution to the intensified Indian monsoon (cf. Menon et al. 2013; Lee et al. 2018). Finally, it should be noted that linking the extreme circulation pattern to actual TCs affecting South Korea remains difficult because of no consideration of TC genesis, large uncertainty in TC track data during pre-satellite period (e.g., Moon et al. 2019), and a lack of objective determination of TCs affecting South Korea.

Acknowledgments. We thank two anonymous reviewers for their thoughtful and constructive comments. This study was supported by the Korea Meteorological Administration Research and Development Program under Grant KMI2018-01214 and by a National Research Foundation of Korea (NRF) grant funded by the Korean government (MSIT) (NRF-2018R1A5A1024958). We acknowledge the World Climate Research Programme, which, through its Working Group on Coupled Modelling, coordinated and promoted CMIP6. We thank the climate modeling groups for producing and making available their model output, the Earth System Grid Federation (ESGF) for archiving the data and providing access (https://esgf-node.llnl.gov/projects/cmip6/), and the multiple funding agencies that support CMIP6 and ESGF.

References

Ciavarella, A., and Coauthors, 2018: Upgrade of the HadGEM3-A based attribution system to high resolution and a new validation framework for probabilistic event attribution. *Wea. Climate Extremes*, **20**, 9–32, https://doi.org/10.1016/j.wace.2018.03.003.

Eyring, V., S. Bony, G. A. Meehl, C. A. Senior, B. Stevens, R. J. Stouffer, and K. E. Taylor, 2016: Overview of the Coupled Model Intercomparison Project Phase 6 (CMIP6) experimental design and organization. *Geosci. Model Dev.*, **9**, 1937–1958, https://doi.org/10.5194/gmd-9-1937-2016.

Ho, C.-H., J.-J. Baik, J.-H. Kim, D.-Y. Gong, and C.-H. Sui, 2004: Interdecadal changes in summertime typhoon tracks. *J. Climate*, **17**, 1767–1776, https://doi.org/10.1175/1520-0442(2004)017<1767:ICISTT>2.0.CO;2.

Kalnay, E., and Coauthors, 1996: The NCEP/NCAR 40-Year Reanalysis Project. *Bull. Amer. Meteor. Soc.*, **77**, 437–472, https://doi.org/10.1175/1520-0477(1996)077<0437:TNYRP>2.0.CO;2.

Kim, M.-K., J.-S. Oh, C.-K. Park, S.-K. Min, K.-O. Boo, and J.-H. Kim, 2019: Possible impact of the diabatic heating over the Indian subcontinent on heat waves in South Korea. *Int. J. Climatol.*, **39**, 1166–1180, https://doi.org/10.1002/joc.5869.

——, and Coauthors, 2020: Performance evaluation of CMIP5 and CMIP6 models on heatwaves in Korea and associated teleconnection patterns. J. Geophys. Res. Atmos., 125, e2020JD032583, https://doi.org/10.1029/2020JD032583.

Lee, D., S.-K. Min, E. Fischer, H. Shiogama, I. Bethke, L. Lierhammer, and J. Scinocca, 2018: Impacts of half a degree additional warming on the Asian summer monsoon rainfall characteristics. *Environ. Res. Lett.*, **13**, 044033, https://doi.org/10.1088/1748-9326/aab55d.

Lee, H., C.-S. Jin, D.-H. Cha, M. Lee, D.-K. Lee, M.-S. Suh, S.-Y. Hong, and H.-S. Kang, 2019: Future change in tropical cyclone activity over the western North Pacific in CORDEX-East Asia multi-RCMs forced by HadGEM2-AO. *J. Climate*, **32**, 5053–5067, https://doi.org/10.1175/JCLI-D-18-0575.1.

Lee, M., D.-H. Cha, J. Moon, J. Park, C.-S. Jin, and J. C. L. Chan, 2019: Long-term trends in tropical cyclone tracks around Korea and Japan in late summer and early fall. *Atmos. Sci. Lett.*, **20**, e939, https://doi.org/10.1002/asl.939.

Liu, K. S., and J. C. Chan, 2013: Inactive period of western North Pacific tropical cyclone activity in 1998–2011. *J. Climate*, **26**, 2614–2630, https://doi.org/10.1175/JCLI-D-12-00053.1.

Mei, W., and S.-P. Xie, 2016: Intensification of landfalling typhoons over the northwest Pacific since the late 1970s. *Nat. Geosci.*, **9**, 753–757, https://doi.org/10.1038/ngeo2792.

Menon, A., A. Levermann, J. Schewe, J. Lehmann, and K. Frieler, 2013: Consistent increase in Indian monsoon rainfall and its variability across CMIP5 models. *Earth Syst. Dyn.*, **4**, 287300, https://doi.org/10.5194/esd-4-287-2013.

Min, S.-K., Y.-H. Kim, S.-M. Lee, S. Sparrow, S. Li, F. C. Lott, and P. A. Stott, 2020: Quantifying human impact on the 2018 summer longest heat wave in South Korea [in "Explaining Extreme Events of 2015 from a Climate Perspective"]. *Bull. Amer. Meteor. Soc.*, **101** (1), S103–S108, https://doi.org/10.1175/BAMS-D-19-0151.1.

Moon, I., S. Kim, and J. C. L. Chan, 2019: Climate change and tropical cyclone trend. *Nature*, **570**, E3–E5, https://doi.org/10.1038/s41586-019-1222-3.

Otto, F. E. L., 2017: Attribution of weather and climate events. *Annu. Rev. Environ. Resour.*, **42**, 627–646, https://doi.org/10.1146/annurev-environ-102016-060847.

Paciorek, C. J., D. A. Stone, and M. F. Wehner, 2018: Quantifying statistical uncertainty in the attribution of human influence on severe weather. *Wea. Climate Extremes*, **20**, 69–80, https://doi.org/10.1016/j.wace.2018.01.002.

Rayner, N. A., D. E. Parker, E. B. Horton, C. K. Folland, L. V. Alexander, D. P. Rowell, E. C. Kent, and A. Kaplan, 2003: Global analyses of sea surface temperature, sea ice, and night marine air temperature since the late nineteenth century. *J. Geophys. Res.*, **108**, 4407, https://doi.org/10.1029/2002JD002670.

Stott, P. A., and Coauthors, 2016: Attribution of extreme weather and climate-related events. *Wiley Interdiscip. Rev.: Climate Change*, **7**, 23–41, https://doi.org/10.1002/wcc.380.

Vautard, R., and Coauthors, 2019: Evaluation of the HadGEM3-A simulations in view of detection and attribution of human influence on extreme events in Europe. *Climate Dyn.*, **52**, 1187–1210, https://doi.org/10.1007/s00382-018-4183-6.

Yeo, S.-R., S.-W. Yeh, and W.-S. Lee, 2019: Two types of heat wave in Korea associated with atmospheric circulation pattern. *J. Geophys. Res. Atmos.*, **124**, 7498–7511, https://doi.org/10.1029/2018JD030170.

Zhang, W., and Coauthors, 2016: Influences of natural variability and anthropogenic forcing on the extreme 2015 accumulated cyclone energy in the western North Pacific [in "Explaining Extreme Events of 2015 from a Climate Perspective"]. *Bull. Amer. Meteor. Soc.*, **97** (12), S131–S135, https://doi.org/10.1175/BAMS-D-16-0146.1.

Zhou, X., and R. Lu, 2019: Interannual variability of the tropical cyclone landfall frequency over the southern and northern regions of East Asia in autumn. *J. Climate*, **32**, 8677–8686, https://doi.org/10.1175/JCLI-D-19-0057.1.

Are Long-Term Changes in Mixed Layer Depth Influencing North Pacific Marine Heatwaves?

Dillon J. Amaya, Michael A. Alexander, Antonietta Capotondi, Clara Deser, Kristopher B. Karnauskas, Arthur J. Miller, and Nathan J. Mantua

AFFILIATIONS: Amaya—Cooperative Institute for Research in Environmental Sciences (CIRES), University of Colorado Boulder, Boulder, Colorado; **Alexander**—NOAA Physical Sciences Laboratory, Boulder, Colorado; **Capotondi**—CIRES, University of Colorado Boulder, and NOAA Physical Sciences Laboratory, Boulder, Colorado; **Deser**—National Center for Atmospheric Research, Boulder, Colorado; **Karnauskas**—CIRES and Department of Atmospheric and Oceanic Sciences, University of Colorado Boulder, Boulder, Colorado; **Miller**—Scripps Institution of Oceanography, University of California San Diego; **Mantua**—NOAA Southwest Fisheries Science Center, Fisheries Ecology Division

CORRESPONDING AUTHOR: Dillon J. Amaya, dillon.amaya@colorado.edu

DOI:10.1175/BAMS-D-20-0144.1

A supplement to this article is available online (10.1175/BAMS-D-20-0144.2)

The 2019 Northwest Pacific marine heatwave was amplified by natural, multidecadal shoaling of the ocean mixed layer; anthropogenic mixed layer shoaling will amplify marine heatwaves in the future.

In boreal summer 2019, the northeast Pacific Ocean (NEPac) experienced a resurgence of extremely warm upper ocean temperatures (Fig. 1a). The strength and pattern of the sea surface temperature anomalies (SSTAs) earned this event the moniker "Blob 2.0" (Amaya et al. 2020; hereafter A2020), a reference to the original warm "Blob" that initiated a multi-year marine heatwave (MHW) that devastated regional ecosystems over 2014–16 (Bond et al. 2015; Cavole et al. 2016; Amaya et al. 2016; Piatt et al. 2020). In particular, the intraseasonal persistence of the 2019 Blob 2.0 generated similar widespread concern among fishery and wildlife managers for sensitive marine ecosystems along the west coast of North America (NOAA 2019).

Blob 2.0 primarily resulted from a record minimum mixed layer depth (MLD; Fig. 1a shading), which formed due to weaker than normal wind speeds and strong surface heating from reduced cloud cover (A2020). Equation (1) illustrates how shallow mixed layer depths affect mixed layer temperature changes, $\partial T'_m/\partial t$, when consider-

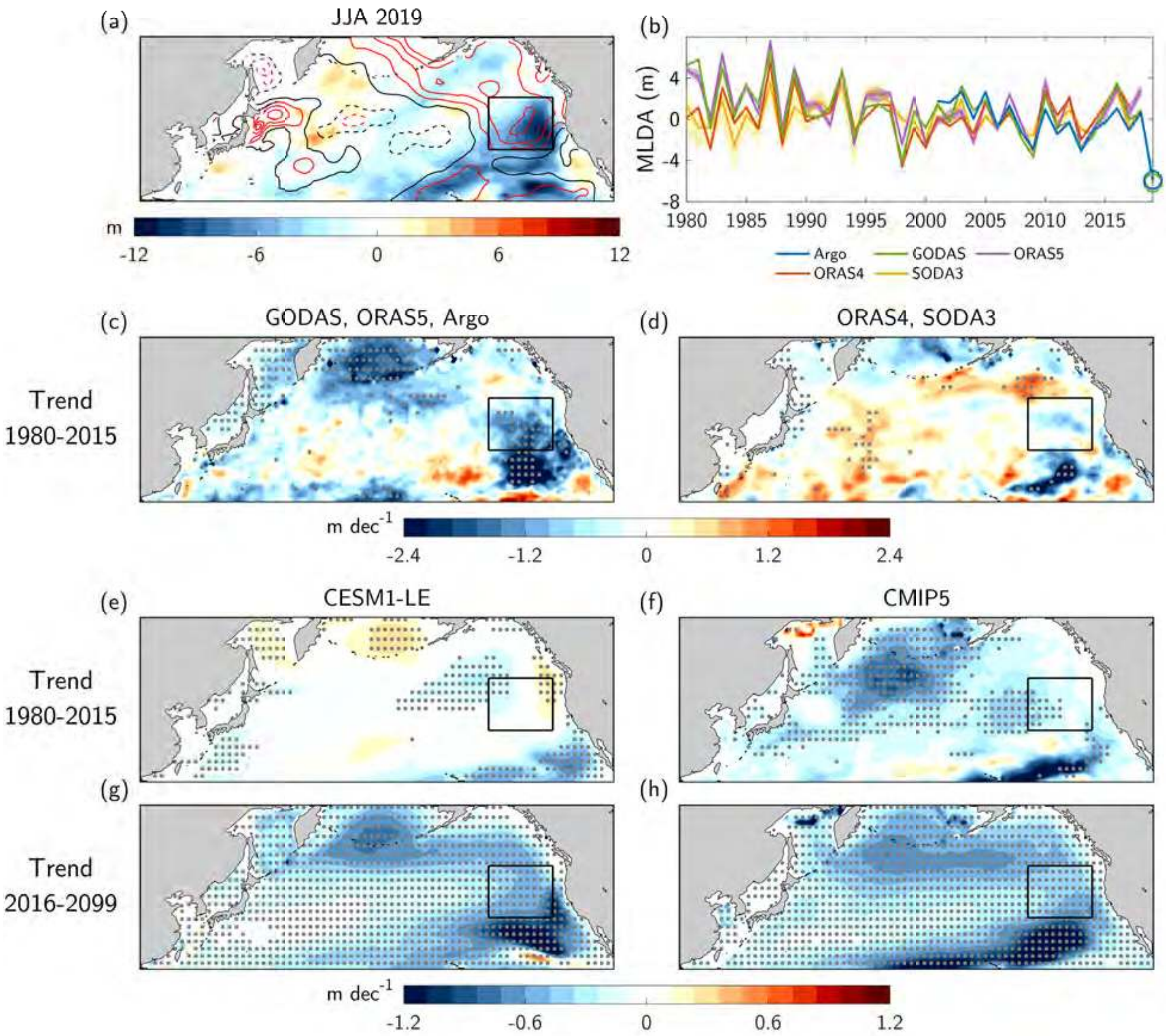

Fig. 1. (a) JJA 2019 MLDAs (m; shading) and SSTAs (°C; contours, positive solid and negative dashed) from Argo and GODAS, respectively. Contour interval is 0.5°C starting at 0.5°C (solid black). (b) MLDAs for five observational analyses (Table 1) averaged in the black box (i.e., 34°–47°N, 213°–232°W) shown in each map. Circles mark 2019 values. Shading for SODA3 and ORAS5 represents the full range (min-to-max) across respective ensembles. (c),(d) Observed JJA MLD trends (m decade^{-1}; shading) from 1980 to 2015 averaged across two groupings: (c) GODAS, ORAS5, and Argo and (d) ORAS4 and SODA3. (e),(f) Simulated JJA MLD trend (m decade^{-1}; shading) from 1980 to 2015 in ensemble means of CESM1-LE and CMIP5. (g),(h) As in (e),(f), but for the period 2016–99. All trends based on linear least squares fit. Stippling represents 95% significance for a Mann-Kendall test.

ing only local heat sources and sinks (i.e., neglecting advection) and separating each budget term into mean and perturbation components:

$$\rho c_p \frac{\partial T'_m}{\partial t} \approx \underbrace{\frac{Q'}{\bar{h}}}_{\text{I}} - \underbrace{\frac{\bar{Q}h'}{\bar{h}^2}}_{\text{II}} - \underbrace{\left(\frac{Q'h' - \overline{Q'h'}}{\bar{h}^2}\right)}_{\text{III}}, \qquad (1)$$

where Q is the net surface heat flux into the ocean, h is the MLD, ρ is seawater density, and c_p is the specific heat of seawater. Primes denote time anomalies and overbars represent time mean values. For the full derivation see Alexander and Penland (1996). For Blob 2.0, strong downward Q anomalies (i.e., positive Q') led to excess heat being distributed over a thin climatological mixed layer, since $\bar{h}$ is small in summer (term I). More importantly, anomalous MLD shoaling (i.e., negative h') contributed to upper ocean warming through term II (A2020).

As discussed in A2020, the 2019 MLD anomalies (MLDAs) superpose on a MLD shoaling trend from 1980 to the present, which they suggest may indicate a role for anthropogenic forcing. Upper ocean warming in response to future climate change is expected to reduce mixing and shoal the mixed layer (Capotondi et al. 2012; Alexander et al. 2018). A long-term trend in the mean MLD would have significant implications for SSTAs since, according to Eq. (1), decreasing the mean MLD ($\bar{h}$) results in a stronger temperature response for the same heat flux and MLD anomalies. Therefore, if the observed MLD shoaling first reported by A2020 is robust across different datasets and consistent with the projected response to anthropogenic climate change, then Blob 2.0 may have been exacerbated by anthropogenic forcing. Here, we investigate the presence of NEPac MLD trends in a suite of observational analyses. We then compare these results to coupled model simulations to assess the potential influence of anthropogenic climate change on NEPac MLD trends, and by extension, on the likelihood and intensity of the 2019 MHW.

Data and methods.

For observed MLD, we use monthly mean data from the NOAA Global Ocean Data Assimilation System (GODAS; Behringer and Xue 2004), ECMWF Ocean Reanalysis System 4 (ORAS4; Balmaseda et al. 2013) and 5 (ORAS5; Zuo et al. 2019), Simple Ocean Data Assimilation version 3 (SODA3; Carton et al. 2018), and gridded Argo profiles (Hosoda et al. 2008). See Table 1 for more details.

We estimate the externally forced MLD trends using the Community Earth System Model version 1 Large Ensemble (CESM1-LE; Kay et al. 2015). Additionally, we use 13 models from phase 5 of the Coupled Model Intercomparison Project (CMIP5; Taylor et al. 2012) with the same radiative forcing protocol. Model details are provided in Table 1 and also Table ES1 in the supplemental material. We use the ensemble mean of each model ensemble (CESM1-LE and CMIP5) as two estimates of the forced response.

To compare trends across datasets, we calculate MLD in each observational analysis and coupled model simulation as the interpolated depth at which potential density first exceeds 0.125 kg m^{-3} greater than the surface value (Suga et al. 2004). For datasets that do not include potential density, we calculate it from monthly mean potential temperature and salinity profiles. To compare to Blob 2.0, we only analyze MLD values averaged over boreal summer [June–August (JJA)]. Unless otherwise specified, all anomalies are relative to the period 2001–15, which is the longest overlapping period for the data used in this study.

Our results are not sensitive to the choice of MLD definition. Additionally, while it is preferred to calculate long-term MLD trends based on daily mean values, many of the datasets only provided monthly means (e.g., ORAS4, ORAS5, CESM1-LE, and CMIP5). However, we do not expect our results or conclusions to be influenced by this choice, since the temperature and density gradients are very strong at the base of the mixed layer in summer. Finally, we define the term “NEPac” to represent the region bounded by 34°–47°N, 213°–232°W (black box, Fig. 1), the same area used in A2020.

Results.

MLD trends in observations. We begin by assessing MLD trends in observations. Interannual MLD variability in the NEPac is quite consistent across the various observational analyses (Fig. 1b, Table 1), particularly during the Argo era (2001–present). However, earlier in the instrumental record, two groupings emerge, with GODAS and ORAS5 exhibiting a more pronounced shoaling trend than ORAS4 and SODA3. While the

Table 1. Observational and coupled model data used in this study and their JJA-averaged MLD trends in the NEPac (black box; Fig. 1a). For ensemble datasets, the mean MLD trend is reported with minimum and maximum ensemble trends in parentheses. For Argo data, the trend is reported for 2001–19. Significant trends are bolded and are based on a 95% Mann-Kendall test. Datasets marked with an asterisk (*) did not provide potential density as a variable. Therefore, the potential density used to calculate MLD for these datasets is based on their respective temperature and salinity fields.

Datasets	Data availability	Ensemble details	NEPac MLD trends (m decade^{-1})
Observations			Trend for 1980–2015
GODAS*	1980–2019		**–1.3**
ORAS5*	1979–2018	5 members, different initial conditions	**–1.2** (**–1.2** to **–1.2**)
Argo	2001–19		**–2.2**
ORAS4*	1958–2017		–0.3
SODA3.X	SODA3.3.2: 1980–2018 SODA3.4.2: 1980–2018 SODA3.11.2: 1980–2015 SODA3.12.2: 1980–2017	4 members, different atmospheric reanalysis forcing	–0.2 (–0.6 to 0.6)
Obs. avg. (excluding Argo)			**–0.7**
Models			Trend for 1980–2015/projected trend for 2016–2099
CESM1-LE	1920–2100	40 members, historical forcing until 2005, RCP8.5 after	–0.0 (**–0.6** to **0.7**)/**–0.6** (**–0.7** to **–0.3**)
CMIP5*	1900–2099	13 models, one member each (see Table ES1 for model details), historical forcing until 2005, RCP8.5 after	**–0.2** (**–0.6** to 0.5)/**–0.4** (**–1.0** to –0.1)
Forced model avg.			–0.1/**–0.5**

magnitude of the observed MLD shoaling varies among datasets, the average NEPac trend (–0.7 m decade^{-1}) is significant at the 95% confidence level (Table 1). Given that the climatological JJA MLD in the NEPac region is ~18 m, such a trend would correspond ~15% decrease in the mean MLD from 1980 to 2015.

Creating two groupings of observational analyses (GODAS, ORAS5, and Argo vs ORAS4 and SODA3), we produce two observational MLD trend maps from 1980 to 2015. The average of GODAS, ORAS5, and Argo shows widespread MLD shoaling trends with two main centers of action, one around the Aleutian Islands and one off the California coast (Figs. 1c,d; see also Fig. ES1). While the average of ORAS4 and SODA3 shows weaker MLD trends overall, the two centers of action are also generally present in these data (Fig. ES1). Additionally, the close spatial correspondence of the 2019 MLDAs near California (Fig. 1a, shading) with some of the observed trends (Fig. 1c and Fig. ES1) suggests that this extreme event was likely exacerbated by these longer-term features.

MLD trends in climate models. Are these and other North Pacific MLD trends attributable to anthropogenic forcing? To address this question, we show maps of JJA MLD trends from 1980 to 2015 for the ensemble means of CESM1-LE and CMIP5 to estimate the forced component (Figs. 1e,f). There is some spatial correspondence with the observational analyses (Fig. 1c and Fig. ES1), especially with CMIP5. The spatial similarities between the historical trends in observations and the forced trends in models are even more apparent when the latter are extended into the future (2016–99; Figs. 1g,h). For the NEPac, the JJA MLD time series show significant forced trends in both the CESM1-LE

(−0.6 m decade^{-1}) and CMIP5 (−0.4 m decade^{-1}) during 2016–99, which amounts to ~4 m MLD shoaling by the end of the twenty-first century (Fig. 2a). However, many of the observed NEPac trend estimates are larger than the CESM1-LE and CMIP5 ensemble mean trends from 1980 to 2015 (Table 1), suggesting that the observations contain significant contributions from internal variability.

Climate change impacts on future MLD extremes. How extreme were the 2019 MLDAs relative to the full range of internal variations in present and future climates? Diagnosing the 2019 event in this context will help us understand how future MLDAs contribute to future MHWs.

Given that the magnitude of interannual variability of NEPac JJA MLD in CESM1-LE compares well with observations (standard deviation of 2.1 vs 2.3 m, respectively, based on detrended data during 1950–2018), this model ensemble can be used to contextualize the observations. Compared to the CESM1-LE probability distribution function (PDF) for a 30-yr period centered on 2019, the observed 2019 NEPac MLDA was an extremely rare event, falling at the far negative tail of the model distribution (Fig. 2b). When viewed against the projected decrease in the model's MLD by 2100, the observed 2019 anomalies become less extreme, rising from percentile ranks of 0.06% and 0.08% to 7.6% and 10.4% for GODAS and Argo, respectively.

Climate change impacts of MLD on future SST extremes. Long-term shoaling of the mean MLD also has important implications for the magnitude of future SST extremes. We illustrate this by calculating Eq. (1) terms I and II in CESM1-LE for the NEPac box. In this region, the CESM1-LE JJA mean net surface heat flux ($\bar{Q}$) increases by ~10 W m^{-2} by the end of the century, while the mean MLD ($\bar{h}$) decreases by ~4 m (Fig. 3a). As a result, the denominators of terms I and II decrease, while the numerator of term II increases, suggesting that both term I and II will contribute to more mixed layer warming for the same heat flux anomaly (Q') and MLDA (h') in the future.

By fixing Q' and h' at observed JJA 2019 values ($Q' = 7.8$ W m^{-2} and $h' = -6.2$ m in NEPac using ERA5 and GODAS, respectively) and calculating terms I and II in a 30-yr sliding window, we see that the superposition of increasing $\bar{Q}$ and decreasing $\bar{h}$ leads to term II dominating over term I (Fig. 3b). In particular, for the same Q' and h', term II is projected to generate SSTAs that are ~4.5°C warmer in 2071–2100 than in 2001–30. Term III, which represents the nonlinear interaction of Q' and h', is negligible. Therefore, in the absence of compensating damping from processes such as

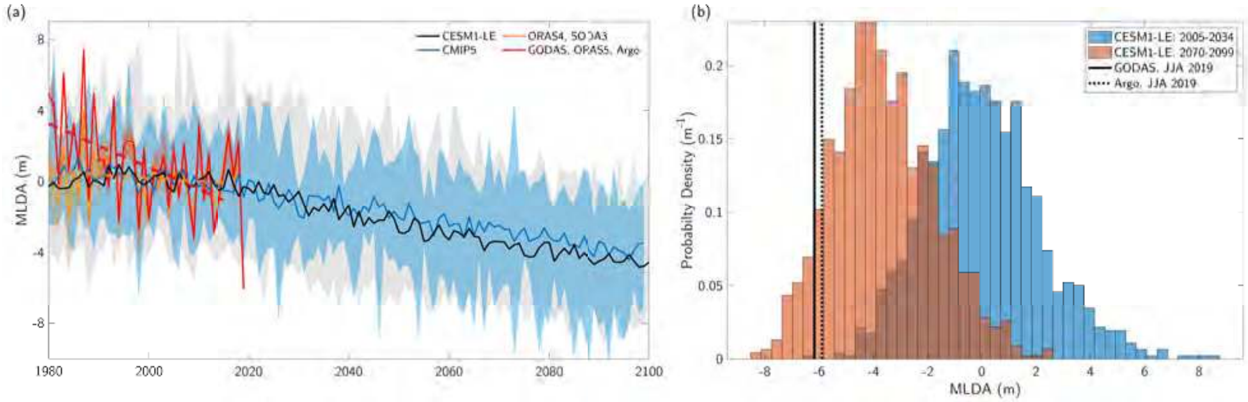

Fig. 2. (a) JJA MLDAs averaged in NEPac (black box, Fig. 1a) for two observational groupings (red/orange) and ensemble means of CESM1-LE (black) and CMIP5 (blue). Shading for each time series represents the full range (min-to-max) across respective ensembles. (b) Probability distributions of JJA ensemble mean CESM1-LE MLDAs averaged in NEPac during the "present" (blue; 2005–34) and "future" (orange; 2070–99). Vertical black lines mark JJA 2019 MLDA values from GODAS (solid) and Argo (dashed) data averaged in same region.

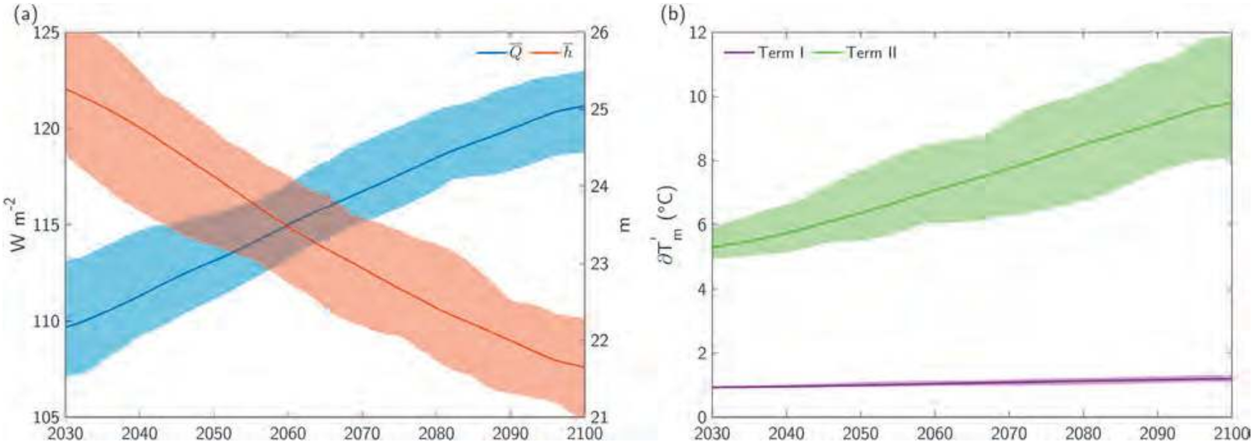

Fig. 3. (a) CESM1-LE JJA mean net surface heat flux ($\bar{Q}$; left axis; blue) and mean MLD ($\bar{h}$; right axis; red) in the NEPac (black box, Fig. 1). (b) Contributions of Eq. (1) terms I (purple) and II (green) to anomalous mixed layer temperature changes ($\partial T'_m$). Each term in (b) is calculated using the time-evolving means in (a) and a fixed net surface heat flux anomaly (Q') and MLDA (h') set to observed JJA 2019 values (see text). Terms I and II are calculated in 30-yr sliding windows starting in 2001; years along the *x* axis denote the end of the window. For example, term I in 2060 represents fixed Q' divided by the projected CESM1-LE $\bar{h}$ for the period 2031–60. CESM1-LE data are subject to a 10-yr running mean prior to calculating changes.

entrainment and ocean–atmosphere feedbacks, extreme MLDAs like that in 2019 will contribute to larger and/or more frequent SST extremes in the future.

Discussion.

We have investigated the influence of climate change on North Pacific MLD trends and, by extension, the likelihood and intensity of the summer 2019 MHW. We showed that some parts of the NEPac have likely experienced long-term MLD shoaling since 1980 (i.e., within the black box in Fig. 1), but significant observational uncertainty regarding the strength of these trends remains (Fig. ES1 and Table 1). Even so, the 2019 MLDAs, which were an important driver of Blob 2.0 (A2020), were likely exacerbated by these multidecadal trends. Consequently, the marine ecosystem impacts generated by this MHW (PFMC 2020; Lambert 2019) may have also been intensified by the shoaling of the ocean mixed layer.

The anthropogenic contribution to these observed MLD trends is less clear. There is model uncertainty in the strength and pattern of the estimated forced NEPac trends from 1980–2015 (Figs. 1e,f, Tables 1 and ES1). Additionally, the fact that the observed MLD trend greatly exceeds the forced trends estimated by the model ensemble means (Table 1) suggests that internal variability makes a strong contribution to the observed trend. However, given the close spatial correspondence between Fig. 1c and the forced trends from 2016 to 2099, it is possible that the models underestimate the strength of the forced response in recent decades. Regardless, it is clear that large internal climate variability complicates the detectability of the forced MLD signal in observations.

Our analysis supports previous findings that pronounced changes in mean MLD may have significant implications for the frequency and strength of MHWs in the future (Alexander et al. 2018). This causal link arises primarily through an enhanced role for the MLDA effect on SSTA (Fig. 3b, term II), which will be further exacerbated as extreme negative MLDAs become more common in response to climate change (Fig. 2b). This process is likely to be more important in summer when mean MLDs are shallowest (Alexander and Penland 1996; Alexander et al. 2000). A shallower MLD and associated smaller heat capacity could further intensify SST warming in summer, contributing to thermal stress on marine organisms. More research is needed into mechanisms that may offset the projected effects of a shallower MLD on future MHWs. Finally, our results emphasize the importance of focusing on the underlying dynamics that modulate the mixed layer heat budget when assessing the influence of climate change on future MHWs, which complements recent studies focusing primarily on the influence of climate change on the SST itself (Frölicher et al. 2018; Jacox et al. 2018; Walsh et al. 2018).

Acknowledgments. Three referees, Stephanie Herring, and Robin Webb provided important comments. James Scott provided MLD estimates from the CMIP5 models. The views expressed herein are those of the authors and do not necessarily reflect the views of NOAA or the DOC. NCAR, sponsored by NSF, partly supported this work. Funding from NSF (OCE1600283, OCE1637632, and OCE2022868) and NOAA (MAPP NA17OAR4310106) is also appreciated.

References

Alexander, M. A., and C. Penland, 1996: Variability in a mixed layer ocean model driven by stochastic atmospheric forcing. *J. Climate*, **9**, 2424–2442, https://doi.org/10.1175/1520-0442(1996)009<2424:VIAMLO>2.0.CO;2.

——, J. D. Scott, and C. Deser, 2000: Processes that influence sea surface temperature and ocean mixed layer depth variability in a coupled model. *J. Geophys. Res.*, **105**, 16 823–16 842, https://doi.org/10.1029/2000JC900074.

——, ——, K. D. Friedland, K. E. Mills, J. A. Nye, A. J. Pershing, and A. C. Thomas, 2018: Projected sea surface temperatures over the 21st century: Changes in the mean, variability and extremes for large marine ecosystem regions of northern oceans. *Elementa*, **6**, 9, https://doi.org/10.1525/elementa.191.

Amaya, D. J., N. E. Bond, A. J. Miller, and M. J. Deflorio, 2016: The evolution and known atmospheric forcing mechanisms behind the 2013–2015 North Pacific warm anomalies. *US CLIVAR Variations Newsletter*, No. 14, International CLIVAR Project Office, Southampton, United Kingdom, 1–6.

——, A. J. Miller, S.-P. Xie, and Y. Kosaka, 2020: Physical drivers of the summer 2019 North Pacific marine heatwave. *Nat. Commun.*, **11**, 1903, https://doi.org/10.1038/s41467-020-15820-w.

Balmaseda, M. A., K. Mogensen, and A. T. Weaver, 2013: Evaluation of the ECMWF ocean reanalysis system ORAS4. *Quart. J. Roy. Meteor. Soc.*, **139**, 1132–1161, https://doi.org/10.1002/qj.2063.

Behringer, D., and Y. Xue, 2004: Evaluation of the global ocean data assimilation system at NCEP: The Pacific Ocean. *Bull. Amer. Meteor. Soc.*, 5889–5894.

Bond, N. A., M. F. Cronin, H. Freeland, and N. Mantua, 2015: Causes and impacts of the 2014 warm anomaly in the NE Pacific. *Geophys. Res. Lett.*, **42**, 3414–3420, https://doi.org/10.1002/2015GL063306.

Capotondi, A., M. A. Alexander, N. A. Bond, E. N. Curchitser, and J. D. Scott, 2012: Enhanced upper ocean stratification with climate change in the CMIP3 models. *J. Geophys. Res.*, **117**, C04031, https://doi.org/10.1029/2011JC007409.

Carton, J. A., G. A. Chepurin, and L. Chen, 2018: SODA3: A new ocean climate reanalysis. *J. Climate*, **31**, 6967–6983, https://doi.org/10.1175/JCLI-D-18-0149.1.

Cavole, L. M., and Coauthors, 2016: Biological impacts of the 2013–2015 warm-water anomaly in the northeast Pacific: Winners, losers, and the future. *Oceanography*, **29**, 273–285, https://doi.org/10.5670/oceanog.2016.32.

Frölicher, T. L., E. M. Fischer, and N. Gruber, 2018: Marine heatwaves under global warming. *Nature*, **560**, 360–364, https://doi.org/10.1038/s41586-018-0383-9.

Hosoda, S., T. Ohira, and T. Nakamura, 2008: A monthly mean dataset of global oceanic temperature and salinity derived from Argo float observations. *JAMSTEC Rep. Res. Dev.*, **8**, 47–59, https://doi.org/10.5918/jamstecr.8.47.

Jacox, M. G., M. A. Alexander, N. J. Mantua, J. D. Scott, G. Hervieux, R. S. Webb, and F. E. Werner, 2018: Forcing of multiyear extreme ocean temperatures that impacted California Current living marine resources in 2016. *Bull. Amer. Meteor. Soc.*, **99**, S27–S33, https://doi.org/10.1175/BAMS-D-17-0119.1.

Kay, J. E., and Coauthors, 2015: The Community Earth System Model (CESM) Large Ensemble Project: A community resource for studying climate change in the presence of internal climate variability. *Bull. Amer. Meteor. Soc.*, **96**, 1333–1349, https://doi.org/10.1175/BAMS-D-13-00255.1.

Lambert, H. R., 2019: 2019 albacore catch blows old record out of the water. KOIN.com, accessed 10 May 2020, https://www.koin.com/news/oregon/2019-albacore-catch-blows-old-record-out-of-the-water/.

NOAA, 2019: New marine heatwave emerges off West Coast, resembles "the Blob". NOAA, accessed 8 May 2020, https://www.fisheries.noaa.gov/feature-story/new-marine-heatwave-emerges-west-coast-resembles-blob.

PFMC, 2020: Review of 2019 Ocean Salmon Fisheries: Stock Assessment and Fishery Evaluation Document for the Pacific Coast Salmon Fishery Management Plan, Pacific Fishery Management Council, 7700 NE Ambassador Place, Suite 101, Portland, OR 97220-1384, 347 pp.

Piatt, J. F., and Coauthors, 2020: Extreme mortality and reproductive failure of common murres resulting from the northeast Pacific marine heatwave of 2014–2016. PLOS ONE, 15, e0226087, https://doi.org/10.1371/journal.pone.0226087.

Suga, T., K. Motoki, Y. Aoki, and A. M. MacDonald, 2004: The North Pacific climatology of winter mixed layer and mode waters. *J. Phys. Oceanogr.*, **34**, 3–22, https://doi.org/10.1175/1520-0485(2004)034<0003:TNPCOW>2.0.CO;2.

Taylor, K. E., R. J. Stouffer, and G. A. Meehl, 2012: An overview of CMIP5 and the experiment design. *Bull. Amer. Meteor. Soc.*, **93**, 485–498, https://doi.org/10.1175/BAMS-D-11-00094.1.

Walsh, J. E., and Coauthors, 2018: The high-latitude marine heat wave of 2016 and its impacts on Alaska. *Bull. Amer. Meteor. Soc.*, **99**, S39–S43, https://doi.org/10.1175/BAMS-D-17-0105.1.

Zuo, H., M. A. Balmaseda, S. Tietsche, K. Mogensen, and M. Mayer, 2019: The ECMWF operational ensemble reanalysis-analysis system for ocean and sea ice: A description of the system and assessment. *Ocean Sci.*, **15**, 779–808, https://doi.org/10.5194/os-15-779-2019.

Was the Extended Rainy Winter 2018/19 over the Middle and Lower Reaches of the Yangtze River Driven by Anthropogenic Forcing?

Zhiyuan Hu, Haiyan Li, Jiawei Liu, Shaobo Qiao, Dongqian Wang, Nicolas Freychet, Simon F. B. Tett, Buwen Dong, Fraser C. Lott, Qingxiang Li, and Wenjie Dong

AFFILIATIONS: Hu, H. Li, Qiao, Q. Li, and W. Dong—School of Atmospheric Sciences, and Key Laboratory of Tropical Atmosphere–Ocean System, Ministry of Education, Sun Yat-sen University, and Southern Marine Science and Engineering Guangdong Laboratory, Zhuhai, China; **Liu**—Collaborative Innovation Center on Forecast and Evaluation of Meteorological Disasters (CIC-FEMD)/Key Laboratory of Meteorological Disasters, Ministry of Education (KLME)/Joint International Research Laboratory of Climate and Environment Change (ILCEC), Nanjing University of Information Science and Technology, Nanjing, China; **Wang**—National Climate Center, China Meteorological Administration, Beijing, China; **Freychet and Tett**—School of Geosciences, University of Edinburgh, Edinburgh, United Kingdom; **B. Dong**—National Centre for Atmospheric Science, Department of Meteorology, University of Reading, United Kingdom; **Lott**—Met Office Hadley Centre, Exeter, United Kingdom

CORRESPONDING AUTHOR: Dr. Shaobo Qiao, qiaoshb3@mail.sysu.edu.cn

DOI:10.1175/BAMS-D-20-0127.1

A supplement to this article is available online (10.1175/BAMS-D-20-0127.2)

Anthropogenic forcing reduced the probability of rainfall amount in the extended rainy winter of 2018/19 over the middle and lower reaches of the Yangtze River, China, by ~19%, but exerted no influence on the excessive rainy days, based on HadGEM3-GA6-N216 ensembles. Instead the natural variability played a large and important role in this event.

During December 2018 to February 2019, the middle and lower reaches of the Yangtze River Valley (MLYRV) experienced an unprecedentedly extended rainy extreme weather event. This extreme event had more than 50 rainy days over the MLYRV in 2018/19 winter, resulting in a dramatic decrease in sunshine hours. According to the records from the China Meteorological Administration (CMA), daily-mean sunshine duration was less than 2 h during this event in many stations, reaching the lowest record in historical observations since 1961. This has led to severe impacts on natural systems, such as reduced agriculture productivity and increased load on power system supplies and transportations, and on human health (Liu et al. 2020). As such, this extended rainy event was defined as one of the top 10 extreme weather and climate events over China in 2019 by the CMA (http://www.cma.gov.cn/2011xwzx/2011xqxxw/2011xqxyw/202001/t20200103_543940.html).

Before this extreme event occurred (about September 2018), the tropical Pacific entered into a weak El Niño state (see Fig. ES1a in the online supplemental material), which favors a westward shift of the western Pacific subtropical high (WPSH) and excessive rainfall over the MLYRV (Wang et al. 2000; Wu et al. 2003; Zhou and Wu 2010). Anthropogenic warming since preindustrial times has been found to have affected extreme rainfall over East Asia, intensifying particularly short-term extreme rainfall (Burke et al. 2017; Zhang et al. 2007, 2017; Min et al. 2011; Westra et al. 2014; Dong et al. 2020). The aim of this study is to investigate whether anthropogenic warming changed the likelihood of the extended rainy winter of 2018/19.

Data and methods.

Daily rainfall observations for the period of 1961–2019 from ~2,400 stations are obtained from the CMA, and interpolated into 0.5° × 0.5° grid cells with the thin plate spline method (Shen et al. 2010). To analyze circulation fields associated with this event, monthly wind and geopotential height datasets from the NCEP–NCAR reanalysis (Kalnay et al. 1996) are used.

Simulations at 0.56° × 0.83° horizontal resolution with 85 vertical levels from the Met Office HadGEM3-GA6-N216 model (Ciavarella et al. 2018) are employed to assess anthropogenic influences on the probability of this extreme event. These simulations are driven by observed monthly sea surface temperature (SST) and sea ice concentration (SIC) from the Hadley Centre Sea Ice and Sea Surface Temperature dataset (Rayner et al. 2003) with both natural and anthropogenic forcings (HistoricalExt), and with natural forcing only for which anthropogenic contributions to the observed SST and SIC are removed (HistoricalNatExt). More details about the forcings used can be found in Christidis et al. (2013). Each experiment comprises an ensemble of 15 initial-condition simulation members for the period of 1960–2013 from which 525 members are extended up to 2019. This study particularly uses the 2018/19 winter simulations. Extreme rainfall events at local to regional spatial scales can be influenced greatly by internal climate variability, and the large ensemble of initial-condition simulations helps obtain reliable attribution results by providing a more adequate sampling of internal variability (Li et al. 2019).

The 2018/19 winter rainfall event is concentrated in 27°–32°N, 112°–122°E (Fig. 1a) and so this region is the focus of the analysis. Both the number of days with rainfall as well as the cumulative rainfall amount are considered. A rainy day is a day with more than 1 mm of precipitation, including rain and snow. The total number of rainy days and accumulated rainfall amount are computed for each winter (December to February) during 1961/62–2018/19, and are expressed as anomalies relative to the 1961/62–2010/11 climatology for both observations and simulations.

To test the reliability of model simulations, a Kolmogorov–Smirnoff (K–S) test comparing the distributions of observed and simulated anomalies of the number of rainy

Fig. 1. (facing page) (a),(b) Observed rainy days anomaly and rainfall amount anomaly in 2018/19 winter relative to the 1961/62–2010/11 climatology. (c),(d) Observed regional-mean rainy day anomaly and rainfall amount anomaly over the MLYRV in each winter for 1961/62–2018/19. (e),(f) Return periods and associated 95% confidence intervals for anomalies of regional-mean rainy days and rainfall amount, where the red dot denotes the value in 2018/19 winter. (g) 2018/19 winter 850-hPa moisture flux anomaly (arrows; g m^{-1} s^{-1} Pa^{-1}) and convergence (shaded; 10^{-7} g m^{-2} s^{-1} Pa^{-1}) 5,860 gpm contours of 500-hPa height for 2018/19 winter (red line) and climatology (blue line). (h) 500-hPa height anomalies in 2018/19 winter (contours; gpm). The regression of 500-hPa height anomalies onto the standardized rainy day number anomaly for 1961/62–2010/11 is also shown (shaded; gpm), where the dotted area is the region exceeding the 95% confidence level.

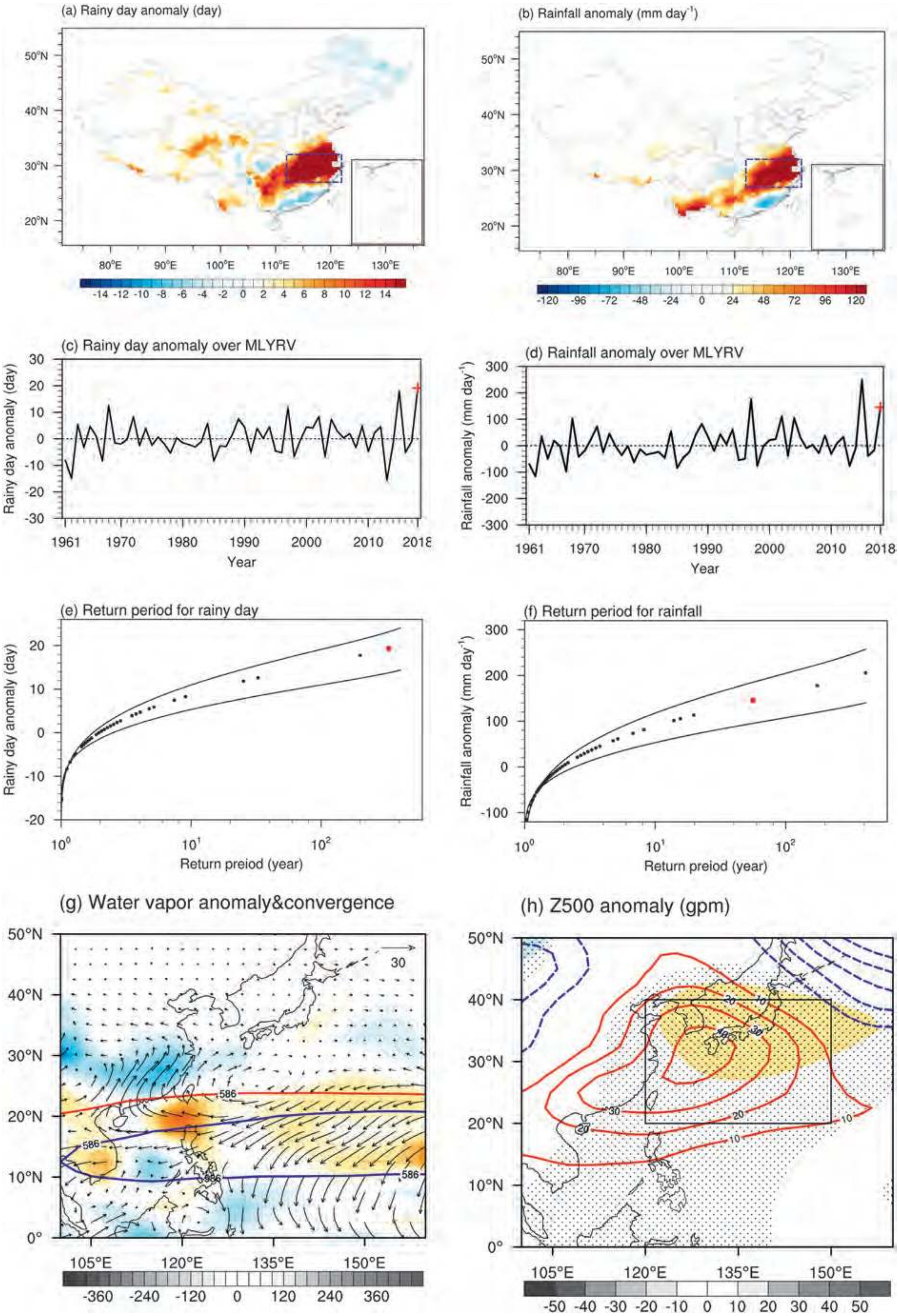
(a) Rainy day anomaly (day)
50°N
40°N
30°N
20°N
80°E
90°E
100°E
110°E
120°E
130°E
-14 -12 -10 -8 -6 -4 -2 0 2 4 6 8 10 12 14
(b) Rainfall anomaly (mm day⁻¹)
-120 -96 -72 -48 -24 0 24 48 72 96 120
(c) Rainy day anomaly over MLYRV
Rainy day anomaly (day)
Year
1961
1970
1980
1990
2000
2010
2018
(d) Rainfall anomaly over MLYRV
Rainfall anomaly (mm day⁻¹)
(e) Return period for rainy day
Rainy day anomaly (day)
Return preiod (year)
(f) Return period for rainfall
Rainfall anomaly (mm day⁻¹)
Return preiod (year)
(g) Water vapor anomaly&convergence
30
586
105°E
120°E
135°E
150°E
-360 -240 -120 0 120 240 360
(h) Z500 anomaly (gpm)
10
20
30
40
-50 -40 -30 -20 -10 0 10 20 30 40 50

days and rainfall amount is used. As both the number of rainy day and rainfall amount anomaly follow closely a normal distribution according to the F test for variances and K–S test (Figs. ES1d,e), Gaussian fits are used to quantify the occurrence probabilities and return periods of the number of rainy days and rainfall amount for 2018/19 in both observations and simulations with and without anthropogenic influence. Then, the risk ratio comparing the occurrence probability of the extended rainy event is computed, and the corresponding 5%–95% confidence interval are estimated via a bootstrapping procedure for 1,000 times, in which 525 samples are drawn from the 525 ensemble members with each time replacement.

Results.

The observations show significant positive anomalies in rainy days (Fig. 1a) and rainfall amount (Fig. 1b) over the MLYRV during 2018/19 winter. The regional-mean rainy days anomaly is more than 19 days relative to the 1961/62–2010/11 climatology, approaching 1.5 times the long-term mean value and breaking the historical record since 1961/62 (Fig. 1c). The regional-mean rainfall amount anomaly observed over the MLYRV exceeds 140 mm (Fig. 1b), which is the third wettest event during the whole period (Fig. 1d). In terms of return periods, rainy days and rainfall amount anomalies are greater than 100 (Fig. 1e) and 20 years (Fig. 1f) respectively, indicating the unusual rareness of an extended rainy event like the 2018/19 winter.

Although this extreme rainfall event occurred during a weak El Niño event, it is primarily driven by a persistent northwestward shift of the WPSH, as evidenced by the geopotential height contours of 5,860 gpm at 500 hPa extending to southern China (~22°N), about 5°–8°N of its climatological mean position (Fig. 1g). The associated low-level southwesterly winds over the northwest side of WPSH carry warm moist air that converges over the MLYRV, producing more-than-normal rainy days and rainfall amount in this region. Correspondingly, the positive 500-hPa height anomalies over the northwestern Pacific are obvious in 2018/19 winter, as supported by the regional-mean (20°–40°N, 120°–150°E) height anomaly that is as high as +24 gpm (Fig. 1h). The magnitude of the 500-hPa height anomalies over the northwestern Pacific in 2018/19 winter is about 2 times larger than that in regression pattern for 1961/62–2010/11, consistent with the record-breaking rainy day anomaly in this winter (Fig. 1a).

The HadGEM3-A-N216 model simulations for 1961/62–2012/13 reasonably capture the observed rainy day and rainfall amount variabilities (Figs. 2a,b). The distributions of rainy day and rainfall amount anomalies are comparable in model simulations and observations. Further, the observations fall within the range of model simulations. A K-S test reveals that the distributions of simulated and observed anomalies during 1961/62–2012/13 are statistically indistinguishable at 95% confidence level (p value = 0.39 for rainy day; p value = 0.31 for rainfall amount). Overall, the model provides reasonably well simulations of rainy day and rainfall amount over the MLYR that enable a reliable attribution analysis.

Although distributions of rainy day anomalies exhibit a small drying shift from HistoricalNatExt to HistoricalExt, they are very close in the upper tails where the number of rainy days in 2018/19 winter is observed. In particular, 7 of 525 ensemble members exceeds the observed anomaly of 19 days in both HistoricalNatExt and HistoricalExt. Correspondingly, the occurrence probability is 0.12 for both HistoricalNatExt (0.001–0.025) and HistoricalExt (0.002–0.024), with a risk ratio of 1.00 (0.90–1.18). The associated return period is estimated to be about 86 years (56–131 years; 5th–95th percentiles) in both ensembles, indicating that the anthropogenic forcing has relatively little influence on the rainy day anomaly (Fig. 2e), which might be a manifestation of the large local-to-regional internal variability.

Although the observed rainfall anomaly of 145 mm is slightly more likely without anthropogenic warming, the changed distribution between HistoricalNatExt and HistoricalExt is similar to that for rainy day anomalies (Fig. 2d). Correspondingly, the an-

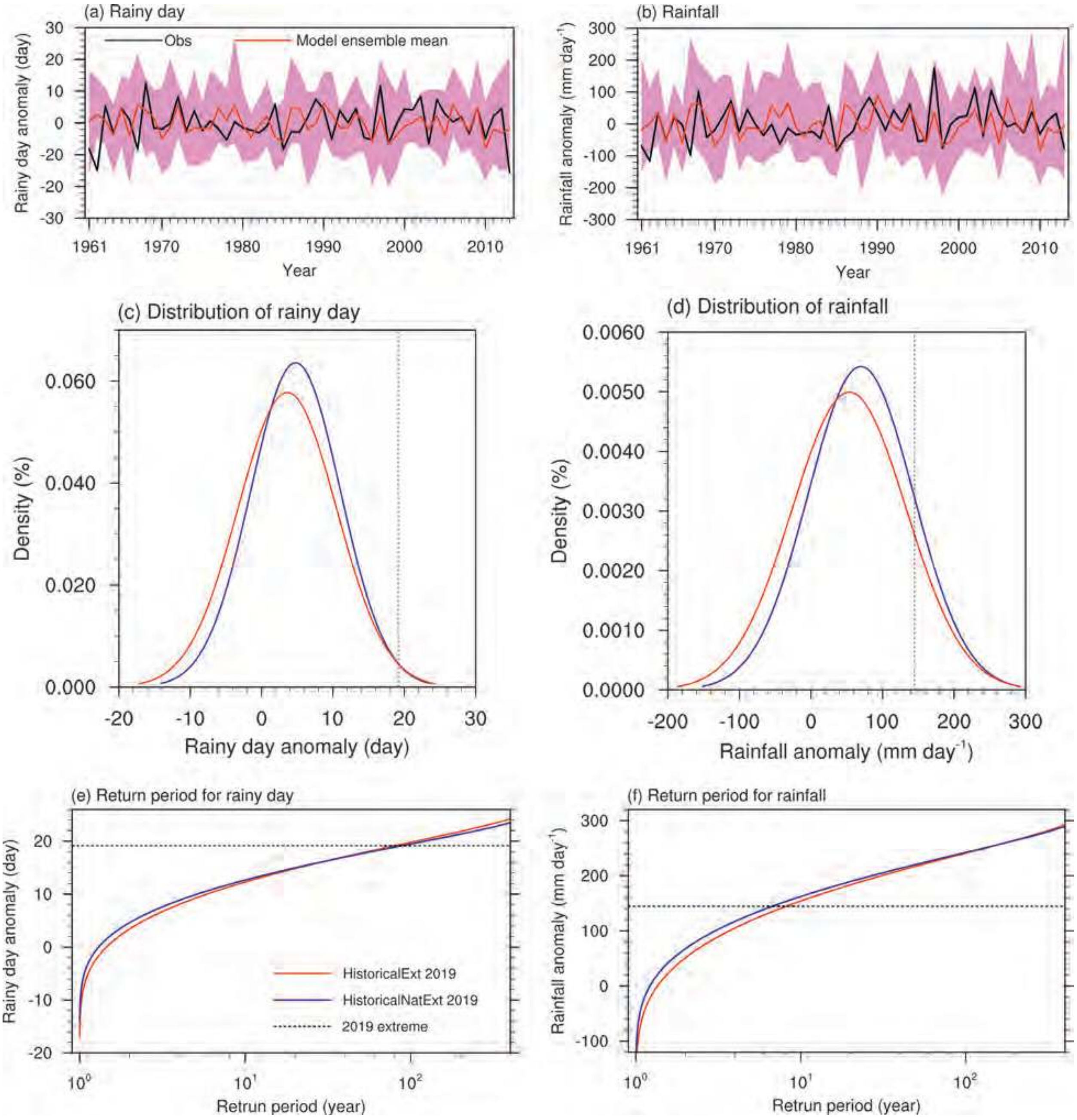

Fig. 2. (a),(b) Time series of observed (blue line) and simulated ensemble mean (red line) of rainy day anomaly and rainfall amount anomaly over the MLYRV in each winter for 1961/62–2012/13, with 15-member spread shown as light pink shading. (c),(d) Probability density function, using Gaussian fits, of rainy days anomaly and rainfall amount anomaly in 2018/19 winter with 525-member HistoricalExt (red line) and HistoricalNatExt (blue line) simulations. The dashed line denotes the observed 2018/19 winter. (e),(f) As in (c),(d), but for return periods.

thropogenic forcing is estimated to have decreased the occurrence probability from 0.16 (0.09–0.19) in HistoricalNatExt to 0.13 (0.07–0.18) in HistoricalExt, with a risk ratio of 0.81 (0.75–0.99). Compared to observations, the return period (~10 years) in rainfall amount anomalies is significantly decreased in model simulations (Fig. 1f vs Fig. 2f). The obviously different return period for rainfall amount anomaly between the simulations and observations is associated with the overestimated rainfall interannual variability in simulations (Figs. ES1d,e). Moreover, the circulation pattern anomalies are consistent regardless of the presence of anthropogenic warming (Figs. ES1b,c). These different lines of evidence suggest that the natural variability played a large and important role in the extended rainy event in 2018/19 winter over MLYRV.

Conclusions and discussion.

In 2018/19 winter, an unprecedented extended rainy event occurred over the middle and lower reaches of the Yangtze River Valley, with more than 50 rainy days breaking the historical record since 1961/62. This event was primarily driven by persistent northwestward shift of the WPSH, where the associated low-level southwesterly winds could carry warm moist air that converges over the region. By analyzing two large ensemble simulations with and without the influence of anthropogenic warming from the HadGEM3-A-N216 model, we found that anthropogenic forcing has reduced the probability of rainfall amount in this event by ~19%, but exerted no influence on the excessive rainy days. Instead the natural variability played a large and important role in this event.

Generally, the extratropical land precipitation at monthly to seasonal time scales is dominated by atmospheric internal processes with external forcings (SST, SIC, etc.) played a secondary role (Hu et al. 2020). The shift of the PDF in 2018/19 winter, relative to the mean climatology, to wetter conditions for both rainy day and rainfall amount anomalies in both ensembles (Fig. 2c vs Fig. ES1e; Fig. 2d vs Fig. ES1d) suggests that this event is driven by the external forcings. This conclusion is consistent with the study of Liu et al. (2020), which further indicates that tropical Atlantic warming, interdecadal variation, and central tropical Pacific warming are three major factors leading to this extended rainy winter. Also, a drying shift of the probability density functions for anomalies of rainfall amount in HistoricalExt compared HistoricalNatExt suggests the anthropogenic signal is detected to some extent, and thus more work is necessary to separate the human influences on this shift (Power et al. 2013; Balan Sarojini et al. 2016).

Additionally, our conclusions are only based on daily observed rainfall from CMA and ensembles from a single atmospheric model forced by observed SST or SIC with and without anthropogenic warming. Multiple observational datasets (Hegerl et al. 2015) and a comparison with estimates from fully coupled models (Sun et al. 2014; Massey et al. 2015; Ren et al. 2020) are needed to test our results, as ocean–atmosphere interaction is important for East Asian climate (Wang et al. 2005).

Acknowledgments. This study was largely carried out during a workshop on Operational Attribution at Sun Yat-Sen University, China, sponsored by the U.K.–China Research and Innovation Partnership Fund through the Met Office Climate Science for Service Partnership China as part of the Newton Fund, the National Key R&D Program of China (Grant 2018YFC1507700) and the Natural Science Foundation of China (Grant 41975105). Z. H. was funded by the Natural Science Foundation of China (Grants 41905013 and 41805116), S. Q. was funded by the Natural Science Foundation of China (Grants 41905057 and 41875096) and the Postdoctoral Science Foundation of China (Grant 2018M640848), H. L. was funded by the Postdoctoral Science Foundation of China (Grant 2019M663204), J. L. is supported by the National Natural Science Foundation of China (Grants 41575077 and 41490643). N. F., S. F. B. T., B. D., and F. L. are all supported by the Met Office Climate Science for Service Partnership China as part of the Newton Fund.

References

Belan Sarojini, B., P. A. Stott, and E. Balck, 2016: Detection and attribution of human influence on regional precipitation. *Nat. Climate Change*, **6**, 669–675, https://doi.org/10.1038/nclimate2976.

Burke, C., and P. Stott, 2017: Impact of anthropogenic climate change on the East Asian summer monsoon. *J. Climate*, **30**, 5205–5220, https://doi.org/10.1175/JCLI-D-16-0892.1.

Christidis, N., P. A. Stott, A. A. Scaife, A. Arribas, G. S. Jones, D. Copsey, J. R. Knight, and W. J. Tennant, 2013: A new HadGEM3-A-based system for attribution of weather- and climate-related extreme events. *J. Climate*, **26**, 2756–2783, https://doi.org/10.1175/JCLI-D-12-00169.1.

Ciavarella, A., and Coauthors, 2018: Upgrade of the HadGEM3-A based attribution system to high resolution and a new validation framework for probabilistic event attribution. *Wea. Climate Extremes*, **20**, 9–32, https://doi.org/10.1016/j.wace.2018.03.003.

Dong, S., Y. Sun, and C. Li, 2020: Detection of human influence on precipitation extremes in Asia. *J. Climate*, **33**, 5293–5304, https://doi.org/10.1175/JCLI-D-19-0371.1.

Hegerl, G. C., and Coauthors, 2015: Challenges in quantifying changes in the global water cycle. *Bull. Amer. Meteor. Soc.*, **96**, 1097–1115, https://doi.org/10.1175/BAMS-D-13-00212.1.

Hu, Z.-Z., A. Kumar, B. Jha, and B. Huang, 2020: How much of monthly mean precipitation variability over global land is associated with SST anomalies? *Climate Dyn.*, **54**, 701–712, https://doi.org/10.1007/s00382-019-05023-5.

Kalnay, E., and Coauthors, 1996: The NCEP/NCAR 40-Year Reanalysis Project. *Bull. Amer. Meteor. Soc.*, **77**, 437–471, https://doi.org/10.1175/1520-0477(1996)077<0437:TNYRP>2.0.CO;2.

Li, C., F. Zwiers, X. Zhang, and G. Li, 2019: How much information is required to well constrain local estimates of future precipitation extremes? *Earth's Future*, **7**, 11–24, https://doi.org/10.1029/2018EF001001.

Liu, Y., Z. Hu, and R. Wu, 2020: Was the extremely wet winter of 2018/2019 in the lower reach of the Yangtze River driven by El Niño–Southern Oscillation? *Int. J. Climatol.*, https://doi.org/10.1002/joc.6591, in press.

Massey, N., and Coauthors, 2015: weather@home—Development and validation of a very large ensemble modelling system for probabilistic event attribution. *Quart. J. Roy. Meteor. Soc.*, **141**, 1528–1545, https://doi.org/10.1002/qj.2455.

Min, S., X. Zhang, F. Zwiers, and G. Hegerl, 2011: Human contribution to more-intense precipitation extremes. *Nature*, **470**, 378–381, https://doi.org/10.1038/nature09763.

Power, S., F. Delage, C. Chung, G. Kociuba, and K. Keay, 2013: Robust twenty-first-century projections of El Niño and related precipitation variability. *Nature*, **502**, 541–545, https://doi.org/10.1038/nature12580.

Rayner, N. A., D. E. Parker, E. B. Horton, C. K. Folland, L. V. Alexander, D. P. Rowell, E. C. Kent, and A. Kaplan, 2003: Global analyses of sea surface temperature, sea ice, and night marine air temperature since the late nineteenth century. *J. Geophys. Res.*, **108**, 4407, https://doi.org/10.1029/2002JD002670.

Ren, L., and Coauthors, 2020: Anthropogenic influences on the persistent night-time heat wave in summer 2018 over northeast China. *Bull. Amer. Meteor. Soc.*, **101**, S83–S88, https://doi.org/10.1175/BAMS-D-19-0152.1.

Shen, Y., A. Xiong, Y. Wang, and P. Xie, 2010: Performance of high-resolution satellite precipitation products over China. *J. Geophys. Res.*, **115**, D02114, https://doi.org/10.1029/2009JD012097.

Sun, Y., X. Zhang, F. W. Zwiers, L. C. Song, H. Wan, T. Hu, H. Yin, and G. Y. Ren, 2014: Rapid increase in the risk of extreme summer heat in eastern China. *Nat. Climate Change*, **4**, 1082–1085, https://doi.org/10.1038/nclimate2410.

Wang, B., R. Wu, and X. Fu, 2000: Pacific–East Asian teleconnection: How does ENSO affect East Asian climate? *J. Climate*, **13**, 1517–1536, https://doi.org/10.1175/1520-0442(2000)013<1517:PEATHD>2.0.CO;2.

Wang, B., Q. Ding, X. Fu, I.-S. Kang, K. Jin, J. Shukla, and F. Doblas-Reyes, 2005: Fundamental challenges in simulation and prediction of summer monsoon rainfall. *Geophys. Res. Lett.*, **32**, L15711, https://doi.org/10.1029/2005GL022734.

Westra, S., and Coauthors, 2014: Future changes to the intensity and frequency of short-duration extreme rainfall. *Rev. Geophys.*, **52**, 522–555, https://doi.org/10.1002/2014RG000464.

Wu, R., Z. Hu, and B. Kirtman, 2003: Evolution of ENSO-related rainfall anomalies in East Asia. *J. Climate*, **16**, 3742–3758, https://doi.org/10.1175/1520-0442(2003)016<3742:EOERAI>2.0.CO;2.

Zhang, X., F. Zwiers, G. Hegerl, F. Lambert, N. Gillett, S. Solomon, P. Stott, and T. Zozawa, 2007: Detection of human influence on twentieth-century precipitation trends. *Nature*, **448**, 461–465, https://doi.org/10.1038/nature06025.

Zhang, X., F. Zwiers, G. Li, H. Wan, and A. Cannon, 2017: Complexity in estimating past and future extreme short-duration rainfall. *Nat. Geosci.*, **10**, 255–259, https://doi.org/10.1038/ngeo2911.

Zhou, L., and R. Wu, 2010: Respective impacts of the East Asian winter monsoon and ENSO on winter rainfall in China. *J. Geophys. Res.*, **115**, D02107, https://doi.org/10.1029/2009JD012502.

Roles of Anthropogenic Forcing and Natural Variability in the Record-Breaking Low Sunshine Event in January–February 2019 over the Middle-Lower Yangtze Plain

Yanyi He, Kaicun Wang, and Dan Qi

The record-low January–February 2019 sunshine in the Middle-Lower Yangtze Plain was favored by a circulation pattern, while anthropogenic aerosols and greenhouse gases increased their probability in recent decades by 3.1 and 1.3 times, respectively.

AFFILIATIONS: He and Wang—State Key Laboratory of Earth Surface Processes and Resource Ecology, College of Global Change and Earth System Science, Beijing Normal University, Beijing, China; **Qi**—National Meteorological Center, China Meteorological Administration, Beijing, China

CORRESPONDING AUTHOR: Kaicun Wang, kcwang@bnu.edu.cn

DOI:10.1175/BAMS-D-20-0185.1

A supplement to this article is available online (10.1175/BAMS-D-20-0185.2)

In January–February 2019, the Middle-Lower Yangtze Plain, accounting for ~1/8 of China's territorial areas, endured the shortest sunshine duration (SD) since 1961 (Figs. 1a–b and Fig. ES1a). The regional average of daily SD (1.6 h) was approximately 57% shorter than the 1961–90 climatology (3.7 h). Due to the continuous rainy and low sunshine in early 2019, the acreage and yield per unit of early rice were reported to decrease by 341.3 thousand hectares and 64.8 kg ha^{-1} compared with 2018, respectively (National Bureau of Statistics of China; www.stats.gov.cn/tjsj/sjjd/201908/t20190826_1693488.html).

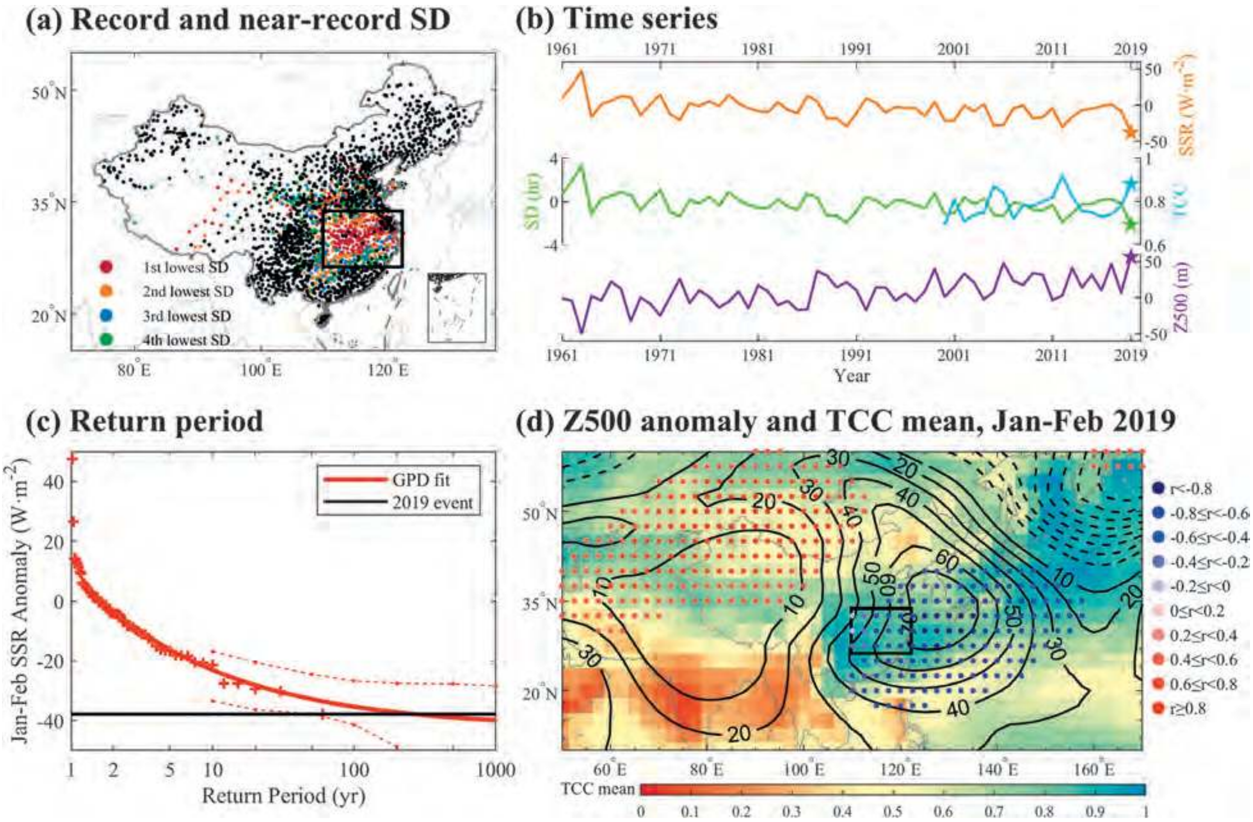

(a) Record and near-record SD

(b) Time series

(c) Return period

(d) Z500 anomaly and TCC mean, Jan-Feb 2019

Fig. 1. (a) Spatial distribution of the CMDC stations that registered record- and near-record (since 1961) SD for January–February 2019. (b) Time series of January–February mean SSR (in orange curve), SD (in green curve), and Z500 (in purple curve) anomalies averaged over the Middle-Lower Yangtze Plain (black box in Fig. 1a) from 1961 to 2019. The blue curve denotes the mean TCC from MODIS during the period of 2000–19. The pentagram represents the records broken in 2019. (c) Return period (in red curve) and 95% confidence intervals (in red dotted lines) for the observed regional mean SSR (red "+") based on the GPD fit. The black line represents the observed SSR for January–February 2019. (d) Spatial distribution of Z500 anomalies (contours) and averaged TCC (shading) in January–February 2019. Dashed contours represent negative anomalies. Color-filled circles indicate the correlations between the detrended regional mean SSR and gridded Z500 anomalies ($p < 0.01$).

Sunshine is largely affected by cloud cover, which is regulated by regional atmospheric circulation (Christidis et al. 2016). At the end of 2018 and in early 2019, the equatorial Pacific entered an El Niño warm phase (index >0.5, Fig. ES1d). Under this phase, the western Pacific subtropical high (WPSH) shifted northward and westward, then remained stable to form an anomalous anticyclonic circulation over and east of the Sea of Japan. The southwest airflow from anticyclonic circulation transported moisture from the northwest Pacific and the South China Sea to the Middle-Lower Yangtze Plain, resulting in continuous cloudy and rainy weather and thus the persistent low sunshine there (Fig. 1d and Fig. ES1c) (Rayner et al. 2003; Wu et al. 2009). Therefore, the contribution of the atmospheric circulation anomaly to the likelihood of such a short SD event is first investigated in this study.

With the rapid urbanization and industrial development in China, anthropogenic aerosols emissions are increasing in recent decades (Wang and Chen 2016). The direct and indirect radiative effects associated with this increase are most likely to reduce the SD (Kim and Ramanathan 2008; Sanchez-Romero et al. 2014; Christidis et al. 2016; He and Wang 2020). The direct effect means that solar radiation is directly scattered or absorbed by aerosols and the indirect effect refers to the effect of aerosols on solar radiation by altering properties of clouds (Boers et al. 2017). In addition, global warming due to greenhouse gas (GHG) emission is likely responsible for intensifying anticyclonic circulation in recent decades by tropical oceanic warming (Zhou et al. 2009; He et al. 2015; Takahashi et al. 2019; Wang et al. 2020). Therefore, the roles of anthropogenic forcings including anthropogenic aerosols and GHGs in such a short SD event are also quantified in this study.

This study tries to explore three questions: 1) How extreme is low sunshine over the Middle-Lower Yangtze Plain in January–February 2019 in a historical context? 2) What are the contributions of the anomalous anticyclonic circulation over the northwest Pacific, anthropogenic aerosols, and GHGs to the probability of the event? 3) What are the roles of anthropogenic aerosols and GHGs for the development of the anomalous anticyclonic circulation?

Data and methods.

Daily SD observation data from 1961 to 2019 at ~2,000 meteorological stations in China (Fig. 1a) were obtained from the China Meteorological Data Service Center (CMDC; http://data.cma.cn/en). These data were subjected to quality control to eliminate spurious shifts in the time series (Zhou et al. 2018) and have complete temporal continuity at all the stations. A total of 744 stations in the study region (black box in Fig. 1a) were included in this study. Since CMIP6 does not provide SD data, we used surface incident solar radiation (SSR) as a proxy of SD. The SSR observation dataset was from He et al. (2018). The detrended January–February mean SSR has a strong correlation (R = 0.98, $p < 0.01$) with the detrended SD from 1961 to 2019 in the study region (Fig. ES1b).

The monthly geopotential height at 500 hPa (Z500) from 1961 to 2019 was downloaded from the JRA-55 reanalysis product (https://jra.kishou.go.jp/JRA-55/index_en.html) (Kobayashi et al. 2015; Harada et al. 2016). The circulation anomaly pattern in January–February 2019 is shown in Fig. 1d. The monthly total cloud cover (TCC) data from 2000 to 2019 were derived from the Moderate Resolution Imaging Spectroradiometer (MODIS, https://modis.gsfc.nasa.gov/data/dataprod/mod08.php) (Platnick et al. 2015).

CMIP6 model outputs (https://esgf-node.llnl.gov/projects/cmip6/) (Eyring et al. 2016) were used to quantify the roles of internal atmospheric variability, GHG-based warming, and anthropogenic aerosols in the 2019 low sunshine event, including historical all-forcing (ALL), historical anthropogenic aerosol-only (AER), and historical greenhouse gas–only (GHG) simulations. The AER (GHG) simulation is forced by anthropogenic aerosol (well-mixed greenhouse gas) forcing only and does not include natural forcing, so the preindustrial control (PIC) simulation was used as a reference to quantify the impacts of anthropogenic aerosols and GHGs on this event. To ensure an equal weight for different CMIP6 models, the "r1i1p1f1" realizations were adopted in this study. We selected 17 models (see Table ES1) based on two steps referring to the method of Zhou et al. (2020). First, 31 out of 34 models were selected by comparing the January–February SSR and Z500 anomalies from CMIP6 ALL runs with those from observations via a Kolmogorov–Smirnov test ($h = 0$, $p > 0.05$). Second, 17 out of 31 models were selected with a significant negative correlation ($p < 0.05$) between the detrended January–February SSR and Z500 anomalies. SSR and Z500 from these models have similar probability density distribution to those from observation (Fig. ES2). The temporal correlation coefficients between area averaged SSR and Z500 over the study region from multi-model means of the ALL runs and observations are 0.448 ($p < 0.01$) and 0.447 ($p < 0.01$), respectively. The SSP2–4.5 runs (the combination of the second type of the shared socioeconomic pathways (SSP), i.e., the fossil-fueled development pathways, and the 4.5 forcing levels of the representative concentration pathways (RCP)] (O'Neill et al. 2016) were used to extend the ALL runs through 2019. To be consistent, all the observations and model data were converted as anomalies relative to the 1961–90 climatology and then integrated on the 2.5° × 2.5° grids, which were averaged as regional time series with area as weight.

We used the generalized Pareto distribution (GPD) (Schaller et al. 2016) to fit the distribution of SSR from 1961 to 2019 in order to estimate the event probabilities (P)

and return periods. Figures ES2c and ES2d show that GPD has a good ability to fit SSR and Z500 anomalies in the study region. Probability ratios (PRs) were adopted to assess the contributions of atmospheric circulation, anthropogenic aerosols, and GHGs to the event probability. To estimate the contribution of the anomalous circulation to the likelihood of this event, $P_{\text{ALL-highZ500}}/P_{\text{ALL-neutralZ500}}$ was calculated. Here, $P_{\text{ALL-highZ500}}$ and $P_{\text{ALL-neutralZ500}}$ represent the probabilities under the high-correlation and neutral-correlation Z500 regimes from ALL simulations, respectively. A trend in Z500 would have little impact on the calculation of the PR relative to the contribution of an anomalous circulation. The high-correlation Z500 regimes from CMIP6 individual model run denote similar circulation patterns to that from JRA-55 in January–February 2019 (pattern correlation ≥ 0.5, $p < 0.05$), and the neutral-correlation Z500 regimes are with pattern correlations of −0.1 to 0.1 (Christidis and Stott 2015; Zhou et al. 2020). The spatial patterns of the multimodel mean Z500 anomalies from the ALL runs under two regimes are shown in Figs. ES3a and ES3b. The effect of anthropogenic aerosols (GHGs) on the likelihood of this event was calculated as $P_{\text{AER}}/P_{\text{PIC}}$ ($P_{\text{GHG}}/P_{\text{PIC}}$), where P_{PIC} and P_{AER} (P_{GHG}) indicate the probabilities under the PIC and AER (GHG) runs, respectively. The 95% confidence intervals (CIs) of the probabilities were estimated via bootstrap random resampling 1,000 times.

Results.

From January to February 2019, the almost entire Middle-Lower Yangtze Plain (black box in Fig. 1a) experienced the shortest or near-shortest mean SD since 1961 (Fig. 1a). New historical record lows of −2.1 h and −37.9 W m^{-2} were observed for SD and SSR anomalies relative to the 1961–90 climatology in the study region, respectively (Fig. 1b). The observed regional mean values of SSR anomaly were used as a threshold (i.e., −37.9 W m^{-2}) to depict this extremely low SD event in the following analyses. A GPD fit of the observed SSR anomalies indicates that the extremely low SSR event in 2019 is a 1-in-265-year event (95% CI: 66–∞) for the Middle-Lower Yangtze Plain (Fig. 1c), which may be overestimated due to small sample size.

Since the late winter 2018, the WPSH has been strong and close to mainland China. The Z500 anomaly in the Middle-Lower Yangtze Plain in January–February 2019 also registered a new record in the historical context (Fig. 1b). The mean January–February 2019 total cloud cover data are close to 1 in the study region to explicitly demonstrate that it is cloudy weather affected by the WPSH (Fig. 1d). The changes in TCC are opposite to those in SSR and SD from 2000 to 2019 (Fig. 1b). We also found that the gridded Z500 anomalies (associated with local anticyclonic circulation) have significantly negative correlations with the detrended regional mean SSR over the Middle-Lower Yangtze Plain (Fig. 1d), which indicates the anomalous anticyclonic circulation is probably responsible for this low sunshine event. The detrended time series of January–February SSR anomaly significantly correlates with that of the Z500 anomaly ($R = -0.38$, $p < 0.01$) (Fig. ES1b). To quantify the role of the anticyclonic circulation, we compared the probabilities of this short SD event between from high- and neutral-correlation Z500 regimes and found the PR to be approximately 4.8 (95% CI: 1.6–9.3) (Figs. 2a,d), indicating that the anomalous anticyclonic circulation is a main driver of the extreme event.

To assess the influence of anthropogenic aerosols, based on the GPD fit, the best estimate of the probabilities of the SSR anomalies to be less than the 2019 threshold is 0.84% (0.24%–1.55%) and 0.27% (0.10%–0.42%) for the AER and PIC runs, respectively (Fig. 2b). In other words, anthropogenic aerosols increase the probability of the extremely short SD in 2019 to 3.1 (95% CI: 0.9–5.9) (Fig. 2d) through their direct and indirect radiative effects. We further estimated the PR due to GHGs and found it to be 1.3 (95% CI: 1.2–5.8) (Figs. 2b,d). Stronger impact of anthropogenic aerosols on the likelihood of the low SSR anomalies is also reflected in the significant decline trend [−2.6 W m^{-2} (10 yr)$^{-1}$, $p < 0.01$] of SSR from 1961 to 2019 in the AER runs, while SSR trend in the GHG runs is non-significant [−0.5 W m^{-2} (10 yr)$^{-1}$, $p > 0.1$].

Anthropogenic forcing has been argued to contribute to increase the likelihood of anomalous atmosphere circulation (Horton et al. 2015; Zhang et al. 2020; Zhou et al. 2020). Compared with multimodel mean Z500 anomalies under the AER and PIC runs, the spatial distribution of Z500 anomalies simulated by the GHG runs shows an enhanced anticyclonic circulation in the northwest Pacific (Fig. ES3d). The regional mean Z500 anomaly in the GHG runs also displays a significant increase [6.7 m (10 yr)$^{-1}$] from 1961 to 2019. The probabilities of Z500 anomalies to exceed the threshold of the observed Z500 anomaly in January–February 2019 (i.e., 56.4m) are 0.1% (95% CI: 0.0%–0.2%), 1.3% (0.4%–2.1%), and 0.3% (0.0%–0.7%) for AER, GHG, and PIC runs, respectively (Fig. 2c). It is concluded that GHGs emissions might have increased the likelihood of the extreme Z500 anomaly to 4.6 times (95% CI: 0.6–10.6), while anthropogenic aerosols seem to have no significant contribution to it (PR = 0.04, 95% CI: 0.003–2.4).

Conclusions.

The SD in January–February 2019 hit a record low in the Middle-Lower Yangtze Plain and its return period was estimated to 1-in-265-years based on the generalized Pareto distribution fit. Based on analyses of reanalysis data, the strengthening of the anomalous anticyclonic circulation caused the extreme Z500 anomaly in January–February 2019 to show the highest record since 1961. The SSR (as a proxy of SD) and Z500 anomalies from 1961 to 2019 show a significantly negative correlation ($R = -0.38$, $p < 0.01$).

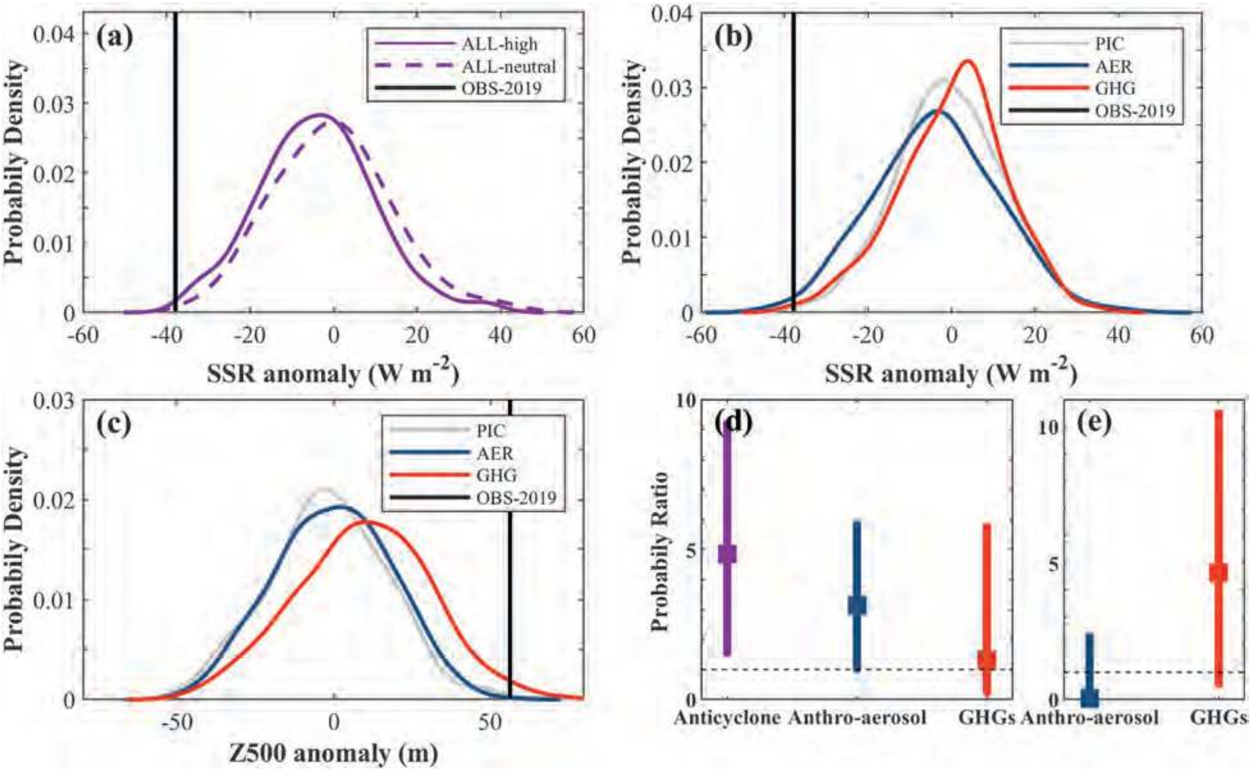

Fig. 2. (a) Probability density of the January–February mean SSR anomalies under high-correlation (solid purple) and neutral-correlation (dashed purple) Z500 regimes in historical all-forcing (ALL, purple) runs from 1961 to 2019. (b) Probability density of the January–February mean SSR anomalies in the preindustrial control (PIC, gray), historical anthropogenic aerosol forcing-only (AER, blue), and historical GHG forcing-only (GHG, red) runs from 1961 to 2019. The black line represents the observed SSR for January–February 2019. (c) As in (b), but for Z500 anomalies. (d) Probability ratio (PR) of the extremely low SSR event in 2019 due to anticyclonic circulation (Anticyclone, purple), anthropogenic aerosols (Anthro-aerosol, blue), and greenhouse gases (GHGs, red). The bottom and top edges of the bar indicate the 95% confidence intervals. The black dashed line represents the PR equal to 1. (e) PR of the extreme Z500 anomaly in 2019 due to anthropogenic aerosols and GHGs.

Through the analyses using CMIP6 model simulations, it is found that the anomalous anticyclonic circulation might have increased the probability of this low SSR event to be 4.8 times, making it the main driver for this extreme event. Furthermore, anthropogenic aerosols and greenhouse gases might have increased the probability of this event by a factor of 3.1 and 1.3, respectively. Besides, greenhouse gases may have potential impacts on the likelihood of extreme Z500 anomalies.

Acknowledgments. This work was supported by the National Key Research and Development Program of China (2017YFA0603601) and the National Natural Science Foundation of China (41525018 and 41930970). The observed meteorological data are available from the China Meteorological Data Service Center (http://data.cma.cn/en). CMIP6 model data were obtained at https://esgf-node.llnl.gov/projects/cmip6/. The ERA5 data were obtained at www.ecmwf.int/en/forecasts/datasets/reanalysis-datasets/era5.

References

Boers, R., T. Brandsma, and A. P. Siebesma, 2017: Impact of aerosols and clouds on decadal trends in all-sky solar radiation over the Netherlands (1966–2015). *Atmos. Chem. Phys.*, **17**, 8081–8100, https://doi.org/10.5194/acp-17-8081-2017.

Christidis, N., and P. A. Stott, 2015: Extreme rainfall in the United Kingdom during winter 2013/14: The role of atmospheric circulation and climate change. *Bull. Amer. Meteor. Soc.*, **96**, S46–S50, https://doi.org/10.1175/BAMS-D-15-00094.1.

——, M. McCarthy, A. Ciavarella, and P. A. Stott, 2016: Human contribution to the record sunshine of winter 2014/15 in the United Kingdom. *Bull. Amer. Meteor. Soc.*, **97**, S47–S50, https://doi.org/10.1175/BAMS-D-16-0143.1.

Eyring, V., S. Bony, G. A. Meehl, C. A. Senior, B. Stevens, R. J. Stouffer, and K. E. Taylor, 2016: Overview of the Coupled Model Intercomparison Project Phase 6 (CMIP6) experimental design and organization. *Geosci. Model Dev.*, **9**, 1937–1958, https://doi.org/10.5194/gmd-9-1937-2016.

Harada, Y., and Coauthors, 2016: The JRA-55 reanalysis: Representation of atmospheric circulation and climate variability. *J. Meteor. Soc. Japan*, **94**, 269–302, https://doi.org/10.2151/jmsj.2016-015.

He, C., T. Zhou, and B. Wu, 2015: The key oceanic regions responsible for the interannual variability of the western North Pacific subtropical high and associated mechanisms. *J. Meteor. Res.*, **29**, 562–575, https://doi.org/10.1007/s13351-015-5037-3.

He, Y., and K. Wang, 2020: Variability in direct and diffuse solar radiation across China from 1958 to 2017. *Geophys. Res. Lett.*, **47**, e2019GL084570, https://doi.org/10.1029/2019GL084570.

——, ——, C. Zhou, and M. Wild, 2018: A revisit of global dimming and brightening based on the sunshine duration. *Geophys. Res. Lett.*, **45**, 4281–4289, https://doi.org/10.1029/2018GL077424.

Horton, D. E., N. C. Johnson, D. Singh, D. L. Swain, B. Rajaratnam, and N. S. Diffenbaugh, 2015: Contribution of changes in atmospheric circulation patterns to extreme temperature trends. *Nature*, **522**, 465–469, https://doi.org/10.1038/nature14550.

Kim, D., and V. Ramanathan, 2008: Solar radiation budget and radiative forcing due to aerosols and clouds. *J. Geophys. Res.*, **113**, D02203, https://doi.org/10.1029/2007JD008434.

Kobayashi, S., and Coauthors, 2015: The JRA-55 reanalysis: General specifications and basic characteristics. *J. Meteor. Soc. Japan*, **93**, 5–48, https://doi.org/10.2151/jmsj.2015-001.

O'Neill, B. C., and Coauthors, 2016: The Scenario Model Intercomparison Project (ScenarioMIP) for CMIP6. *Geosci. Model Dev.*, **9**, 3461–3482, https://doi.org/10.5194/gmd-9-3461-2016.

Platnick, S., K. M. P. Hubanks, and M. D. King, 2015: MODIS atmosphere L3 monthly product (08_L3). NASA MODIS Adaptive Processing System, http://dx.doi.org/10.5067/MODIS/MOD08_M3.006.

Rayner, N. A., D. E. Parker, E. B. Horton, C. K. Folland, L. V. Alexander, D. P. Rowell, and E. C. Kent, and A. Kaplan, 2003: Global analyses of sea surface temperature, sea ice, and night marine air temperature since the late nineteenth century. *J. Geophys. Res.*, **108**, 4407, https://doi.org/10.1029/2002JD002670.

Sanchez-Romero, A., A. Sanchez-Lorenzo, J. Calbó, J. González, and C. Azorin-Molina, 2014: The signal of aerosol-induced changes in sunshine duration records: A review of the evidence. *J. Geophys. Res. Atmos.*, **119**, 4657–4673, https://doi.org/10.1002/2013JD021393.

Schaller, N., and Coauthors, 2016: Human influence on climate in the 2014 southern England winter floods and their impacts. *Nat. Climate Change*, **6**, 627–634, https://doi.org/10.1038/nclimate2927.

Takahashi, C., and Coauthors, 2019: The effects of natural variability and climate change on the record low sunshine over Japan during August 2017. *Bull. Amer. Meteor. Soc.*, **100**, S67–S71, https://doi.org/10.1175/BAMS-D-18-0107.1.

Wang, H. J., and H. P. Chen, 2016: Understanding the recent trend of haze pollution in eastern China: Roles of climate change. *Atmos. Chem. Phys.*, **16**, 4205–4211, https://doi.org/10.5194/acp-16-4205-2016.

Wang, Y., C. He, and T. Li, 2020: Impact of global warming on the western North Pacific circulation anomaly during Developing El Niño. *J. Climate*, **33**, 2333–2349, https://doi.org/10.1175/JCLI-D-19-0588.1.

Wu, B., T. J. Zhou, and T. Li, 2009: Seasonally evolving dominant interannual variability modes of East Asian climate. *J. Climate*, **22**, 2992–3005, https://doi.org/10.1175/2008JCLI2710.1.

Zhang, L., T. Zhou, X. Chen, P. Wu, N. Christidis, and F. C. Lott, 2020: The late spring drought of 2018 in South China. *Bull. Amer. Meteor. Soc.*, **101**, S59–S64, https://doi.org/10.1175/BAMS-D-19-0202.1.

Zhou, C., Y. He, and K. Wang, 2018: On the suitability of current atmospheric reanalyses for regional warming studies over China. *Atmos. Chem. Phys.*, **18**, 8113–8136, https://doi.org/10.5194/acp-18-8113-2018.

——, D. L. Chen, K. C. Wang, A. G. Dai, and D. Qi, 2020: Conditional attribution of the 2018 summer extreme heat over northeast China: Roles of urbanization, global warming, and warming-induced circulation changes. *Bull. Amer. Meteor. Soc.*, **101**, S71–S76, https://doi.org/10.1175/BAMS-D-19-0197.1.

Zhou, T. J., and Coauthors, 2009: Why the western Pacific subtropical high has extended westward since the late 1970s. *J. Climate*, **22**, 2199–2215, https://doi.org/10.1175/2008JCLI2527.1.

Attribution of the Extreme Drought-Related Risk of Wildfires in Spring 2019 over Southwest China

Jizeng Du, Kaicun Wang, Baoshan Cui

The 2019 extreme wildfire in South China was largely related to both anthropogenic warming and El Nino event. They increased the weather-related risk of extreme wildfire by 7.2 times and 3.6 times, respectively.

From March to May 2019, the total precipitation in southwest China (21°–29°N, 98°–105°E) was less than half of the historical average and was the lowest since 1960. Moreover, the air temperature was approximately 1.6°C warmer than the historical average since 1960, leading to the daily maximum temperature reaching or breaking historical records in more than 24 cities in southwest China (Zeng et al. 2020). Higher temperatures and reduced precipitation led to severe meteorological drought, which notably reduced agricultural production and increased the forest fire risk in the region (Ding and Gao 2020). In particular, a lightning-caused forest fire in Muli County killed 31 firefighters and burned about 30 ha of forest (Li 2019; Liu et al. 2020).

Consistent with global warming, southwest China has warmed, and precipitation has declined, resulting in a significant drought trend in this region, especially after

AFFILIATIONS: Du and Cui—State Key Joint Laboratory of Environmental Simulation and Pollution Control, School of Environment, Beijing Normal University, Beijing, China; **Wang**—College of Global Change and Earth System Science, Beijing Normal University, Beijing, China

CORRESPONDING AUTHOR: Kaicun Wang, kcwang@bnu.edu.cn

DOI:10.1175/BAMS-D-20-0165.1

A supplement to this article is available online (10.1175/BAMS-D-20-0165.2)

2000 (Ma et al. 2017; M. Zhang et al. 2013). An El Niño phase started in September 2018 and lasted until June 2019. The northwestern Pacific subtropical high (NWPSH) strengthened, with an anomalously strong anticyclone appearing near the Philippines. At same time, the Tibetan Plateau high moved eastward and caused abnormal downward airflows in southwest China, which blocked moisture convergence from the Bay of Bengal to this region. As a result, the lower precipitation with a higher temperature caused severe drought in spring 2019, thus greatly increasing the risk of forest fires in southwest China (Lin et al. 2015; Zhang and Zhou 2015; W. Zhang et al. 2013).

It is important to explore how anthropogenic contribution to the risk of forest fire in the context of changing climate (Di Virgilio et al. 2019; Dupuy et al. 2020). Here, based on daily meteorological observations and the fire weather index (FWI) risk model, we quantified the impacts of anthropogenic factors and El Niño events on the weather-related forest fire risk in southwest China.

Dataset and method.

The study region (21°–29°N, 98°–105°E) encompasses the spatial extent of extreme drought in the spring of 2019, and it includes Yunnan Province and the southern portion of Sichuan Province (see Fig. ES1 in the online supplemental material; https://doi.org/10.1175/BAMS-D-20-0165.2). This region is an important forest region in Southwest China with complex terrain, thus making it difficult to control and fight forest fires. The spring (March–May) is the season with a high risk of wildfires in the study region, with more than half of the total number of fires in the whole year occurring during the spring seasons (Tian et al. 2010).

The daily observations from 1960 to 2019 at 31 meteorological stations in this region were obtained from the China Meteorological Data Service Center (http://data.cma.cn/en) (see Fig. ES1). The map of land cover in 2010 with a 1-km resolution (http://glc30.tianditu.com/) was used to extract the forest areas. The MODIS Thermal Anomalies and Fire product (MOD14A2, https://modis.gsfc.nasa.gov/) was used to obtain a time series of spatial fire records during the period from 2001 to 2019. This product has an 8-day temporal resolution and a 1-km spatial resolution, and each pixel is a maximum composite of the level-2 pixel classes for the 8-day period (de Klerk 2008).

The FWI system developed based on forest regions in Canada is used to assess the weather conditions for the risk of forest fires (de Groot 1987), which has been found to be suitable for variable regions including Europe and China (Satir et al. 2016; Tian et al. 2014; Tian et al. 2011). The FWI system evaluates the risk of forest fires based on six components that provide information about fuel, moisture, the rate of fire spread, fuel consumption and the fire intensity. All FWI system components were calculated based on the measured daily air temperature (T_a), minimum relative humidity ($\mathrm{RH}_{\min}$), wind speed (WS), and daily total precipitation (P) (see also the online supplementary material).

The persistent high FWI event is defined as the maximum average FWI over three consecutive months in each year (hereafter $\mathrm{FWI}_{\mathrm{x3m}}$). We selected neutral years (including La Niña years) and El Niño years from the FWI time series of both observations and simulations based on the Niño-3.4 index, which reflects the average equatorial sea surface temperature (SST) anomaly across the Pacific (5°N–5°S, 170°W–120°W). El Niño events are defined when the Niño 3.4 index exceeds 0.4°C for a period of 6 months or more (Bunge and Clarke 2009; Smith et al. 2008).

Taking observation as a reference, we used a quantile-matching algorithm to adjust the climate variables of simulations from HadGEM3-A-based attribution system (hereafter called HadGEM3-A) and CMIP6 before the attribution process (Christidis et al. 2013; Ciavarella et al. 2018; Eyring et al. 2016). A detailed description of the adjustment procedure was given by Wang et al. (2010). We used the Kolmogorov–Smirnoff (K-S) test to select the model simulations whose all-forcings simulations have no significant difference with observation in probability distribution of FWI. Based on above criteria

($p > 0.1$), there are 15 simulations from HadGEM3A during the period of 1960–2015 (56 × 15 samples). There are 27 simulations from 9 models from CMIP6 during 2009–29 (20 × 27 samples), assuming similar climate condition to 2019. Historical simulations with all-forcings (ALL; 2009–14) were combined with corresponding shared socioeconomic pathway (SSP) 2–4.5 scenarios (2015–29). The corresponding natural-forcings-only simulations (NAT) from CMIP6 were selected from 1960 to 2014 (55 × 27 samples).

Based on the simulations mentioned above, we constructed the distribution of $\mathrm{FWI}_{\mathrm{x3m}}$ in ALL and NAT, and estimated the occurrence probability and return periods of the extreme $\mathrm{FWI}_{\mathrm{x3m}}$ greater than that in 2019 with/without anthropogenic forcings. Then, we compared the difference in the likelihood between ALL and NAT to determine the anthropogenic warming on the extreme FWI events.

Generalized extreme value (GEV) distribution is a flexible three-parameter distribution, which can provide a conservative estimation of the probability and return period for extreme events based on observations or model simulations (Huang et al. 2016; Jenkinson 1955). Here, GEV distribution was then applied to the time series of $\mathrm{FWI}_{\mathrm{x3m}}$ in the two scenarios with stationary climate, including neutral years with natural forcings only and El Niño years with natural forcings only. The scenarios with all forcings are not stationary climates, and their mean is not representative of 2019. So the scaled GEV distributions are determined to fit the $\mathrm{FWI}_{\mathrm{x3m}}$ in scenarios with all forcings (see the online supplemental material). The sample size of the four scenarios are shown in Table ES1.

The likelihoods of $\mathrm{FWI}_{\mathrm{x3m}}$ with anomalies above that in 2019 were estimated in every scenario (Coles et al. 2001). Additionally, the fraction of attributable risk (FAR) and the corresponding probability ratio (PR) were used to estimate the effects of the anthropogenic warming and El Niño events (Stott et al. 2016). Sampling uncertainty was estimated using a Monte Carlo bootstrap procedure with replacement, and this procedure was run 1,000 times for all ensemble members in the individual scenarios (Christidis et al. 2013).

Results.

Observed extreme FWI in the spring of 2019. As shown in Fig. 1a, during spring 2019, the surface air temperature was 1.54°C higher (the second-highest temperature) than the historic value, and the precipitation was 1.19 mm day^{-1} less than that in the same period historically (the lowest since 1960). The total precipitation in this region decreased by 57.8% relative to the multiyear mean value for the spring season. The high temperature and low precipitation resulted in a severe meteorological drought in this region (see Fig. 1b).

We used the FWI as an indicator of forest fire risk in the study region. As shown in Fig. 1c, the FWI performed reasonably in estimating the forest fire risk. The correlation coefficient between the FWI and the density of forest fire points was 0.662 ($p < 0.05$; see Fig. 1c). Based on the records from 1960 to 2019, the regional mean March–May FWI was 12.31 in 2019, which was 93.5% higher than the contemporaneous multiyear average and the third-highest value in recorded history (see Fig. 1d). Forest fire areas in 2019 showed a marked upturn compared with the previous years since 2014. However, the density of forest fire points in 2019 was not significantly higher than that in other years, possibly due to the government's increased efforts to prevent forest fires in the region (Xiong et al. 2020; Zhai et al. 2018).

As shown in Figs. 2a and 2b, according to the fitted curve of scaled GEV distribution, the return periods of high T_a and low P in spring 2019 were 53 and 90 years, respectively. The return period of the $\mathrm{FWI}_{\mathrm{x3m}}$ in this period was 51 years (see Fig. 2c). Based on the FWI system, we quantified the contribution of individual variables to extreme FWI and the method was introduced in supplementary material (Du et al. 2019). The anomalies of T_a and P were the main driving factors of the $\mathrm{FWI}_{\mathrm{x3m}}$ in 2019, accounting for 36.8% and 29.7% of the trend, respectively. The contributions of $\mathrm{RH}_{\mathrm{min}}$

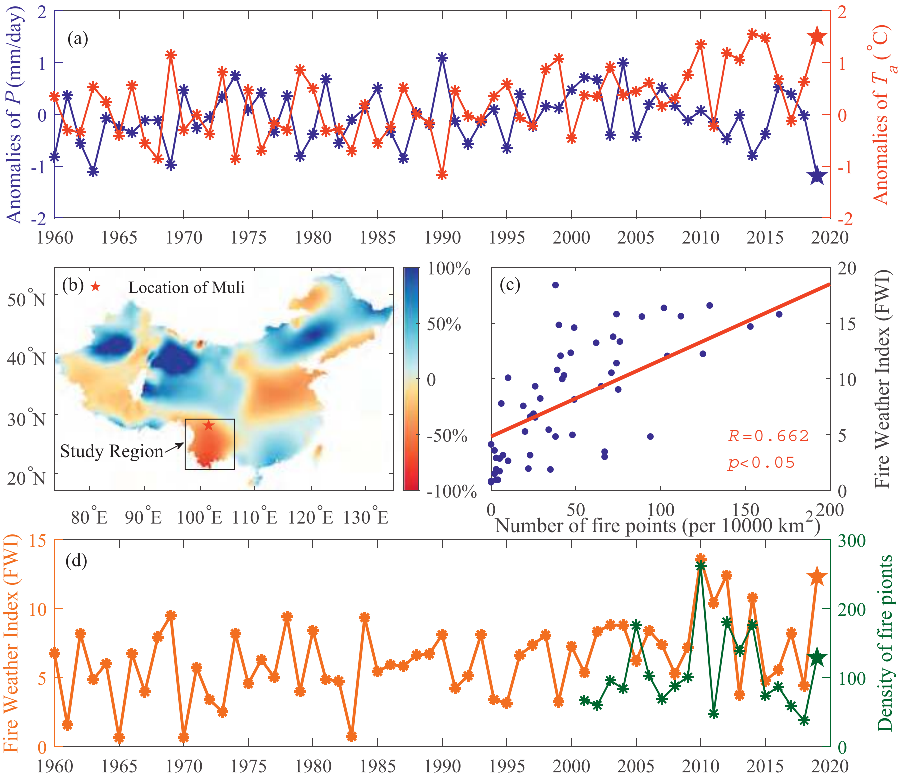

Fig. 1. (a) Time series of March–May daily mean precipitation (P; blue) and air temperature (T_a; red) in southwest China; P and T_a are expressed as anomalies relative to the 1970–2000 mean. (b) The anomalies of total precipitation [ATP = $(P_i - \bar{P})/\bar{P}$] are calculated based on the total precipitation (P_i) from March to May (MAM; defined as spring) and March–May precipitation ($\bar{P}$) between 1960 and 2018 in China. (c) The fire weather index and the density of forest fire points in spring in Southwest China were significantly correlated at the 95% confidence level (R = 0.663). (d) Time series of the March–May FWI (yellow) and the density of forest fire points in spring in southwest China (green).

and WS were relatively small, accounting for only 11.5% and 5.3% of the overall effect, respectively (see Fig. 2d).

As shown in Fig S3, FWI_{x3m} had a significant positive correlation with Niño 3.4 ($p < 0.05$), which indicates El Niño may increase the likelihood of extreme FWI_{x3m}. Therefore, we selected two groups from the time series of observations: one for detrended El Niño years (18 samples) with only the effect of El Niño events considered and the other for neutral years (42 samples) with only the effects of the long-term trend of climate variables considered. As shown in Fig. 2a and 2b, the likelihood of observing extreme T_a and P was much higher in El Niño years than in neutral years. Therefore, the likelihood of 2019 FWI_{x3m} during El Niño years was higher than that during neutral years (Fig. 2c). Note that the relationship between El Niño and FWI_{x3m} is sensitive to the occurrence time, duration, and magnitude of El Niño (see Fig S3). Hence, we only estimate the average effect of all El Niño events during 1960–2019.

During neutral years, the contribution of T_a was much higher than that of P, with values of 54.1% and 14.6%, respectively. However, during the El Niño phase, the contribution of P to the extreme FWI_{x3m} in 2019 was 40.2%, which was higher than that of T_a at 25.3% (see Fig. 2d). Therefore, long-term trends in regional climate mainly increase the likelihood of extreme FWI by increasing temperature, and El Niño events mainly increase the likelihood of extreme FWI by both reducing precipitation and increasing air temperature (see Table 1). Other climate variables and the interaction among variables have little effect on the extreme FWI (5.1%–16.3%).

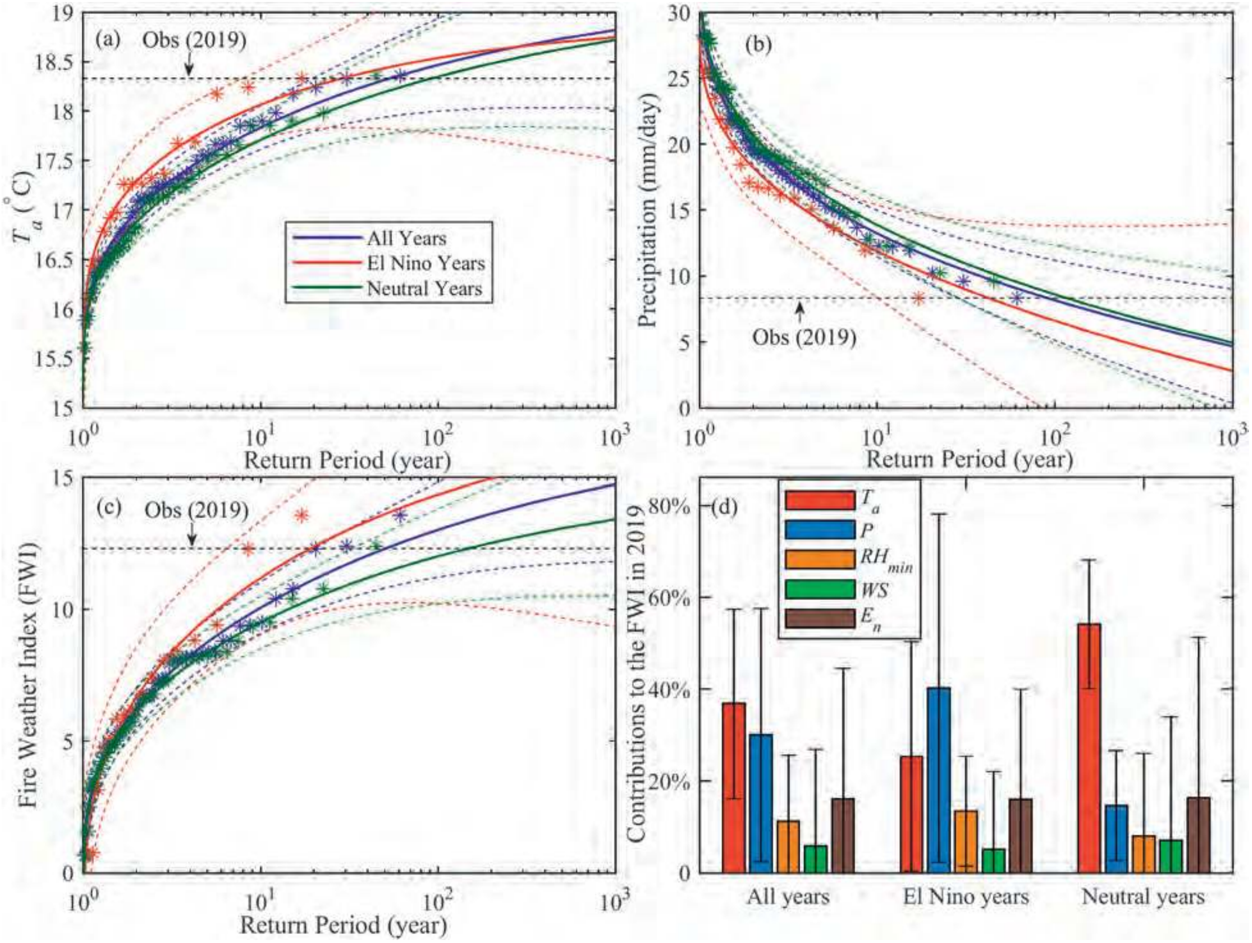

Fig. 2. (a) Return periods for the mean air temperature (T_a) with FWI_{x3m} based on the observations in all years, El Niño years, and neutral years from 1960 to 2019. The color dashed lines denote the 95% confidence intervals. The crosses are estimated from the empirical distributions of the observed T_a with the black dashed line denoting the observed T_a with FWI_{x3m} in 2019. (b) As in (a), but for precipitation (P). (c) As in (a), but for the FWI_{x3m}. (d) The contributions of T_a, P, daily minimum relative humidity (RH_{min}), wind speed (WS), and the interaction among variables (E_n) to the likelihood of the extreme FWI_{x3m} in 2019. The whiskers show the 95% confidence intervals.

Attribution analysis based on simulations. According to the HadGEM3A attribution system, we found that the likelihood of occurrence of the 2019 FWI_{x3m} anomaly under all forcings was 7.21 times (95% CI: 1.64–12.93) that under natural forcings only (see Fig. 3a). El Niño events increased the likelihood of the 2019 FWI_{x3m} anomaly by 3.57 times (95% CI: 1.32–10.02). The compound anthropogenic and El Niño effects resulted

Table 1. Statistics (mean plus and minus standard deviation) of climate variables and FWI in the study area from 1960 to 2018, which are classified based on different phases of ENSO, including El Niño years and neutral years.

Variables	El Niño years (18 samples)	Neutral years (42 samples)
T_a (°C)	0.270 ± 0.601	-0.076 ± 0.554
P (mm day^{-1})	–2.041 ± 1.76	0.712 ± 4.899
RH_{min} (%)	–1.263 ± 1.015	0.369 ± 2.656
Win (km h^{-1})	0.510 ± 1.789	–0.155 ± 2.22
FWI	0.345 ± 3.542	–0.125 ± 2.493

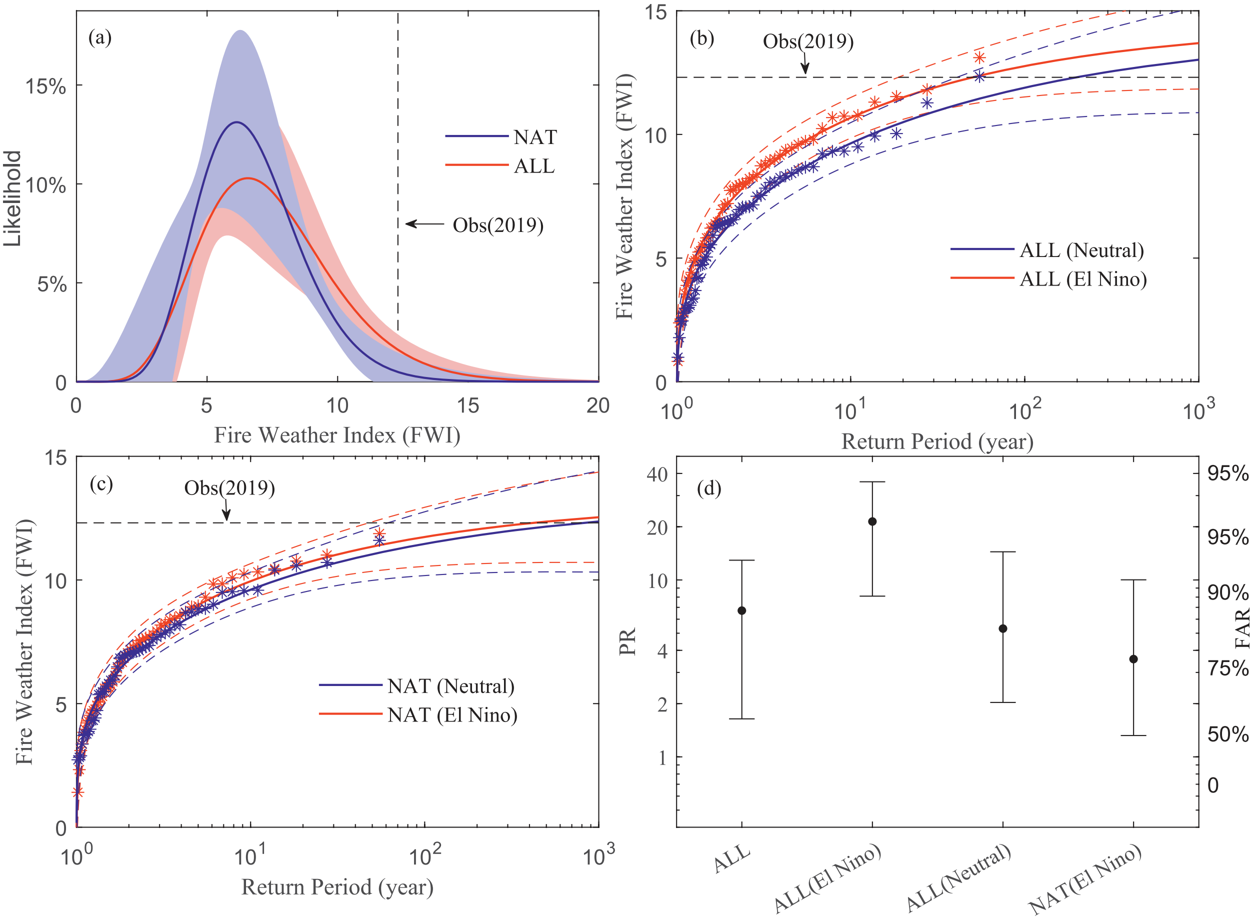

Fig. 3. (a) Probability density of FWI$_{x3m}$ estimated from HadGEM3A for the all-forcings (ALL; red) and natural-forcing-only (NAT; blue) simulations during 1960–2013. The best estimate is marked by the solid lines, and the thick black line is the FWI$_{x3m}$ in 2019 over the study region. (b) Scaled GEV fits 2019 (color solid lines) for FWI$_{x3m}$ from 1960 to 2013 based on the HadGEM3A simulations during El Niño years (red) and neutral years (blue) under ALL. The crosses are estimated from the empirical distributions of the simulated FWI$_{x3m}$ with the black dashed line denoting the 2019 extreme FWI$_{x3m}$. (c) As in (b), but for NAT. (d) The fraction of attributable risk (FAR) and corresponding probability ratios (PR) calculated using different scenario combinations. The bars show the interquartile range (5th–95th percentiles), and the asterisks indicate the best estimates for the fraction of attributable risk.

in a 21.4-fold (95% CI: 8.1–35.9) increase in the risk of the extreme FWI experienced in spring 2019 (see Figs. 3b–d).

According to the CMIP6 experiments, the likelihood of the 2019 extreme FWI$_{x3m}$ under ALL was 17.39 times (95% CI: 7.42–26.83) that under NAT (see Figs. ES5a). El Niño years increased the likelihood of the extreme FWI$_{x3m}$ by 3.11 times (95% CI: 1.63–6.29) higher than that in neutral years. Anthropogenic warming and El Niño together resulted in a 37.2-fold (95% CI: 5.45–81.3) increase in the likelihood of 2019 extreme FWI$_{x3m}$ (see Figs. ES5b–d).

Note that there may be complicated relationship between anthropogenic climate change and El Niño events, namely, that the influence of El Niño on the extreme FWI$_{x3m}$ is partly due to the indirect effects of anthropogenic climate change. However, how El Niño amplitude and frequency respond to anthropogenic warming is important while has been no consensus on it (Cai et al. 2015; Collins et al. 2010; Kim et al. 2014). The uncertainty of attribution analysis is sensitive to the synergy effect of anthropogenic warming with El Niño events in global scale, as well as the performance of FWI model and attribution system.

Conclusions.

According to the analysis of observational data, both El Niño events and human-induced climate change are driving factors of extreme FWI. The human-induced climate change exacerbate the likelihood of extreme FWI by increasing T_a, and El Niño events increase the likelihood of extreme FWI by both reducing P and increasing T_a. Based on observations, El Niño events significantly increased the risk of extreme FWI in spring 2019 (Fig. 2c).

Furthermore, we quantify the effect of anthropogenic warming on the extreme FWI event. The simulation experiments of HadGEM3A (CMIP6) showed that anthropogenic warming increased the likelihood of the extreme FWI_{3xm} in 2019 by 7.21 (17.39) times. El Niño events increased the likelihood of the extreme FWI_{x3m} in 2019 by 3.57 (3.11) times. Combined, anthropogenic warming and El Niño events may result in a more than 21-fold (21.4–37.2 times) increase in the likelihood of occurrence of an extreme FWI_{x3m}.

Acknowledgments. This study was funded by the National Basic Research Program of China (2018YFC1507701 and 2017YFA0603601), the Fundamental Research Funds for the Central Universities (2019NTST10), and the National Natural Science Foundation of China (42005019). The Met Office for the HadGEM3-A-based attribution system (http://catalog.ceda.ac.uk/) and the World Climate Research Programme's Working Group on Coupled Modeling (http://cmip.pcmi.llnl.gov/cmip6/) for the model simulations.

References

Bunge, L., and A. J. Clarke, 2009: A verified estimation of the El Niño index Niño-3.4 since 1877. *J. Climate*, **22**, 3979–3992, https://doi.org/10.1175/2009JCLI2724.1.

Cai, W., and Coauthors, 2015: ENSO and greenhouse warming. *Nat. Climate Change*, **5**, 849–859, https://doi.org/10.1038/nclimate2743.

Christidis, N., and Coauthors, 2013: A new HadGEM3-A-based system for attribution of weather-and climate-related extreme events. *J. Climate*, **26**, 2756–2783, https://doi.org/10.1175/JCLI-D-12-00169.1.

Ciavarella, A., and Coauthors, 2018: Upgrade of the HadGEM3-A based attribution system to high resolution and a new validation framework for probabilistic event attribution. *Wea. Climate Extremes*, **20**, 9–32, https://doi.org/10.1016/j.wace.2018.03.003.

Coles, S., J. Bawa, L. Trenner, and P. Dorazio, 2001: An Introduction to Statistical Modeling of Extreme Values. Springer, 209 pp.

Collins, M., and Coauthors, 2010: The impact of global warming on the tropical Pacific Ocean and El Niño. *Nat. Geosci.*, **3**, 391–397, https://doi.org/10.1038/ngeo868.

de Groot, W. J., 1987: Interpreting the Canadian forest fire weather index (FWI) system. Proc. Fourth Central Region Fire Weather Committee Scientific and Technical Seminar, Winnipeg, MB, Canada, Canadian Forest Service, 3–14, https://webcache.googleusercontent.com/search?q=cache:XJ-Hi2fANSUJ:https://cfs.nrcan.gc.ca/publications%3Fid%3D23688+&cd=1&hl=en&ct=clnk&gl=in.

de Klerk, H., 2008: A pragmatic assessment of the usefulness of the MODIS (Terra and Aqua) 1-km active fire (MOD14A2 and MYD14A2) products for mapping fires in the fynbos biome. *Int. J. Wildland Fire*, **17**, 166–178, https://doi.org/10.1071/WF06040.

Ding, T., and H. Gao, 2020: The record-breaking extreme drought in Yunnan Province, Southwest China during spring and early summer of 2019 and possible causes. *J. Meteor. Res.*, **34**, 997–1012, https://doi.org/10.1007/s13351-020-0032-8.

Di Virgilio, G., J. P. Evans, S. A. Blake, M. Armstrong, A. J. Dowdy, J. Sharples, and R. McRae, 2019: Climate change increases the potential for extreme wildfires. *Geophys. Res. Lett.*, **46**, 8517–8526, https://doi.org/10.1029/2019GL083699.

Du, J., K. Wang, S. Jiang, B. Cui, J. Wang, C. Zhao, and J. Li, 2019: Urban dry island effect mitigated urbanization effect on observed warming in China. *J. Climate*, **32**, 5705–5723, https://doi.org/10.1175/JCLI-D-18-0712.1.

Dupuy, J., and Coauthors, 2020: Climate change impact on future wildfire danger and activity in southern Europe: A review. *Ann. For. Sci.*, **77**, 35, https://doi.org/10.1007/s13595-020-00933-5.

Eyring, V., S. Bony, G. A. Meehl, C. A. Senior, B. Stevens, R. J. Stouffer, and K. E. Taylor, 2016: Overview of the Coupled Model Intercomparison Project phase 6 (CMIP6) experimental design and organization. *Geosci. Model Dev.*, **9**, 1937–1958, https://doi.org/10.5194/gmd-9-1937-2016.

Huang, W. K., M. L. Stein, D. J. McInerney, S. Sun, and E. J. Moyer, 2016: Estimating changes in temperature extremes from millennial-scale climate simulations using generalized extreme value (GEV) distributions. *Adv. Stat. Climatol. Meteor. Oceanogr.*, **2**, 79–103, https://doi.org/10.5194/ascmo-2-79-2016.

Jenkinson, A. F., 1955: The frequency distribution of the annual maximum (or minimum) values of meteorological elements. *Quart. J. Roy. Meteor. Soc.*, **81**, 158–171, https://doi.org/10.1002/qj.49708134804.

Kim, S. T., W. Cai, F.-F. Jin, A. Santoso, L. Wu, E. Guilyardi, and S.-I. An, 2014: Response of El Niño sea surface temperature variability to greenhouse warming. *Nat. Climate Change*, **4**, 786–790, https://doi.org/10.1038/nclimate2326.

Li, Q., 2019: Causes of forest fires and prevention and control measures—A case study of "3.30" fire in Muli county. *Sichuan Linye Keji*, **40**, 108–111, https://doi.org/10.16779/j.cnki.1003-5508.2019.04.022.

Lin, W., C. Wen, Z. Wen, and H. Gang, 2015: Drought in Southwest China: A review. *Atmos. Ocean. Sci. Lett.*, **8**, 339–344, https://doi.org/10.3878/AOSL20150043.

Liu, Y., J. Zhu, X. Shao, N. C. Adusumilli, and F. Wang, 2020: Diffusion patterns in disaster-induced internet public opinion: Based on a Sina Weibo online discussion about the 'Liangshan fire' in China. *Environ. Hazards*, https://doi.org/10.1080/17477891.2020.1758608 , in press.

Ma, S., T. Zhou, O. Angélil, and H. Shiogama, 2017: Increased chances of drought in southeastern periphery of the Tibetan Plateau induced by anthropogenic warming. *J. Climate*, **30**, 6543–6560, https://doi.org/10.1175/JCLI-D-16-0636.1.

Satir, O., S. Berberoglu, and C. Donmez, 2016: Mapping regional forest fire probability using artificial neural network model in a Mediterranean forest ecosystem. *Geomatics Nat. Hazards Risk*, **7**, 1645–1658, https://doi.org/10.1080/19475705.2015.1084541.

Smith, T. M., R. W. Reynolds, T. C. Peterson, and J. Lawrimore, 2008: Improvements to NOAA's historical merged land–ocean surface temperature analysis (1880–2006). *J. Climate*, **21**, 2283–2296, https://doi.org/10.1175/2007JCLI2100.1.

Stott, P. A., and Coauthors, 2016: Attribution of extreme weather and climate-related events. *Wiley Interdiscip. Rev.: Climate Change*, **7**, 23–41, https://doi.org/10.1002/wcc.380.

Tian, X., F. Zhao, L. Shu, and M. Wang, 2010: Hotspots from satellite monitoring and forest fire weather index analysis for southwest China. *For. Res.*, **23**, 523–529.

——, L. Shu, F. Zhao, M.-y. Wang, and D. J. McRae, 2011: Future impacts of climate change on forest fire danger in northeastern China. *J. For. Res.*, **22**, 437–446, https://doi.org/10.1007/s11676-011-0185-5.

——, F. Zhao, L. Shu, and M.-y. Wang, 2014: Changes in forest fire danger for south-western China in the 21st century. *Int. J. Wildland Fire*, **23**, 185–195, https://doi.org/10.1071/WF13014.

Wang, X. L., H. Chen, Y. Wu, Y. Feng, and Q. Pu, 2010: New techniques for the detection and adjustment of shifts in daily precipitation data series. *J. Appl. Meteor. Climatol.*, **49**, 2416–2436, https://doi.org/10.1175/2010JAMC2376.1.

Xiong, Q., and Coauthors, 2020: Fire from policy, human interventions, or biophysical factors? Temporal–spatial patterns of forest fire in southwestern China. *For. Ecol. Manage.*, **474**, 118381, https://doi.org/10.1016/j.foreco.2020.118381.

Zeng, H., C. Xiao, X. Chen, Y. Chen, and D. Ye, 2020: State of China's climate in 2019. *Atmos. Ocean. Sci. Lett.*, **13**, 356–362, https://doi.org/10.1080/16742834.2020.1762159.

Zhai, H., X. Wei, P. Zhao, and Y. Chen, 2018: The situation analysis of forest fire control in China. *Linchan Gongye*, **45**, 43–48.

Zhang, L., and T. Zhou, 2015: Drought over East Asia: A review. *J. Climate*, **28**, 3375–3399, https://doi.org/10.1175/JCLI-D-14-00259.1.

Zhang, M., J. He, B. Wang, S. Wang, S. Li, W. Liu, and X. Ma, 2013: Extreme drought changes in Southwest China from 1960 to 2009. *J. Geogr. Sci.*, **23**, 3–16, https://doi.org/10.1007/s11442-013-0989-7.

Zhang, W., F.-F. Jin, J.-X. Zhao, L. Qi, and H.-L. Ren, 2013: The possible influence of a nonconventional El Niño on the severe autumn drought of 2009 in Southwest China. *J. Climate*, **26**, 8392–8405, https://doi.org/10.1175/JCLI-D-12-00851.1.

Attribution of 2019 Extreme Spring–Early Summer Hot Drought over Yunnan in Southwestern China

Shanshan Wang, Jianping Huang, and Xing Yuan

AFFILIATIONS: Wang and Huang—Key Laboratory for Semi-Arid Climate Change of the Ministry of Education, College of Atmospheric Sciences, Lanzhou University, Lanzhou, China; **Yuan**—School of Hydrology and Water Resources, Nanjing University of Information Science and Technology, Nanjing, Jiangsu, China

CORRESPONDING AUTHOR: Jianping Huang, jhuang@lzu.edu.cn

DOI:10.1175/BAMS-D-20-0121.1

A supplement to this article is available online (10.1175/BAMS-D-20-0121.2)

Anthropogenic influence has increased the risk of 2019 March–June hot and dry extremes over Yunnan province in southwestern China by 123%–157% and 13%–23%, respectively.

In spring to early summer of 2019, Yunnan province in southwestern China was dominated by persistently and extensively hot and dry weather, especially during May. The mean rainfall deficit during March–June in 2019 was ranked first since 1961, with the hottest temperature on record over Yunnan. According to the statistics reported by the Chinese government, this severe drought together with high temperature caused water scarcity that affected nearly 7 million residents and resulted in crop failure over at least 1.35×10^4 km^2 cropland (Fig. 1). More than 94% of the total area in the province was drought-stricken and around 2 million people faced drinking water shortages, with direct economic loss of about 6.56 billion RMB (Fig. 1f; https://www.kunming.cn/news/c/2019-08-19/12704597.shtml).

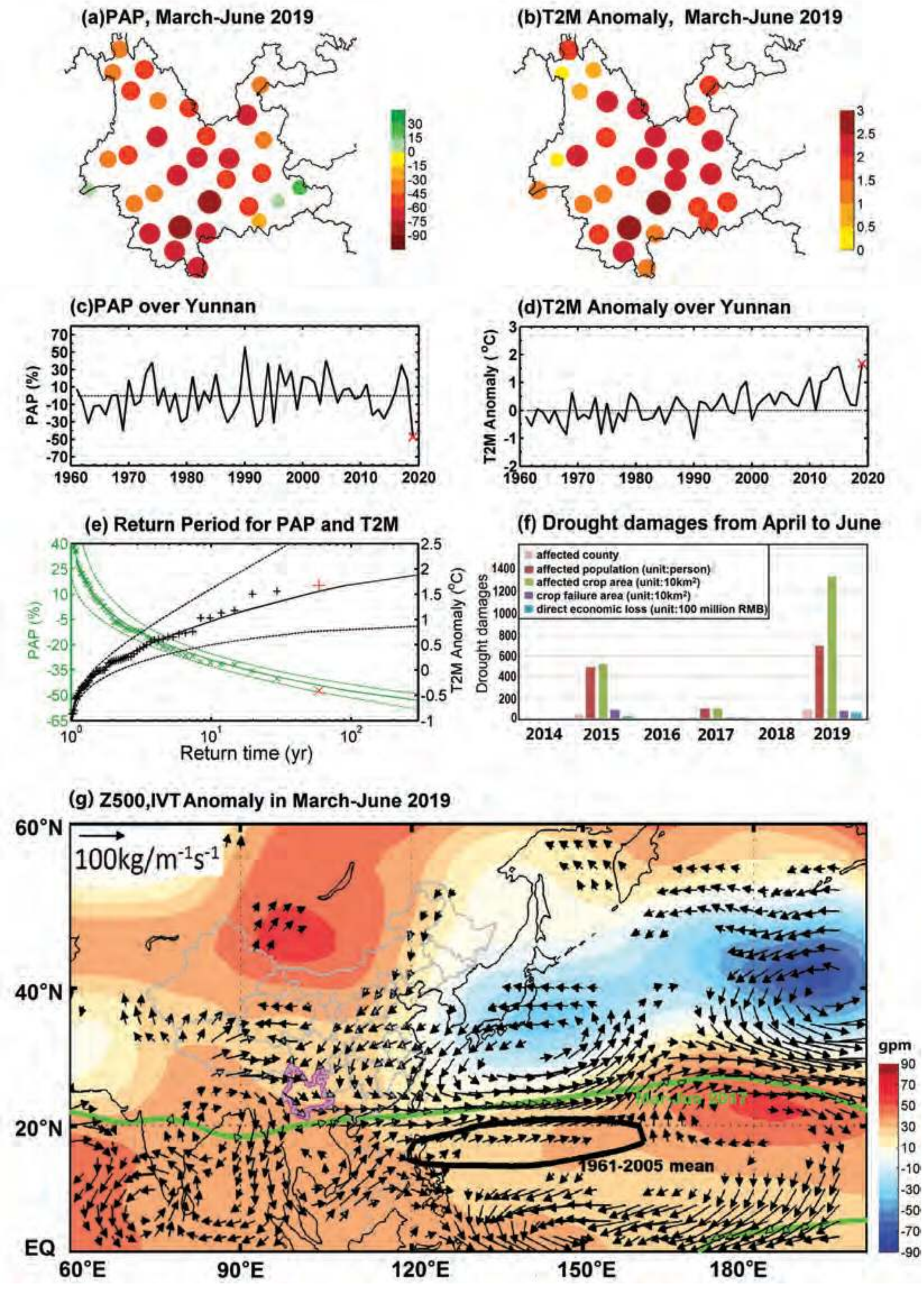

Fig. 1. (a) Precipitation anomaly percentage (PAP; %) and (b) temperature (T2M) anomaly (°C) during March–June of 2019 relative to the 1961–2005 climatology based on CMA/NMIC station observations. (c),(d) Observed regional PAP and mean T2M anomaly over Yunnan for the period of 1961–2019. (e) Return periods and 95% confidence intervals for regional mean March–June T2M anomaly and PAP, where the red markers represent year 2019. (f) Drought damages in the second quarter (April–June) during 2014 to 2019 from the Emergency Management Office of Yunnan Province. (g) 200-hPa geopotential height anomalies (gpm; shading) and the 587-dagpm contours (in green) during March–June of 2019, superimposed with corresponding vertically integrated atmospheric water vapor transport between 300 and 1000 hPa (IVT; vectors). The thick black contour is the climatological March–June mean 587-dagpm contour for 1961–2005.

In recent decades, Yunnan province has suffered from frequent and severe droughts, especially since 2006 (Qiu 2010; Wang et al. 2015b; Ren et al. 2017). Numerous research has explored the causes of drought in Yunnan and its neighboring zones, and the results indicate that the persistently abnormal sea surface temperature (SST) over the tropical Pacific and Indian Oceans (Yang et al. 2011; Feng et al. 2014; Wang et al. 2015a), anomalous snow cover in Northern Hemisphere (He et al. 2013) and the abnormality of the high-latitude Arctic Oscillation (AO; Barriopedro et al. 2012; Yang et al. 2012) and low-latitude Madden–Julian oscillation (MJO; Lü et al. 2012) contribute greatly to the Yunnan drought (Wang et al. 2015b; Ren et al. 2017). However, it is still unclear and even disputable as to what extent the above SST anomalies and circulation patterns affect Yunnan drought because of the complexity of drought and the presence of strong nonlinearity. Particularly, the effect of anthropogenic forcing on the hot droughts (concurrent hot and dry conditions) over Yunnan remains unclear.

Therefore, in addition to assessing the contribution of anthropogenic climate change on Yunnan spring–early summer hot drought in 2019, we also briefly discussed the cause of this persistent hot drought from the perspective of anomalous circulations. This case study is timely for developing appropriate strategies and plans for mitigating the threats of drought over Yunnan.

Data and methods.

Daily surface air temperature (T2M) and precipitation observations for the period 1961–2019 at 839 stations are collected from China Meteorological Administration (CMA) National Meteorological Information Center (NMIC; available http://data.cma.cn/), and converted into monthly means. The precipitation anomaly percentage (PAP) is used to represent drought severity relative to the 1961–2005 climatology. The generalized extreme value (GEV) distribution is used here to fit the observed and modeled March–June mean and extreme T2M and PAP distribution.

To analyze the possible causes for this concurrent hot and dry extreme event, monthly atmospheric circulation data during 1961–2019 at 2.5° resolution from NCEP–NCAR reanalysis (Kalnay et al. 1996) is also used in this study.

Monthly T2M and precipitation simulations from multiple the Coupled Model Intercomparison Project Phase 5 (CMIP5; Taylor et al. 2012) models driven by all (ALL) and natural only (NAT) forcings since 1961 are used in this study (see Table ES1 in the supplemental information for the model list and information). Due to the data availability, only one pair of realizations (r1i1p1) is used to assure an equal weight for different CMIP5 models. All simulations are bilinearly regridded into 0.5° resolution and matched well with the observed distribution via a Kolmogorov–Smirnov test ($p < 0.05$; see Figs. ES1a,b). We further evaluate the relationship of March–June mean temperature and precipitation in Yunnan, and results show that the CMIP5 models capture the inverse correlation between temperature and precipitation that is evident in the observations (Fig. ES1c). To quantitatively assess the contributions of anthropogenic influence on 2019 extreme hot drought in Yunnan, the fraction of attributable risk (FAR; Stott et al. 2004) and the probability ratio (PR; Fischer and Knutti 2015) are both calculated with definition of $\mathrm{FAR} = 1 - P_{\mathrm{NAT}}/P_{\mathrm{ALL}}$ and $\mathrm{PR} = P_{\mathrm{ALL}}/P_{\mathrm{NAT}}$. Here, P_{NAT} denotes the probability of exceeding the 2019 high temperature and drought conditions in the natural-forcing scenarios and P_{ALL} denotes the equivalent for the all-forcings scenarios. Bootstrapping is performed 1000 times to estimate the FAR and PR uncertainty by resampling (Yuan et al. 2018; Wang et al. 2019). To identify the significance level of the difference between ALL and NAT forcings for a given period, p values are calculated with a right-tailed test at the 1% significance level.

In this paper, the highest (lowest) 15% of the regional mean T2M anomalies (PAP) on all months during March–June are considered as the extreme hot (dry) events, which ensure there are enough samples to examine the tails of the distribution of climate variables (Wang et al. 2019). If both extremes occur in the same year (e.g., 2019), it is considered as a hot drought event (Diffenbaugh et al. 2015; Chen and Sun 2017). This is similar to the concurrent hot and dry extremes investigated by Wang et al. (2016), but at a longer time scale.

Results.

Combined with the spatial distribution of March–June mean PAP during 2019 and the corresponding time series of area-averaged values during 1961–2019, it is found that Yunnan was much drier than normal, with a widespread rainfall deficit over most of the province and particularly in the southern region, which received only 10% of its expected precipitation over that period (Fig. 1a). The area-averaged rainfall in March–June 2019 was unprecedentedly low (Fig. 1c), and a GEV fit denotes the 2019 extreme drought is a 1-in-94-yr event (>11 years at 95% confidence level) in Yunnan province (Fig. 1e). In addition, Yunnan suffered the hottest season from spring to early summer since records began in 1961 (Fig. 1b). Taking Yuanjiang county in the south central region as an example, there were 15 days exceeding 40°C in May. The area-averaged T2M anomaly in March–June 2019 is ranked highest since 1961 (Fig. 1d), with a return period of 93 years (>52 years at 95% confidence level; Fig. 1e).

Generally, the maintenance of drought over the region is often regulated by persistently abnormal SST and the resulting anomalous atmospheric conditions. These concurrent hot and dry extremes over Yunnan province in 2019 occurred during weak El Niño and in the context of a warmer Indian Ocean. During March–June in 2019, the low-latitude region was dominated by the high pressure anomalies, and the western Pacific subtropical high (WPSH) was strengthened with its ridge line shifting northward and extending westward (Fig. 1g). The intensification and westward shift of the WPSH further weakened the southern branch trough (SBT) and enhanced the local downward motion over southwestern China (Yang et al. 2012; Ding and Gao 2020). The vertically integrated atmospheric water vapor transport fields show that there was an anomalous anticyclone over the Bay of Bengal and the Indochina Peninsula impeding the water vapor transport from the Bay of Bengal and Indian Ocean into the Yunnan region (Wang et al. 2015b; Ren et al. 2017; Ding and Gao 2020). Meanwhile, there were both a high pressure anomaly around Lake Baikal and a low pressure anomaly around Japan over the Eurasian midlatitudes. This circulation pattern resulted in a deepened and eastward East Asian trough, where the northerly cold air invaded into the eastern part of China rather than the southwestern region, which is unbeneficial for water vapor convergence in Yunnan. Therefore, the spring and early summer in Yunnan were characterized by high temperature and severe drought in 2019 (Wang et al. 2015b; Ren et al. 2017).

To compare the likelihood of occurrence of such extreme spring–early summer hot drought events over Yunnan like 2019 due to anthropogenic climate change, CMIP5 model simulations with all and with natural only forcings are used. Results show an overall mean shift of T2M and PAP toward a hotter and drier condition due to the anthropogenic forcing by fitting GEV distributions, with FAR values of 0.43 (±0.04) and 0.12 (±0.04) (Figs. 2a,b). Furthermore, the attribution of anthropogenic influences on high temperature and low rainfall extremes are also carried out as indicated in Figs. 2c and 2d, and results show that the extreme events are more sensitive to anthropogenic climate change than the monthly mean. The likelihood of the extreme hot events like 2019 increases from 21% to 49% due to the anthropogenic climate change, with FAR of 0.58 (±0.03) and PR of 2.40 (±0.17). In other words, anthropogenic influence has increased the risk of 2019 Yunnan persistent high temperature extremes by 123%–157%. The extreme low rainfall occurs more frequently in Yunnan under the influence of the anthropogenic climate change, with FAR of 0.15 (±0.03) and PR of 1.18 (±0.05). Moreover, the concurrent extreme high temperature and low precipitation shows a tendency to increase in ALL simulations for the study period, particularly entering into the twenty-first century, with a FAR value of up to 0.42 compared with NAT simulations for the recent decade. Between the first and last decades, CMIP5 simulated ensembles show shifts toward warmer and slightly drier conditions in Yunnan (Fig. 2f).

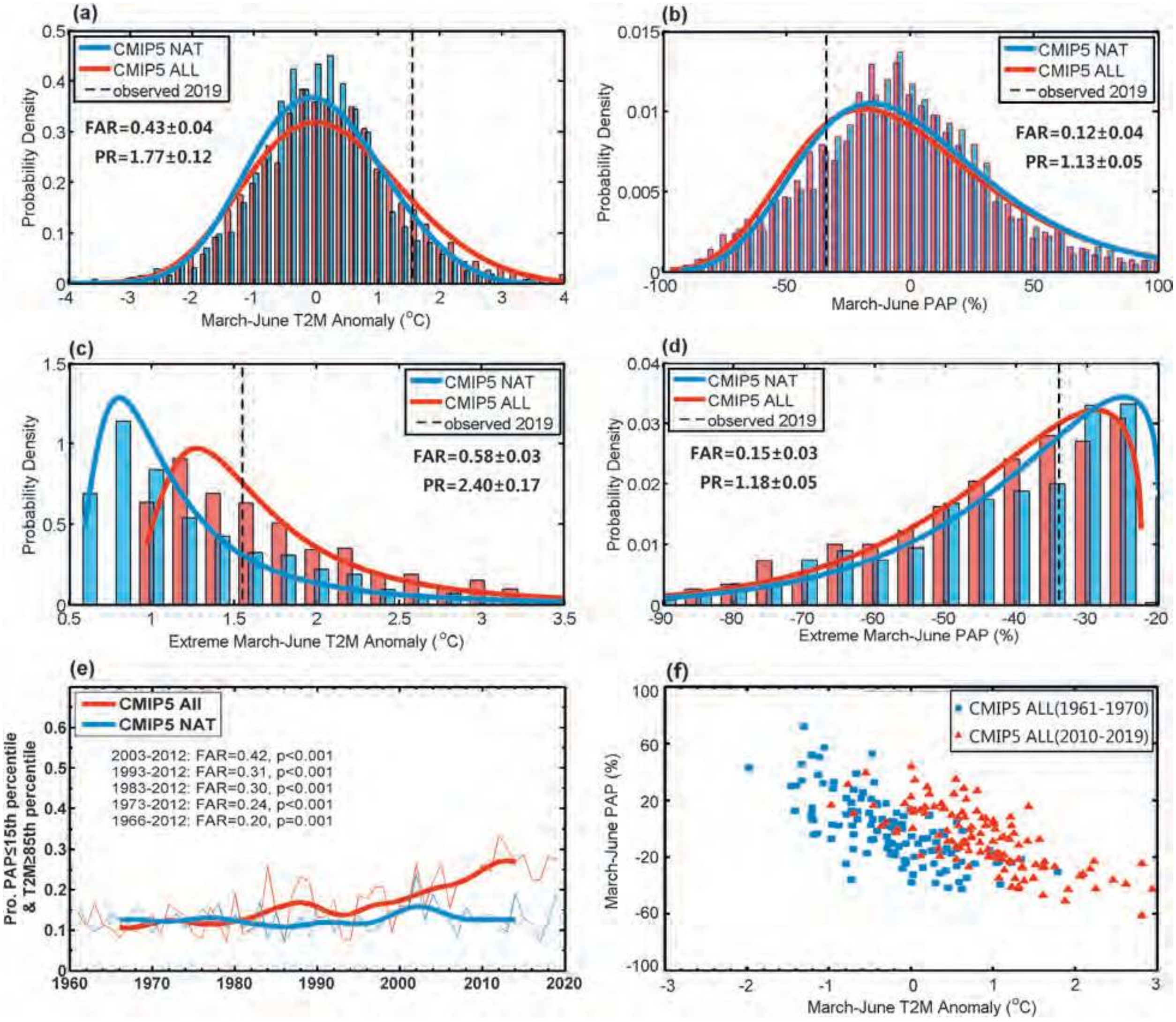

Fig. 2. Histogram (bars) and probability density functions (PDFs; curve) for Yunnan province in southwest China March–June (a) T2M anomaly and (b) PAP from CMIP5 simulations under all (ALL; in red) and natural only (NAT; in blue) forcings. (c),(d) As in (a) and (b), but for the high temperature and low precipitation extremes. (e) The probability of concurrent extremely low precipitation and high temperature where both the PAP is less than the 15th percentile and T2M anomaly is greater than the 85th percentile. The bold curves show 11-yr running mean of the annual time series. The p values indicate the difference between the ALL and NAT forcings for the most recent 10- (2003–12), 20- (1993–2012), 30- (1983–2012), and 40-yr (1973–2012) periods of the CMIP5 protocol. The p values are calculated using the block bootstrap resampling approach. (f) The scatters of PAP against T2M anomalies in CMIP5 ALL simulations. The blue denotes the first decade (1961–70) and the red denotes the last decade (2010–19).

Conclusions.

In March–June 2019, an unprecedented rainfall deficit combined with record-breaking high temperature hit Yunnan province in southwestern China. Observational analysis shows that the persistent strengthening WPSH and anomalous anticyclone over the Bay of Bengal–India region played a crucial role on this extreme event, via reducing the water vapor transportation to Yunnan and enhancing the local downward motion over southwestern China (Yang et al. 2012; Feng et al. 2014; Wang et al. 2015b; Ren et al. 2017; Ding and Gao 2020). Attribution analysis based on the CMIP5 simulations with and without anthropogenic forcings indicates that the likelihood of extremely high temperature in Yunnan like the year of 2019 increased by about 140% (123%–157%)

due to anthropogenic climate change, and the extremely low precipitation increased by about 18% (13%–23%). Furthermore, the concurrence of such hot and dry extremes exhibited an increasing risk of 43% in the recent 30-yr period due to anthropogenic climate change. Recently, research by Yuan et al. (2019) warned that southern China, including Yunnan, faces a higher flash drought risk during the growing seasons in a warming future climate. This increase in drought risk over Yunnan, a southern nontraditional drought region (humid region) of China, poses serious challenges for decision makers in water resource management and economic development.

Acknowledgments. We acknowledge the World Climate Research Programme's Working Group on Coupled Modeling, which is responsible for CMIP. This work was jointly supported by the Strategic Priority Research Program of Chinese Academy of Sciences (Grant XDA2006010301), the National Science Foundation of China (42075018, 41521004, 91837209, and 41775093), and the China University Research Talents Recruitment Program (111 project, B13045).

References

Barriopedro, D., C. M. Gouveia, R. M. Trigo, and L. Wang, 2012: The 2009/10 drought in China: Possible causes and impacts on vegetation. *J. Hydrometeor.*, **13**, 1251–1267, https://doi.org/10.1175/JHM-d-11-074.1.

Chen, H., and J. Sun, 2017: Anthropogenic warming has caused hot droughts more frequently in China. *J. Hydrol.*, **544**, 306–318, https://doi.org/10.1016/j.jhydrol.2016.11.044.

Diffenbaugh, N. S., D. L. Swain, and D. Touma, 2015: Anthropogenic warming has increased drought risk in California. *Proc. Natl. Acad. Sci. USA*, **112**, 3931–3936, https://doi.org/10.1073/PNAS.1422385112.

Ding, T., and H. Gao, 2020: The record-breaking extreme drought in Yunnan Province during spring and early summer of 2019 and possible causes. *J. Meteor. Res.*, **34** (5), 1–16, https://doi.org/10.1007/s13351-020-0032-8.

Feng, L., T. Li, and W. Yu, 2014: Cause of severe droughts in Southwest China during 1951–2010. *Climate Dyn.*, **43**, 2033–2042, https://doi.org/10.1007/s00382-013-2026-z.

Fischer, E. M., and R. Knutti, 2015: Anthropogenic contribution to global occurrence of heavy-precipitation and high-temperature extremes. *Nat. Climate Change*, **5**, 560–564, https://doi.org/10.1038/nclimate2617.

He, Y., R. Yang, J. Wen, and J. Cao, 2013: Influences of snow cover of the Northern Hemisphere on precipitation of Yunnan province in May (in Chinese). *Plateau Meteor.*, **32**, 1712–1719. .

Kalnay, E., and Coauthors, 1996: The NCEP/NCAR 40-Year Reanalysis Project. *Bull. Amer. Meteor. Soc.*, **77**, 437–471, https://doi.org/10.1175/1520-0477(1996)077<0437:TNYRP>2.0.CO;2.

Lü, J., J. Ju, J. Ren, and W. Gan, 2012: The influence of the Madden–Julian Oscillation activity anomalies on Yunnan's extreme drought of 2009–2010. *Sci. China Earth Sci.*, **55**, 98–112, https://doi.org/10.1007/s11430-011-4348-1.

Qiu, J., 2010: China drought highlights future climate threats: Yunnan's worst drought for many years has been exacerbated by destruction of forest cover and a history of poor water management. *Nature*, **465**, 142–143, https://doi.org/10.1038/465142a.

Ren, J., W. Zhang, Y. Wan, and Y. Chen, 2017: Advances in the research of Yunnan's arid climate and extreme drought. *Atmos. Climate Sci.*, **7**, 23–35, https://doi.org/10.4236/acs.2017.71003.

Stott, P. A., D. A. Stone, and M. R. Allen, 2004: Human contribution to the European heatwave of 2003. *Nature*, **432**, 610–614, https://doi.org/10.1038/nature03089.

Taylor, K. E., R. J. Stouffer, and G. A. Meehl, 2012: An overview of CMIP5 and the experiment design. *Bull. Amer. Meteor. Soc.*, **93**, 485–498, https://doi.org/10.1175/BAMS-D-11-00094.1.

Wang, L., W. Chen, W. Zhou, and H. Huang, 2015a: Teleconnected influence of tropical northwest Pacific sea surface temperature on interannual variability of autumn precipitation in southwest China. *Climate Dyn.*, **45**, 2527–2539, https://doi.org/10.1007/s00382-015-2490-8.

Wang, L., W. Chen, W. Zhou, and G. Huang, 2015b: Drought in Southwest China: A review. *Atmos. Oceanic Sci. Lett.*, **8**, 339–344, https://doi.org/10.3878/AOSL20150043.

Wang, L., X. Yuan, Z. Xie, P. Wu, and Y. Li, 2016: Increasing flash droughts over China during the recent global warming hiatus. *Sci. Rep.*, **6**, 30571, https://doi.org/10.1038/SREP30571.

Wang, S., X. Yuan, and R. Wu, 2019: Attribution of the persistent spring–summer hot and dry extremes over Northeast China in 2017. *Bull. Amer. Meteor. Soc.*, **100**, S85–S89, https://doi.org/10.1175/BAMS-D-18-0120.1.

Yang, J., and Coauthors, 2012: Extreme drought event of 2009/2010 over southwestern China. *Meteor. Atmos. Phys.*, **115**, 173–184, https://doi.org/10.1007/s00703-011-0172-6.

Yang, Y., Y. Du, H. S. Chen, and Y. S. Zhang, 2011: Influence of ENSO event on rainfall anomaly over Yunnan Province and its neighboring regions during late spring–early summer (in Chinese). *Chin. J. Atmos. Sci.*, **35**, 729–738, https://doi.org/10.3878/j.issn.1006-9895.2011.04.12.

Yuan, X., S. Wang, and Z. Z. Hu, 2018: Do climate change and El Niño increase likelihood of Yangtze River extreme rainfall? *Bull. Amer. Meteor. Soc.*, **99**, S113–S117, https://doi.org/10.1175/BAMS-D-17-0089.1.

Yuan, X., L. Wang, P. Wu, P. Ji, J. Sheffield, and M. Zhang, 2019: Anthropogenic shift towards higher risk of flash drought over China. *Nat. Commun.*, **10**, 4661, https://doi.org/10.1038/s41467-019-12692-7.

Anthropogenic Influence on 2019 May–June Extremely Low Precipitation in Southwestern China

Chunhui Lu, Jie Jiang, Ruidan Chen, Safi Ullah, Rong Yu, Fraser C. Lott, Simon F. B. Tett, and Buwen Dong

AFFILIATIONS: Lu—National Climate Center, China Meteorological Administration, Beijing, China; **Jiang**—LASG, Institute of Atmospheric Physics, Chinese Academy of Sciences, and University of Chinese Academy of Sciences, Beijing, China; **Chen**—Center for Monsoon and Environment Research/Guangdong Province Key Laboratory for Climate Change and Natural Disaster Studies/School of Atmospheric Sciences, Sun Yat-sen University, Guangzhou, and Southern Marine Science and Engineering Guangdong Laboratory (Zhuhai), Zhuhai, China; **Ullah**—Key Laboratory of Meteorological Disaster, Ministry of Education, Joint International Research Laboratory of Climate and Environmental Change, Collaborative Innovation Center on Forecast and Evaluation of Meteorological Disasters, Nanjing University of Information Science and Technology, Nanjing, and Department of Atmospheric and Oceanic Sciences and Institute of Atmospheric Sciences, Fudan University, Shanghai, China; **Yu**—State Key Laboratory of Severe Weather, Chinese Academy of Meteorological Sciences, Beijing, China; **Lott**—Met Office Hadley Centre, Exeter, United Kingdom; **Tett**—School of Geosciences, University of Edinburgh, Edinburgh, United Kingdom; **Dong**—National Centre for Atmospheric Science, Department of Meteorology, University of Reading, United Kingdom

CORRESPONDING AUTHOR: Jie Jiang, jiangj@lasg.iap.ac.cn

DOI:10.1175/BAMS-D-20-0128.1

A supplement to this article is available online (10.1175/BAMS-D-20-0128.2)

Anthropogenic forcing has likely increased the likelihood of the May–June 2019 severe low precipitation event in southwestern China by approximately 6 (1.4) times based on the HADGEM3-GA6 (CMIP6) simulations.

From late April to June 2019, southwestern China experienced a severe precipitation deficit. At the peak of this event (May and June), the area-averaged precipitation anomaly was 42% lower than climatology and the lowest on record since 1960 in the region. Yunnan and western Sichuan were most severely affected by this disaster, where the precipitation deficit affected more than 640,100 hectares of crops with rice, corn, and potatoes greatly damaged. Over 100 rivers and 180 reservoirs dried out (CMA 2020a). A severe drought that accompanied this precipitation deficit led to over 824,000 people and 566,000 head of livestock having a severe lack of drinking water, with a direct economic loss of 2.81 billion Chinese Yuan ($400 million; CMA 2020b). Therefore, it is timely to investigate the cause of this extremely low precipitation event.

In recent years, spring and summer precipitation in southwestern China have shown decreasing trends

(Wang et al. 2015; Lu et al. 2020), accompanied by more frequent drought events (Xin et al. 2006; Yuan et al. 2019), which have caused great damage to the local ecology, agriculture, and economy. Changes in atmospheric circulation, such as the westward shift and intensification of western Pacific subtropical high (Yang et al. 2012) and the northward shift of the midlatitude westerlies (Sun and Yang 2012), have been shown to contribute to the precipitation deficit. Anthropogenic influences have been found on extreme precipitation events in other parts of China (Sun et al. 2019; Zhang et al. 2020; Li et al. 2021), while it is still unclear whether the attribution of human influence is detectable in precipitation deficit events in southwestern China. Thus, we have used a large ensemble of simulations to investigate the contribution of human-induced climate change on the likelihood of the severe precipitation deficit in May–June 2019 over southwestern China.

Data and methods.

The 2019 precipitation deficit event was largely confined to 20°–30°N, 96°–104°E (box in Fig. 1a) and we explored the sensitivity of our results to details of this region by varying the spatial domain. We used observations of precipitation at 180 stations in the region for 1960–2019. The station data have been rigorously quality controlled and homogenized at the China National Meteorological Information Center (Yang and Li 2014). We divided the region into multiple grid boxes of 0.56° lat × 0.83° lon resolution, consistent with the grid of the HadGEM3-GA6 model (see below), and averaged the station precipitation within each grid box. Both observed and simulated gridded values are area-weight averaged to obtain regional mean precipitation time series, which are finally used to compute the precipitation anomaly (PA; namely, the anomaly of the total precipitation from May to June) relative to the 1961–2010 base period. The NCEP–NCAR reanalysis data (Kalnay et al. 1996) are used to investigate the atmospheric circulation.

The Met Office Hadley Centre event attribution system is based on the atmospheric model HadGEM3-GA6 and, currently, is the highest resolution global model used in attribution studies, with 85 vertical levels and an N216 horizontal resolution of 0.56° × 0.83° (Ciavarella et al. 2018). Four ensemble sets are used: the historical experiment, a 15-member ensemble of HadGEM3-GA6 forced with observed sea surface temperatures (SSTs) and anthropogenic and natural forcings (ALL) for the period 1960–2013; the historicalNat experiment, also a 15-member ensemble but with observed SSTs having anthropogenic influences removed (Christidis et al. 2013) and natural forcings (NAT); the historicalExt experiment, a 525-member ensemble similar to historical but only for 2019; and the historicalNatExt experiment, also a 525-member ensemble similar to historicalNat but for 2019. From these, the change in probability, expressed as the probability ratio (PR), due to human influences was computed. Simulations from the Coupled Model Intercomparison Project Phase 6 (CMIP6; Eyring et al. 2016) were used to assess the robustness of the HadGEM3-GA6 results (see the online supplemental material).

The May–June mean PA in southwestern China is used as the indicator, due to its important influence on water shortage and agricultural failure. Consecutive dry days (CDD; Zhang et al. 2011) and gridded soil moisture observational data (Shi et al. 2011) were also used to characterize the precipitation deficit. Circulation changes are characterized by 500-hPa geopotential height (Z500) and 850-hPa zonal and meridional winds (UV850). Subsequently, May–June mean precipitation, CDD, and circulation are computed from all simulations, and anomalies are calculated relative to the 1961–2010 climatologies. The probabilities of an exceptional precipitation deficit like the 2019 event in the real (P_{ALL}) and natural (P_{NAT}) world are calculated when precipitation anomalies are at or below the observed 2019 threshold. The probability ratio is defined as PR $= P_{\mathrm{ALL}}/P_{\mathrm{NAT}}$. Uncertainties in PR are obtained using 1,000 bootstraps, with PR computed for each bootstrap realization (Christidis and Stott 2015), and we show the empirical

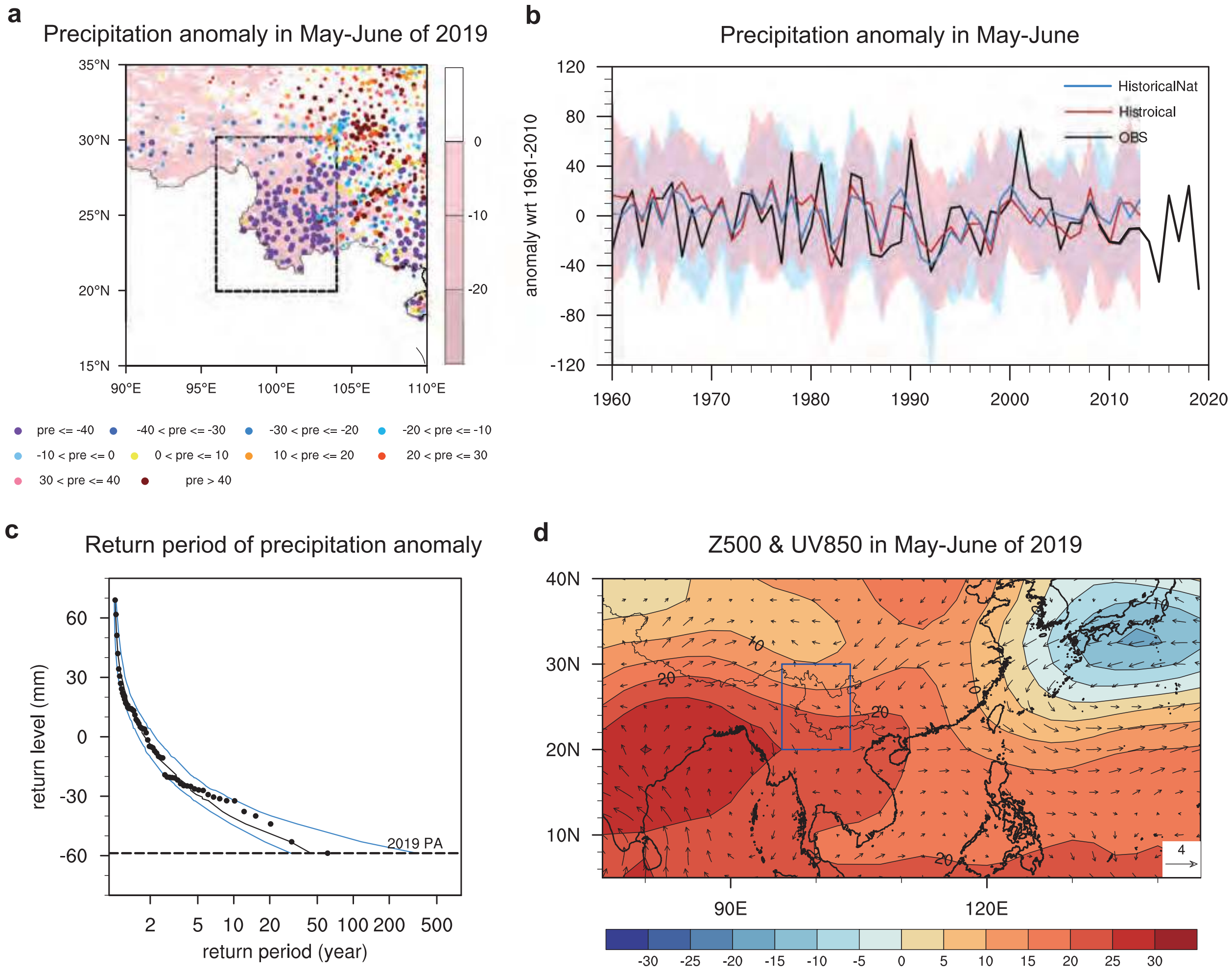

Fig. 1. (a) Precipitation (mm) and relative soil moisture (%; shaded part) anomalies in May–June for observations in 2019. (b) Regional mean PA (mm) in May–June for observations (black), historical simulations (red), and historicalNat simulations (blue) for 1960–2013. Thick lines denote ensemble average, and shading denotes the 15-member spread. (c) Return period (black dots) of observed PA during the period of 1960–2019. The solid black line shows the results of kernel estimate and 90% confidence intervals. The dashed black line denotes the observed event in 2019. (d) Geopotential height anomaly (relative to 1961–2010) at 500 hPa (contour: m) and winds anomalies (relative to 1961–2010) at 850 hPa (vector: m s-1) in May–June 2019.

5th–95th percentile ranges. The probability density functions (PDFs) were estimated by kernel density estimation (KDE), which has been widely used to estimate the PDFs of precipitation events at monthly scales (Ma et al. 2017). We also tried other fitting methods and similar PR evaluation results were obtained (see the supplemental material).

Results.

Figure 1a shows that the observed May–June negative precipitation and relative soil moisture anomalies were centered in Yunnan province. In this region, the PA in most stations is less than –40 mm with many stations experiencing their record-breaking lowest precipitation. Figure 1b shows the temporal evolution of May–June PA over southwestern China based on observations and simulations. It is apparent that May–June 2019 was the driest since 1960 (with PA value at –58.14 mm), and it is a one-in-60-yr event in observations (Fig. 1c). These dry conditions were associated with abnormally high pressure extending from the west at 500 hPa and anomalous northerlies over Yunnan at 850 hPa (Fig. 1d). These circulation patterns lead to anomalous subsidence and reduced water vapor transport from the Indian Ocean (Feng et al. 2014), favoring a severe precipitation deficit.

The model reasonably represents the temporal evolution and probability distribution for PA over southwestern China for the period 1960–2013. In Fig. 1b, the model results under ALL and NAT forcings cover most of the observed range. Figure 2a shows the histogram and KDE estimate of the probability distribution of the observed and simulated May–June PA. HadGEM3-GA6 produces similar distribution in the historical experiment to observations, confirmed using a two-sided Kolmogorov–Smirnov test with p values equal to 0.36. The shift of probability distribution toward a drier condition under ALL forcing with a probability ratio near 5.14 (3.33–10.50) suggests that human influences have dried southwestern China relative to the preindustrial period.

An overall mean shift of PA toward a drier condition under ALL forcing relative to NAT forcing is clearly seen in the 2019 ensemble (Fig. 2b), suggesting an increase of probability of such precipitation deficit events over southwestern China due to human influences. The probability of the 2019-like event defined by PA is around 12% (9.54%–13.92%) in the 525 samples in the historicalExt experiment, while in the historicalNatExt ensemble the probability decreases to 2% (1.21%–2.95%). This gives a probability ratio of 6.16 (3.81–9.78). When we vary the spatial domain by reducing it by up to 3° or increasing it by up to 5° from all sides, the corresponding probability ratios and their 90% confidence intervals are still greater than 1. The maximum probability ratio is observed when each boundary is expanded by 1°, reaching 7.52. The shift of CDD probability distribution toward longer duration under ALL forcing relative to NAT forcing (Fig. 2c) further suggests that the anthropogenic influence tends to increase the probability of long dry spells and therefore favors a precipitation deficit. Previous studies indicated that the cooling effect of increased aerosols from human activities in East Asia could reduce the thermal differences between land and ocean during the late spring, which favors the formation of anomalous high pressure center in southwestern China (Kim et al. 2007; Hu and Liu 2013). Thus, we compared the PDFs of geopotential height anomaly in historicalExt and historicalNatExt simulations (Fig. 2e) and found that the Z500 over southwestern China under ALL forcing is significantly higher than that under NAT forcing. The differences in precipitation and Z500 between historicalExt and historicalNatExt (Fig. 2f) also prove this. An anomalous high height center is simulated in southwestern China, corresponding to negative anomalies of precipitation and high risk of precipitation deficit events.

In the CMIP6 simulations, the distributions of PA derived from historical and hist-nat experiments are significantly distinguished from each other for 2005–14, as the p value of the Kolmogorov–Smirnov test is near zero (see Fig. ES1a in the supplemental material). The distribution shifts toward a drier regime from the hist-nat to historical experiments with a probability ratio near 1.4 (1.14–1.94), indicating a clear human influence for the observed precipitation deficit event. Further comparison of the historical, hist-aer, and hist-GHG simulation results (Fig. ES1b) shows that a 2019-like event is more frequent under anthropogenic aerosol forcing but less frequent under greenhouse gas forcing relative to the hist-nat simulation, thus suggesting that the increased probability of low PA under historical forcing experiment relative to hist-nat forcing is due to changes in aerosols.

Conclusions.

The human influence on the severe May–June 2019 precipitation deficit in southwestern China is analyzed with observational, HadGEM3-GA6, and CMIP6 model data. The results based on HadGEM3-GA6 ensembles show that the probability of extremely low precipitation in May–June similar to or more severe than the observed 2019 event has increased by about sixfold in the ALL simulations compared to the NAT simulations. Anthropogenic influence has significantly increased the chance for the occurrence of such events through increasing the probability of anomalous high pressure in south-

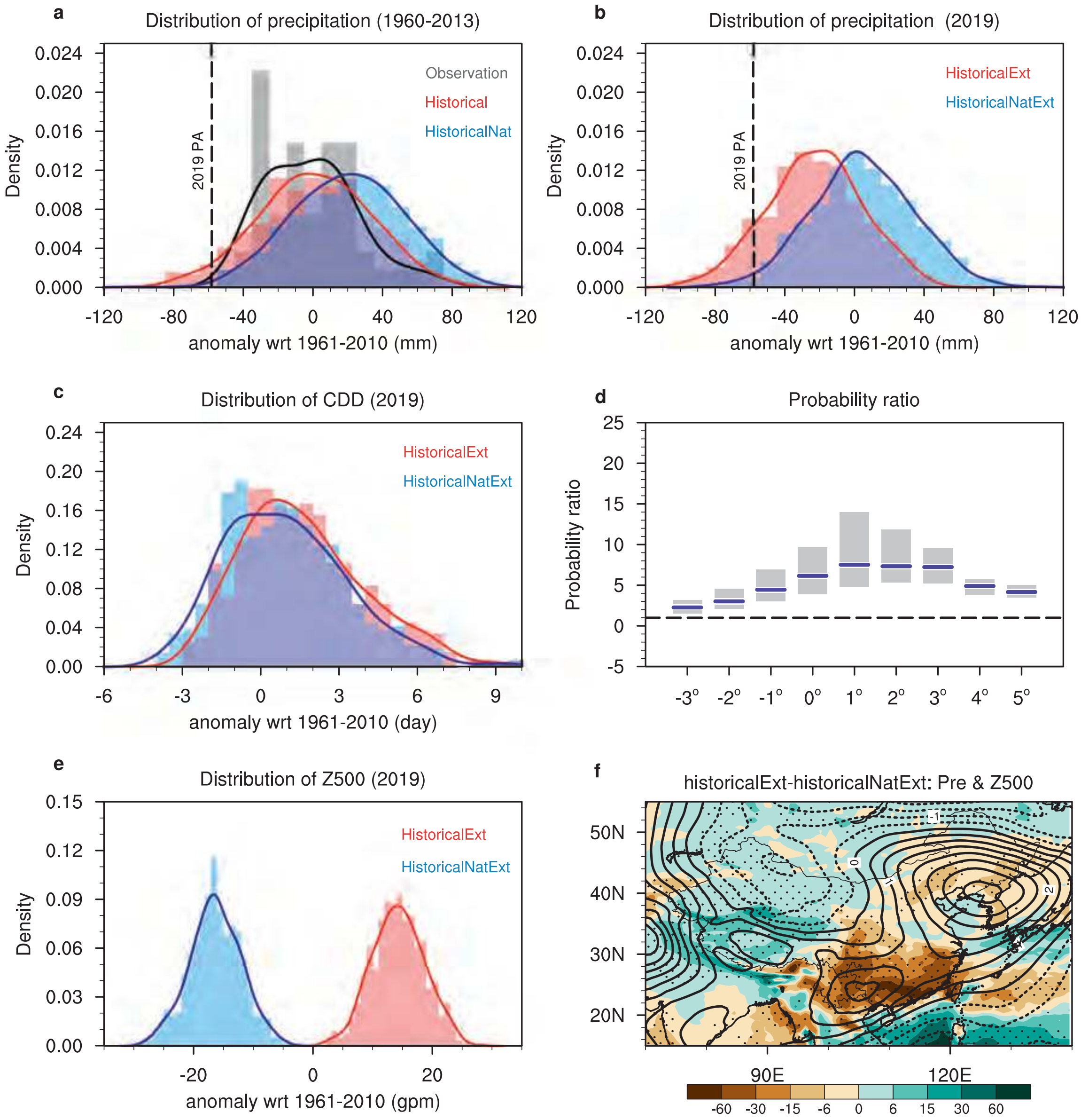

Fig. 2. Kernel estimate of the probability density function and histograms of (a),(b) PA (mm), (c) CDD (day) anomalies, averaged over Yunnan (black box of Fig. 1a), and (e) Z500 anomalies averaged over 15°–30°N, 90°–120°E. Anomalies in model simulations are relative to 1961–2010 climatology in historical simulation. Results are shown for (a) observations (black), historical (red), and historicalNat simulations (blue) during 1960–2013 and (b),(c),(e) historicalExt (red) and historicalNatExt (blue) 2019 simulations. The dashed black line denotes the observed event in 2019. (d) The probability ratios (blue lines) and 90% confidence intervals (gray shadings) for different study areas; 0° denotes the selected area in the study, 1° denotes increasing area by moving each boundary by 1°, and –1° denotes reducing area by moving each boundary by 1°. (f) Differences of precipitation (shading; mm) and Z500 (contour; m) between historicalExt and historicalNatExt ensembles. Dots indicate 5% significance level for precipitation.

western China (Figs. 2f, Fig. ES2). This result is robust to perturbations in the region definition. Analysis of the CMIP6 ensemble also finds an increasing risk of severe precipitation deficit, while the smaller PR in CMIP6 also implies that the HadGEM3-GA6 model might overestimate the response to anthropogenic forcing. Compared with the observation results, the stronger drying trend in HadGEM3-GA6 historical simulations also implies this, but compared with the historicalNat results this stronger trend indicates an apparent signal of anthropogenic influence.

Acknowledgments. This study was supported by the National Key R&D Program of China (2018YFA0605604, 2018YFC1507701), the National Natural Science Foundation of China (41775082) and largely carried out during a workshop at Sun Yat-sen University, China sponsored by the U.K.–China Research and Innovation Partnership Fund through the Met Office Climate Science for Service Partnership (CSSP) China as part of the Newton Fund. SFBT, BD and FL supported by the U.K.–China Research and Innovation Partnership Fund through the Met Office Climate Science for Service Partnership (CSSP) China as part of the Newton Fund.

References

Christidis, N., and P. A. Stott, 2015: Extreme rainfall in the United Kingdom during winter 2013/14: The role of atmospheric circulation and climate change. *Bull. Amer. Meteor. Soc.*, **96**, S46–S50, https://doi.org/10.1175/BAMS-D-15-00094.1.

——, ——, A. A. Scaife, A. Arribas, G. S. Jones, D. Copsey, J. R. Knight, and W. J. Tennant, 2013: A new HadGEM3-A based system for attribution of weather- and climate-related extreme events. *J. Climate*, **26**, 2756–2783, https://doi.org/10.1175/JCLI-D-12-00169.1.

Ciavarella, A., and Coauthors, 2018: Upgrade of the HadGEM3-A based attribution system to high resolution and a new validation framework for probabilistic event attribution. *Wea. Climate Extremes*, **20**, 9–32, https://doi.org/10.1016/j.wace.2018.03.003.

CMA, 2020a: China Climate Bulletin 2019 (in Chinese with English abstract). China Meteorological Administration, 54 pp.

——, 2020b: Yearbook of Meteorological Disasters in China 2019 (in Chinese with English abstract). China Meteorological Administration, in press.

Eyring, V., S. Bony, G. A. Meehl, C. A. Senior, B. Stevens, R. J. Stouffer, and K. E. Taylor, 2016: Overview of the Coupled Model Intercomparison Project Phase 6 (CMIP6) experimental design and organization. *Geosci. Model Dev.*, **9**, 1937–1958, https://doi.org/10.5194/gmd-9-1937-2016.

Feng, L., T. Li, and W. Yu, 2014: Cause of severe droughts in Southwest China during 1951–2010. *Climate Dyn.*, **43**, 2033–2042, https://doi.org/10.1007/s00382-013-2026-z.

Hu, N., and X. Liu, 2013: Modeling study of the effect of anthropogenic aerosols on late spring drought in south China. *Acta Meteor. Sin.*, **27**, 701–715, https://doi.org/10.1007/s13351-013-0506-z.

Kalnay, E., and Coauthors, 1996: The NCEP/NCAR 40-Year Reanalysis Project. *Bull. Amer. Meteor. Soc.*, **77**, 437–471, https://doi.org/10.1175/1520-0477(1996)077<0437:TNYRP>2.0.CO;2.

Kim, M.-K., W. K. M. Lau, K.-M. Kim, and W.-S. Lee, 2007: AGCM study of effects of radiative forcing of sulfate aerosol on large scale circulation and rainfall in East Asia during boreal spring. *Geophys. Res. Lett.*, **34**, L24701, https://doi.org/10.1029/2007GL031683.

Li, R., and Coauthors, 2021: Anthropogenic influences on heavy precipitation during the 2019 extremely wet rainy season in southern China. *Bull. Amer. Meteor. Soc.*, **102**, S103–S109, https://doi.org/10.1175/BAMS-D-20-0135.1

Lu, C., F. Lott, Y. Sun, P. Stott, and N. Christidis, 2020: Detectable anthropogenic influence on changes in summer precipitation in China. *J. Climate*, **33**, 5357–5369, https://doi.org/10.1175/JCLI-D-19-0285.1.

Ma, S., T. Zhou, O. Angélil, and H. Shiogama, 2017: Increased chances of drought in southeastern periphery of the Tibetan Plateau induced by anthropogenic warming. *J. Climate*, **30**, 6543–6560, https://doi.org/10.1175/JCLI-D-16-0636.1.

Shi, C., Z. Xie, H. Qian, M. Liang, and X. Yang, 2011: China land soil moisture EnKF data assimilation based on satellite remote sensing data. *Sci. China Earth Sci.*, **54**, 1430–1440, https://doi.org/10.1007/s11430-010-4160-3.

Sun, C., and S. Yang, 2012: Persistent severe drought in southern China during winter –spring 2011: Large-scale circulation patterns and possible impacting factors. *J. Geophys. Res.*, **117**, D10112, https://doi.org/10.1029/2012JD017500.

Sun, Y., S. Dong, T. Hu, X. Zhang, and P. Stott, 2019: Anthropogenic influence on the heaviest June precipitation in southeastern China since 1961. *Bull. Amer. Meteor. Soc.*, **100**, S79–S83, https://doi.org/10.1175/BAMS-D-18-0114.1.

Wang, L., W. Chen, W. Zhou, and G. Huang, 2015: Drought in southwest China: A review. *Atmos. Oceanic Sci. Lett.*, **8**, 339–344, https://doi.org/10.3878/AOSL20150043.

Xin, X., R. Yu, T. Zhou, and B. Wang, 2006: Drought in late spring of South China in recent decades. *J. Climate*, **19**, 3197–3206, https://doi.org/10.1175/JCLI3794.1.

Yang, J., D. Gong, W. Wang, and R. Mao, 2012: Extreme drought event of 2009/2010 over southwestern China. *Meteor. Atmos. Phys.*, **115**, 173–184, https://doi.org/10.1007/s00703-011-0172-6.

Yang, S., and Q. Li, 2014: Improvement in homogeneity analysis method and update of China precipitation data (in Chinese with English abstract). *Adv. Climate Change Res.*, **10**, 276–281, https://doi.org/10.3969/j.issn.1673-1719.2014.04.008.

Yuan, X., L. Wang, P. Wu, P. Ji, J. Sheffield, and M. Zhang, 2019: Anthropogenic shift towards higher risk of flash drought over China. *Nat. Commun.*, **10**, 4661, https://doi.org/10.1038/s41467-019-12692-7.

Zhang, W., and Coauthors, 2020: Anthropogenic influence on 2018 summer persistent heavy rainfall in central western China. *Bull. Amer. Meteor. Soc.*, **101**, S65–S70, https://doi.org/10.1175/BAMS-D-19-0147.1.

Zhang, X., L. Alexander, G. C. Hegerl, P. Jones, A. Klein Tank, T. C. Peterson, B. Trewin, and F. W. Zwiers, 2011: Indices for monitoring changes in extremes based on daily temperature and precipitation data. *Wiley Interdiscip. Rev.: Climate Change*, **2**, 851–870, https://doi.org/10.1002/wcc.147.

Anthropogenic Influences on Heavy Precipitation during the 2019 Extremely Wet Rainy Season in Southern China

Rouke Li, Delei Li, Nergui Nanding, Xuan Wang, Xuewei Fan, Yang Chen, Fangxing Tian, Simon F. B. Tett, Buwen Dong, and Fraser C. Lott

AFFILIATIONS: R. Li—State Key Laboratory of Loess and Quaternary Geology, Institute of Earth Environment, Chinese Academy of Sciences, Xi'an, and National Climate Center, China Meteorological Administration, Beijing, China; **D. Li**—CAS Key Laboratory of Ocean Circulation and Waves, Institute of Oceanology, Chinese Academy of Sciences, Qingdao, China; **Nanding**—Guangdong Province Key Laboratory for Climate Change and Natural Disaster Studies, School of Atmospheric Sciences, Sun Yat-sen University, Guangdong, China; **Wang**—Key Laboratory of Mesoscale Severe Weather, School of Atmospheric Sciences, Nanjing University, Nanjing, China; **Fan**—State Key Laboratory of Earth Surface Processes and Resource Ecology, Faculty of Geographical Science, Beijing Normal University, Beijing, China; **Chen**—State Key Laboratory of Severe Weather, Chinese Academy of Meteorological Sciences, Beijing, China; **Tian and Dong**—National Centre for Atmospheric Science, Department of Meteorology, University of Reading, Reading, United Kingdom; **Tett**—School of Geosciences, University of Edinburgh, Edinburgh, United Kingdom; **Lott**—Met Office Hadley Centre, Exeter, United Kingdom

CORRESPONDING AUTHOR: Nergui Nanding, mongolnandin@gmail.com

DOI:10.1175/BAMS-D-20-0135.1

A supplement to this article is available online (10.1175/BAMS-D-20-0135.2)

Anthropogenic forcings have reduced the likelihood of heavy precipitation in southern China like the 2019 March–July event by about 60%

During March to July 2019, southern China witnessed an extraordinarily long rainy season that was the third wettest on record with total precipitation (1,303 mm) exceeding the climatological (1961–2010) average by 281 mm (Fig. 1a). The so-called first rainy season (FRS), normally spanning from April to June, is the main contributor (40%–50%) to annual precipitation totals over southern China and dominates the rainfall variability there (Gu et al. 2018). Heavy precipitation can cause flooding and landslides, resulting in huge economic losses (Field et al. 2012).

Southern China, home to megacities like Guangzhou and Shenzhen, is highly populated, meaning a high exposure of population and infrastructure to precipitation extremes and resultant hydrological hazards (Burke and Stott 2017; Li et al. 2018; Zhang et al. 2020). During 6–13 June 2019, over 6 million people across several southern China provinces were affected by heavy rains, floods, and landslides. These extremes caused at least 91 deaths, collapsed over 19,000 houses, damaged around

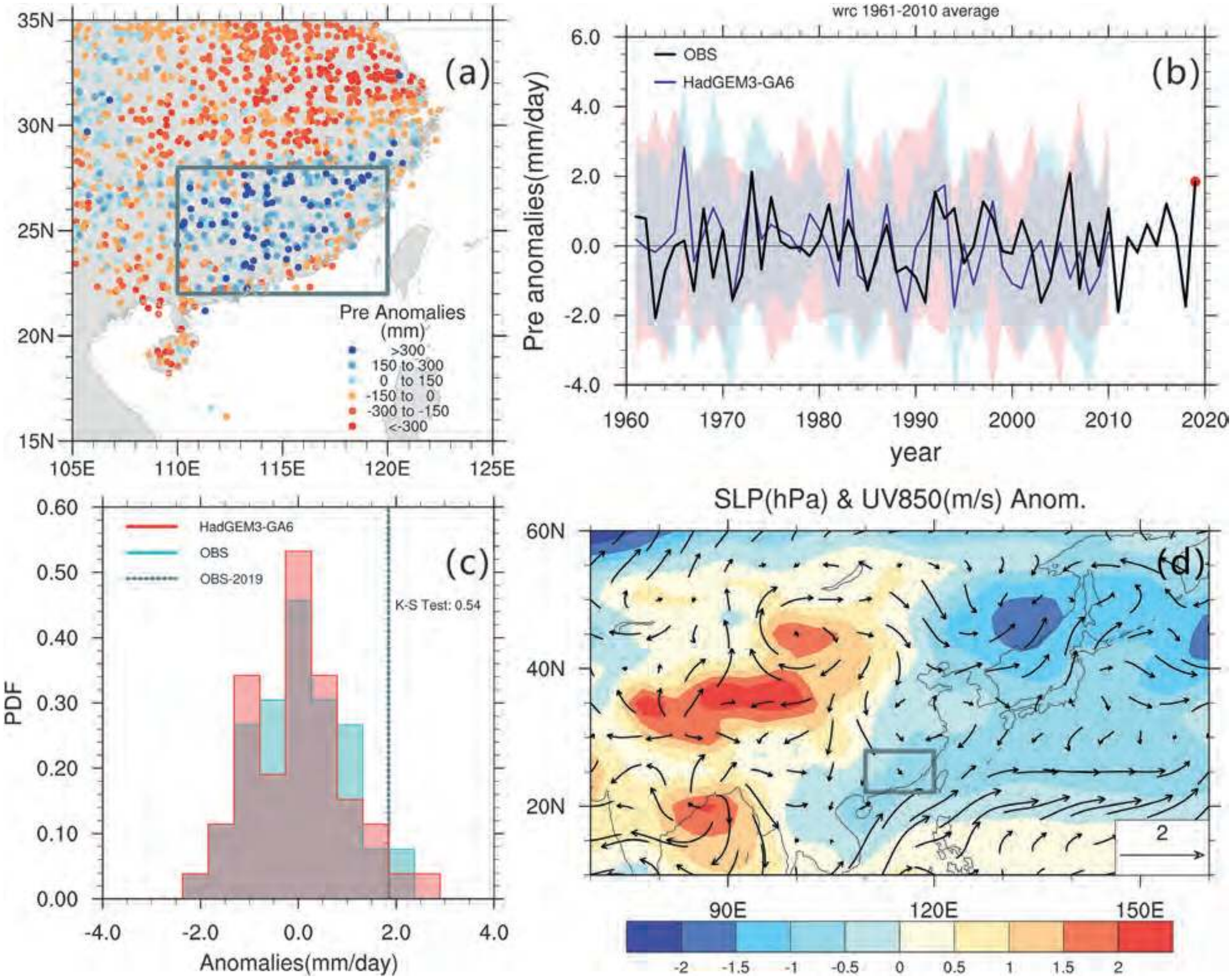

Fig. 1. (a) Observed March–July 2019 precipitation anomalies [mm (5 months)$^{-1}$] from rain gauges. (b) Time series of observations and simulated ensemble means of precipitation anomalies (solid lines), and uncertainty bounds of 15 members of HadGEM3-GA6 and 53 members of CMIP5 spread shown as pink and blue shading, respectively. (c) Probability density functions for the precipitation anomalies in the study region during March–July from 1961 to 2010 constructed with data from the HadGEM3-GA6 historical experiments (red) and OBS (green). (d) SLP (shading) and 850-hPa wind (vector) anomalies from NCEP reanalysis in March–July 2019. All anomalies are relative to 1961–2010 climatology. The gray box in (a) and (d) marks the study region.

83,000 houses, and affected 419,400 ha of crops (China Ministry of Emergency Management 2020). The direct economic loss was estimated to be more than 20 billion RMB (equivalent to 3 billion USD) (China Ministry of Emergency Management 2020). Understanding the driver for precipitation extremes is a key step toward formulating adaptation and mitigation strategies. This study aims to shed light on this scientific question by addressing potential anthropogenic influences on the probability of extremely wet seasons similar to the March–July 2019 event in this region.

Data and methods.

The March–July 2019 extreme precipitation event was bounded by 22°–28°N, 110°–120°E over southern China (Fig. 1a). Quality-controlled daily rainfall over 2,400 meteorological stations (Shen et al. 2010) during 1961–2019 was provided by the China National Meteorological Information Center. March–July 2019 precipitation at most rain gauges in this region was around 150 mm (1 mm day^{-1}) larger than normal (Fig. 1a).

Raw gauge observations were interpolated onto a 0.56° × 0.83° grid (the same as the model resolution) by using bilinear interpolation. These gridded values were area-weight averaged to obtain regional seasonal total precipitation time series. Then precipitation time series anomalies were calculated and a positive anomaly of 1.84 mm day^{-1} for the March–July 2019 event was used as the threshold (Fig. 1b) for the subsequent attribution analyses.

The HadGEM3-GA6 model (Ciavarella et al. 2018) at an N216 resolution of 0.56° × 0.83° was applied to investigate the role of anthropogenic forcings on the changing risks of the 2019-like seasonal precipitation extremes over southern China. The model outputs include all-forced simulations (historical) conditioned on the observed sea surface temperatures (SST) and sea ice (HadISST; Rayner et al. 2003) and natural simulations (historicalNat) with anthropogenic signals removed from observed SSTs and with preindustrial forcings. Both historical and historicalNat ensembles consist of 15 members during the historical period (1961–2013), and 525 members for 2019. Accordingly, occurrence probabilities and resultant attribution conclusions are conditioned on the 2019 SST patterns. The 1961–2010 climatology was constructed from the 15-member ensembles.

The models from phase 5 of the Coupled Model Intercomparison Project (CMIP5) were also included to further corroborate the attribution results. Since the historical runs terminate at the end of 2005, the CMIP5 historical runs were extended through 2006 with the representative concentration pathway 8.5 (RCP8.5) runs. This is because the projected greenhouse gas forcings of RCP8.5 are more consistent with the present realization than the other scenarios (Peters et al. 2013). The RCP8.5 simulations for 2009–28 are used as All and the natural-only forcing runs for 1961–80 are used as Nat (see Table ES1 in the online supplemental material for more details). The selection of time periods for both CMIP5 All and Nat simulations is to avoid impacts from major volcano activates like the 1991 eruption of Mount Pinatubo. Note that, unlike the HadGEM3-GA6 simulations based on 2019 SSTs, the CMIP5 simulations encompasses a wide range of ocean states. Consequently, the event probabilities estimated hereafter are differently conditioned, such that the results from the two datasets will not be directly comparable.

A Kolmogorov–Smirnoff (K-S) test was applied to test if the distributions of the observed and simulated precipitation anomalies during 1961–2010 are from the same population (Table ES1). The occurrence probability of events with equivalent or heavier precipitation than the 2019 event (anomaly of 1.84 mm day^{-1} with respect to the 1961–2010 climatology) in the entire HadGEM3-GA6 historical and historicalNat (or CMIP5 All and Nat) ensembles are indicated as P_{ALL} and P_{NAT} respectively, and the risk ratio (RR) is computed from P_{ALL}/P_{NAT}. The RR uncertainty with 90% confidence interval (90% CI) was estimated by identifying the empirical 5th and 95th percentile among 1,000 times resampling of model ensemble members by using Monte Carlo bootstrapping procedure (Christidis et al. 2013). Doing each bootstrap, model ensemble simulations are randomly resampled with replacement to get a set of new data with the same length as the original. Note that precipitation anomalies estimated from each model were calculated with their own 1961–2010 climatology, serving to remove the model climatological mean bias (Zhang et al. 2020).

Results and discussions.

The domain-averaged seasonal precipitation during March–July 2019 was 1.84 mm day^{-1} larger than the 1961–2010 climatology (Fig. 1b), equivalent to a 1-in-28-yr event in the 1961–2019 observations. This prolonged extreme seasonal precipitation event was mainly due to the early onset (by 28 days) and late cessation (by 22 days) of the first rainy season (CMA 2020).

The event was associated with an anomalous negative sea level pressure (SLP) covering southern China (Fig. 1d) and anomalous westerlies in the southwest of the center of the East Asian westerly jet stream at 200-hPa (Fig. ES1d), indicating an enhanced and southward displaced East Asian westerly jet stream in 2019. This anomalous circulation strengthens the high-level divergence and is conducive to the enhancement of deep convection and precipitation in southern China. The western Pacific subtropical high is enhanced and extended to the southwest (Fig. ES1c). This is accompanied by 850-hPa westerly and southwesterly wind anomalies over southern China and the northeastern portion of Indochina Peninsula (Fig. 1d), which enhances the climatological mean southwesterlies in southern China (Fig. ES1f). The wind anomalies further enhance the water vapor transport from the Indochina Peninsula (Fig. ES1b). This produces anomalous moisture flux convergence over southern China (negative values in Fig. ES1e), providing a favorable moisture environment for abundant precipitation. Meanwhile, the anomalous southwesterlies advect warm air toward southern China. With more evaporation from land, increased water vapor is further enhanced. These conditions are consistent with previous studies finding that above-normal FRS precipitation is often associated with an enhanced and southwestward-extended western Pacific subtropical high and an enhanced Asian westerly jet (Zhang et al. 2009; Gu et al. 2018).

Evaluation of the HadGEM3-GA6 simulations was carried out to see if this model could accurately reproduce the characteristics of precipitation in the study region. The distributions of observed and simulated precipitation anomalies (Fig. 1c) during March–July in 1961–2010 cannot be distinguished based on the K-S test (p value = 0.54; Table ES1). Note that while precipitation anomalies are reasonably simulated, HadGEM3-GA6 overestimates actual precipitation values. Moreover, both the HadGEM3-GA6 and CMIP5 models overestimate seasonal precipitation variability (figures omitted), leading to the underestimation of return periods for the 2019-like precipitation event, particularly for HadGEM3-GA6 (Table 1). These results are consistent with the precipitation variability maps shown in Knutson and Zeng (2018).

The probability density functions (PDFs) of the 2019-like persistent precipitation events from both models show the historical simulations shifting toward drier rainy seasons compared to the historicalNat simulations (Figs. 2a,c). This gives a estimated risk ratio of 0.43 (90% CI: 0.31, 0.57) and 0.38 (90% CI: 0.32, 0.44) for the CMIP5 and HadGEM3-GA6 ensembles respectively (Table 1), which implies that anthropogenic forcings have reduced the likelihood of a 2019-like extreme seasonal precipitation event over southern China by around 60%. Most of the best estimates of RR values of individual CMIP5 models are less than 1, except for GFDL-ESM2M and GISS-E2-H (Fig. ES2). Moreover, the changes in return periods also demonstrate that the 2019-like prolonged rainy seasonal precipitation occurs less frequently due to anthropogenic influences and it changes from a 1-in-4-yr event for historicalNat simulations to a 1-in-9-yr event for Historical simulations (Figs. 2b,d; Table 1). Although the HadGEM3-GA6 2019 simulations are atmospheric model simulations and conditional to 2019 SST pattern, their attribution results are consistent with the CMIP5 results, which take into account the variability in SST patterns.

The results are consistent with the findings in Zhang et al. (2020) that anthropogenic forcings reduced the probability of long-lasting heavy rainfall in central western China. The reduced probability of persistent heavy rainfall due to anthropogenic

Table 1. The best estimate and 90% confidence intervals of return period and risk ratio estimated with HadGEM3-GA6 and CMIP5 models.

Models		Return period (yr) (90% CI)	Risk ratio (90% CI)
HadGEM3-GA6	historical	8.78 (6.12, 13.17)	0.38 (0.32, 0.44)
	historicalNat	3.31 (2.83, 4.35)	
CMIP5	All	15.79 (9.46, 33.10)	0.43 (0.31, 0.57)
	Nat	6.95 (5.48, 9.92)	

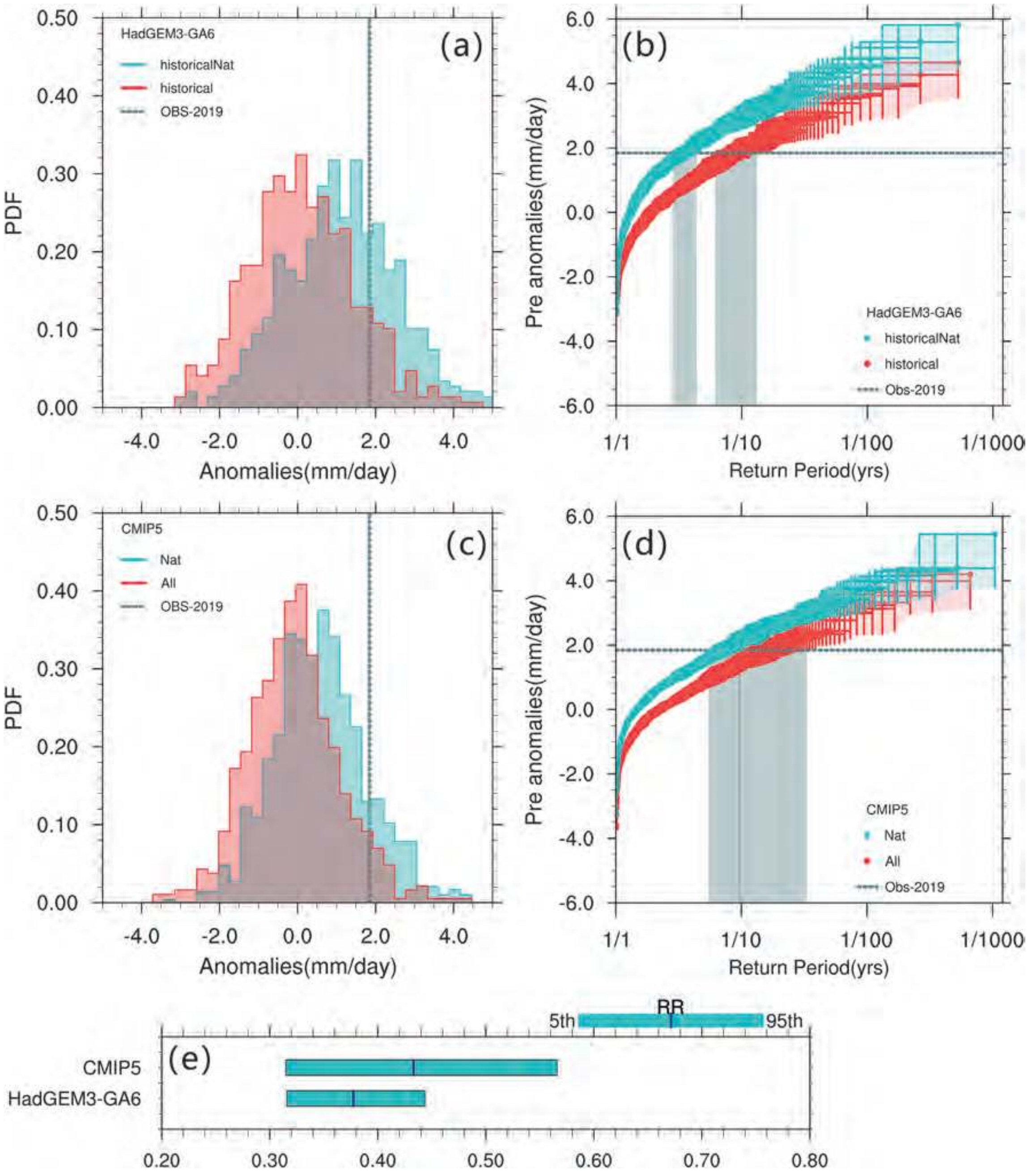

Fig. 2. Probability density functions of (a) HadGEM3-GA6 and (c) CMIP5 All (2009–28) and Nat (1961–80) ensembles simulations of March–July 2019 precipitation anomalies (mm day^{-1}) in the study region. Return period for the (b) HadGEM3-GA6 and (d) CMIP5 All and Nat ensemble simulations. Each marker represents an ensemble member, and the green and red lines indicate the return period for historical and historicalNat, respectively. The errors bars indicate the 90% confidence interval using bootstrap resampling by 1,000 times. (e) Best estimates (blue lines) and 90% confidence intervals (aqua shadings) of risk ratio for CMIP5 and HadGEM3-GA6.

forcings could be mainly due to increased aerosols in the climate system (Song et al. 2014; Li et al. 2015; Zhang and Li 2016; Burke and Stott 2017). Specifically, by scattering and absorbing solar radiation, aerosols can induce surface cooling through aerosol–radiation interactions, and therefore can lead to reduced precipitation by increasing atmospheric stability. Aerosols also interact directly with cloud by serving as cloud condensation nuclei or ice nuclei, leading to changes in cloud radiative properties and reducing precipitation efficiency (Rosenfeld et al. 2008). In addition, increased aerosols can weaken land–sea thermal contrast and therefore lead to weakening of the monsoon circulation and reduced precipitation over monsoon regions (Dong et al. 2019; Zhou et al. 2020). The impacts of anthropogenic forcings on changing risks of persistent precipitation events are also emphasized by the findings in Ji et al. (2020). They demonstrated that the anthropogenically induced climate change has reduced the likelihood of extreme flooding by around 34% over the Yellow River basins during summer, consistent with our result. In addition, Lu et al. (2021) used HadGEM3-GA6 to reveal that anthropogenic forcings have reduced precipitation in favor of severe drought development during May–June over southwestern China.

Conclusions.

Using large ensembles of HadGEM3-GA6 and CMIP5 models, anthropogenic influences on changing risks of the 2019 March-to-July-like extreme rainy seasonal precipitation in southern China were quantified. Results based on these two models consistently indicate similar cases are less likely to occur in the current climate compared to the natural world. Specifically, anthropogenic forcings have made the probability of an extreme seasonal precipitation event like 2019 approximately 60% less likely.

Acknowledgments. This study was conducted during the Operational Attribution Workshop at Sun Yat-Sen University, jointly sponsored by the National Key R&D Program (2018YFC1507700), the U.K.-China Research and Innovation Partnership Fund through the Met Office Climate Science for Service Partnership (CSSP) China as part of the Newton Fund, and the Natural Science Foundation (NSF) of China (41975105), RL was funded by the National Key R&D Program (2017YFA0605004) and the NSF of China (41991254), DL was funded by the NSF of China (41706019) and the Strategic Priority Research Program of the Chinese Academy of Sciences (XDB42000000), NN was funded by the NSF of China (41905101, 41975113, and 41861144014) and the Fundamental Research Funds for the Central Universities (20lgpy25), ST, BD, and FL were supported by the U.K.-China Research and Innovation Partnership Fund through the Met Office Climate Science for Service Partnership (CSSP) China as part of the Newton Fund.

References

Burke, C., and P. Stott, 2017: Impact of anthropogenic climate change on the East Asian summer monsoon. *J. Climate*, **30**, 5205–5220, https://doi.org/10.1175/JCLI-D-16-0892.1.

China Ministry of Emergency Management, 2020: 2019 top 10 natural disasters in China, accessed 13 April 2020, https://www.mem.gov.cn/xw/bndt/202001/t20200116_343570.shtml.

Christidis, N., P. A. Stott, A. A. Scaife, A. Arribas, G. S. Jones, D. Copsey, J. R. Knight, and W. J. Tennant, 2013: A new HadGEM3-A-based system for attribution of weather- and climate-related extreme events. *J. Climate*, **26**, 2756–2783, https://doi.org/10.1175/JCLI-D-12-00169.1.

Ciavarella, A., and Coauthors, 2018: Upgrade of the HadGEM3-A based attribution system to high resolution and a new validation framework for probabilistic event attribution. *Wea. Climate Extreme*, **20**, 9–32, https://doi.org/10.1016/j.wace.2018.03.003.

CMA, 2020: China Climate Bulletin 2019. China Meteorological Administration, 20 pp.

Dong, B., L. J. Wilcox, E. J. Highwood, and R. T. Sutton, 2019: Impacts of recent decadal changes in Asian aerosols on the East Asian summer monsoon: Roles of aerosol–radiation and aerosol–cloud interactions. *Climate Dyn.*, **53**, 3235–3256, https://doi.org/10.1007/s00382-019-04698-0.

Field, C. B., and Coauthors, 2012: Managing the Risks of Extreme Events and Disasters to Advance Climate Change Adaptation. Cambridge University Press, 582 pp.

Gu, W., L. Wang, Z.-Z. Hu, K. Hu, and Y. Li, 2018: Interannual variations of the first rainy season precipitation over South China. *J. Climate*, **31**, 623–640, https://doi.org/10.1175/JCLI-D-17-0284.1.

Ji, P., X. Yuan, Y. Jiao, C. Wang, S. Han, and C. Shi, 2020: Anthropogenic contributions to the 2018 extreme flooding over the upper Yellow River basin in China. *Bull. Amer. Meteor. Soc.*, **101**, S89–S94, https://doi.org/10.1175/BAMS-D-19-0105.1.

Knutson, T. R., and F. Zeng, 2018: Model assessment of observed precipitation trends over land regions: Detectable human influences and possible low bias in model trends. *J. Climate*, **31**, 4617–4637, https://doi.org/10.1175/JCLI-D-17-0672.1.

Li, C., and Coauthors, 2018: Attribution of extreme precipitation in the lower reaches of the Yangtze River during May 2016. *Environ. Res. Lett.*, **13**, 014015, https://doi.org/10.1088/1748-9326/aa9691.

Li, X., M. Ting, C. Li, and N. Henderson, 2015: Mechanisms of Asian summer monsoon changes in response to anthropogenic forcing in CMIP5 models. *J. Climate*, **28**, 4107–4125, https://doi.org/10.1175/JCLI-D-14-00559.1.

Lu, C., J. Jiang, R. Chen, S. Ullah, R. Yu, F. C. Lott, S. F. B. Tett, and B. Dong, 2021: Anthropogenic influence on 2019 May–June extremely low precipitation in southwestern China [in "Explaining Extremes of 2019 from a Climate Perspective"]. *Bull. Amer. Meteor. Soc.*, **102,** S97–S102, https://doi.org/10.1175/BAMS-D-20-0128.1.

Peters, G. P., and Coauthors, 2013: The challenge to keep global warming below 2°C. *Nat. Climate Change*, **3**, 4–6, https://doi.org/10.1038/nclimate1783.

Rayner, N. A., D. E. Parker, E. B. Horton, C. K. Folland, L. V. Alexander, D. P. Rowell, E. C. Kent, and A. Kaplan, 2003: Global analyses of sea surface temperature, sea ice, and night marine air temperature since the late nineteenth century. *J. Geophys. Res.*, **108**, 4407, https://doi.org/10.1029/2002JD002670.

Rosenfeld, D., U. Lohmann, G. B. Raga, C. D. O'Dowd, M. Kulmala, S. Fuzzi, A. Reissell, and M. O. Andreae, 2008: Flood or drought: How do aerosols affect precipitation? *Science*, **321**, 1309–1313, https://doi.org/10.1126/science.1160606.

Shen, Y., A. Xiong, Y. Wang, and P. Xie, 2010: Performance of high-resolution satellite precipitation products over China. *J. Geophys. Res.*, **115**, D02114, https://doi.org/10.1029/2009JD012097.

Song, F., T. Zhou, and Y. Qian, 2014: Responses of East Asian summer monsoon to natural and anthropogenic forcings in the 17 latest CMIP5 models. *Geophys. Res. Lett.*, **41**, 596–603, https://doi.org/10.1002/2013GL058705.

Zhang, J., T. Zhou, R. Yu, and X. Xin, 2009: Atmospheric water vapor transport and corresponding typical anomalous spring rainfall patterns in China. *Chin. J. Atmos. Sci.*, **33**, 121–134.

Zhang, L., and T. Li, 2016: Relative roles of anthropogenic aerosols and greenhouse gases in land and oceanic monsoon changes during past 156 years in CMIP5 models. *Geophys. Res. Lett.*, **43**, 5295–5301, https://doi.org/10.1002/2016GL069282.

Zhang, W., and Coauthors, 2020: Anthropogenic influence on 2018 summer persistent heavy rainfall in central western China. *Bull. Amer. Meteor. Soc.*, **101**, S65–S70, https://doi.org/10.1175/BAMS-D-19-0147.1.

Zhou, T., W. Zhang, L. Zhang, X. Zhang, Y. Qian, D. Peng, S. Ma, and B. Dong, 2020: The dynamic and thermodynamic processes dominating the reduction of global land monsoon precipitation driven by anthropogenic aerosols emission. *Sci. China Earth Sci.*, **63**, 919–933, https://doi.org/10.1007/s11430-019-9613-9.